Western University
Scholarship@Western

Electronic Thesis and Dissertation Repository

April 2016

Engineered quantum dots for EVA nanocomposite films and TiO2 photocatalysts

Md Abdul Mumin
The University of Western Ontario

Supervisor
Paul A. Charpentier
The University of Western Ontario

© Md Abdul Mumin 2016

Abstract

Polymer/inorganic nanocomposites are of great interest because they can significantly improve the properties of existing polymeric materials. Currently, light absorbing inorganic nanoparticles in transparent plastics such as poly(ethylene-co-vinyl acetate) (EVA) are of enormous interest in emerging solar materials, including photovoltaic (PV) modules and commercial greenhouse films. However, achieving a high level of nanoparticle dispersion without compromising optical, and thermal properties has been a key challenge in the production of such advanced materials. Nanocrystalline semiconductor or quantum dots (QDs) have the potential to absorb UV light and selectively emit visible light. However, how to stabilize the QDs for long product life spans without "blinking" while enabling their easy integration into polymer systems is lacking. This work examines different approaches for loading mesoporous silica encapsulated QDs into EVA polymer films which can control plant growth in greenhouses or enhance PV panel efficiencies.

Highly luminescent CdS and CdS-ZnS core-shell QDs with 5 nm sizes were synthesized using a modified facile approach based on the pyrolysis of single molecule precursor, cadmium diethyldithiocarbamate and capping the core CdS QDs with a thin shell layer of ZnS. To make both the bare and core-shell structure QDs more resistant against photochemical reactions, a mesoporous silica layer was grown onto the QDs through a reverse microemulsion technique based on hydrophobic interactions, controlling the shell thickness. By careful experimental tuning, this encapsulation technique was found to provide high quantum yields (~65%) and high photostability compared to the bare QDs. Both the encapsulated bare and core-shell QDs were then melt-mixed with EVA pellets using a mini twin-screw extruder and pressed into thin films with controlled thickness. A novel supercritical carbon dioxide ($scCO_2$) processing method was also explored that utilizes $scCO_2$ to disperse silica encapsulated core-shell quantum dots into EVA.

The results demonstrated that mesoporous silica not only enhanced the quantum yield and photostability of the QDs but also improved the compatibility and dispersibility of QDs

throughout the EVA films. The novel light selective films show high visible light transmission (~90%) and decreased UV transmission (~75%). Also, the experimental MSNs showed improved infrared and thermal wavebands retention in the EVA transparent films compared to commercial silica additives, even at lower concentrations.

A *grafting from* methodology examining ethylene and vinyl acetate co-polymerization from the functionalized nanoparticles of silica encapsulated CdS-ZnS QDs in supercritical CO_2 was also developed. To improve the compatibility with polymer, the silica was functionalized by using a vinyltrimethoxy silane linker molecule. The functionalization and polymerization were explored both by one-step (together) and two-step (separately) processes. Silica encapsulated QDs synthesized by the two-step process showed excellent compatibility and uniform dispersion throughout the EVA network. The novel light selective EVA nanocomposites also showed improved optical properties with more than 50% UV shielding while retaining more than 95% visible light transmission even for a very low loading of nanoparticles (~1%).

Beside polymer nanocomposites, a facile process has been developed to fabricate nanocomposite photo-catalysts of porous TiO_2 nanowires with bare CdS or core-shell CdS-ZnS QDs, where the QD particles are linked covalently to the titania surface through a bifunctional organic linker, mercapto propionic acid (MPA). The bifunctional linking molecule, MPA, was found to effectively disperse and stabilize the QD nanoparticles. The photocatalytic activities of the prepared catalysts were evaluated under ultraviolet and visible light solar irradiation for the photodegradation of methylene blue (MB), an organic dye. A maximum photodegradation efficiency of MB dye (~88%) was obtained by core-shell CdS-ZnS QDs linked with nano TiO_2. After 3 cycling tests of degradation, the loss of photoactivity was significantly minimized (from 68% to 10%) by CdSZnS-MPA-TiO_2 compared to CdSZnS-TiO_2 (by direct deposition).

Keywords

Quantum dots, Encapsulation, Surface functionalization, Photostability, Poly(ethylene-co-vinyl acetate), Optical properties, Thermal Properties, Supercritical CO_2, *Grafting from* polymerization, TiO_2 nanowires, Photocatalysis.

Co-authorship statement

Title: Quantum dots/silica/polymer nanocomposite films with high visible light transmission and UV shielding properties

Authors: Md Abdul Mumin, William Z. Xu, Paul A. Charpentier

The experimental works were conducted by Md Abdul Mumin under the guidance of advisor Prof. Paul A. Charpentier. Dr. William Z. Xu had help in fruitful discussion and experimental set-up during optical properties experiments. Data analysis and the manuscript was written by Md Abdul Mumin under the close supervision of Prof. Paul A. Charpentier. The final version of this article was published by the Nanotechnology, 2015, **26**, 315702-315715.

Title: Multifunctional mesoporous silica nanoparticles in poly(ethylene-co-vinyl acetate) for transparent heat retention films

Authors: Md Abdul Mumin, Kazi Farida Akhter, Sara Dresser, Sasha T. van Dinther, Wei Wu, Paul A. Charpentier

The nanoparticles and nanocomposites development, experimental works were conducted by Md Abdul Mumin under the guidance of advisor Prof. Paul A. Charpentier. Thermicity testing and confocal imaging were carried out with help of Kazi Farida Akhter. AFM analysis was done by Sara Dresser. Nanocomposite films of different thickness using universal film maker were prepared with the help of Sasha T. van Dinther. Dr. Wei Wu had help in fruitful discussion and experimental set-up during thermal conductivity experiments. The manuscript was written by Md Abdul Mumin corrected by Prof. Paul A. Charpentier. The final version of this article was published by the Journal of Polymer Science Part B: Polymer Physics, 2015, **53**, 851-859.

Title: Supercritical CO_2 dispersion of quantum dots@silica nanoparticles in EVA nanocomposites and their optical properties

Authors: Md Abdul Mumin, William Z. Xu, Paul A. Charpentier

The experimental works were conducted by Md Abdul Mumin under the guidance of advisor Prof. Paul A. Charpentier. Dr. William Z. Xu had help in fruitful discussion on experimental design and execution of polymerization experiments. Data analysis and the draft of this chapter was written by Md Abdul Mumin and corrected by Prof. Paul A. Charpentier. This manuscript is under preparation for publication.

Title: Supercritical CO_2 synthesized TiO_2 nanowires covalently linked with core-shell CdS-ZnS quantum dots: enhanced photocatalysis and stability

Authors: Md Abdul Mumin, Golam Moula, Paul A. Charpentier

The nanoparticles synthesis, functionalization, and nanocomposites development, characterization were conducted by Md Abdul Mumin under the guidance of advisor Prof. Paul A. Charpentier. TiO_2 nanowires synthesis using supercritical CO_2 was carried out by Dr. Golam Moula. All photocatalysis experiments were done by Md Abdul Mumin. The manuscript was written by Md Abdul Mumin corrected by Prof. Paul A. Charpentier. The final version of this article was published by the RSC Advances, 2015, **5**, 67767-67779.

Dedication

To the people whose love and support make my life meaningful

my wife

my son

my parents

and

my parents-in-laws

Acknowledgments

I would like to gratefully acknowledge to my supervisor Prof. Paul A. Charpentier for his enthusiastic support and continued guidance throughout the course of my PhD research. The encouragement and support he has provided me over the past years have been and will continue to be indispensable for my professional development.

My special thanks to Dr. William Z. Xu for his great support and helpful discussion during supercritical reactor set-up and optical property studies.

I would also thank all my colleagues in Prof. Charpentier's Lab for their continuous support, encouragement, throughout this endeavor, and nice time that we have had together.

Also, I would dearly like to thank my family including my wife, my son, my parents, my siblings, and in-laws family. They all deserve much credit for their immeasurable love, support, encouragement, tremendous patience and prayer for me.

Table of Contents

List of Schemes

List of Figures

List of Tables

List of Appendices

List of Abbreviations

AFM	atomic force microscopy
ATR	attenuated total refraction
BET	Brunauer-Emmett-Teller
CB	conduction band
CBD	chemical bath deposition
DEPDC	diethyl peroxy dicarbonate
DMSO	dimethyl sulfoxide
EDX	energy dispersive X-ray spectroscopy
EVA	ethylene-*co*-vinyl acetate
FIB	focused ion beam
FTIR	Fourier transform infrared spectroscopy
HALS	hindered amine light stabilizer
HR-TEM	high resolution-transmission electron microscopy
HUVEC	human umbilical vein endothelial cell lines
LED	light emitting diode
LSCM	laser scanning confocal microscopy
LSM	laser scanning microsopy
MB	methylene blue
MCM	mobile ctrystalline material
MPA	mercapto propionic acid
MPS	3-mercapsto propyl trimethoxy silane
MSNs	mesoporous silica nanoparticles
MTT	3-(4,5-dimethylthiazol-2-yl)-2,5-diphenyltetrazolium bromide

NCs	nanocrystals
NPs	nanoparticles
NIR	near infrared
NMR	nuclear magnetic resonance
OA	oleic acid
OLA	oleyl amine
PAR	photosynthetic active radiation
P_c	critical pressure
PEN	poly(ethylene nanphthalate)
PET	poly(ethylene ptherephthalate)
PEVA	poly(ethylene vinyl acetate)
PL	photoluminescence
PMMA	poly(methyl methacrylate)
PP	polypropylene
PS	polystyrene
PV	photovoltaic
QDs	quantum dots
QY	quantum yield
SEM	scanning electron microscopy
SCF	supercritical fluid
$scCO_2$	supercritical carbon dioxide
T_c	critical temperature
TEM	transmission electron microscopy
TEOS	tetraethyl orthosilicate
TGA	thermo gravimetric analysis

THF	tetra hydro furan
TiO_2	titania
TIP	titanium isopropoxide
TOA	trioctyl amine
TOP	tri-n-octyl phospine
UFM	universal film maker
UV	ultraviolet
VA	vinyl acetate
VB	valance band
Vis	visible
VTMS	vinyl trimethoxy silane
XPS	X-ray photoelectron spectroscopy
XRD	X-ray diffraction

Chapter 1

General Introduction

1.1 Quantum Dots (QDs)

Quantum dots (QDs) are tiny particles or nanocrystals of a semiconducting material with diameters in the range of 2-10 nanometers, being comprised of a few to several thousand of atoms [1]. QDs were first discovered in solids in 1980 by Russian physicist Alexei Ekimov while working at the Vavilov State Optical Institute [2]. In late 1982, American chemist Louis E. Brus, then working at Bell Laboratories (and now a professor at Columbia University), discovered the same phenomenon in colloidal solutions. These two scientists shared the Optical Society of America's 2006 R.W. Wood Prize for their pioneering work. Professor Moungi Bawendi, at MIT, invents a technique in 1993 based on pyrolysis of organometallic precursors for the preparation of QDs with consistent structure, surface derivatization and a high degree of monodispersity [3].

QDs display unique electronic properties, intermediate between those of bulk semiconductors and discrete molecules, that are partly the result of the enormously high surface area for these particles [4-6]. QDs generate multiple exciton (photoinduced electron-hole pairs) from the absorption of a single photon that improves the efficiency of the solar photoconversion [7, 8]. In QDs, quantum confinement effects increase the separation between the energy levels in both the valence and conduction bands. This increased separation reduces waste heat, enhances multiple exciton generation process, and inhibits photons cooling [9]. One of the most interesting properties of QDs is fluorescence, wherein the nanocrystals can produce distinctive colors determined by the size of the particles (Figure 1.1**)**. QDs can emit photons corresponding to their respective energy band gaps when their electrons fall to stable ground states after reaching their respective excited states. The band gaps of the QDs can be tailored by changing the type of QD, and/or the size, which are tunable by controlling the reaction conditions such as residence time and reaction temperature [10]. The most common QDs are the binary semiconductor compounds consisting of II-VI elements, i.e., cadmium sulfide (CdS), cadmium selenide (CdSe), cadmium telluride (CdTe), zinc selenide (ZnSe), lead sulfide (PbS), and mercury sulfide (HgS), etc. QDs composed of group III-V elements, i.e., indium phosphide (InP), gallium nitride (GaN), indium arsenide (InAs), etc. are also of tremendous interest. Moreover, some QDs composed of single element
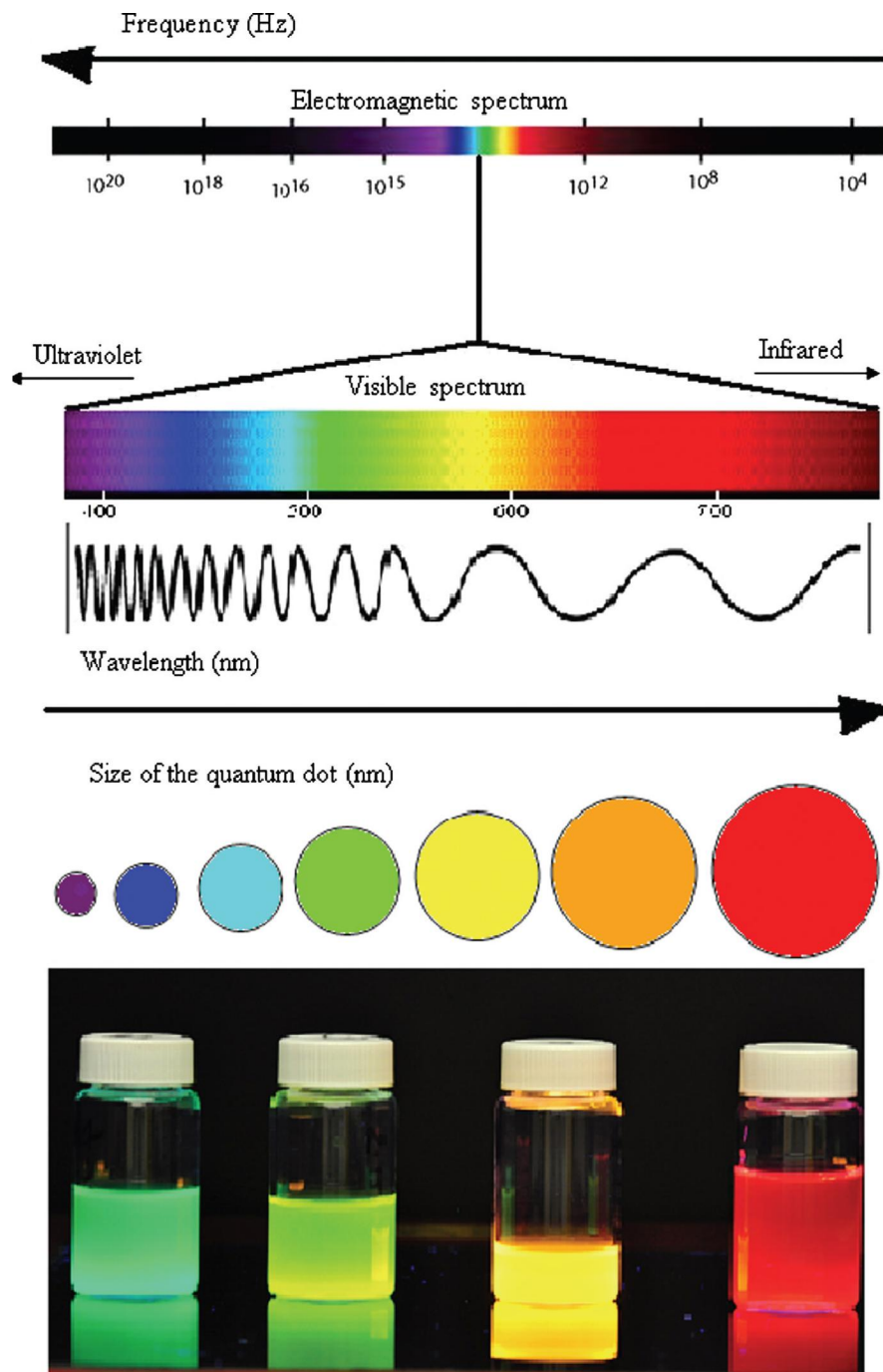
Figure 1.1. Ultraviolet, visible, and infrared light in the electromagnetic spectrum, and size tunable emission of the QDs (adapted from [1]).

(such as silicon), or of ternary elements with two of them in either cation or anion site (such as CdTeS, CdZnS, CdSSe, InNP, etc.) have also been reported. All these QDs compositions are semiconductors with the bulk band gap energy of usually less than 4 eV [11]. Recently carbon-based QDs consisting of carbon QDs (CQDs or CDs) or graphene QDs (GQDs) have emerged as a new class of semiconductor nanocrystals with superior aqueous solubility, chemical inertness, biocompatibility, facile passivation and modification potentialities [12, 13].

1.1.1   Photo-physical properties of QDs

The unique physical properties of quantum dots originate from the quantum confinement of the electron–hole pair. In QDs, the electronic energy levels are not continuous as in the bulk but are discrete (finite density of states), because of the confinement of the electronic wave function to the physical dimensions of the particles. This phenomenon is called quantum confinement. When the radii of the QDs is smaller than the exciton Bohr radius (exciton Bohr radius is the average distance between the electron in the conduction band and the hole it leaves behind in the valence band), there is quantization of the energy levels according to Pauli's exclusion principle (Figure 1.2) [14, 15]. Generally, as the size of the crystal decreases, the difference in energy between the highest valence band and the lowest conduction band increases. More energy is then needed to excite the dot, and concurrently, more energy is released when the electron returns to its ground state, resulting in a color shift from red to blue in the emitted light. As a result of this phenomenon, quantum dots can emit any color of light from the same material simply by changing the dot size. Additionally, because of the high level of control possible over the size of the nanocrystals produced, quantum dots can be tuned during manufacturing to emit any color of light [16].

So far, QDs have attracted interest because of their unique and tunable optical properties. Different from many organic dyes, QDs can be excited by many light sources within a large wavelength range, since QDs have continuous and broad absorption spectra. Furthermore,

many kinds of QDs can be excited by the same light source and their emission can be easily separated. The emission light spectra of QDs is narrower and more symmetric than conventional organic dyes, making the sensitivity of detection higher than for organic dyes [17]. The size of the QDs has a direct effect on the optical properties and the frequency of fluorescent light emitted or absorbed. Smaller dots emit higher energy light that is bluer in color, whereas larger dots emit lower energy red light. The shape and structure of the QDs also plays a role in the tuning of the fluorescent emission. A protective shell (core/shell QDs) also lengthens its lifespan and increases the frequency of fluorescent emission.
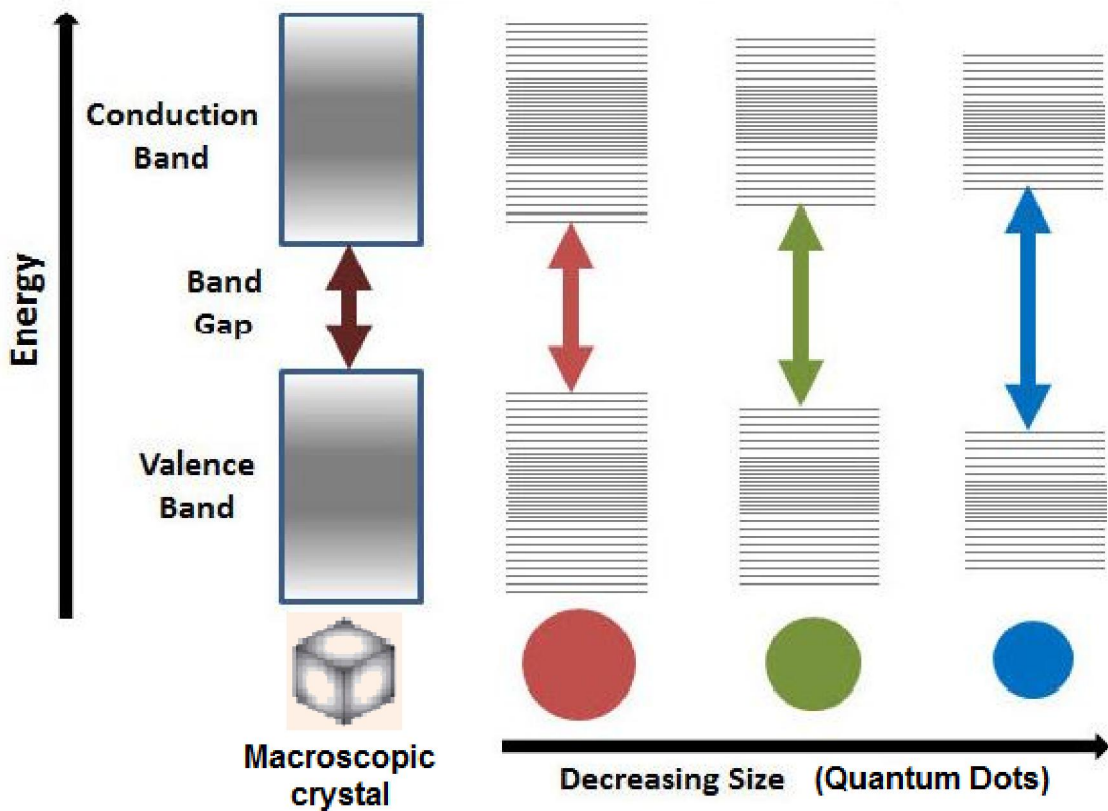
Figure 1.2. Splitting of energy levels in quantum dots and band gap increases with decrease in size of the QDs (adapted from [18]).

1.1.2   Applications of QDs

The unique size and composition tunable electronic property of these very small, semiconducting QDs makes them very appealing for a variety of applications and new technologies. A significant amount of research has been carried out to utilize QDs in display devices and solar cells based on their electroluminescence and photovoltaic properties. The integration of organic and inorganic materials at the nanometer scale into hybrid optoelectronic structures enables active devices that combine the diversity of organic materials with the high-performance electronic and optical properties of QDs [19].

QD-based light emitting diodes (QLEDs) have attracted intense research and commercialization efforts over the last decade [20]. In fact, QLEDs have several advantages compared to organic LEDs (OLEDs), including (i) sharp emission compared to their organic counterpart, which is necessary for a high quality image, (ii) inorganic materials usually show better thermal stability than organic materials providing longer lifetimes, (ii) the same chemical composition of QDs exhibits similar degradation with time, whereas the display color of OLEDs generally changes with time due to the different lifetimes of the red, green and blue pixels [21].

Still in the world of optics, QDs are being hailed as a breakthrough technology in the development of more efficient solar cells. QD sensitized solar cells have been shown better efficiency and charge separation compared to dye sensitized solar cells (DSSCs). Usually dyes have a strong absorption band in the visible region but very low absorption in the UV and NIR regions. In addition, dyes in DSSCs suffer from photodegradation. Whereas, the absorption of QDs can be tuned from UV through the visible into the NIR, and band-edge absorption is favourable for effective light harvesting [22].

QDs show unique down-conversion potentiality and can efficiently convert undesirable higher-energy UV radiation into desirable lower-energy visible wavelengths which is beneficial for their recently attractive application as greenhouse films, photovoltaic (PV) encapsulants, etc [23, 24].

Recently, QDs sensitized onto nano TiO_2 as heterogeneous photocatalysts have drawn considerable interest. QDs enhance the electronic conversion efficiency of TiO_2,

improving the charge separation, increasing UV absorption, as well as extending the absorption to a lower wavelength visible range [25].

QDs are also finding important medical applications, including biological imaging, drug delivery, and potential cancer treatment [21]. Much of optical bioimaging is based on traditional organic dyes, but there are several drawbacks associated with their use. QDs, on the other hand, are of interest in biology for several reasons, including (1) higher extinction coefficients; (2) higher quantum yields (QYs); (3) less photobleaching; (4) their absorbance and emissions can be tuned with size; (5) generally broad excitation windows but narrow emission peaks; (6) multiple QDs can be used in the same assay with minimal interference with each other; (7) toxicity may be less than conventional organic dyes, (8) the QDs may be functionalized with different bio-active agents, (9) QDs can be designed to target a single organ and then deliver drugs bound to them [21].

Despite the unique size tuneable optical properties of QDs, their uncontrollable sizes, aggregation tendency, inconsistent photoluminescence, toxicity, and degradation under prolonged photoexcitation have hindered recent progress of QDs in composites [23, 26]. Compared to bare QDs, a core-shell structured QD with a thin shell of a higher band gap element are advantageous and have been shown to enhance photo-physical properties and minimize the aggregation tendency. However, encapsulation by silica has shown the best approach providing long-term photostability and high photo-physical properties [23].

1.2   Mesoporous silica nanoparticles (MSNs)

Since the discovery of MCM-41 (Mobile Crystalline Material) by Mobil researchers in 1992 [27], mesoporous silica materials have attracted widespread interest because of their versatility in pore structure, surface chemistry, and macroscopic form (particles, coatings, and bulk materials) [28].

1.2.1   Properties of MSNs

Mesoporous silica reveals several key structural features, such as large surface area, high pore volume, uniform and tunable pore size within the range of 2 to 50 nm, and a stable and rigid frame network [29, 30]. Mesoporous silica coating on hydrophobic QDs allows diversity in surface functionalization and also make it possible to disperse colloids in a wide range of solvents from very polar to apolar. There are several advantages for using silica shells instead of other stabilizers. Silica, a biocompatible material which is chemically inert and optically transparent. It does not affect redox reactions at the QDs surface. It also provides chemical and physical shielding between the core QDs surface and the surrounding environment [31, 32].

The unusual properties of silica, especially in aqueous media provides the particle with enhanced colloidal stability, so they remain stable over a much wider range of solution conditions, such as ionic strength, temperature, pH, solvent polarity, etc. Additionally, the ability to control the thickness of the silica shell can enhance the separation between neighbouring particles enabling one to tailor their properties [32, 33]. Most obviously, the colloid chemistry of silica is well known and the silica surface can be modified or conjugated with different functionalities for linking to polymeric species and biomolecules [26, 34].

1.2.2   Mesoporous silica encapsulation of QDs

QDs are highly sensitive to oxygen, which can change their properties and facilitate the release of cytotoxic ions to the surrounding environment. By forming core-shell QDs or using organic ligands, the bare QDs can be stabilized to some extent. However, the long-term photostability of these capped QDs is limited [35]. Commonly used organic ligands, including mercaptoacetic acid, mercaptopropionic acid, 11- mercaptoundecanoic acid, 2-aminoethanethiol are also very toxic [36]. Bare, core-shell, or surface functionalized QDs are generally hydrophobic, therefore, tending to agglomerate, especially in an aqueous environment. Therefore, silica encapsulation of QDs has attracted substantial interest both in research and potential technological applications [37]. A silica coating can prevent aggregation and photo-oxidation of QDs and improve their hydrophilicity.

Unlike polymeric layers, silica is not subject to microbial attack and there is no porosity change occurring in these particles with a pH variation. The silica layer is more efficient than amphiphilic polymer layer or small molecular ligands to reduce the possible leaking of toxic metal ions under physiological environments [38]. Uniform encapsulation using small molecule ligands is difficult and an amphiphilic polymer layer is usually thicker [38].

1.3   Polymer nanocomposites

Nanocomposites made up of inorganic nanoparticles and organic polymers represent a new class of materials that exhibit improved performance when compared with their macroscopic counterparts [39]. These nanocomposites combine the unique properties of inorganic components with the processaibility of polymer in one material and makes them attractive in various area in high added-value applications [40, 41].

Polymers are considered to be good hosting matrices for composite materials because they can be easily tailored to a variety of physical properties. Moreover, organic polymers generally have long-term stability and good processability. Inorganic nanoparticles possess outstanding optical, catalytic, electronic and magnetic properties, which are significantly different than their bulk states [39]. The addition of inorganic nanoparticles to the polymer matrix allows unique physical properties as well as the implementation of new end-use features [42] .

Depending on the particle size, particle shape, specific surface area and chemical nature of the inorganic nanoparticles, the following polymer matrix properties can be modified [40, 42]:
- physical properties such as optical, magnetic, or dielectric properties.
- electrical and thermal conductivity

- polymer phase behaviour and thermal stability
- mechanical properties like stiffness, Young's modulus, wear, fatigue, and others
- flame retardancy
- density

Polymer films with luminescent nanomaterials offer a useful and promising approach to improve solar energy harvesting and increase the efficiency of solar devices [43, 44]. Among different luminescent materials, semiconductor nanocrystals (NCs), also known as quantum dots (QDs) have drawn enormous research interest, arising from the benefits of their unique size- and shape- dependent optical properties, which are very different from their bulk counterparts due to the quantum confinement effect [10]. QDs can efficiently convert undesirable higher energy UV radiation into desirable lower energy visible wavelengths, which is beneficial for their application as greenhouse films, photovoltaic (PV) encapsulants, etc [24, 45].

1.4   Greenhouse coverings

Greenhouse polymer films are of tremendous interest as North American consumers are demanding fresh fruits and vegetables that are disease, insect and blemish free. The ability to offer fresh, safe produce year round is made possible through the use of commercial greenhouses. The recent significant growth of greenhouse operations in Ontario is utilizing plastic films, which account for over 80% of greenhouse coverings. Over the past 40 years remarkable progress has been made in terms of the use and quality of greenhouse technology through the development of innovative plastic greenhouse covers. Greenhouse light quality manipulation has been shown to reduce energy requirements by up to 40%, virtually eliminating the need for forced ventilation in greenhouses. By spectral light manipulation, most commonly shown through light-emitting diode (LED) use, plant heights can be controlled, and both water usage and

disease growth minimized. But, LED approaches would be extremely capital and energy intensive for commercial operation. Greenhouse cultivation is reported as the most intensive form of biomass production per unit of cultivated area with up to 10 times superior than that of a field crop [46]. By better understanding how to "tune" the effects of light and heat through greenhouse plastics using advances in nanotechnology we can both lower energy and water costs significantly, and boost biomass production.

Light outside the visible region also influences the plant growth. The ultraviolet component of solar radiation (especially 200-380nm) has been shown to degrade crops, and support harmful insect behavior causing damage to crops [47-49]. Insects have different optical photoreceptors for different bandwidths of light. Wavelengths in the UV region encourage specific insect behaviour such as orientation, navigation, host finding and feeding. Furthermore these pests and parasites can act as vectors for several harmful viruses. UV radiation absorbed by the polymer films also causes photochemical degradation of the films by leading to bond cleavage and depolymerization [23]. Commercially available UV stabilizers, such as benzophenones, benzotriazoles, nickel quenchers, hindered amine light stabilizers (HALS) have shown prevention of crop damage from pests and their diseases by filtering out much of the UV component from the plant's light environment [48, 50-52]. However, little information is available about their incorporation into the polymer matrix. In addition, uniform distribution, long term stability, transparency of the films, and lowering costs are still major concerns [53]. Polymer films with QDs offer a useful and promising approach to improve solar energy harvesting, as QDs can efficiently convert undesirable higher energy UV radiation into desirable lower energy visible lights [24].

Commercial greenhouse covering materials posses a range of characteristics and properties targeted to specific spectral transmittance and energy functions. There are three main types of greenhouse films commonly available in the Ontario market, referred to as direct light, diffused light, and thermic films.
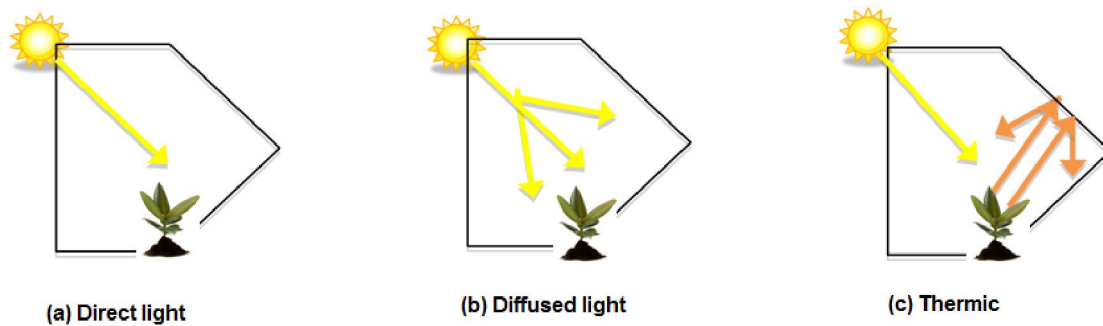
Figure 1.3. Schematics showing the direction of absorbed and reflected light for (a) direct light films (b) diffused light films, and (c) thermic films.

Direct light films characterized by high light transmission and clarity with low haze values allow for maximum light transmission of PAR (photosynthetic active radiation) light required for photosynthesis. Whereas, diffused light films split the incident light into direct and diffused components. Light diffusion offers a moderate cooling effect, it prevents plant burning, it reduces shadows and ensures more uniform distribution of light, so that it reaches even the lower parts of plants resulting in both a higher photosynthetic rate and quality of harvest [54]. The choice of the most appropriate level of diffusion depends on the climate of the area, the crop and the season(s) of growing. For instance, during winter months and cloudy days, films with medium to low diffusion are preferable [54].

In addition to light, heat is another significant environmental factor for plant growth and plays an important role in plant development. Thermic films contain thermal additives allowing them to absorb significantly more infrared radiation. This reduces the transmission of long-wave infrared and thermal radiation from inside a greenhouse to the outdoors, causing significant radiative heat losses [55, 56]. However, commercially available thermic films suffer from a loss of transparency in the visible region of the solar spectrum which is important for the photosynthesis process [47].

1.5 Photovoltaic encapsulants

Crystalline photovoltaic (PV) cells are brittle and have to be protected from the environment by incorporating into a module. This PV module is, in general, a sandwich consisting of a front glass plate, an encapsulant, and a polymeric back sheet as shown in Figure 1.4. The PV encapsulant provides structural support, electrical isolation, physical protection, and thermal conduction for solar circuits, as well as to help maximize the service life of the solar module [57]. The main encapsulant used in today's PV module is EVA, a copolymer of ethylene and vinyl acetate. EVA shows excellent transparency, high tensile strength and impact resistance, water proof and humidity durability, and outstanding adhesion with other layer of the module [58]. However, weathering and UV degradation, discoloration and mechanical properties loss over time are major challenges [59]. Encapsulants play an increasingly multifunctional role in next generation PV modules. Therefore, the types of nanofillers and their incorporation within polymer matrix, wavelength selectivity, UV performance, optical, mechanical, and thermal properties, all these need to be addressed to optimize the encapsulants.

1 Tempered glass
2 EVA
3 Cells
4 EVA
5 Triple-layer back sheet
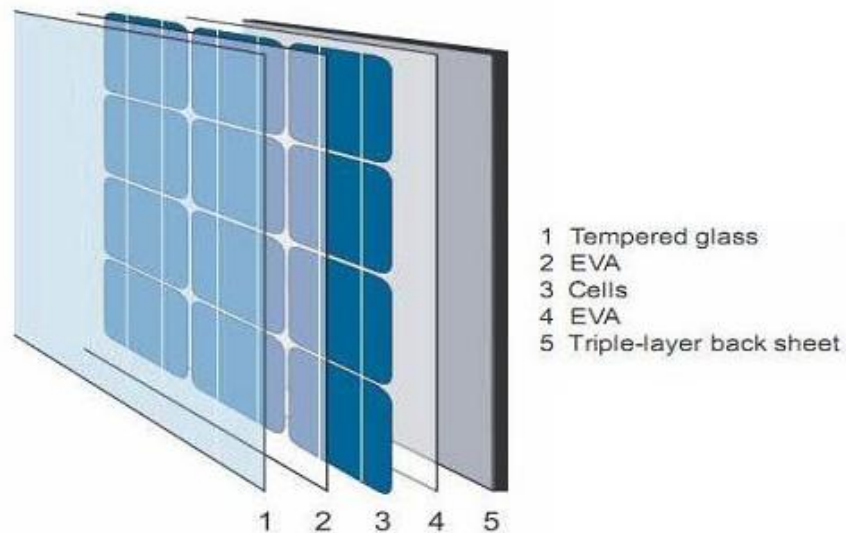
Figure 1.4. A typical solar cell module sandwich with EVA encapsulant films on top and bottom of the solar cell (adapted from [60]).

1.6 QDs decoration on TiO$_2$ and photocatalysis

In order to meet the increasingly serious environmental and energy crises, the development of highly active heterogeneous photocatalysts has attracted a great deal of attention in recent years. Many investigations are mainly focused on semiconductor-based photocatalysts for pollutant degradation and water splitting under ultraviolet or visible light irradiation [61]. Among various oxide and non-oxide semiconductor photocatalysts, nano-sized titanium dioxide (TiO$_2$) has been proven to be the most suitable for wide environmental and energy applications because of its suitable valence band and conduction band positions, low cost, abundance, good stability, non-toxicity, strong oxidizing power, and unique optoelectronic properties [25, 62].

Usually, the photocatalytic activity of TiO$_2$ is strongly dependent on its phase structure, crystalline size, specific surface areas, and pore structure [63]. Structurally, TiO$_2$ exists in three polymorphs: anatase, rutile, and brookite. It is well accepted that anatase TiO$_2$ exhibits higher photocatalytic activities than rutile and brookite TiO$_2$ [61, 64]. The indirect band gap anatase shows a longer charge carrier lifetime to participate in surface reactions compared to direct band gap rutile and brookite TiO$_2$. Anatase TiO$_2$ also enhances faster migration of photogenerated electrons and holes from the interior to the surface, resulting in a lower recombination rate for charge carriers [61, 64].

However, due to its wide band gap (3.2 eV), TiO$_2$ can only be excited by a small UV fraction (less than 6 %) of solar light, making it impractical for use under natural sunlight [65]. Structural imperfections in the TiO$_2$ lattice generate trap sites which may act as recombination centres, leading to a decrease in the levels of electrons and holes, resulting in a low quantum yield and poor efficiency in these applications [66]. In order to enhance TiO$_2$ photocatalysis as well as the response into the visible spectrum of solar light, there has been various attempts by doping TiO$_2$ with QDs, metal oxides, transition metals, non-metals, ionic components, polymers etc [67].

Recently, compared to metal and non-metal doping, semiconductor QDs have been attracting extensive attention to sensitize TiO_2 due to their unique size dependent optoelectronic properties, large extinction coefficient, possibility of multiexciton generation, and more controlled and stable decoration on TiO_2 surfaces [68]. A lower band gap QD like CdSe, CdS with higher conduction band (CB) can enhance the electronic conversion efficiency of TiO_2 [69-71]. When a QD particle is excited by a photon of ultraviolet or lower wavelength visible irradiation, and electron-hole pair is formed, and subsequently the photogenerated electron from the CB of the light activated QD is quickly transferred to the non-activated TiO_2 that has a CB edge more positive than QDs [72]. These electrons participate in reduction reactions according to the conduction band energy level of TiO_2. The photogenerated holes theoretically migrate to the surface and participate in the oxidation of organic pollutants. There is no holes transfer from the QD particles, so electrons at the CB of TiO_2 have no holes to recombine with leading to efficient and longer charge separation, increased UV absorption by QDs, as well as extending the absorption to the visible range [73, 74].

For removing organic pollutants by photocatalysis, three components are required, a catalytic surface, a strong oxidizing agent (in most cases oxygen) and a photon with equal or higher energy than the band gap energy of the photocatalyst [75]. The absorption of photons with energy lower than the band gap energy or longer wavelengths usually causes energy dissipation in the forms of heat. The illumination of the photocatalytic surface with sufficient energy leads to the formation of a positive hole (hv+) in the valence band and an electron (e−) in the conduction band (CB). The positive hole oxidizes either pollutant directly or water to produce ·OH radicals, whereas the electron in the conduction band reduces the oxygen and produces another active species superoxide radial anions ($O_2^{-\bullet}$) [76].

The superoxide radial anions can decompose the pollutants by photoreduction or protonated itself and hydrolyzed to yielding hydroxyl radicals $OH^\bullet$ [25]. The highly reactive $OH^\bullet$ radicals are strong oxidizing agents which decompose organic pollutants [77, 78]. In the photocatalytic degradation of pollutants, when the reduction process of

oxygen and the oxidation of pollutants do not advance simultaneously, there is an electron accumulation in the CB, thereby causing an increase in the rate of recombination of e− and h+ [76]. Thus it is of paramount importance to prevent electron accumulation in efficient photocatalytic oxidation.
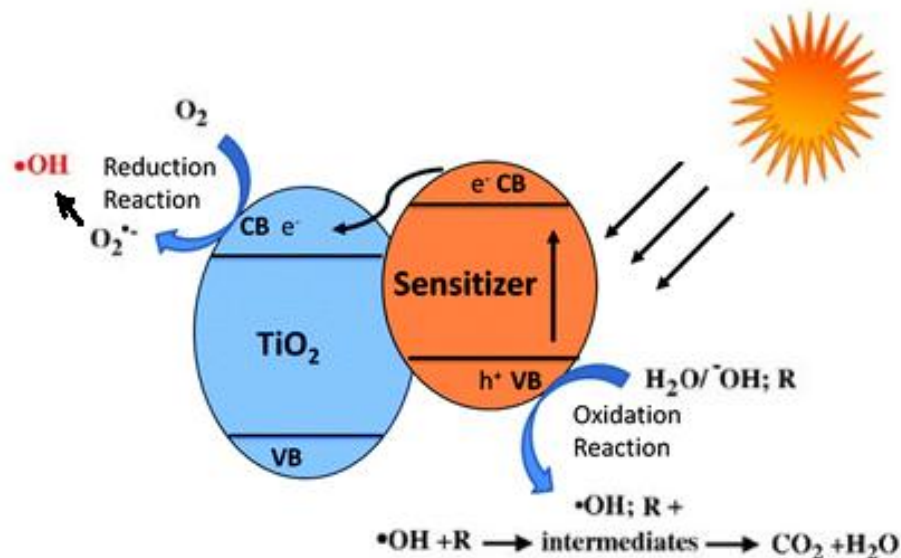
Figure 1.5. Schematic diagram of charge transfer and photocatalysis by QDs sensitized TiO_2 (reproduced from [76, 79]).

One of the challenges investigated recently is the type of attachment of the QDs to the TiO_2 matrix. In fact, uniform deposition and stability of QD particles on TiO_2 is often a problem due to the lack of attachment approaches and poor surface interactions under typical experimental conditions [80]. In most of the reported works, a direct contact between the QDs and TiO_2 is achieved by different synthesis approaches, but there is no control of QD coverage, size, and stability [81]. A favorable link between QDs and TiO_2 nanoparticles can minimize these drawbacks, also enhancing the transfer of electron injection [69, 82].

1.7   Scope of research

Semiconductor QDs have been attracting extensive interest due to their size dependent optoelectronic properties. Therefore, controlling the size of the QDs during synthesis is an important goal. Recently, core-shell QDs with a thin shell of a higher band gap element become more advantageous than bare QDs and have been shown to enhance their photo-physical properties. For further processing of either bare and core-shell QDs, including incorporation into polymers, the QDs need to be stabilized. The most efficient approach to stabilize the QDs is silica encapsulation. However, in previous works, most attention has been paid to fabricating and tuning the silica shell but the achieved quantum efficiencies were not well retained. Therefore, controlling the distribution of QDs at the core, avoiding aggregation and non-radiative emission, and then growing a silica shell that can improve their quantum efficiency are still major concerns.

In chapter 3, it is explained that highly luminescent CdS core and CdS-ZnS core-shell QDs were synthesized using a modified facile approach, where the monodispersity of the core-shell QDs was improved. By careful experimental tuning of the silica encapsulation process, both the quantum yield and photostability were enhanced significantly.

Recently, transparent polymer nanocomposite films with luminescent nanomaterials have attracted substantial research and technological interest. However, little information is available about their incorporation into a polymer matrix. In addition, uniform distribution, long term photostability, transparency of the films, and lowering the cost are still major concerns. Previously, different types of QDs and ligand exchanged QDs were attempted to incorporate into polymers, but photostability and compatibility of QDs with polymer are limited.

In chapter 3 it is shown that both bare and core-shell QDs can be melt mixed into EVA pellets using a twin screw extruder and pressed into films with controlled thickness. The results also demonstrate that mesoporous silica encapsulation not only enhances the quantum yield and photostability of the QDs but also improves the compatibility and dispersibility of QDs throughout the polymer films. The novel light selective films also show high visible light transmission and UV shielding properties.

The radiative heat loss is a current limitations of the polymer nanocomposites films. Controlling long-wave infrared and thermal radiation from inside a greenhouse or PV module to the outdoors can provide for longer material life-spans, while enhancing PV efficiencies by down-regulation, or increasing biomass production in greenhouses. Silica is transparent in UV-visible light, whereas it blocks infrared radiation. There are several commercial thermic EVA films available used silica based additives. But due to large particle size of the fillers, these thermic films suffer from a loss of transparency in the visible region of the solar spectrum which is important for the photosynthesis process. One possibility to overcome these drawbacks would be to use nanoparticles of silica well dispersed in the polymer matrix.

In chapter 4, thermal properties including thermicity and thermal conductivity are studied for EVA nanocomposites films incorporated with mesoporous silica nanoparticles and silica encapsulated QDs. The silica thickness on QDs was also tuned to evaluate the effect of thickness on these thermal properties. The novel EVA nanocomposites films show the possibility of simultaneously enhancing both the light selective and heat retention properties by using a single nanoadditive.

Grafting polymerization is a very promising and versatile approach for synthesizing polymer nanocomposites, where polymerization of monomer(s) occurs in presence of pre-made or functionalized inorganic nanoparticles. The blending approach is a simple and convenient process for polymer nanocomposite synthesis that is also suitable for large scale industrial applications. But, due to the high surface energy of the nanoparticles and low compatibility with polymer, it becomes difficult to maintain good dispersibility of nanoparticles within the polymer matrix. This leads to deterioration of the toughness and stability of the resulting composites for long span applications.

In chapter 6, a novel facile approach using supercritical CO_2 is investigated based on activation of the surface of silica encapsulated QDs with a silane coupling agent followed by *grafting from* polymerization of ethylene and vinyl acetate monomers. This approach is shown to enhance both the distribution and stability of the nanoparticles as well as the optical properties of the nanocomposites.

Semiconductor QDs sensitized onto nano TiO_2 as heterogeneous photocatalysts have also drawn considerable interest over the past few years. However, stability of the QDs attached to TiO_2 and consistent photocatalysis are still major challenges of this approach. Recently, intensive efforts have been undertaken to link bare QDs with nano TiO_2 but long aging time (more than 24 hours) and high temperatures (200 - 400 ^{o}C) are required for these linking processes. In previous works, most attention has been paid to the synthesis and optical properties rather than activity and stability during photodegradation.

In chapter 5, a facile process is described to fabricate nanocomposites from porous TiO_2 nanowires and bare CdS and core-shell CdS-ZnS QDs, where the QD particles are linked covalently to the titania surface through a bifunctional organic linker, mercapto propionic acid (MPA). TiO_2 nanowires were synthesized in $scCO_2$ using sol-gel polycondensation of Ti-alkoxides and acetic acid. The photocatalyst samples were characterized in detail and the energy transfer mechanism investigated. The experimental catalysts were investigated for degradation of methylene blue, an organic dye under UV, visible, and also simulated solar lights and the results compared with bare TiO_2 and directly deposited QDs in TiO_2.

1.8   References

[1] S.B. Rizvi, S. Ghaderi, M. Keshtgar, A.M. Seifalian, Semiconductor quantum dots as fluorescent probes for in vitro and in vivo bio-molecular and cellular imaging, Nano Reviews, 1 (2010) 1-15.

[2] A.I. Ekimov, A.A. Onushchenko, Quantum size effect in three-dimensional microscopic semiconductor crystals, ZETP Letters, 34 (1981) 345-349.

[3] C. Murray, M. Nirmal, D. Norris, M. Bawendi, Synthesis and structural characterization of II–VI semiconductor nanocrystallites (quantum dots), Zeitschrift für Physik D Atoms, Molecules and Clusters, 26 (1993) 231-233.

[4] M.A. Kasfner, Artificial atoms, Physics Today, 46 (1993) 24-31.

[5] R. Ashoori, Electrons in artificial atoms, Nature, 379 (1996) 413-419.

[6] C. Collier, T. Vossmeyer, J. Heath, Nanocrystal superlattices, Annual Review of Physical Chemistry, 49 (1998) 371-404.

[7] A.J. Nozik, Multiple exciton generation in semiconductor quantum dots, Chemical Physics Letters, 457 (2008) 3-11.

[8] M.C. Beard, Multiple exciton generation in semiconductor quantum dots, The Journal of Physical Chemistry Letters, 2 (2011) 1282-1288.

[9] C. Smith, D. Binks, Multiple exciton generation in colloidal nanocrystals, Nanomaterials, 4 (2013) 19-45.

[10] C.B. Murray, D.J. Norris, M.G. Bawendi, Synthesis and characterization of nearly monodisperse CdE (E= sulfur, selenium, tellurium) semiconductor nanocrystallites, Journal of the American Chemical Society, 115 (1993) 8706-8715.

[11] G. Palmisano, V. Augugliaro, M. Pagliaro, L. Palmisano, Photocatalysis: a promising route for 21st century organic chemistry, Chemical Communications, (2007) 3425-3437.

[12] S.Y. Lim, W. Shen, Z. Gao, Carbon quantum dots and their applications, Chemical Society Reviews, 44 (2015) 362-381.

[13] Y. Wang, A. Hu, Carbon quantum dots: synthesis, properties and applications, Journal of Materials Chemistry C, 2 (2014) 6921-6939.

[14] S.M. Reimann, M. Manninen, Electronic structure of quantum dots, Reviews of Modern Physics, 74 (2002) 1283-1342.

[15] M.G. Bawendi, M.L. Steigerwald, L.E. Brus, The quantum mechanics of larger semiconductor clusters (" quantum dots"), Annual Review of Physical Chemistry, 41 (1990) 477-496.

[16] A. Yoffe, Semiconductor quantum dots and related systems: electronic, optical, luminescence and related properties of low dimensional systems, Advances in Physics, 50 (2001) 1-208.

[17] U. Resch-Genger, M. Grabolle, S. Cavaliere-Jaricot, R. Nitschke, T. Nann, Quantum dots versus organic dyes as fluorescent labels, Nature Methods, 5 (2008) 763-775.

[18] C. Jonathon, A quantum paintbox, Chemistry World, (2003) 1-8.

[19] V. Colvin, M. Schlamp, A. Alivisatos, Light-emitting diodes made from cadmium selenide nanocrystals and a semiconducting polymer, Nature, 370 (1994) 354-357.

[20] S. Coe-Sullivan, Optoelectronics: Quantum dot developments, Nature Photonics, 3 (2009) 315-316.

[21] D. Bera, L. Qian, T.-K. Tseng, P.H. Holloway, Quantum dots and their multimodal applications: a review, Materials, 3 (2010) 2260-2345.

[22] R. Vogel, P. Hoyer, H. Weller, Quantum-sized PbS, CdS, Ag_2S, Sb_2S_3, and Bi_2S_3 particles as sensitizers for various nanoporous wide-bandgap semiconductors, The Journal of Physical Chemistry, 98 (1994) 3183-3188.

[23] M.A. Mumin, W.Z. Xu, P.A. Charpentier, Quantum dots/silica/polymer nanocomposite films with high visible light transmission and UV shielding properties, Nanotechnology, 26 (2015) 315702-315715.

[24] J.M. Allan, M.A. Mumin, W.Z. Xu, Q. Al Sharari, P.A. Charpentier, Surface functionalized bare and core–shell quantum dots in poly (ethylene-co-vinyl acetate) for light selective nanocomposite films, Solar Energy Materials and Solar Cells, 123 (2014) 30-40.

[25] M.A. Mumin, G. Moula, P.A. Charpentier, Supercritical CO_2 synthesized TiO_2 nanowires covalently linked with core–shell CdS–ZnS quantum dots: enhanced photocatalysis and stability, RSC Advances, 5 (2015) 67767-67779.

[26] M. Darbandi, G. Urban, M. Krüger, A facile synthesis method to silica coated CdSe/ZnS nanocomposites with tuneable size and optical properties, Journal of Colloid and Interface Science, 351 (2010) 30-34.

[27] J. Beck, J. Vartuli, W. Roth, M. Leonowicz, C. Kresge, K. Schmitt, C. Chu, D.H. Olson, E. Sheppard, A new family of mesoporous molecular sieves prepared with liquid crystal templates, Journal of the American Chemical Society, 114 (1992) 10834-10843.

[28] T. Suteewong, H. Sai, R. Hovden, D. Muller, M.S. Bradbury, S.M. Gruner, U. Wiesner, Multicompartment mesoporous silica nanoparticles with branched shapes: An epitaxial growth mechanism, Science, 340 (2013) 337-341.

[29] C.V. Durgadas, K. Sreenivasan, C.P. Sharma, Bright blue emitting CuSe/ZnS/silica core/shell/shell quantum dots and their biocompatibility, Biomaterials, 33 (2012) 6420-6429.

[30] A.M. Mumin, J.W. Barrett, G.A. Dekaban, J. Zhang, Dendritic cell internalization of foam-structured fluorescent mesoporous silica nanoparticles, Journal of Colloid and Interface Science, 353 (2011) 156-162.

[31] M. Qhobosheane, S. Santra, P. Zhang, W. Tan, Biochemically functionalized silica nanoparticles, Analyst, 126 (2001) 1274-1278.

[32] X. Gao, K.K. Yu, K.Y. Tam, S.C. Tsang, Colloidal stable silica encapsulated nano-magnetic composite as a novel bio-catalyst carrier, Chemical Communications, (2003) 2998-2999.

[33] V. Salgueiriño-Maceira, F. Caruso, L.M. Liz-Marzán, Coated colloids with tailored optical properties, The Journal of Physical Chemistry B, 107 (2003) 10990-10994.

[34] M. Bruchez, M. Moronne, P. Gin, S. Weiss, A.P. Alivisatos, Semiconductor nanocrystals as fluorescent biological labels, Science, 281 (1998) 2013-2016.

[35] A.P. Alivisatos, W. Gu, C. Larabell, Quantum dots as cellular probes, Annual Review of Biomedical Engineering, 7 (2005) 55-76.

[36] W.Y. William, E. Chang, R. Drezek, V.L. Colvin, Water-soluble quantum dots for biomedical applications, Biochemical and Biophysical Research Communications, 348 (2006) 781-786.

[37] X. Hu, P. Zrazhevskiy, X. Gao, Encapsulation of single quantum dots with mesoporous silica, Annals of biomedical engineering, 37 (2009) 1960-1966.

[38] A.L. Rogach, A. Kornowski, M. Gao, A. Eychmüller, H. Weller, Synthesis and characterization of a size series of extremely small thiol-stabilized CdSe nanocrystals, The Journal of Physical Chemistry B, 103 (1999) 3065-3069.

[39] I.-Y. Jeon, J.-B. Baek, Nanocomposites derived from polymers and inorganic nanoparticles, Materials, 3 (2010) 3654-3674.

[40] S. Kango, S. Kalia, A. Celli, J. Njuguna, Y. Habibi, R. Kumar, Surface modification of inorganic nanoparticles for development of organic–inorganic nanocomposites—A review, Progress in Polymer Science, 38 (2013) 1232-1261.

[41] C. Lü, B. Yang, High refractive index organic–inorganic nanocomposites: design, synthesis and application, Journal of Materials Chemistry, 19 (2009) 2884-2901.

[42] T. Hanemann, D.V. Szabó, Polymer-nanoparticle composites: from synthesis to modern applications, Materials, 3 (2010) 3468-3517.

[43] L.H. Slooff, E.E. Bende, A.R. Burgers, T. Budel, M. Pravettoni, R.P. Kenny, E.D. Dunlop, A. Büchtemann, A luminescent solar concentrator with 7.1% power conversion efficiency, Rapid Research Letters, 2 (2008) 257-259.

[44] Y. Zhou, F.S. Riehle, Y. Yuan, H.-F. Schleiermacher, M. Niggemann, G.A. Urban, M. Krüger, Improved efficiency of hybrid solar cells based on non-ligand-exchanged CdSe quantum dots and poly (3-hexylthiophene), Applied Physics Letters, 96 (2010) 013304-013309.

[45] W.Z. Xu, P.A. Charpentier, Light-selective nanofilms of quantum dot-poly (ethylene-co-vinyl acetate) synthesized with supercritical CO_2, The Journal of Physical Chemistry C, 113 (2009) 6859-6870.

[46] G. Vox, M. Teitel, A. Pardossi, A. Minuto, F. Tinivella, E. Schettini, Sustainable greenhouse systems, Sustainable Agriculture: Technology, Planning and Management, (2010) 1-79.

[47] E. Espi, A. Salmeron, A. Fontecha, Y. García, A. Real, Plastic films for agricultural applications, Journal of Plastic Film and Sheeting, 22 (2006) 85-102.

[48] C. von Zabeltitz, Light Transmittance of Greenhouses, Integrated Greenhouse Systems for Mild Climates, Springer2011, pp. 137-143.

[49] O. Almanza, M. Rodríguez-Pérez, J. De Saja, Prediction of the radiation term in the thermal conductivity of crosslinked closed cell polyolefin foams, Journal of Polymer Science Part B: Polymer Physics, 38 (2000) 993-1004.

[50] B. Díaz, A. Fereres, Ultraviolet-blocking materials as a physical barrier to control insect pests and plant pathogens in protected crops, Pest Technology, 1 (2007) 85-95.

[51] E. Schettini, L. Stefani, G. Vox, Interaction between agrochemical contaminants and UV stabilizers for greenhouse EVA plastic films, Applied Engineering in Agriculture, 30 (2014) 229-239.

[52] F. Liu, L. Jiang, S. Yang, Ultra-violet degradation behavior of polymeric backsheets for photovoltaic modules, Solar Energy, 108 (2014) 88-100.

[53] A.M. Abdel-Ghany, I.M. Al-Helal, S.M. Alzahrani, A.A. Alsadon, I.M. Ali, R.M. Elleithy, Covering materials incorporating radiation-preventing techniques to meet greenhouse cooling challenges in arid regions: a review, The Scientific World Journal, 2012 (2012) 1-11.

[54] F. Cabrera, A. Baille, J. López, M. González-Real, J. Pérez-Parra, Effects of cover diffusive properties on the components of greenhouse solar radiation, Biosystems Engineering, 103 (2009) 344-356.

[55] G.A. Giacomelli, W.J. Roberts, Greenhouse covering systems, HortTechnology, 3 (1993) 50-58.

[56] M.A. Mumin, K.F. Akhter, S. Dresser, S.T. van Dinther, W. Wu, P.A. Charpentier, Multifunctional mesoporous silica nanoparticles in poly (ethylene-co-vinyl acetate) for transparent heat retention films, Journal of Polymer Science Part B: Polymer Physics, 53 (2015) 851-859.

[57] R.F. Lange, Y. Luo, R. Polo, J. Zahnd, The lamination of (multi) crystalline and thin film based photovoltaic modules, Progress in Photovoltaics: Research and Applications, 19 (2011) 127-133.

[58] F. Pern, A. Czanderna, Characterization of ethylene vinyl acetate (EVA) encapsulant: Effects of thermal processing and weathering degradation on its discoloration, Solar Energy Materials and Solar Cells, 25 (1992) 3-23.

[59] P. Klemchuk, M. Ezrin, G. Lavigne, W. Holley, J. Galica, S. Agro, Investigation of the degradation and stabilization of EVA-based encapsulant in field-aged solar energy modules, Polymer Degradation and Stability, 55 (1997) 347-365.

[60] PV solar module, CETC Solar, China, (www.alibaba.com/product-detail/185W-Mono-PV-solar-module_401066797.html).

[61] J. Zhang, P. Zhou, J. Liu, J. Yu, New understanding of the difference of photocatalytic activity among anatase, rutile and brookite TiO_2, Physical Chemistry Chemical Physics, 16 (2014) 20382-20386.

[62] N. Farhangi, R.R. Chowdhury, Y. Medina-Gonzalez, M.B. Ray, P.A. Charpentier, Visible light active Fe doped TiO_2 nanowires grown on graphene using supercritical CO_2, Applied Catalysis B: Environmental, 110 (2011) 25-32.

[63] J. Yu, C.Y. Jimmy, M.K.-P. Leung, W. Ho, B. Cheng, X. Zhao, J. Zhao, Effects of acidic and basic hydrolysis catalysts on the photocatalytic activity and microstructures of bimodal mesoporous titania, Journal of Catalysis, 217 (2003) 69-78.

[64] T. Luttrell, S. Halpegamage, J. Tao, A. Kramer, E. Sutter, M. Batzill, Why is anatase a better photocatalyst than rutile?-Model studies on epitaxial TiO_2 films, Scientific Reports, 4 (2014) 4043-4049.

[65] M.D. Hernández-Alonso, F. Fresno, S. Suárez, J.M. Coronado, Development of alternative photocatalysts to TiO_2: challenges and opportunities, Energy & Environmental Science, 2 (2009) 1231-1257.

[66] C. Su, C. Shao, Y. Liu, Electrospun nanofibers of TiO_2/CdS heteroarchitectures with enhanced photocatalytic activity by visible light, Journal of Colloid and Interface Science, 359 (2011) 220-227.

[67] A.N. Banerjee, The design, fabrication, and photocatalytic utility of nanostructured semiconductors: focus on TiO_2-based nanostructures, Nanotechnology, Science and Applications, 4 (2011) 35.

[68] Y. Xie, G. Ali, S.H. Yoo, S.O. Cho, Sonication-assisted synthesis of CdS quantum-dot-sensitized TiO_2 nanotube arrays with enhanced photoelectrochemical and photocatalytic activity, ACS Applied Materials & Interfaces, 2 (2010) 2910-2914.

[69] Y. Medina-Gonzalez, W.Z. Xu, B. Chen, N. Farhanghi, P.A. Charpentier, CdS and CdTeS quantum dot decorated TiO_2 nanowires: synthesis and photoefficiency, Nanotechnology, 22 (2011) 065603-065611.

[70] G.-S. Li, D.-Q. Zhang, J.C. Yu, A new visible-light photocatalyst: CdS quantum dots embedded mesoporous TiO_2, Environmental Science & Technology, 43 (2009) 7079-7085.

[71] L. Yang, S. Luo, R. Liu, Q. Cai, Y. Xiao, S. Liu, F. Su, L. Wen, Fabrication of CdSe nanoparticles sensitized long TiO_2 nanotube arrays for photocatalytic degradation of

anthracene-9-carbonxylic acid under green monochromatic light, The Journal of Physical Chemistry C, 114 (2010) 4783-4789.

[72] S.S. Srinivasan, J. Wade, E.K. Stefanakos, Visible light photocatalysis via CdS/TiO$_2$ nanocomposite materials, Journal of Nanomaterials, 87326 (2006) 1-7.

[73] P. Thakur, R. Chadha, N. Biswas, S.K. Sarkar, T. Mukherjee, S.S. Joshi, S. Kapoor, Synthesis and characterization of CdS doped TiO$_2$ nanocrystalline powder: A spectroscopic study, Materials Research Bulletin, 47 (2012) 1719-1724.

[74] M. Feng, H. Zhan, L. Miao, Facile assembly of cadmium sulfide quantum dots on titanate nanobelts for enhanced nonlinear optical properties, ACS Applied Materials & Interfaces, 2 (2010) 1129-1135.

[75] M.R. Prairie, L.R. Evans, B.M. Stange, S.L. Martinez, An investigation of titanium dioxide photocatalysis for the treatment of water contaminated with metals and organic chemicals, Environmental Science & Technology, 27 (1993) 1776-1782.

[76] S. Ahmed, M. Rasul, W.N. Martens, R. Brown, M. Hashib, Heterogeneous photocatalytic degradation of phenols in wastewater: a review on current status and developments, Desalination, 261 (2010) 3-18.

[77] H. Weib, A. Fernandez, H. Kisch, Electronic semiconductor–support interaction—a novel effect in semiconductor photocatalysis, Angewandte Chemie International Edition, 40 (2001) 3825-3827.

[78] J.C. Kim, Y.B. Lee, J.H. Hong, J.I. Lee, J.W. Yang, W.I. Lee, N.H. Hur, Enhanced photocatalytic activity in composites of TiO$_2$ nanotubes and CdS nanoparticles, Chemical Communications, (2006) 5024-5026.

[79] Y. Wang, Q. Wang, X. Zhan, F. Wang, M. Safdar, J. He, Visible light driven type II heterostructures and their enhanced photocatalysis properties: a review, Nanoscale, 5 (2013) 8326-8339.

[80] A. Pareek, R. Purbia, P. Paik, N.Y. Hebalkar, H.G. Kim, P.H. Borse, Stabilizing effect in nano-titania functionalized CdS photoanode for sustained hydrogen generation, International Journal of Hydrogen Energy, 39 (2014) 4170-4180.

[81] N. Guijarro, T. Lana-Villarreal, I. Mora-Seró, J. Bisquert, R. Gómez, CdSe quantum dot-sensitized TiO_2 electrodes: effect of quantum dot coverage and mode of attachment, The Journal of Physical Chemistry C, 113 (2009) 4208-4214.

[82] S. Arya, T. Vats, S.N. Sharma, K. Singh, A. Narula, Effect of mercaptopropionic acid as linker on structural, thermal, and optical properties of TiO_2–CdSe nanocomposites, Journal of Thermal Analysis and Calorimetry, 107 (2011) 555-560.

Chapter 2

Literature Review

2.1 Quantum Dots (QDs)

2.1.1 Colloidal synthesis of QDs

Colloidal synthesis is an attractive approach to produce QDs of different compositions, sizes and shapes. This technique, for synthesizing QDs utilizes various chemical reactions in solution on a nanometer scale. The inorganic nanoparticles grown through chemical reactions of their precursors and, sometimes, controlled precipitation of the reaction product(s) in a properly chosen solvent. The solvents might be low temperature polar solvents such as water, methanol etc. or high temperature non-polar solvents such as tri-n-octyl phosphine (TOP), oleic acid (OA), or oleylamine (OLA) [1]. Generally, the growth process starts with the formation of a large number of nuclei due to supersaturation. Then, more and more of the solid particles deposit onto the nuclei, so the sizes of the crystallites grow slowly until the desired size is reached, at which time the reaction must be quenched. Otherwise, the QDs would keep growing through a process known as Ostwald ripening, which is the growth of larger dots through the transfer of material from smaller ones, which have a higher solubility. Nanoparticles are needed to be arrested during the reaction either by an electrostatic effect or by adding surface protecting reagents such as organic ligands, as described in more detail further below.

Initiated by pioneering work in the early 1980s, the research on QDs using different colloidal synthesis routes achieved remarkable progress, particularly after the development of a high-temperature thermolysis route reported by Prof. Bawendi group [2]. This route led to QDs with excellent quality in terms of particle size distribution (size range of 2–12 nm) and optical properties, relying on the rapid injection of organometallic precursors into a hot organic solvent. For example CdSe QDs were prepared by reacting $Cd(oleate)_2$ with trioctylphosphine selenide (TOPSe) in alkylamine at 250^oC [3]. Thermal decomposition mechanism of these reaction is shown in Figure 2.1.
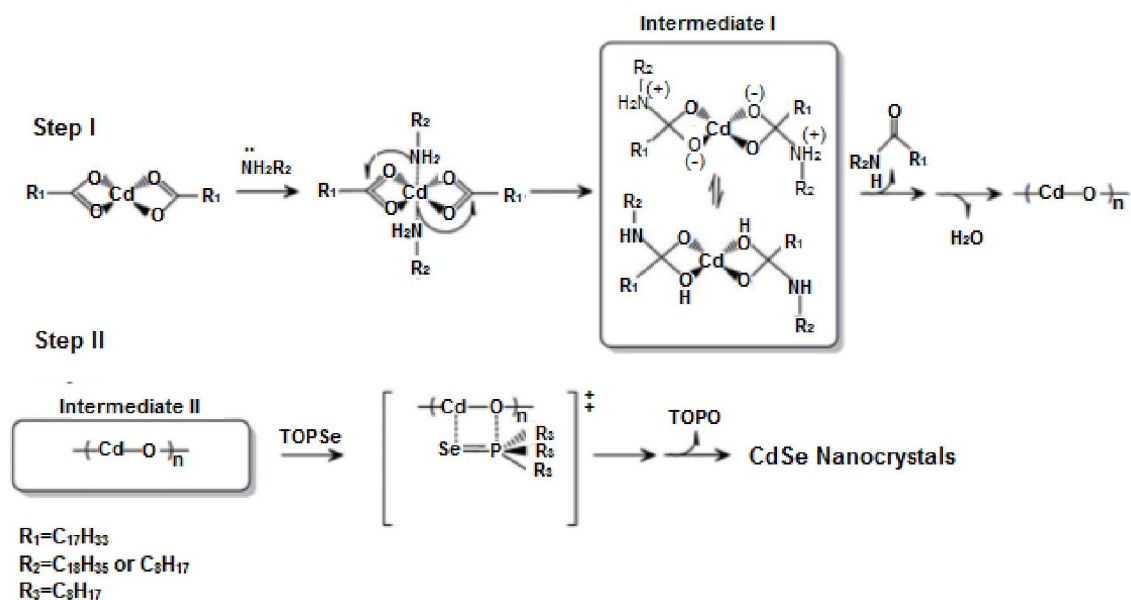
Figure 2.1. Thermal decomposition mechanism of Cd(oleate)$_2$ in the presence of alkylamine to form CdSe QDs in two steps: formation of intermediates I and II (Step I), and CdSe QD formation from intermediate II and TOPSe (Step II) (adapted from [3]) .

Several research groups have investigated single-molecular precursors such as bis(diethyldithio-/diselenocarbamate) of cadmium (II)/zinc (II) for the preparation of QDs [4, 5]. Here, the precursors transform into monomers when heated to a sufficiently high temperature. Once the monomers reach a high enough supersaturation level, the nanocrystal growth starts with a nucleation process. Single-molecular precursors have significant advantages of being less toxic, insensitive to air and moisture, easier to purify, and provide highly monodisperse nanoparticles, with the synthesis generally undertaken at desirable lower temperatures. A more ambitious possibility is that the single precursor method can potentially open a way for obtaining a wide range of nanodispersed semiconductors with desired properties by tailoring the precursor structure. Other than the choice of the organic solvent, the colloidal synthesis method in aqueous media, in microemulsion, ionic liquids and in supercritical fluids have also reported by different researchers [6-8].

In aqueous solvents and the microemulsion processes, QDs grown at lower temperatures contain more defects and a wide particle size distribution. These processes are very time consuming and result in a low yield. However in the case of single precursors using organic solvents, high temperatures are favorable that reduces defects by annealing during growth. At high temperatures, the ligands are mobile enough to provide access to the addition of monomer units to the growing nanocrystal and help sterically stabilize the particles against agglomeration [9].

2.1.2 Enhancement of stability and properties of QDs

Surface defects in the QDs act as temporary 'traps' for the electron, hole or excitons, quenching radiative recombination and reducing the quantum yield (QY). Therefore, capping or passivation of the QD surface (surface modification) is essential to improve the stability and photophysical properties of the QDs. This surface modification step is generally carried out by attaching an organic or inorganic capping layer to the "bare" QDs [10].

A typical approach to passivate the QD surface is by using inorganic layers, meaning the synthesis of core/shell structures (e.g., CdSe/ZnSe, CdS/ZnS, CdSe/CdS, etc). These core-shell nanostructures consist of a semiconductor core surrounded by another semiconductor material with a larger band-gap [11, 12]. The shell material does not absorb the emission from the core and helps to eliminate the broadband emission of the QDs. Core/shell systems are intensively studied due to their superior optical properties and higher stability as compared to core NCs. The maximum PL efficiency or QY of core/shell QDs is also dependent upon the thickness of the shell layer (generally 0.5-2nm). Thicker capping layers lead to the formation of misfit dislocations which are also nonradiative recombination sites that decrease the PL-QY. Also, core-shell-shell nanocrystals have been developed (e.g., CdSe/CdS/ZnS, CdSe/ZnSe/ZnS) which have two different shell layers [13]. The middle shell of the nano-architecture allows considerable strain relaxation between the inner core and the outer shell, and helps to

further improve the photoluminescence efficiency and photostability, exceeding those of core or core/shell nanocrystals.

In general, there are three major mechanisms for passivation and encapsulation of hydrophobic QDs. These are ligand exchange, hydrophobic interaction, and coupling reactions [14]. Phosphenes and mercaptans are the most widely used organic ligands. These ligands are typically electron donating to allow coordination to the electron-poor metal atoms at the nanocrystal surface. The major advantages of organic modification layers include simultaneous achievements of colloidal suspension and the ability for further conjugation. However, the selection of organic ligands that bond with surface atoms of the QDs is a very delicate issue. Also ligand exchange may alter the chemical and physical nature of the QD surface and also decrease the quantum efficiency. Simultaneous passivation of both anionic and cationic surface sites is difficult, and coverage of surface atoms may cause steric hindrance effects [10]. A more promising approach is to use long chain-length amphiphilic polymers or surfactants to help form micelle-like structures through hydrophobic interaction between their hydrophobic ends and the surface ligands of QDs, providing a hydrophilic exterior. Use of coupling agents (e.g., agents containing mercapto-group on one end and a silane-group on the other end) is a simple and effective way to encapsulate QDs within silica [15].
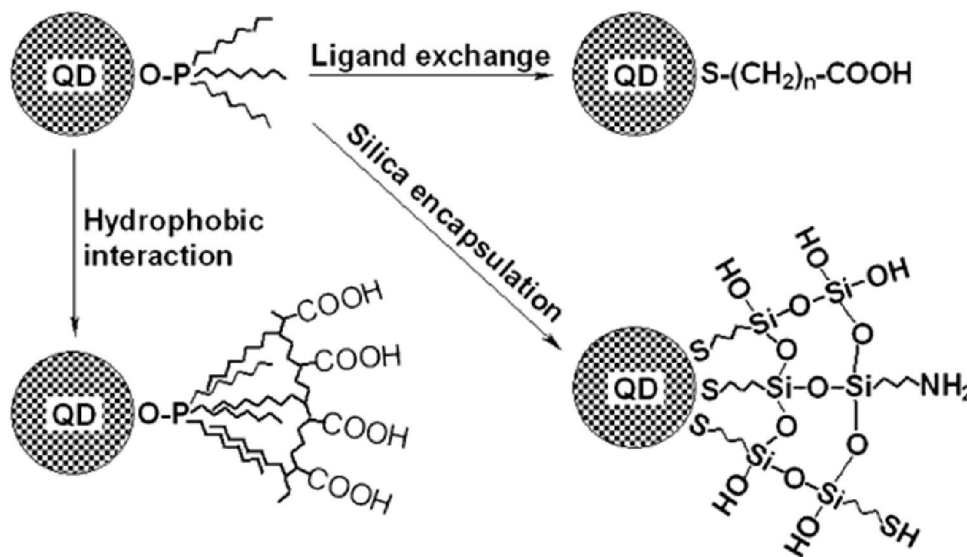
Figure 2.2. Surface passivation and encapsulation strategies of QDs (adapted from [14]).

2.2　Mesoporous silica encapsulation of QDs

2.2.1 Water-in-oil (reverse micro-emulsion) approach

Nano-sized mesoporous silica was first successfully synthesized and reported by the research groups of Cai [16], Mann [17], and Ostafin [18]. Then the term MSN was popularized by Victor Lin to represent mesoporous silica nanoparticles/nanospheres [19]. Over the past decade, MSNs with various morphologies, dimensions, surface areas, and porosity have been synthesized and investigated systematically by many different research groups all over the world [20]. The encapsulation of QDs in silica spheres has been accomplished using two major techniques called the "Stöber method" and the "microemulsion method". The use of silica coatings itself is certainly not new. Stöber and co-workers in 1968 developed this pioneering method for synthesizing monodispersed spherical particles involving the base catalyzed hydrolysis in excess of water and condensation of silica alkoxide precursors in low molecular weight alcohol (e.g. ethanol) in the presence of aqueous ammonia catalyst [21]. Professor Unger group first modified the Stöber approach by adding a cationic surfactant to the reaction mixtures and obtained the sub-micrometer scaled ordered mesoporous spherical particles [22]. Since then, mixtures of alcohol, water, and ammonia have been widely used with different template systems to prepare uniform MSNs with different mesorstructures [20]. In recent years, the modified Stöber approach has also been widely used QD encapsulation [23, 24]. Major disadvantages of the Stöber method for silica encapsulation are the high requirements on purity of the reactants, the difficulty and multiplicity of the preparation steps, and the fact that nanoparticles with nonpolar ligands cannot be coated easily or directly. By using conventional Stöber approach, it is also difficult to prepare silica nanospheres with particle size less than 80 nm [25].

Mesoporous silica nanoparticles (MSNs) synthesis by using a water-in-oil microemulsion technique was first reported by Arriagada and Osseo-Asare in 1995 [26]. Since then, several research groups have been using this microemulsion approach as an efficacious technique to encapsulate the QDs [15, 27, 28]. This method depends on the controlled aqueous pool inside the micelles of the oil phase (an organic solvent, which is present in a high proportion relative to water) with surfactant, that finally forms monodispersed spherical MSNs.

The water nano-droplets containing reagents undergo rapid coalescence that allows mixing, precipitation reactions and aggregation processes for the synthesis of MSNs. The water pool is spherical in shape, and surfactant molecules surround the wall. These walls act as cages for the growing particles and thereby reduce the average size of the particles during the collision and aggregation processes [29]. Varying the concentration of the dispersed phase and the surfactant it is possible to tailor the size of the droplets in the range 1–100 nm, approximately [30]. In comparison to the "Stöber" approach, the microemulsion method is considered less complicated (e.g., no prior ligand exchange is required), very robust against changing reaction conditions, with the resulting particles having smooth surfaces with good monodispersity, and also provide the possibility to encapsulate the QDs with non-polar ligands [27]. The pore diameter can be controlled by changing the length of the surfactant molecules. Moreover, Changing the silica precursors, types of surfactant, or reaction parameters (temperature, pH, aging time, solvent, reactant mole ratio) lead to the production of diverse mesoporous systems [31]. In addition, these changes all affect the thermal, hydrothermal, and mechanical stabilities of the mesoporous synstems.
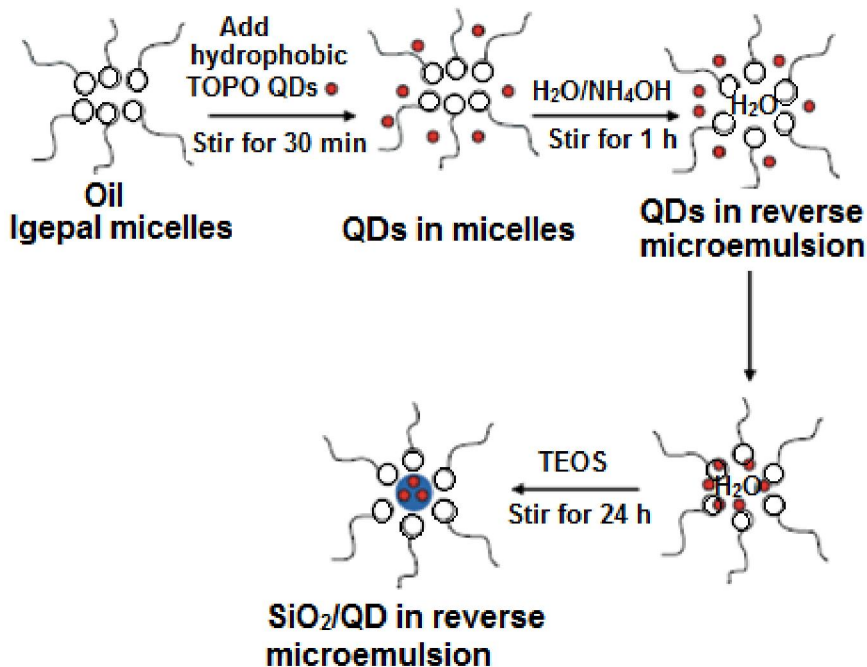
Figure 2.3. Silica encapsulation of hydrophobic QDs using a reverse microemulsion approach based on sol-gel of silica precursor (adapted from [15]).

2.2.2 Properties improvement after encapsulation

A significant research effort has been devoted to prepare core-shell nanoarchitectures with QDs at the core and a cross-linked shell to protect the QDs better than thiol-based surface functionalization. The most popular approach is silica coating although other methods such as ligand or polymer bridging are also widely explored [32]. Although a variety of functional NPs or QDs have been synthesized by silica or polymer coating, each coating method has inherent advantages and limitations. It would be ideal to have a thin, cross-linked coating that could protect the core, improve colloidal stability, and introduce chemical functionality that can be used for end-use applications such as

bioconjugation [33]. Efforts are still underway in various groups in order to make a library of robust functional NPs for the design of nanostructured materials.

Single or multiple QDs can be encapsulated within a single or multiple silica shell [27, 34]. The silica shell thickness can be altered by varying the silica precursor e.g. TEOS concentration. Varying the amount of water and ammonia in the microemulsion also was shown to affect the silica shell thickness, since this altered the aqueous domain size [32]. The ability to control the thickness of the silica shell implies that the separation between neighbouring particles can be tuned, so that the collective behaviour of the particles within the nanostructure can be tailored [24]. Many research groups have examined and reported that even a thin layer of silica can significantly improve the colloidal stability, photostability, and optical properties of QDs [15, 24, 35, 36]. The higher initial quantum yield (QY) cannot guarantee higher QY's after silica encapsulation. In the past, QY was well retained due to fluorescent quenching during silanization of hydrophobic QDs [23]. However, recently it is reported that by improving silanization conditions, uniform distribution of QDs at the core avoiding aggregation and non-radiative emission, and controlled growing of silica shell, the QY can be enhanced after silica encapsulation, which is still a major concern [23, 37, 38]. Additionally, the silica surface can be easily modified or functionalized with different functional groups by conventional surface chemistry, facilitating the dispersibility of encapsulated QDs in different solvents, composites, and diverse applications [24].

2.3   Polymer nanocomposites

2.3.1 QDs/polymer nanocomposites

During the last 20 years, extensive scientific research has been performed on QDs, and tremendous progress in their synthesis as well as in our understanding of their optical and electronic properties has been achieved [39]. Polymer matrices reinforced with QDs offer a useful and promising approach to combine the functionalities of polymer matrices,

which include low weight and easy processability, with the unique size and shape dependent optical properties of QDs. Besides playing the role of the matrix, polymers also provide mechanical and chemical stability to the nanocomposite material. Additionally, polymers offer processability into technologically relevant structures like thin films, or micro- and nano-spheres [39, 40]. Despite many advantages that a combination of QDs with polymeric materials has to offer, the development in this field of research has been relatively slow. The main difficulties encountered include a strong tendency of the QDs to undergo agglomeration followed by poor compatibility and insufficient dispersal of the QDs in the polymer matrix, degrading the electronic or optical properties of the QDs once they are combined with the polymers [40]. To avoid these drawbacks, research efforts have become concentrated on the surface engineering of the QD and development of methods to incorporate and distribute QDs in polymer matrices.

2.3.2   Synthesis approaches

Nanocomposites comprising a polymer and an inorganic NP or surface can be generally prepared by three main methods; blending, *in situ* preparation, and sol-gel synthesis. The most conventional and simple method suitable for the synthesis of polymer/inorganic nanocomposites for large scale industrial applications is direct mixing of the nanoparticles into the polymer [40]. The mixing can generally be done by melt blending or solution blending. In melt processing, particles are dispersed into a polymer melt and polymer inorganic nanocomposites are then obtained by extrusion. But, due to the high surface energy of the nanoparticles and low compatibility with polymer, it is difficult to maintain good dispersibility of nanoparticles within the polymer matrix which leads to deterioration of the toughness and stability of the resulting composites for long span applications [41, 42]. In solution blending, the uniform transparent dispersion of nanoparticles in a solution of polymer or oligomers with reactive groups is cast into a container or deposited on a glass or plastic substrate by a spin-coating or dip-coating process, then the transparent nanocomposite films or sheets can be obtained after heating.

Some of the limitations of melt blending can be overcome by solution blending but there is a cost depending on the solvent and its recovery [43]. In both of these blending processes, the compatibility of nanoparticles and polymer matrices is considered to be a crucial issue for improving the transparency and properties of nanocomposites [41]. Blending methods have been studied extensively for QDs and silica nanoparticles separately with different polymers. Silica nanoparticles with polypropylene (PP) or polyethylene naphthalate (PEN) composites carried out with melt blending have shown improved mechanical and rheological properties [44-46]. Surface-treated ZnO nanoparticles were also dispersed in polypropylene via extrusion [47]. Hong et al. [48] reported that nano-ZnO and low-density polyethylene were melt compounded in a high-shear mixer to prepare nanocomposites with an increased resistance to thermal degradation. Recently Allan et al. reported surface functionalized bare and core-shell QDs incorporated into EVA by melt-mixing with enhanced optical properties [49]. No reports have been published on mesoporous silica encapsulated QDs loaded into EVA using a melt-mixing approach, that can be potentially used applications in greenhouse coverings and PV encapsulants.

The sol–gel processing of nanoparticles inside of a polymer dissolved in non-aqueous or aqueous solutions results in the formation of interpenetrating networks between inorganic and organic moieties at mild temperatures. This interpenetrating network improves the compatibility between constituents and builds strong interfacial interaction between the two phases [40]. The sol-gel approach has been used successfully to prepare nanocomposites with silica, alumina, calcium oxide, and titania in a wide range of polymer matrices [50].

Several sol–gel process strategies can be applied to form hybrid materials. One method involves the polymerization of organic functional groups from a preformed sol–gel network; vinyl or epoxy groups and free radical or cationic polymerization processes are common [51]. Hsiue et al. reported the synthesis of PS/silica nanocomposites by a sol–gel method [52]. The miscibility of the PS-silica copolymers was enhanced by covalent incorporation of silica into a PS matrix. Alternatively, sol–gel hydrolysis and condensation of a precursor, such as tetraethyloxysilane (TEOS), tetrabutyl titanate, or aluminum iso-propoxide can be carried out starting from a preformed functional organic

polymer, such as polyvinyl acetate, polymethylmethacrylate (PMMA) [53], polyetherimide [54], polyvinyl alcohol [55], polyamides [56], polyimide and several other polymers [57]. Alkoxysilane containing polymers can also be used in the sol-gel process as silica precursors [58]. Du et al. carried out the sol–gel synthesis of a ZnO/polyvinylpyrrolidone nanocomposite thin film for superoxide radical sensor applications [59].

Much attention has been paid to the *in situ* polymerization method which involves the modification of the nanoparticle surface by using a ligand or coupling agent, then dispersion of functionalized nanoparticles mix with monomer(s), initiator, and followed by bulk or solution polymerization. Advantages of this method include ease of handling, rapid reaction and better performance of the final products [41]. This method has been studied extensively for silica nanoparticles with different polymers, such as PMMA [60], vinyl polymer [61], and polystyrene [62]. There are two general routes usually followed to graft linear polymer chains to the surface of the particles. One method is the "*grafting-to*" polymerization technique, in which preformed polymer and functionalized nanoparticles are mixed together, leading the polymer chains which either physically adsorb (post-modification) or covalently bind ("*grafting to*") to the inorganic surface. The other method is the "*grafting-from*" polymerization technique, in which the inorganic surface is functionalized with an initiator or a coupling agent and then polymerization of the desired monomer is carried out [39, 63, 64]. In situ fabrication of NPs in a polymer matrix has been shown as a very effective route for preparing thicker bulk nanocomposites with improved interfacial interactions, including those that are electronic–driven, between NPs and the polymer matrix [40]. However, a key challenge is to obtain stable and transparent dispersions of nanoparticles before subsequent polymerization because the low viscosity of particle dispersions in monomers may result in the precipitation of inorganic particles during the long polymerization process [41]. Generally, for a given monomer used for preparing nanocomposites, the design and tailoring of the surface characteristics of the inorganic particles is very important in order to make the particles compatible with the monomers through the strong interfacial

interaction between the monomer molecules and the inorganic particles or the inorganic particle cores protected with organic capping shells [41].
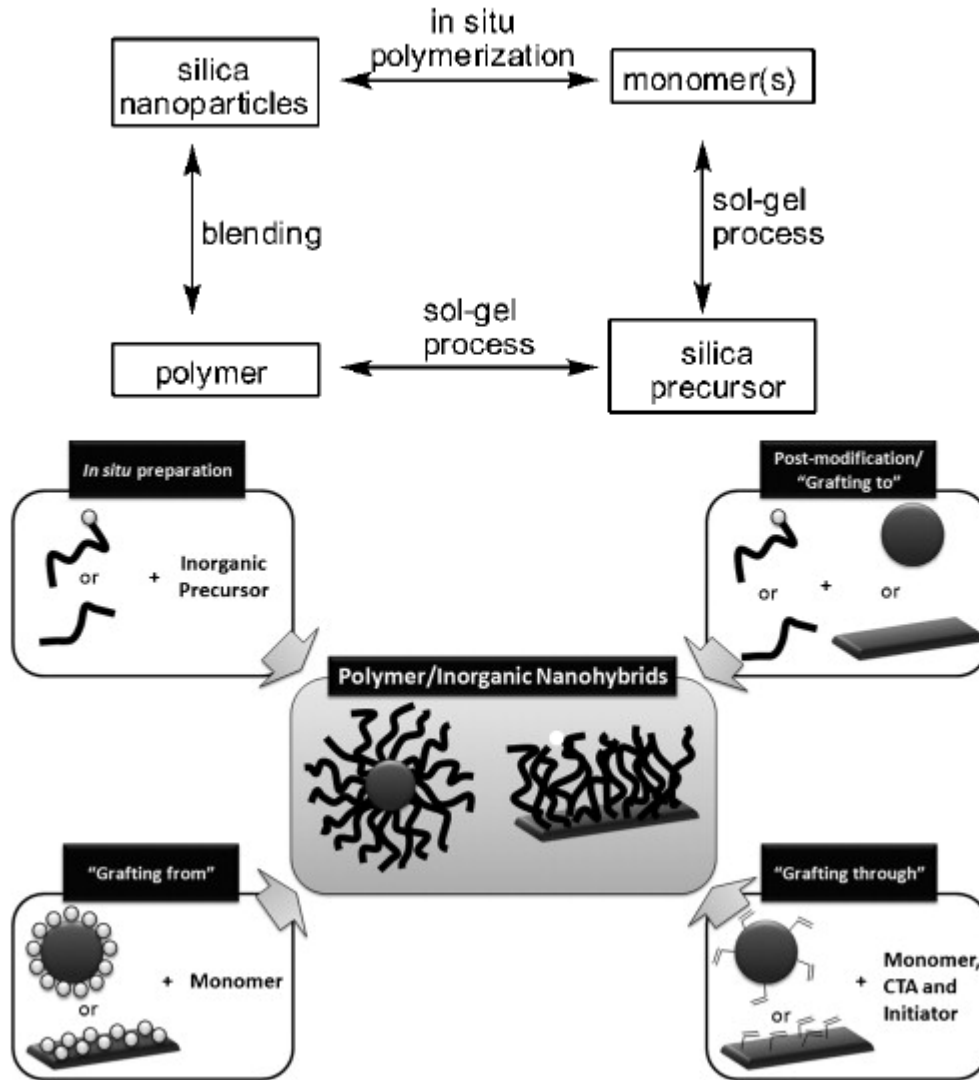
Figure 2.4. General approaches and grafting strategies of polymer/inorganic (e.g. QDs, silica nanoparticles) nanocomposites preparation (adapted from [58, 63]).

Other major challenges involve multiple synthesis steps and traditional hazardous solvents, high sensitivity of porous structure to porogenic diluents and solvents, volume shrinkage during polymerization, change in structure or crack formation after removal of

solvents, and the large amount of solvents required [65]. Therefore, alternative synthesis design and approaches utilizing green solvents are highly desirable. During the last decade, researchers have found that supercritical CO_2 (scCO_2) can replace these hazardous solvents during the synthesis of silica-polymer nanocomposites. scCO_2 is cheap, non-toxic, non-flammable, naturally abundant, environmentally benign with a convenient critical temperature and pressure (T_c = 31.1°C, P_c = 7.38 MPa) [66]. scCO_2 can be very beneficial for synthesizing nanomaterials and nanocomposites as it has low viscosity, "zero" surface tension and high diffusivity. These properties can also help to increase the reaction rates by enhancing both mass and heat transfer [67]. The physical properties such as density and solvating strength can be "tuned" by adjusting the operating temperature and pressure which provide an easily tunable reaction medium [68]. This greener approach has been studied by several groups including the Charpentier group that reduced complex multi-step procedure to a one-step synthesis route with scCO_2 working as a solvent, modification agent, and drying agent [66].

The scCO_2 environment enhances mass transfer and reaction kinetics, also allowing penetration of nanoparticles into pores of the polymer network. Recently, QDs/polymer-based nanocomposites synthesis using scCO_2 has emerged and reported by different research groups [69-71], but the strong interactions, uniform distribution, and stability are still the major challenges that play a key role for long term applications of these nanocomposites.

2.3.3   Polymer nanocomposites synthesis in supercritical fluids

Surface modification is a critical step for the synthesis of polymer nanocomposites, typically required large amount of organic solvents that are harmful to the environment [72]. To solve this problem, many researchers have attempted to synthesize polymer-inorganic nanoparticles nanocomposites by supercritical fluid (SCF) based technology [73-75]. SCFs (e.g. scCO_2) has a high permeation rate virtually in all polymers and

exposure to $scCO_2$ results in various extents of swelling and enhancement of polymer chain mobility, which makes easier the incorporation of metallic $scCO_2$-soluble precursors or pre-synthesized and functionalized nanomaterials into various polymers [71].

Methods exploring SCFs have been used to obtain nanocomposites by the direct formation of inorganic nanoparticles in polymer hosts, *in situ* polymerization in presence of functionalized nanoparticles, or dispersive mixing of the nanoscale phase into the polymer matrix for various polymers, including PE, PP, PET, PS, PEVA, PMMA etc [71, 72, 76, 77]. The Charpentier group has reported $scCO_2$ reactor fabricated with *in situ* ATR-FTIR that helps to monitor the process in $scCO_2$, and the parallel reactions of polymerization, hydrolysis/condensation of precursor to form nanoparticles, and linkage to the polymer matrix [66]. The set up of such a reactor is shown in Figure 2.5.

Although a significant number of studies reported on QDs/polymer-based nanocomposites, the major challenges are interaction between QDs and polymer, uniform distribution and stability of QDs in the polymer matrix [69]. Recently QDs/polymer nanocomposites of CdS, ZnS, CdSe, or ZnO QDs in PMMA, PET, PEVA synthesis using $scCO_2$ has emerged and reported by different research groups [69, 71, 72]. It has been observed that low viscosity $scCO_2$ enhances QDs distribution by minimizing the aggregation tendency [72, 76]. However, unmodified QDs are quenched in $scCO_2$ and are also difficult to interact with polymer [72]. Ligand exchange or surface modification improves the interactions [69], but uniform distribution and photostability are still the major challenges that play a key role for long term applications of these nanocomposites.
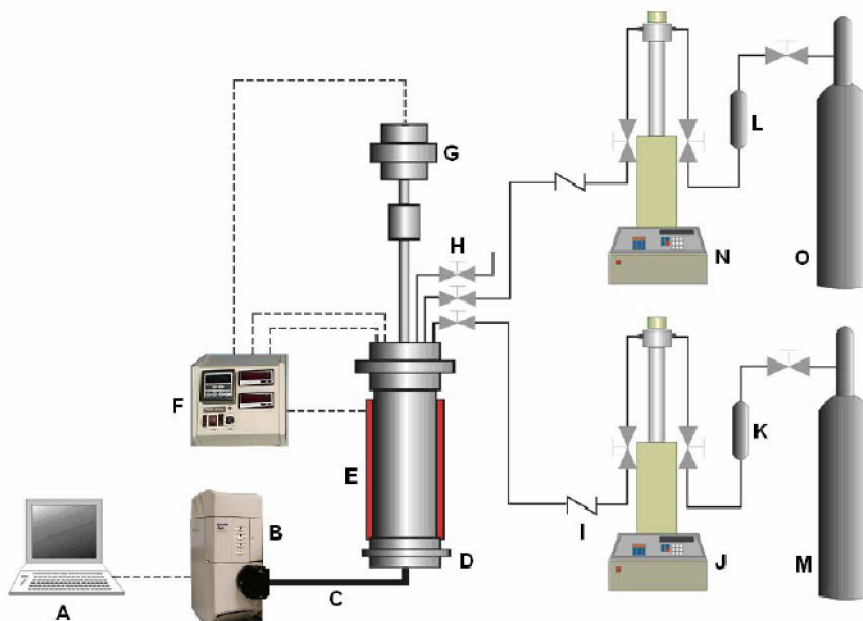
Figure 2.5. Schematic diagram of a batch reactor for scCO$_2$: [(A) Computer; (B) ATR-FTIR; (C) K4 conduit; (D) Autoclave equipped with IR probe; (E) heating mantle; (F) temperature and stirring speed controller with pressure display; (G) stirrer; (H) needle valve; (I) check valve; (J) syringe pump; (K) & (L) purification columns; (M) CO$_2$ cylinder; (N) syringe pump; (O) ethylene cylinder] (Adapted from [78]).

2.4 QDs decoration on TiO$_2$ and photocatalysis

Many methods have been reported for the production of TiO$_2$ nanopowders such as precipitation, decomposition, chemical vapor decomposition, two-step wet chemical method, ultrasonic irradiation, template-assisted synthesis, electrochemical, hydrothermal, and sol-gel techniques [78, 79]. Recent literature has revealed that sol–gel chemistry has evolved as a powerful approach and commonly used method for the preparation of photocatalysts, whether only TiO$_2$ or doped TiO$_2$ [79, 80].

The sol-gel process involves inorganic precursors (a metal salt or organometallic molecule) that is hydrolyzed to form a dispersion of colloidal particles (the sol). Further reaction causes bonds to form between the sol particles resulting in a three dimensional

molecular network (the gel). The gel is then typically heated to yield the desired material [81, 82].

To date, various approaches have been reported to decorate TiO_2 with QDs, such as physisorption, chemical bath deposition (CBD), successive ionic layer adsorption, electrochemical deposition, or using a bi-functional organic linker [83, 84]. Direct deposition by physisorption is the most straightforward method and exhibited enhancement of photoefficiency under visible light [85]. In this method, QDs are synthesized beforehand with tuned size and properties, and the TiO_2 substrate is directly modified by their attachment. This method is sensitive to the solvent due to the small binding forces between QDs and TiO_2 [86]. QDs are commonly synthesized in organic solvents and in the presence of many hydrophobic ligands. Therefore, it can be expected that the resulting QDs are less likely to adsorb onto a hydrophilic surface of TiO_2 [83]. In chemical bath deposition, the QDs are deposited in a precursor salt solution formed on the TiO_2. This is also a straightforward approach, and CdS QDs decorated onto TiO_2 nanotubes using this technique showed enhanced photoactivities under visible irradiation [87]. However, it is very difficult to control the coverage, size, and spectral properties of the QDs [88]. Also the precipitation reaction is rather sudden which can lead to the agglomeration of QDs on the top surface of TiO_2, which block the pores. In addition, the precursor solution tends not to penetrate fully the inner side of TiO_2 nanotubes because of a surface tension of the solution. As a result, both the inside surface and the bottom surface of the tubes are not fully decorated with QDs, which thereby weakens their light harvesting [84].

 Recently, intensive efforts have been undertaken to link bare QDs with nano TiO_2 for photocatalytic applications [86, 89, 90]. Using a bifunctional organic linker, QDs are tethered to TiO_2 surfaces through the linkers which usually have two functional ends, thiol and carboxyl. Thiol binds strongly to the surface of QDs particles and the end of the carboxyl group firmly binds to the surface of TiO_2. o the linker molecule, in pricnciple, could not only control the size of the QD particles by being covered with the linker, but also form strong adhesion between QDs and TiO_2 [86, 91]. The works reported so far are based on only bare QDs linking with TiO_2 and mostly, long aging time (more than 24

hours) and higher temperatures (200-400 $^{\circ}$C) that are required for improving the coupling of the two semiconducting materials and their crystallinity [92].

2.5 References

[1] Y. Yin, A.P. Alivisatos, Colloidal nanocrystal synthesis and the organic–inorganic interface, Nature, 437 (2005) 664-670.

[2] C.B. Murray, D.J. Norris, M.G. Bawendi, Synthesis and characterization of nearly monodisperse CdE (E= sulfur, selenium, tellurium) semiconductor nanocrystallites, Journal of the American Chemical Society, 115 (1993) 8706-8715.

[3] T. Kim, Y.K. Jung, J.-K. Lee, The formation mechanism of CdSe QDs through the thermolysis of Cd (oleate)$_2$ and TOPSe in the presence of alkylamine, Journal of Materials Chemistry C, 2 (2014) 5593-5600.

[4] T. Trindade, P. O'Brien, X.-m. Zhang, Synthesis of CdS and CdSe nanocrystallites using a novel single-molecule precursors approach, Chemistry of Materials, 9 (1997) 523-530.

[5] C.J. Barrelet, Y. Wu, D.C. Bell, C.M. Lieber, Synthesis of CdS and ZnS nanowires using single-source molecular precursors, Journal of the American Chemical Society, 125 (2003) 11498-11499.

[6] X. Peng, Green Chemical Approaches toward High-Quality Semiconductor Nanocrystals, Chemistry-A European Journal, 8 (2002) 334-339.

[7] Z. Lu, Z. Zhu, X. Zheng, Y. Qiao, J. Guo, C.M. Li, Biocompatible fluorescence-enhanced ZrO$_2$–CdTe quantum dot nanocomposite for in vitro cell imaging, Nanotechnology, 22 (2011) 155604-155610.

[8] K. Byrappa, S. Ohara, T. Adschiri, Nanoparticles synthesis using supercritical fluid technology–towards biomedical applications, Advanced Drug Delivery Reviews, 60 (2008) 299-327.

[9] C. Murray, S. Sun, H. Doyle, T. Betley, Monodisperse 3d transition-metal (Co, Ni, Fe) nanoparticles and their assembly into nanoparticle superlattices, MRS Bulletin, 26 (2001) 985-991.

[10] D. Bera, L. Qian, T.-K. Tseng, P.H. Holloway, Quantum dots and their multimodal applications: a review, Materials, 3 (2010) 2260-2345.

[11] J.S. Steckel, J.P. Zimmer, S. Coe-Sullivan, N.E. Stott, V. Bulović, M.G. Bawendi, Blue luminescence from (CdS) ZnS core–shell nanocrystals, Angewandte Chemie International Edition, 43 (2004) 2154-2158.

[12] P. Reiss, J. Bleuse, A. Pron, Highly luminescent CdSe/ZnSe core/shell nanocrystals of low size dispersion, Nano Letters, 2 (2002) 781-784.

[13] D.V. Talapin, I. Mekis, S. Götzinger, A. Kornowski, O. Benson, H. Weller, CdSe/CdS/ZnS and CdSe/ZnSe/ZnS core-shell-shell nanocrystals, The Journal of Physical Chemistry B, 108 (2004) 18826-18831.

[14] W.Y. William, E. Chang, R. Drezek, V.L. Colvin, Water-soluble quantum dots for biomedical applications, Biochemical and Biophysical Research Communications, 348 (2006) 781-786.

[15] S.T. Selvan, T.T. Tan, J.Y. Ying, Robust, Non-Cytotoxic, Silica-Coated CdSe Quantum Dots with Efficient Photoluminescence, Advanced Materials, 17 (2005) 1620-1625.

[16] Q. Cai, Z.-S. Luo, W.-Q. Pang, Y.-W. Fan, X.-H. Chen, F.-Z. Cui, Dilute solution routes to various controllable morphologies of MCM-41 silica with a basic medium, Chemistry of Materials, 13 (2001) 258-263.

[17] C. Fowler, D. Khushalani, B. Lebeau, S. Mann, Nanoscale materials with mesostructured interiors, Advanced Materials, 13 (2001) 649-652.

[18] R.I. Nooney, D. Thirunavukkarasu, Y. Chen, R. Josephs, A.E. Ostafin, Synthesis of nanoscale mesoporous silica spheres with controlled particle size, Chemistry of Materials, 14 (2002) 4721-4728.

[19] C.-Y. Lai, B.G. Trewyn, D.M. Jeftinija, K. Jeftinija, S. Xu, S. Jeftinija, V.S.-Y. Lin, A mesoporous silica nanosphere-based carrier system with chemically removable CdS nanoparticle caps for stimuli-responsive controlled release of neurotransmitters and drug molecules, Journal of the American Chemical Society, 125 (2003) 4451-4459.

[20] S.-H. Wu, C.-Y. Mou, H.-P. Lin, Synthesis of mesoporous silica nanoparticles, Chemical Society Reviews, 42 (2013) 3862-3875.

[21] W. Stöber, A. Fink, E. Bohn, Controlled growth of monodisperse silica spheres in the micron size range, Journal of Colloid and Interface Science, 26 (1968) 62-69.

[22] M. Grün, I. Lauer, K.K. Unger, The synthesis of micrometer-and submicrometer-size spheres of ordered mesoporous oxide MCM-41, Advanced Materials, 9 (1997) 254-257.

[23] B. Zhang, X. Gong, L. Hao, J. Cheng, Y. Han, J. Chang, A novel method to enhance quantum yield of silica-coated quantum dots for biodetection, Nanotechnology, 19 (2008) 465604-465612.

[24] M. Darbandi, G. Urban, M. Krüger, A facile synthesis method to silica coated CdSe/ZnS nanocomposites with tuneable size and optical properties, Journal of Colloid and Interface Science, 351 (2010) 30-34.

[25] K. Tadanaga, K. Morita, K. Mori, M. Tatsumisago, Synthesis of monodispersed silica nanoparticles with high concentration by the Stöber process, Journal of Sol-Gel Science and Technology, 68 (2013) 341-345.

[26] F. Arriagada, K. Osseo-Asare, Synthesis of nanosize silica in aerosol OT reverse microemulsions, Journal of Colloid and Interface Science, 170 (1995) 8-17.

[27] M. Darbandi, R. Thomann, T. Nann, Single quantum dots in silica spheres by microemulsion synthesis, Chemistry of Materials, 17 (2005) 5720-5725.

[28] M. Chu, Y. Sun, S. Xu, Silica-coated quantum dots fluorescent spheres synthesized using a quaternary 'water-in-oil'microemulsion system, Journal of Nanoparticle Research, 10 (2008) 613-624.

[29] H. Mader, X. Li, S. Saleh, M. Link, P. Kele, O.S. Wolfbeis, Fluorescent silica nanoparticles, Annals of the New York Academy of Sciences, 1130 (2008) 218-223.

[30] M.A. Malik, M.Y. Wani, M.A. Hashim, Microemulsion method: a novel route to synthesize organic and inorganic nanomaterials: 1st nano update, Arabian Journal of Chemistry, 5 (2012) 397-417.

[31] Z.A. ALOthman, A review: fundamental aspects of silicate mesoporous materials, Materials, 5 (2012) 2874-2902.

[32] S.T. Selvan, Silica-coated quantum dots and magnetic nanoparticles for bioimaging applications (Mini-Review), Biointerphases, 5 (2010) FA110-FA115.

[33] N.R. Jana, C. Earhart, J.Y. Ying, Synthesis of water-soluble and functionalized nanoparticles by silica coating, Chemistry of Materials, 19 (2007) 5074-5082.

[34] Q. Ma, I.C. Serrano, E. Palomares, Multiplexed color encoded silica nanospheres prepared by stepwise encapsulating quantum dot/SiO$_2$ multilayers, Chemical Communications, 47 (2011) 7071-7073.

[35] Isanaeni, L.-H. Jin, Y.-H. Cho, Silica encapsulation of toluene soluble quantum dots with high photostability, Journal of Colloid and Interface Science, 395 (2013) 45-49.

[36] D. Gerion, F. Pinaud, S.C. Williams, W.J. Parak, D. Zanchet, S. Weiss, A.P. Alivisatos, Synthesis and properties of biocompatible water-soluble silica-coated

CdSe/ZnS semiconductor quantum dots, The Journal of Physical Chemistry B, 105 (2001) 8861-8871.

[37] M.A. Mumin, W.Z. Xu, P.A. Charpentier, Quantum dots/silica/polymer nanocomposite films with high visible light transmission and UV shielding properties, Nanotechnology, 26 (2015) 315702-315715.

[38] L. Qian, D. Bera, T.-K. Tseng, P.H. Holloway, High efficiency photoluminescence from silica-coated CdSe quantum dots, Applied Physics Letters, 94 (2009) 3112.

[39] N. Tomczak, D. Jańczewski, M. Han, G.J. Vancso, Designer polymer–quantum dot architectures, Progress in Polymer Science, 34 (2009) 393-430.

[40] S. Kango, S. Kalia, A. Celli, J. Njuguna, Y. Habibi, R. Kumar, Surface modification of inorganic nanoparticles for development of organic–inorganic nanocomposites—A review, Progress in Polymer Science, 38 (2013) 1232-1261.

[41] C. Lü, B. Yang, High refractive index organic–inorganic nanocomposites: design, synthesis and application, Journal of Materials Chemistry, 19 (2009) 2884-2901.

[42] X. Ji, J.E. Hampsey, Q. Hu, J. He, Z. Yang, Y. Lu, Mesoporous silica-reinforced polymer nanocomposites, Chemistry of Materials, 15 (2003) 3656-3662.

[43] M.Q. Zhang, M.Z. Rong, K. Friedrich, Processing and properties of nonlayered nanoparticle reinforced thermoplastic composites, Handbook of organic-inorganic hybrid materials and nanocomposites, 2 (2003) 113-150.

[44] Y. Thio, A. Argon, R. Cohen, Improvement of tensile properties of nano-SiO_2/PP composites in relation to percolation mechanism, Polymer, 42 (2002) 3661-3674.

[45] N. Erdem, A.A. Cireli, U.H. Erdogan, Flame retardancy behaviors and structural properties of polypropylene/nano-SiO_2 composite textile filaments, Journal of Applied Polymer Science, 111 (2009) 2085-2091.

[46] S.H. Kim, S.H. Ahn, T. Hirai, Crystallization kinetics and nucleation activity of silica nanoparticle-filled poly (ethylene 2, 6-naphthalate), Polymer, 44 (2003) 5625-5634.

[47] H. Zhao, R.K. Li, A study on the photo-degradation of zinc oxide (ZnO) filled polypropylene nanocomposites, Polymer, 47 (2006) 3207-3217.

[48] J. Hong, K. Cho, C. Chung, L. Schadler, R. Siegel, Retarded cross-linking in ZnO-low-density polyethylene nanocomposites, Journal of Materials Research, 17 (2002) 940-943.

[49] J.M. Allan, M.A. Mumin, W.Z. Xu, Q. Al Sharari, P.A. Charpentier, Surface functionalized bare and core–shell quantum dots in poly (ethylene-co-vinyl acetate) for light selective nanocomposite films, Solar Energy Materials and Solar Cells, 123 (2014) 30-40.

[50] C.J. Brinker, G.W. Scherer, Sol-gel science: the physics and chemistry of sol-gel processing, Academic press, Toronto, pp 2-10, 2013.

[51] J.V. Crivello, K.Y. Song, R. Ghoshal, Synthesis and photoinitiated cationic polymerization of organic-inorganic hybrid resins, Chemistry of Materials, 13 (2001) 1932-1942.

[52] G.-H. Hsiue, W.-J. Kuo, Y.-P. Huang, R.-J. Jeng, Microstructural and morphological characteristics of PS–SiO$_2$ nanocomposites, Polymer, 41 (2000) 2813-2825.

[53] K.F. Silveira, I.V.P. Yoshida, S.P. Nunes, Phase separation in PMMA/silica sol-gel systems, Polymer, 36 (1995) 1425-1434.

[54] S. Nunes, K. Peinemann, K. Ohlrogge, A. Alpers, M. Keller, A. Pires, Membranes of poly (ether imide) and nanodispersed silica, Journal of Membrane Science, 157 (1999) 219-226.

[55] F. Suzuki, K. Onozato, Y. Kurokawa, A formation of compatible poly (vinyl alcohol)/alumina gel composite and its properties, Journal of Applied Polymer Science, 39 (1990) 371-381.

[56] R. Sengupta, A. Bandyopadhyay, S. Sabharwal, T.K. Chaki, A.K. Bhowmick, Polyamide-6, 6/in situ silica hybrid nanocomposites by sol–gel technique: synthesis, characterization and properties, Polymer, 46 (2005) 3343-3354.

[57] G.H. Hsiue, J.K. Chen, Y.L. Liu, Synthesis and characterization of nanocomposite of polyimide–silica hybrid from nonaqueous sol–gel process, Journal of Applied Polymer Science, 76 (2000) 1609-1618.

[58] H. Zou, S. Wu, J. Shen, Polymer/silica nanocomposites: preparation, characterization, properties, and applications, Chemical Reviews, 108 (2008) 3893-3957.

[59] T. Du, H. Song, O.J. Ilegbusi, Sol–gel derived ZnO/PVP nanocomposite thin film for superoxide radical sensor, Materials Science and Engineering: C, 27 (2007) 414-420.

[60] K. Moller, T. Bein, R.X. Fischer, Entrapment of PMMA polymer strands in micro- and mesoporous materials, Chemistry of Materials, 10 (1998) 1841-1852.

[61] M. Percy, J. Amalvy, C. Barthet, S. Armes, S. Greaves, J. Watts, H. Wiese, Surface characterization of vinyl polymer–silica colloidal nanocomposites using X-ray photoelectron spectroscopy, Journal of Materials Chemistry, 12 (2002) 697-702.

[62] A. Schmid, J. Tonnar, S.P. Armes, A New Highly Efficient Route to Polymer-Silica Colloidal Nanocomposite Particles, Advanced Materials, 20 (2008) 3331-3336.

[63] M. Beija, J.-D. Marty, M. Destarac, RAFT/MADIX polymers for the preparation of polymer/inorganic nanohybrids, Progress in Polymer Science, 36 (2011) 845-886.

[64] L. Wei, N. Hu, Y. Zhang, Synthesis of polymer—mesoporous silica nanocomposites, Materials, 3 (2010) 4066-4079.

[65] B. Yue, J. Yang, C.Y. Huang, R. Dave, R. Pfeffer, Synthesis of macroporous PMMA/silica nanocomposite monoliths in supercritical carbon dioxide, Macromolecular Rapid Communications, 26 (2005) 1406-1411.

[66] P.A. Charpentier, W.Z. Xu, X. Li, A novel approach to the synthesis of SiO_2–PVAc nanocomposites using a one-pot synthesis in supercritical CO_2, Green Chemistry, 9 (2007) 768-776.

[67] I. Smirnova, W. Arlt, Synthesis of silica aerogels: Influence of the supercritical CO_2 on the sol-gel process, Journal of Sol-gel Science and Technology, 28 (2003) 175-184.

[68] J.A. Darr, M. Poliakoff, New directions in inorganic and metal-organic coordination chemistry in supercritical fluids, Chemical Reviews, 99 (1999) 495-542.

[69] W.Z. Xu, P.A. Charpentier, Light-selective nanofilms of quantum dot-poly (ethylene-co-vinyl acetate) synthesized with supercritical CO_2, The Journal of Physical Chemistry C, 113 (2009) 6859-6870.

[70] K. Matsuyama, Y.-k. Maeda, T. Matsuda, T. Okuyama, H. Muto, Formation of poly (methyl methacrylate)-ZnO nanoparticle quantum dot composites by dispersion polymerization in supercritical CO_2, The Journal of Supercritical Fluids, 103 (2015) 83-89.

[71] M.R. Mauricio, F.C. Manso, M.H. Kunita, D.S. Velasco, A.C. Bento, E.C. Muniz, G.M. de Carvalho, A.F. Rubira, Synthesis and characterization of ZnO/PET composite using supercritical carbon dioxide impregnation technology, Composites Part A: Applied Science and Manufacturing, 42 (2011) 757-761.

[72] K. Matsuyama, Y.-k. Maeda, T. Matsuda, T. Okuyama, H. Muto, Formation of poly (methyl methacrylate)-ZnO nanoparticle quantum dot composites by dispersion polymerization in supercritical CO_2, The Journal of Supercritical Fluids, (2015).

[73] S.E. Bozbağ, C. Erkey, Supercritical deposition: Current status and perspectives for the preparation of supported metal nanostructures, The Journal of Supercritical Fluids, 96 (2015) 298-312.

[74] F. Cansell, C. Aymonier, Design of functional nanostructured materials using supercritical fluids, The Journal of Supercritical Fluids, 47 (2009) 508-516.

[75] Y. Haldorai, J.-J. Shim, K.T. Lim, Synthesis of polymer–inorganic filler nanocomposites in supercritical CO_2, The Journal of Supercritical Fluids, 71 (2012) 45-63.

[76] D.L. Tomasko, X. Han, D. Liu, W. Gao, Supercritical fluid applications in polymer nanocomposites, Current Opinion in Solid State and Materials Science, 7 (2003) 407-412.

[77] K. Goren, O.B. Okan, L. Chen, L.S. Schadler, R. Ozisik, Supercritical carbon dioxide assisted dispersion and distribution of silica nanoparticles in polymers, The Journal of Supercritical Fluids, 67 (2012) 108-113.

[78] R. Sui, P. Charpentier, Synthesis of metal oxide nanostructures by direct sol–gel chemistry in supercritical fluids, Chemical Reviews, 112 (2012) 3057-3082.

[79] D. Macwan, P.N. Dave, S. Chaturvedi, A review on nano-TiO_2 sol–gel type syntheses and its applications, Journal of Materials Science, 46 (2011) 3669-3686.

[80] B.B. Lakshmi, C.J. Patrissi, C.R. Martin, Sol-gel template synthesis of semiconductor oxide micro-and nanostructures, Chemistry of Materials, 9 (1997) 2544-2550.

[81] J. Livage, M. Henry, C. Sanchez, Sol-gel chemistry of transition metal oxides, Progress in Solid State Chemistry, 18 (1988) 259-341.

[82] R.A. Caruso, M. Antonietti, Sol-gel nanocoating: an approach to the preparation of structured materials, Chemistry of Materials, 13 (2001) 3272-3282.

[83] T.J. Macdonald, T. Nann, Quantum dot sensitized photoelectrodes, Nanomaterials, 1 (2011) 79-88.

[84] Y. Xie, G. Ali, S.H. Yoo, S.O. Cho, Sonication-assisted synthesis of CdS quantum-dot-sensitized TiO_2 nanotube arrays with enhanced photoelectrochemical and photocatalytic activity, ACS Applied Materials & Interfaces, 2 (2010) 2910-2914.

[85] Y. Medina-Gonzalez, W.Z. Xu, B. Chen, N. Farhanghi, P.A. Charpentier, CdS and CdTeS quantum dot decorated TiO_2 nanowires: synthesis and photoefficiency, Nanotechnology, 22 (2011) 065603-065611.

[86] S. Qian, C. Wang, W. Liu, Y. Zhu, W. Yao, X. Lu, An enhanced CdS/TiO_2 photocatalyst with high stability and activity: effect of mesoporous substrate and bifunctional linking molecule, Journal of Materials Chemistry, 21 (2011) 4945-4952.

[87] C.-F. Chi, Y.-L. Lee, H.-S. Weng, A CdS-modified TiO_2 nanocrystalline photoanode for efficient hydrogen generation by visible light, Nanotechnology, 19 (2008) 125704-125708.

[88] L. Liu, J. Hensel, R.C. Fitzmorris, Y. Li, J.Z. Zhang, Preparation and photoelectrochemical properties of $CdSe/TiO_2$ hybrid mesoporous structures, The Journal of Physical Chemistry Letters, 1 (2009) 155-160.

[89] N. Guijarro, T. Lana-Villarreal, I. Mora-Seró, J. Bisquert, R. Gómez, CdSe quantum dot-sensitized TiO_2 electrodes: effect of quantum dot coverage and mode of attachment, The Journal of Physical Chemistry C, 113 (2009) 4208-4214.

[90] D.R. Pernik, K. Tvrdy, J.G. Radich, P.V. Kamat, Tracking the adsorption and electron injection rates of CdSe quantum dots on TiO_2: linked versus direct attachment, The Journal of Physical Chemistry C, 115 (2011) 13511-13519.

[91] R.S. Dibbell, D.F. Watson, Distance-dependent electron transfer in tethered assemblies of CdS quantum dots and TiO_2 nanoparticles, The Journal of Physical Chemistry C, 113 (2009) 3139-3149.

[92] N. Ghows, M.H. Entezari, Sono-synthesis of core–shell nanocrystal (CdS/TiO_2) without surfactant, Ultrasonics Sonochemistry, 19 (2012) 1070-1078.

Chapter 3

Quantum dots/silica/polymer nanocomposite films with high visible light transmission and UV shielding properties

Abstract

The dispersion of light absorbing inorganic nanomaterials in transparent plastics such as poly(ethylene-co-vinyl acetate) (PEVA) are of enormous current interest in emerging solar materials, including photovoltaic (PV) modules and commercial greenhouse films. Nanocrystalline semiconductor or quantum dots (QDs) have the potential to absorb UV light and selectively emitting visible light, which can control plant growth in greenhouses or enhance PV panel efficiencies. This work provides a new and simple approach for loading mesoporous silica encapsulated QDs into PEVA. Highly luminescent CdS and CdS-ZnS core-shell QDs with 5 nm sizes were synthesized using a modified facile approach based on pyrolysis of the single molecule precursors and capping the CdS QDs with a thin layer of ZnS. To make both the bare and core-shell structure QDs more resistant against photochemical reactions, a mesoporous silica layer was grown on the QDs through a reverse microemulsion technique based on hydrophobic interactions. By careful experimental tuning, this encapsulation technique enhanced the quantum yield (~65%) and photostability compared to the bare QDs. Both the encapsulated bare and core-shell QDs were then melt-mixed with EVA pellets using a mini twin-screw extruder and pressed into thin films with controlled thickness. The results demonstrated for the first time that mesoporous silica not only enhanced the quantum yield and photostability of the QDs but also improved the compatibility and dispersibility of QDs throughout the PEVA films. The novel light selective films show high visible light transmission (~90%) and decreased UV transmission (~75%).

3.1. Introduction

Polymer-inorganic nanocomposites are of significant scientific and technological interest in recent years [1]. These inorganic nanomaterials, even at very low concentrations, can strongly change the macroscopic properties of the polymer matrix, while providing high-performance emerging materials [2-4]. Recently, transparent polymer nanocomposite films with UV blocking properties have attracted substantial research and technological

interest in emerging solar materials, including photovoltaic (PV) modules and commercial greenhouse films [5, 6]. UV radiation absorbed by these polymer films causes photochemical degradation by leading to bond cleavage and depolymerisation. To minimize the degradation there is a wide variety of UV stabilizers that are commonly used, such as UV absorbers, nickel quenchers, and hindered amine light stabilizers (HALS) etc [7, 8]. However, little information is available about their incorporation into the polymer matrix. In addition, uniform distribution, long-term stability, transparency of the films, and lowering cost are still the major concerns [9]. Polymer films with luminescent nanomaterials offer a useful and promising approach to improve solar energy harvesting and increase the efficiency of solar devices [10, 11]. Among different luminescent materials, semiconductor nanocrystals (NCs), also known as quantum dots (QDs) have drawn enormous research interest, arising from the benefits of their unique size- and shape- dependent optical properties, which are very different from their bulk counterparts due to the quantum confinement effect [12]. QDs can efficiently convert undesirable higher energy UV radiation into desirable lower energy visible wavelengths which is beneficial for their application as greenhouse films, photovoltaic (PV) encapsulants, etc [13, 14]. Compared to bare QDs, core-shell structured QDs with a thin shell of a higher band gap element are advantageous and have been shown to enhance photo-physical properties [15-18]. This is attributed to the surface defects in the core acting as temporary 'traps' for the electron, hole or excitons, quenching radiative recombination and reducing the quantum yield (QY) [19].

For further processing of either bare or core-shell QDs, including incorporation into polymers, the QDs need to be stabilized [14, 20]. The earliest approach to stabilize the QDs is to exchange the hydrophobic surface of QDs by surface functionalizing ligands with desired functionalities [13, 14, 21]. However, long term photostability of these capped QDs is limited [22]. The selection of organic ligands that bond with surface atoms of the QDs is also a very delicate issue and coverage of surface atoms may cause steric hindrance effects [19]. Another approach is encapsulation by silica, a biocompatible material which is chemically inert, optically transparent, providing both chemical and physical shielding between the QD surface and the surrounding environment. Other

advantages of silica coating are that it can prevent aggregation and photo-oxidation of QDs and that it can reduce the release of cytotoxic ions; moreover, the silica surface can be modified or conjugated with different functionalities for linking to polymeric species and biomolecules [15, 23-25]. Mesoporous silica reveals several key structural features, such as large surface area, high pore volume, uniform and tunable pore size, stable and rigid mesoporous framework and facile surface functionalize potential [16, 26]. In previous works, most attention has been paid to fabricate and tuning the silica shell but the achieved quantum efficiencies were not well retained [27, 28]. Therefore, controlling the distribution of QDs at the core, avoiding aggregation and non-radiative emission, and then growing of silica shell that can improve their quantum efficiency are still major concerns.

Despite the potential UV absorption capacity of QDs, their uncontrollable sizes, aggregation tendency, inconsistent photoluminescence, and degradation under prolonged photo-excitation have hindered recent progresses of QDs in composites [21, 29], thus requiring new approaches. By using a facile technique, uniform distribution of QDs into polymer films without compromising their transparency and desired light transmittance is also a major challenge. For this work, we were particularly interested in EVA films to integrate photostable QDs. Since the earliest days of PV manufacturing, EVA films have been found the main and ideal encapsulants for PV modules [30]. EVA plastic films are also widely used as commercial greenhouse coverings [31]. EVA, a semi-crystalline polymer, provides excellent transparency due to the vinyl acetate component, durability, structural support, low water absorption and high electrical isolation properties [32]. Recently, we have integrated silane functionalized QDs directly during *in situ* polymerization of ethylene and vinyl acetate under supercritical carbon dioxide (scCO$_2$) [14], where aggregation and lack of using commercial EVA (ethylene-co-vinyl acetate) resins were the issues of this synthesis approach. However, this approach requires *in situ* polymerization. We have also reported recently a simple melt-mixing procedure for surface functionalized QDs loading in EVA resins retaining high visible light transmission and decreased UV transmission [13]. Although the optical properties were improved significantly in that work, we found the major challenges were photostability

and consistent photoluminescence. This led to a new approach to stabilize these materials for long-term applications.

Since EVA shows high compatibility with fillers and additives [33], by integrating QDs with a controlled thickness of silica in EVA, it is not only possible to enhance quantum yield and photostability of the QDs but also to improve the compatibility and dispersibility of QDs throughout the EVA films as well as the stability of the films. No reports have been published on mesoporous silica encapsulated QDs loaded into EVA using a melt-mixing approach, especially for applications in greenhouse coverings or PV encapsulants.

In the present work, highly photoluminescence and monodispersed CdS bare and CdS-ZnS core-shell quantum dots were prepared by using a facile and modified (changed reaction temperature and duration) colloidal synthesis approach. Then a novel concentration-dependent nanoencapsulation was done for both types of QDs in mesoporous silica, with the photo-physical properties examined including morphology, absorption and emission, quantum yield, photostability etc. It was hypothesized that the polar siloxyl group of the silica nanoparticle surface would improve the dispersibility of the QDs in the EVA polymer network. These nanomaterials were then melt-mixed into EVA resins in a mini twin extruder, and then pressed into variable thickness thin films, which were characterized in terms of their morphology, and optical properties including UV and visible light transmission.

3.2. Experimental

3.2.1. Materials

All the reagents were used without further purification unless stated otherwise. Argon (ultra high purity, 99.9%, PRAXAIR), cadmium chloride, sodium diethyldithiocarbamate

trihydrate, zinc diethyldithiocarbamate (98%), trioctylamine (TOA) (98%,), trioctylphosphine (TOP) (97%), anhydrous ethanol ($\geq$ 99.5%), methanol ($\geq$ 99.9%), and toluene ($\geq$ 99%) were purchased from Sigma-Aldrich, Canada and were used for the synthesis of bare CdS and CdS-ZnS core-shell quantum dots. Cyclohexane (99%), chloroform (99.8%), 1-hexanol (98%), tetraethyl orthosilicate (TEOS), ammonia solution (28%), also purchased from Sigma-Aldrich, Canada and were used for the mesoporous silica nanoparticles formation. Ethylene vinyl acetate copolymer (Ateva$^{®}$1075 with 9 wt% vinyl acetate content) was provided by AT Plastics, Canada.

3.2.2. Synthesis of CdS and CdS-ZnS QDs

Both bare (CdS) and core-shell (CdS-ZnS) QDs were prepared by following a minor modification by changing reaction temperature and duration of a single-molecular precursor method reported previously [14, 34]. To formulate the cadmium precursor, $Cd[S_2CN(C_2H_5)_2]_2$ for QD synthesis, equimolar (0.1 M) aqueous solution of sodium diethyldithiocarbamate and cadmium chloride were mixed under vigorous stirring. The rapid reaction proceeds yielding a white precipitate that was collected using vacuum filtration. Further purification was achieved by washing with distilled water, and then dried in a vacuum oven overnight at 50 ^{o}C. For QD synthesis, in a 250 mL three-necked flask under argon, when the temperature of 50 mL of trioctylamine (TOA) was stable at 235 ^{o}C, a solution of 1 g of $Cd[S_2CN(C_2H_5)_2]_2$ in 18 mL of trioctylphophine (TOP) was rapidly injected into the flask and continued heating for 15 min. During cooling at approximately 75 ^{o}C, a large excess of methanol was added followed by separation of the quantum dots through centrifugation. The nanoparticles were then dispersed into toluene and washed with methanol following by at least three rounds of centrifugation. In the case of core-shell (CdS-ZnS) QDs, the temperature of TOA was maintained at 220 ^{o}C for 10 min after addition of the cadmium diethyldithiocarbamate solution, then a solution of 0.4 g of $Zn[S_2CN(C_2H_5)_2]_2$ in 6 mL of TOP was slowly added dropwise. After 15 min the reaction mixture was cooled and the product separated and washed by following the same method described for the CdS QDs.

3.2.3. Mesoporous silica encapsulation of QDs

The encapsulation reaction was carried out by following the water-in-oil microemulsion (also called reverse microemulsion) method based on sol-gel chemistry (as shown in Scheme 3.1). A homogeneous mixture of surfactant in oil phase was prepared by adding 2.6 mL of triton X-100 (surfactant) and 2.5 mL of 1-hexanol (co-surfactant) in 20 mL of cyclohexane (oil). After 15 min of addition of 1 mL of water, 800 μL of QDs solution (5 mg mL^{-1} in chloroform) was also mixed under magnetic stirring at the ambient temperature. Then 160 μL of TEOS as silica precursor was added to the microemulsion. After 1 hr, 300 μL of ammonia solution (28%) was added slowly as a catalyst of TEOS co-hydrolysis and silica polymerization. The reaction mixture was then stirred at the same temperature for 24 hrs. To separate and purify the desired nanoparticles, 30-50 mL of acetone was added to break the emulsion and followed by ultrasonication for 2-3 min and centrifugation at 6500 rpm for 10 min. Finally, the resultant NPs were washed at least 3 times with ethanol, acetone and water 1:1:1 and fridge dried for couple of hrs.

3.2.4. Mesoporous silica encapsulated QDs-EVA nanocomposite films

Both the encapsulated bare and core-shell QDs were integrated into EVA resins through melt mixing. Five grams of EVA pellets were added to a Thermo Scientific HAAKE Mini-Lab II twin-screw micro-compounder at 130 $^{\circ}$C. The virgin PEVA was melted and cycled for 5 min at 50 rpm. Different loading concentrations (0.1%, 0.2%, 0.5%, and 1% by weight) of encapsulated CdS and CdS-ZnS QDs were added to the melted PEVA and left to cycle for a further 15 min in the extruder. The resulting blend (0.03, 0.075, 0.15 g for 100, 250, and 500 μm films respectively) was pressed into thin films using a Spectra-Tech Universal Film Maker (UFM) kit and Carver hydraulic press. The platens of the UFM with samples in the desired thickness spacer were heated to 120 $^{\circ}$C and placed under 2500 psi for 5 min. The films were left under pressure without heat for a further 10 min and then cooled for 5 min in a cooling chamber.

3.2.5. Material characterization

X-ray diffraction (XRD) in a Bruker D2 Phaser bench-top x-ray powder diffractometer using Cu Kα radiation (λ for Kα=1.54059 Å) at 30 kV and 10 mA was used to investigate the crystalline structure and chemical composition. Dry powder samples were used with patterns collected in step-scan mode with a small grazing angle of incident x-ray with a 2θ scan range of 10-80 and a step size of 0.25. Estimates for particle size were calculated for a reference peak from XRD diffraction pattern using the DiffracEVA software provided by Bruker. Transmission electron microscopy (TEM) images were recorded on a Philips CM10 transmission electron microscope to image the mesoporous silica encapsulated QDs to observe their size and shape at 80 kV. The TEM samples were prepared by drop casting ethanol dispersed samples on a copper grid covered with carbon film. High-resolution transmission electron microscopy (HRTEM) images of both the bare and core-shell QDs were recorded with a JEOL 2010F FEG TEM/STEM at the Canadian Centre for Electronic Mcroscopy (McMaster University, Hamilton Ontario) operated at 200 kV. Scanning electron microscopy (SEM) was also done to study the morphology of silica nanoparticles by using a LEO(ZEISS) 1540XB FIB/SEM. Samples for SEM imaging were prepared by applying the nanopowder directly to aluminium stub on carbon adhesion tape. Elemental composition of QDs inside silica was confirmed and quantified using the energy dispersive X-ray detection (EDX) feature of the SEM. A Shimadzu UV-3600 UV-VIS-NIR spectrophotometer was used to measure the absorption spectrum of the QDs dispersed in toluene and encapsulated QDs dispersed in ethanol. A PTI photoluminescence (PL) spectrophotometer was used to measure the PL emissions of QDs before and after encapsulation. Photostability of the QDs was investigated using a Fluorolog-3 spectrofluorometer. The Brunauer–Emmett–Teller (BET) surface area and pore size were determined from nitrogen adsorption and desorption isotherm data obtained at 77 K. BET experiments were carried out with a constant volume adsorption apparatus (Micromeritics TriStar II 3020) with N_2 gas (99.995% pure; obtained from Praxair, Canada). The silica nanoparticle sample was degassed at 150 ^{o}C overnight before measurements.
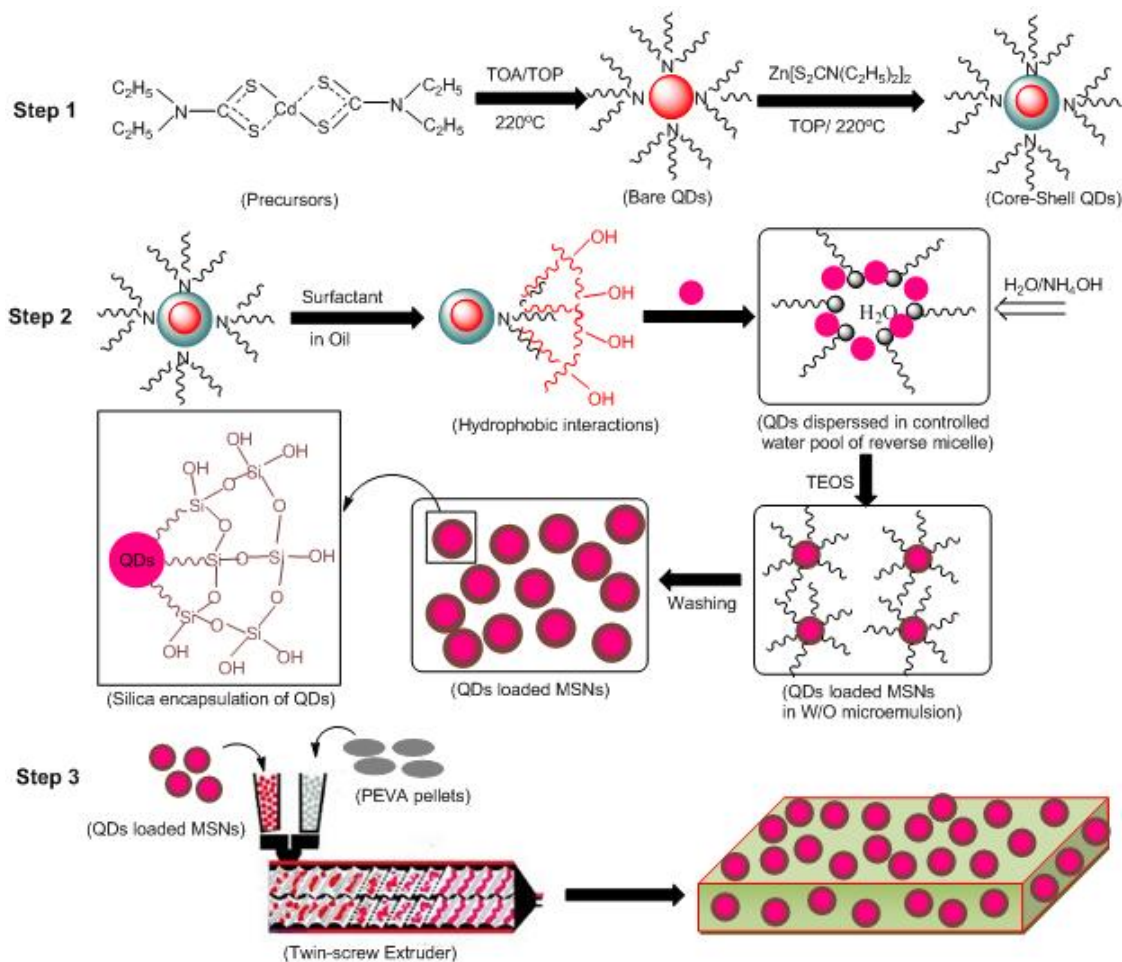
Scheme 3.1. Schematic illustration of (step 1) chemical reactions of bare CdS and core-shell CdS-ZnS QDs from single molecule precursors, (step 2) mesoporous silica encapsulation of QDs by using a water-in-oil microemulsion technique based on hydrophobic interaction, and (step 3) melt mixing of silica encapsulated QDs with PEVA to form light selective polymer nanocomposite.

The integrated sphere compartment of a Shimadzu UV-3600 UV-VIS-NIR spectrophotometer was used to measure the light transmittance and haze values of the film samples. A ZEISS LSM 5 Duo confocal microscope was used to take transmission and fluorescence images of the experimental films using an argon laser at 488 nm. Small section of surface film areas of approximately 500 μm were scanned using an objective

of 20x magnification. A Veeco diMultiMode V atomic force microscope (AFM) was used to image the surface topography, roughness, and phase of the experimental films. The images were taken in tapping mode using an E scanner. Surface roughness and height values were calculated using Nanoscope V7.30 program software.

3.3. Results and discussion

3.3.1. Morphology of QDs and mesoporous silica encapsulated QDs

The XRD pattern of bare CdS and CdS-ZnS core-shell QDs are shown in Figure 3.1a. Crystalline structure and approximate particle size of both types of QDs were determined using XRD analysis. The bare CdS QDs show major diffractions consistent at 2θ values of 24, 26, 29, 36, 44, 48, and 53, matched perfectly with the (100), (002), (101), (102), (110), (103), and (112) of the hexagonal wurtzite structure of CdS (ICDD PDF 02-1310) [17, 35]. Splitting to three peaks in the 24-30 2θ degree region represents the formation of hexagonal crystallinity rather than a single broad peak representing the cubic CdS QDs [36]. It has also been reported that heat treatment or high temperature (~500 ^{o}C) calcination after synthesis is required to change the crystallinity of CdS from cubic to hexagonal [36]. However, by using this modified colloidal synthesis approach, hexagonal CdS was prepared directly at a comparatively lower reaction temperature. In the case of CdS-ZnS core-shell QDs, the influences were observed for prominent peaks (111), (220), and (311) of the zinc-blended ZnS nanocrystals (ICDD PDF 05-0566) [37]. Since the Cd^{+2} and Zn^{+2} ions have the same total ionic charge and their radii are similar, no alteration took place in the form of crystal structures. After core-shell formation, no peak broadening or intensity lowering was observed, which is attributed to the high degree of crystallinity from the presence of the thin ZnS shell, that can preserve the quantum properties of the hexagonal CdS core [23]. Based on the Debye-Scherrer equation, the average particle size for CdS and CdS-ZnS QDs were calculated as 5.9 and 5.1 nm

respectively, using the (110) peak. The CdS-ZnS QDs were found to be smaller than the CdS samples despite the addition of the ZnS shell, due to the lower reaction temperature and time employed in the synthesis of the CdS core. In the case of core-shell QDs, the reaction temperature was changed to 220 °C compared to 180 °C as previously reported [14]. During injection of CdS precursor (at ambient temperature) to the reaction mixture at 180 °C, the temperature was found to drop below 180 °C for the first couple of minutes, minimizing the nucleation and crystal growth of core QDs.

As shown in Figure 3.1b, both bare and core-shell QDs encapsulated with mesoporous silica showed all the characteristic peaks of QDs. In addition, peak broadening was observed at 2θ values between 20 and 30 degrees, demonstrating the presence of an amorphous silica shell on the surface of the nanocrystals. In the case of MSNs, only a single broad peak was observed at the same region confirming the formation of amorphous silica materials that is consistent with recently reported literature [38]. Therefore, the XRD results support the fabrication of QDs encapsulated in MSNs without compromising the crystallinity.
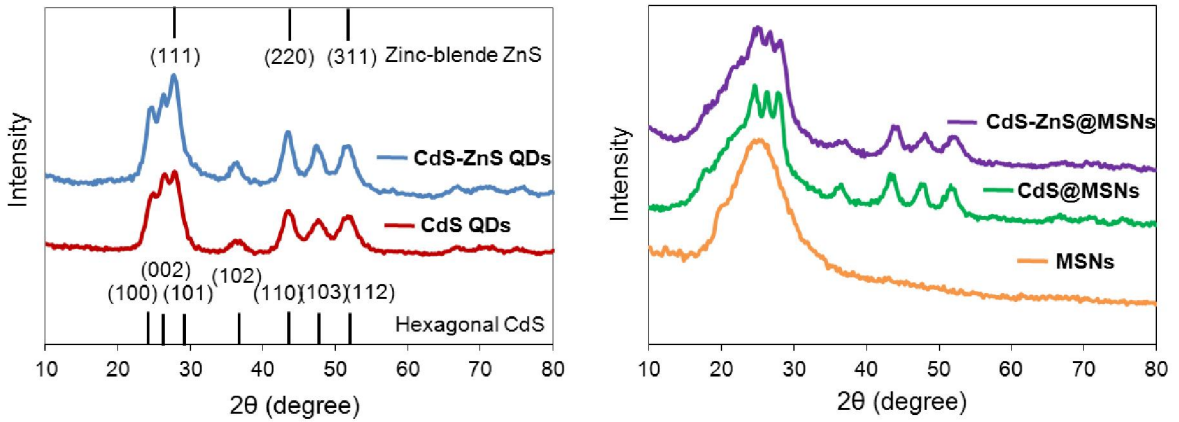
Figure 3.1. Powder X-ray diffraction pattern: (a) CdS quantum dots of hexagonal structure and CdS-ZnS zinc blend quantum dots, (b) mesoporous silica nanoparticles, mesoporous silica encapsulated CdS and CdS-ZnS QDs.

The morphology of both types of QDs was studied using HRTEM as shown in Figure 3.2 a and b. Both samples were present in a dispersed state, showing formation of individual nanoparticles, although better particle separation was observed after core-shell formation. Here, the thin shell of ZnS minimizes the surface crystal defect and aggregation tendency of CdS. The average particle size was found as 6 ± 0.5 nm and 5 ± 0.4 nm for bare and core-shell QDs respectively. The average sizes obtained from XRD analysis and TEM matched each other. From the lattice fringes of the micrograph of CdS or the core part of CdS-ZnS, the interplanar spacing (d) was estimated to be 3.6 Å, which is correlated to the hexagonal phase [19] that also corroborates the finding from the XRD patterns.

The formation of spherical nanoparticles after mesoporous silica encapsulation of both bare and core-shell QDs with a narrow size distribution was directly visualized by TEM. Figure 3.2c inset shows the core-shell nanostructure formation with QDs mostly in the core encapsulated in MSNs shell. The surface of silica is rather smooth and uniform with narrow size distribution, and no aggregation was observed. The average particle size was 60 ± 5 nm with core size from 35 ± 5 nm. The incorporation of hydrophobic QDs within silica spheres follows the hydrophobic interaction mechanism in which non-ionic surfactant enables the transfer of the QDs to the hydrophilic interior of micelles where the silica growth takes place [25].
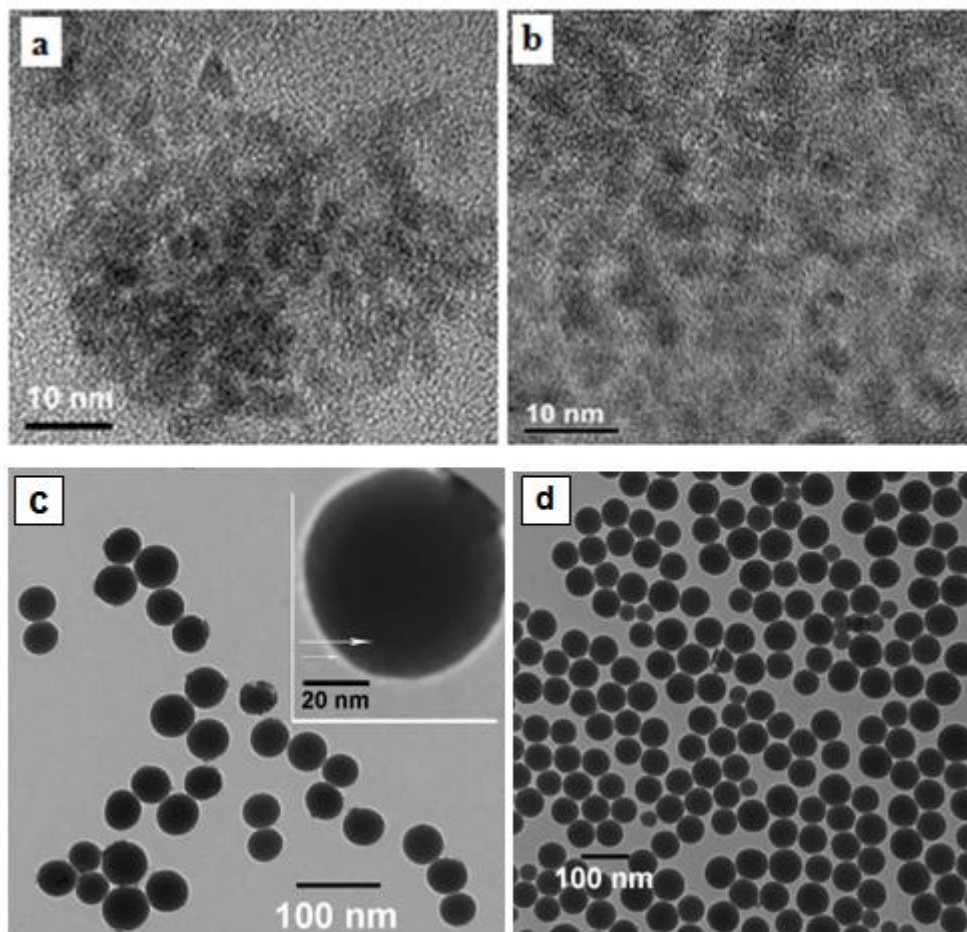
Figure 3.2. High resolution transmission electron microscopic images of (a) CdS QDs; (b) CdS-ZnS QDs; (c) CdS and (d) CdS-ZnS QDs encapsulation within mesoporous silica with loading concentrations 5 mg mL^{-1} in chloroform.

SEM-EDX elemental analysis (Figure 3.3) confirms the successful encapsulation and presence of QDs in the silica spheres. BET analysis was also carried out to evaluate mesoporous structure of silica and it was found after QD loading mesoporous silica can retain its high surface area (950 $\pm$50 m^2 g^{-1}) and mesoporous pore size (3.8 $\pm$ 0.4 nm).

Element	Weight %	Atomic %
C	3.46 ± 0.5	6.32 ± 1.0
O	40.72 ± 5.0	55.90 ± 5.5
Si	42.15 ± 4.5	32.97 ± 4.0
S	2.46 ± 0.5	1.68 ± 0.3
Cd	9.77 ± 1.5	1.91 ± 0.35

Element	Weight %	Atomic %
C	24.01 ± 4.0	37.76 ± 4.5
O	38.15 ± 4.5	45.04 ± 5.0
Si	16.78 ± 2.0	11.29 ± 1.5
S	5.04 ± 0.8	2.97 ± 0.5
Cd	13.94 ± 1.5	2.34 ± 0.5
Zn	2.08 ± 0.3	0.6 ± 0.05
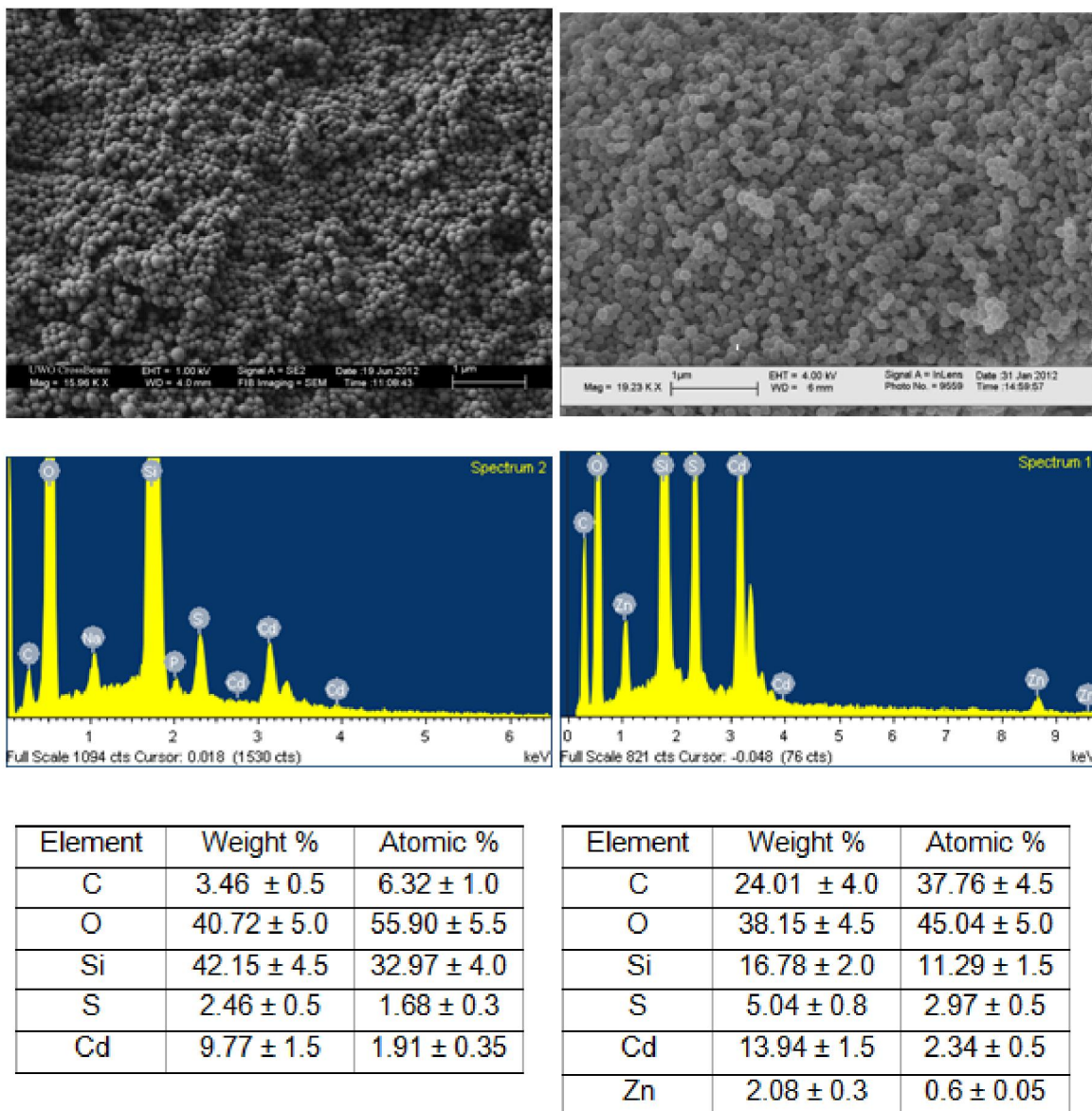
Figure 3.3. Scanning electron microscopic images, SEM-EDX spectra, and elemental compositions of CdS@MSNs (all left side images) and CdS-ZnS@MSNs (all right side images).

3.3.2. Optical properties of QDs and silica encapsulated QDs

The optical properties of both QDs with and without encapsulation in mesoporous silica were studied using UV-vis absorption spectroscopy and photoluminescence (Figure 3.4 a to d). Both QDs showed a broad and continuous excitation spectrum in the UV range and lower wavelength visible range with corresponding absorption edges at 455 and 410 nm for CdS and CdS-ZnS QDs respectively (Figure 3.4 a). These broad absorption spectra of QDs have made them unique and more feasible compared to fluorescent organic dyes. Because organic dyes suffer narrow absorption spectra, requiring excitation within a narrow window of wavelengths [22, 39]. The absorption edge of core-shell QDs shows a blue shift of around 45 nm compared to the bare QDs. This blue shift is attributed to the smaller particle size of the core-shell QDs due to the reduced reaction time during synthesis. Another reason, because of a lower band gap; both the conduction and the valence bands of CdS are located within the energy gap of the ZnS. Typically, electron-hole pairs tend to localize in the semiconductor with lower band gap, in this case CdS. As a result, the increased potential well can lead to an increase of the transitional energies with respect to CdS core and a blue shift of the absorption spectra [17]. For an excitation at 380 nm, PL emission spectra were observed in the visible region for both CdS and CdS-ZnS QDs (Figure 3.4 c). Consistent with the absorption behaviour, the core-shell QDs display a blue shift of around 8 nm.

Silica is transparent under UV and visible light, therefore the absorption and emission behaviour was almost the same except a slight red shift occurred after silica encapsulation of QDs. Similar observations have been reported in the literature for silica encapsulation of II-VI semiconductor QDs [24, 40, 41]. This red shift is also good evidence for avoiding any oxidation of the core surface of the QDs. During encapsulation, the surface of the QD core sometimes oxidizes and this oxide layer shrinks the effective size of the QDs giving higher exciton confinement, resulting in higher energy or lower wavelength emission (blue shift) [42].
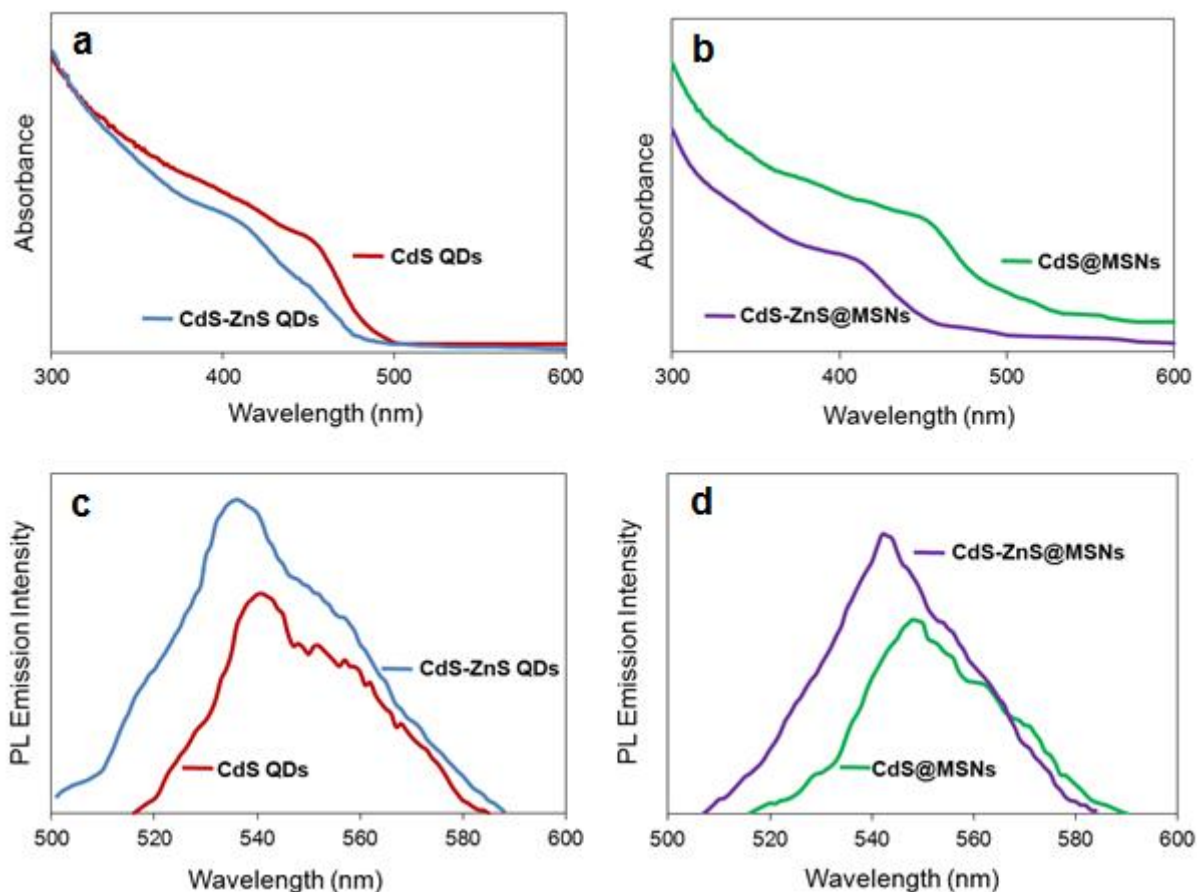
Figure 3.4. UV-vis absorption spectra of (a) CdS and CdS-ZnS QDs, (b) mesoporous silica encapsulated CdS and CdS-ZnS QDs; photoluminescence emission spectra of (c) CdS and CdS-ZnS QDs, (d) mesoporous silica encapsulated CdS and CdS-ZnS QDs excited at 380 nm.

Photostability (change of emission intensity under continuous exposure of excited light) was further determined as shown in Figure 3.5 a. After 6 min continuous exposure, the fluorescence intensity of core-shell QDs was reduced by 20 % compared to the bare QDs by 30 %. This is because the bare CdS is very reactive and can be oxidized resulting in a $CdSO_x$ oxide layer which switches between fluorescent and non-fluorescent states despite continuous illumination. The ZnS shell suppresses the photochemical degradation of CdS, protecting the exciton wavefunction from nonradiative recombination processes as surface traps [39]. However, ZnS capping alone is not sufficient to stabilize the core since

71

for some QDs the ZnS layer is likely imperfect. This poor ZnS layer can be permeable to oxygen, resulting in oxidation of the CdS core [23]. The mesoporous silica encapsulation process minimizes the defect at the ZnS surface abd CdS/ZnS interface, protecting both type of QDs from photobleaching by oxidation.
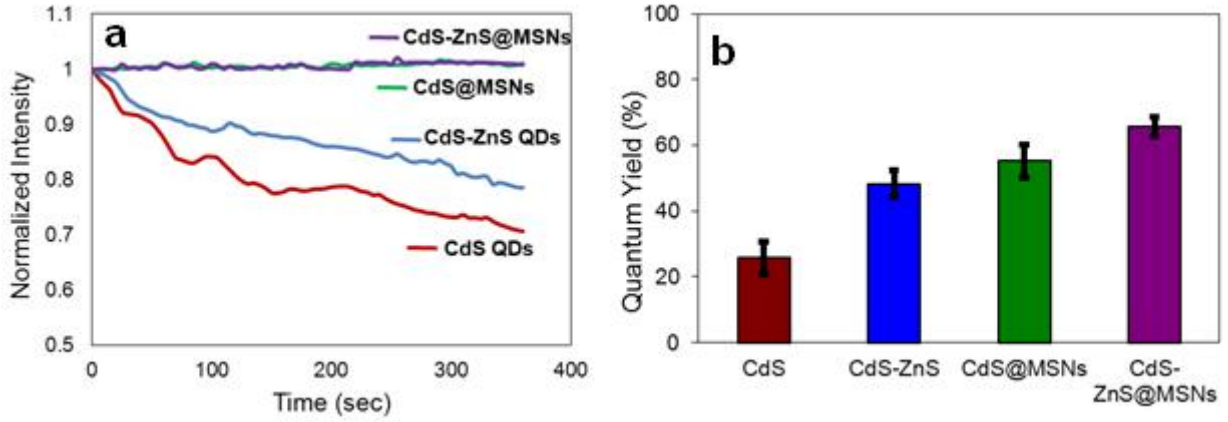
Figure 3.5. (a) Time dependence of photoluminescence intensity under continuous exposure of excited light, and (b) quantum yield of bare and core-shell QDs without and with encapsulation in mesoporous silica nanoparticles (MSNs).

Based on the absorption intensity and emission peak area, the fluorescence quantum yield (QY) was calculated by using the following equation [29].

$$QY_{qdot}(\%) = QY_R \left(\frac{Abs_R}{Abs_{qdot}} \right) \left(\frac{PL_{qdot}}{PL_R} \right) \left(\frac{\eta_{qdot}^2}{\eta_R^2} \right) \quad \text{...(3.1)}$$

Here Rhodamin 101 was used as a reference whose QY is known (99%). Due to hexagonal crystallinity and better monodispersity, the QY of CdS was increased significantly up to 25% (Figure 3.5 b). This increase of QY was almost doubled after ZnS thin shell formation, which would help minimize the surface crystal defect and aggregation tendency of CdS. It was previously reported for II-VI QDs the QY is mostly around 10 % and by capping with higher bandgap semiconducting material it was increased up to 25 % [12, 18, 43]. Normally, the QY decreases after encapsulation [28]. By using a thin shell of ZnS as a protector of the hexagonal CdS core and then proper

silica encapsulation, the QY was enhanced significantly. Mesoporous silica encapsulation prevents QDs from aggregation, as the QDs are dispersed within the porous network of the silica nanoparicles core. By encapsulating the QDs within silica, the nonradiative recombination centers of QDs surfaces decrease and the radiative recombination becomes dominant over nonradiative recombination resulting more fluorescence emission [27].

3.3.3. Dispersion of silica encapsulated QDs into EVA films

As described in Scheme 3.1, the investigated QDs were melt mixed into EVA using a twin-screw extruder. SEM was used first to image the surface of the films but due to the very small size of the particles, the surface morphology was not very clear. Then the distribution of QDs and surface properties (topography and phase) of the experimental light selective films were examined using atomic force microscopy (AFM). The images were taken in tapping mode to avoid surface damage or deformation of the samples. Figure 3.6 a to d shows the height/amplitude and phase images for neat EVA films and EVA films containing 0.5% encapsulated CdS-ZnS QDs. The neat EVA films displayed consistent surface features (Figure 3.6 a and b), however significant variations observed in height and phase images after QD loading (Figure 3.6 c and d) result due to varying material density. The circular topography features in Figure 3.6 c represents the spherical silica encapsulated QDs nanoparticles which are well dispersed throughout the polymer films without particle aggregation. This surface feature was consistent from one region to the next and the size range was also very similar (~60nm), which helps corroborate the TEM and SEM results.

It was previously reported that for dispersion of QDs in polymer films, the QDs need to be stabilized by ligand exchange [13, 44]. This approach still makes it difficult to control the QD aggregation, particularly for a long material application life span. However, here the silica encapsulated QDs show excellent compatibility with EVA, removing the need for ligand exchange. Furthermore, scanning electron microscopy (SEM) was used to

observe the particle distribution (Figure 3.7). However, these imaging methods give an indication of particle dispersion only on a single plane, and are insufficient to confirm the distribution throughout the entire film thickness [13].
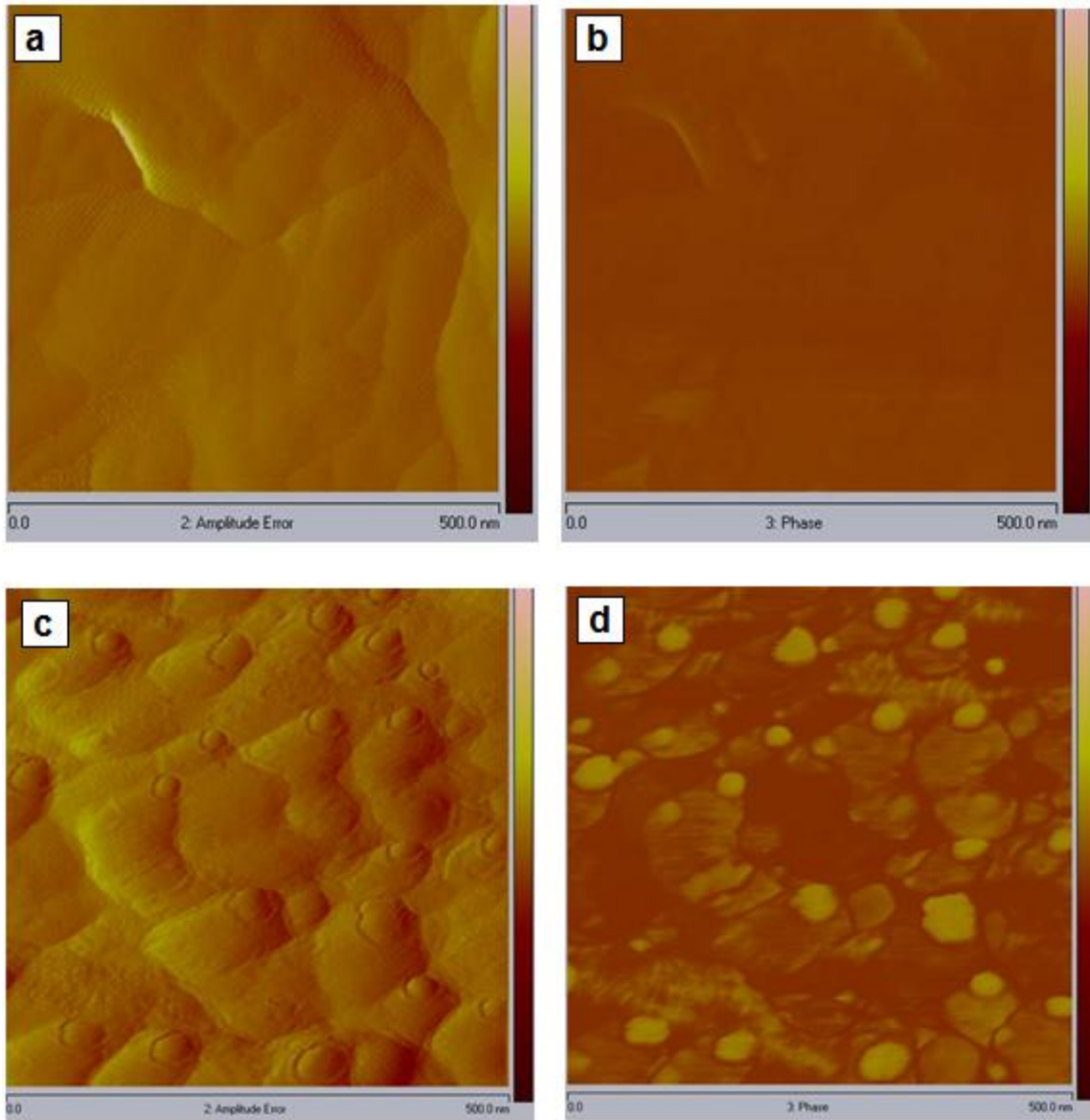
Figure 3.6. AFM (a & c) height and (b & d) phase images of (a & b) neat EVA films, and (c & d) silica encapsulated CdS-ZnS QDs (0.5%) in EVA films. Images were taken in tapping mode.

Therefore, laser scanning confocal microscope (LSCM) was used to examine the distribution of nanoparticles throughout the entire film. Here, the focal planes were excited with an argon laser (488 nm) causing the QDs dispersed in the polymer matrix to be identified as bright dots by their emission. An increase in bright dots with increasing loading concentration for both types of bare and core-shell QDs in EVA films was observed (Figure 3.8 and 3.9). Then, a 3D depth profile of the entire film thickness (100 μm) was produced by accumulating individual optical planes, as shown in Figure 3.10.
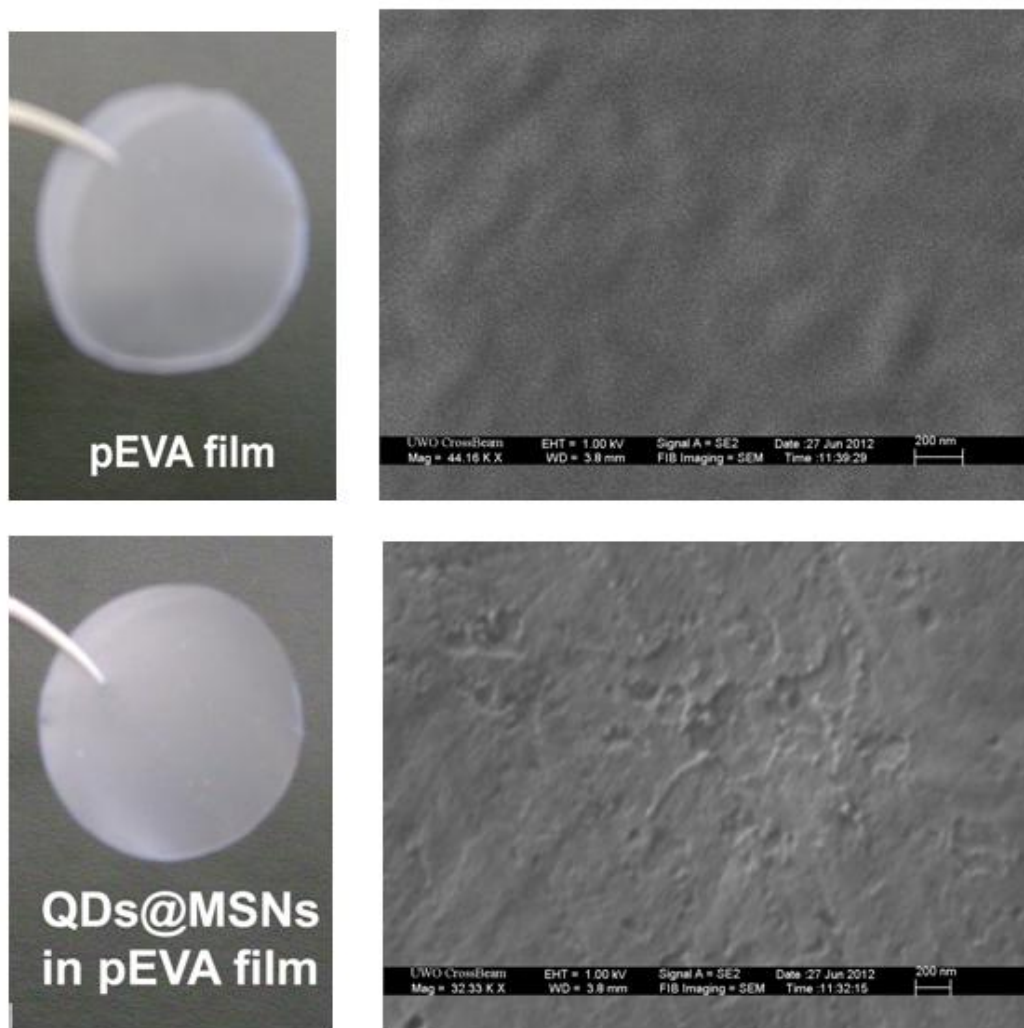
Figure 3.7. The neat EVA film (top) and silica encapsulated QDs incorporated EVA film (bottom) prepared using Universal Film Maker and a Carver hydraulic press, showing similar transparency up to a loading concentration of 0.5 %. The SEM images of the neat EVA film surface (top) and silica encapsulated QDs incorporated EVA film surface (bottom).
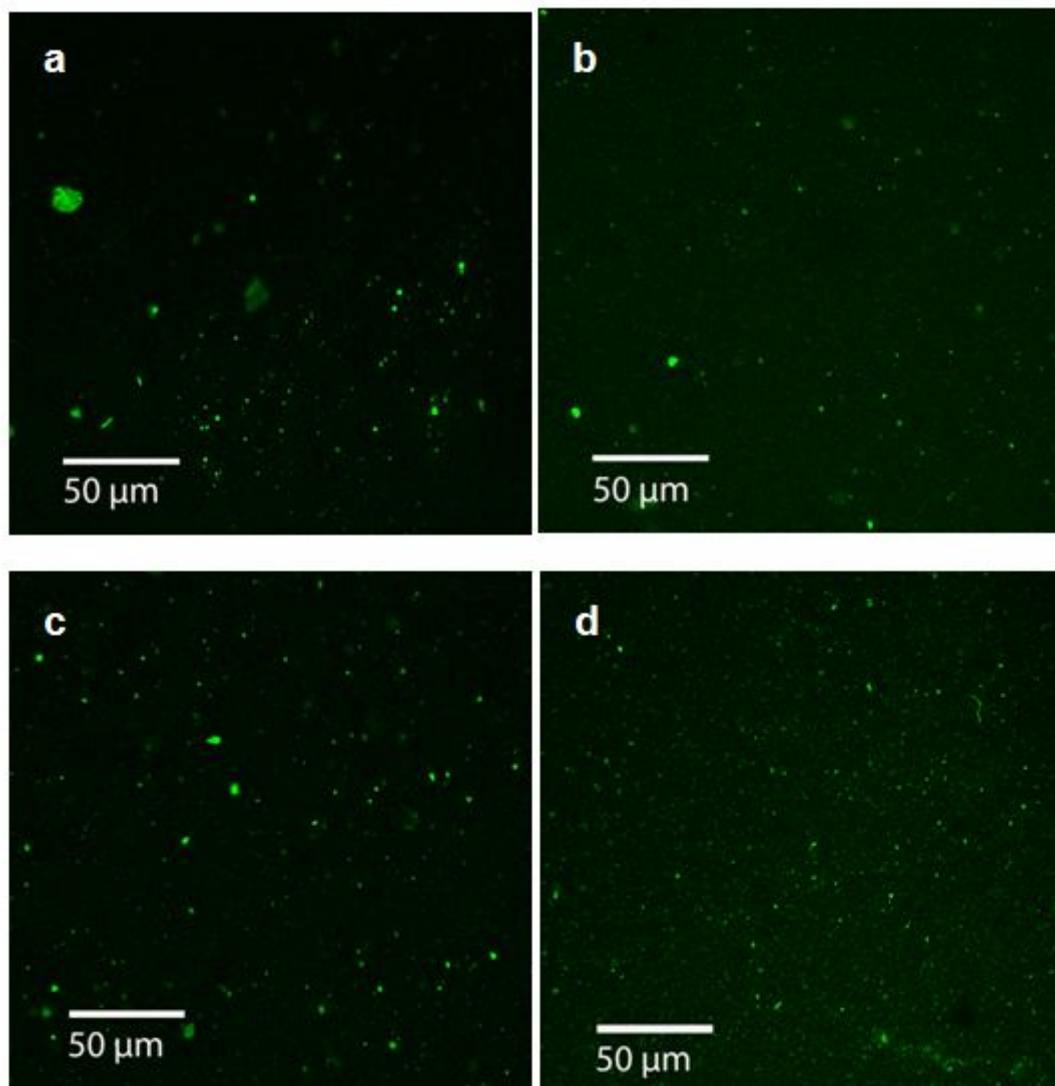
Figure 3.8. Laser scanning confocal microscopic fluorescence images of light selective EVA films incorporated with silica encapsulated bare CdS QDs with different loading concentrations; (a) 0.1 %, (b) 0.2 %, (c) 0.5 %, and (d) 1.0 %. The bright dots from QDs emission are more prominent with increasing loading concentration of nanoparticles.
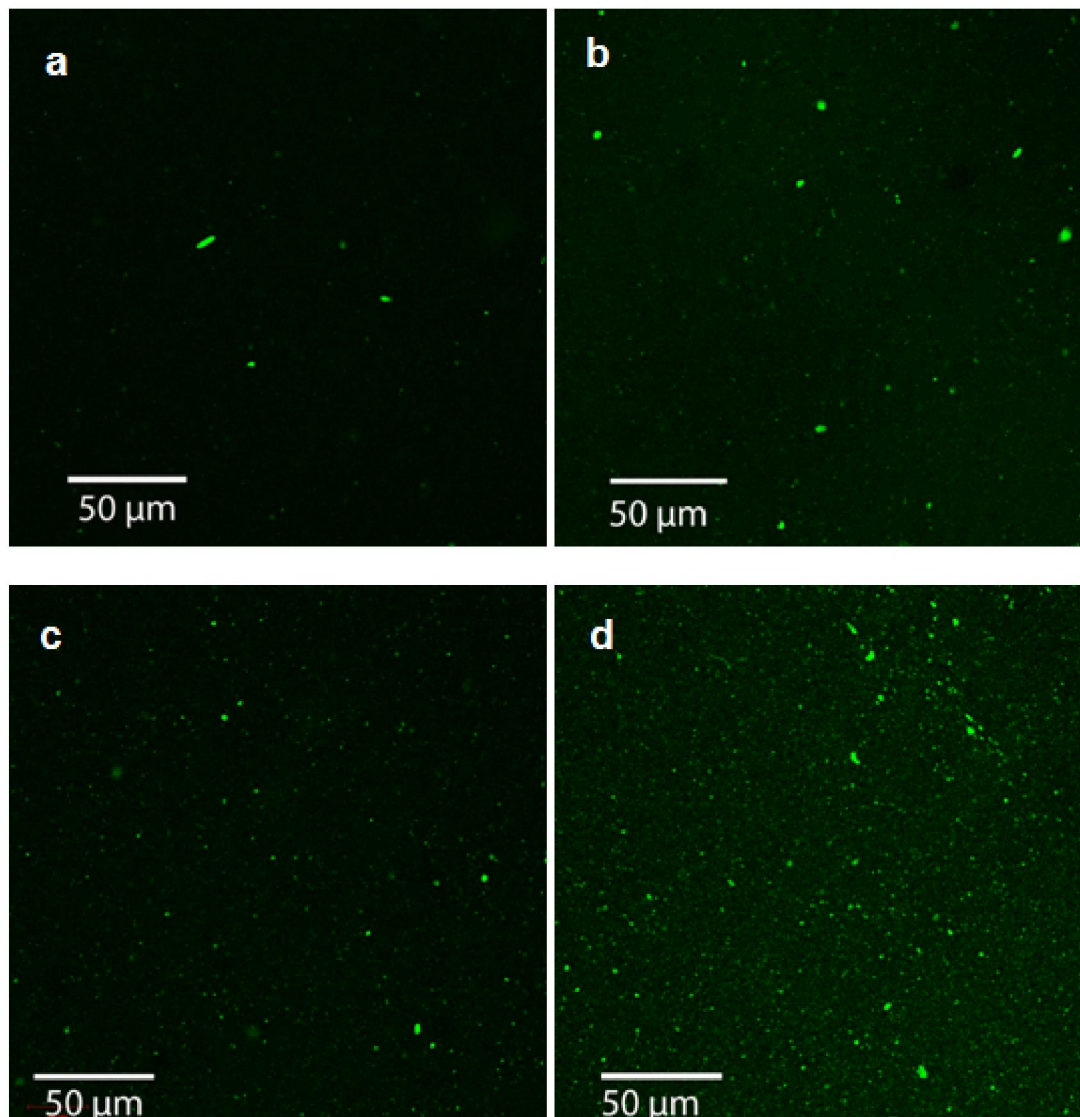
Figure 3.9. Laser scanning confocal microscopic fluorescence images of light selective EVA films incorporated with silica encapsulated core-shell CdS-ZnS QDs with different loading concentrations; (a) 0.1 %, (b) 0.2 %, (c) 0.5 %, and (d) 1.0 %. The bright dots from QDs emission are more prominent with increasing loading concentration of nanoparticles.

From the bright green dots of these images (Figure 3.10) it can be seen that the QDs are well dispersed throughout the thickness of the film. Because of silica encapsulation, both bare CdS and core-shell CdS-ZnS QDs show similar dispersion behaviour in the light selective polymer films. Normally, polymer/inorganic filler nanocomposites are prepared

through solution mixing and even to get a milligram of product can take more than a day [4, 45]. Also, slow solvent evaporation will inevitably introduce aggregation of filler particles into the polymer matrix. The utilized facile melt mixing approach reported here is more feasible and economic for large scale production. Additional solvent evaporation step is not necessary but particles can be distributed throughout the polymer matrix avoiding aggregation.
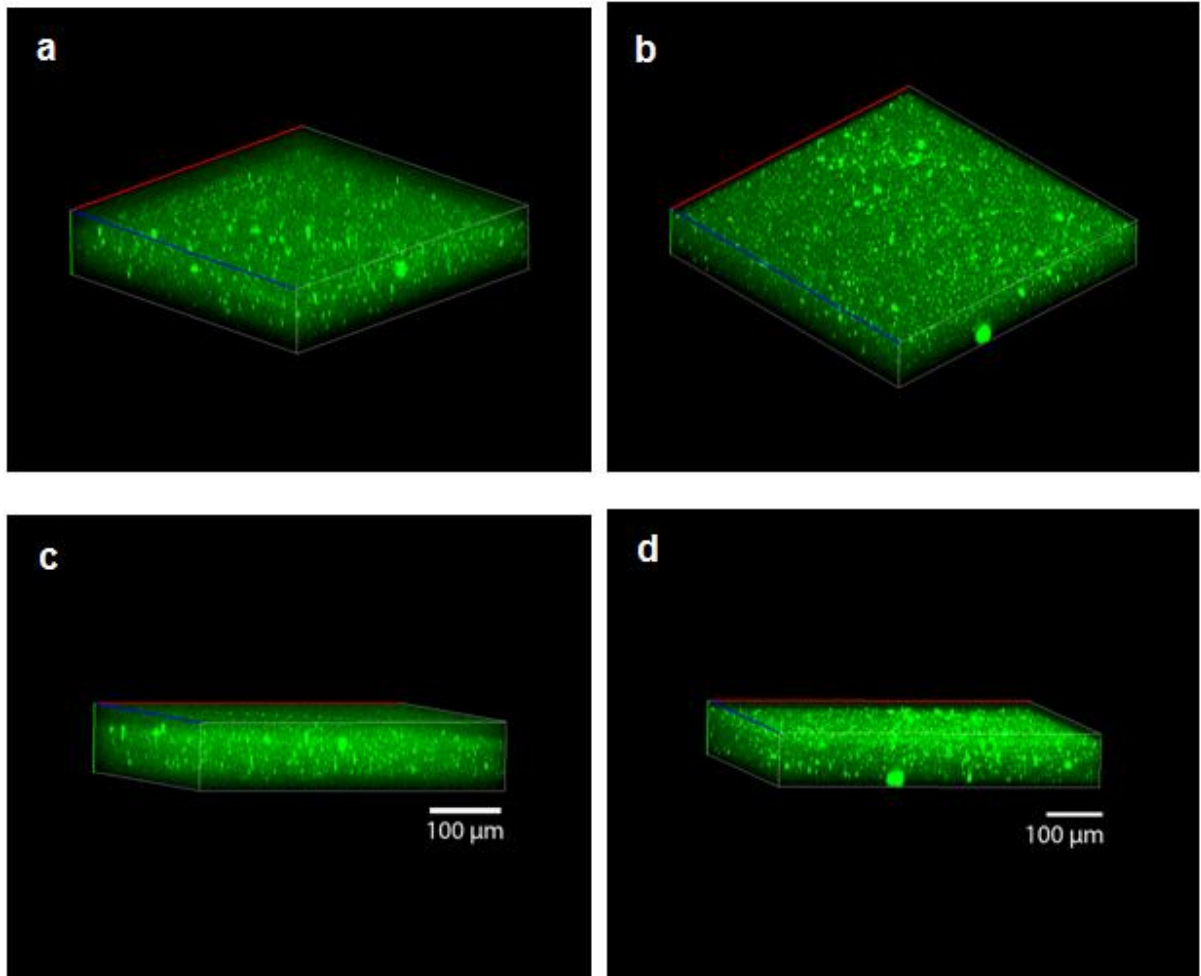
Figure 3.10. Laser scanning confocal microscopy 3D images of light selective EVA films loaded with silica encapsulated (a,b) CdS, (c,d) CdS-ZnS QDs (nanoparticles loading concentration: 0.5%, thickness: 100 μm).

3.3.4. Optical properties of silica encapsulated QDs into EVA films

The optical properties of the experimental EVA films were investigated using UV-vis spectroscopy with an integrated sphere compartment. Figure 3.11 shows the total light transmission in the UV and visible region for experimental films of different thickness with and without loading encapsulated CdS-ZnS QDs into EVA for a loading concentration of 0.5%. For other loading concentrations, the transmittance behaviour for both types of QDs are summarized in Table 3.1. Both before and after nanoparticles loading, the transmittance decreases with increasing thickness of the films. This is consistent with the Bouguer-Lambert-Beer law, as the absorbance of a film is directly proportional to the film thickness [46].
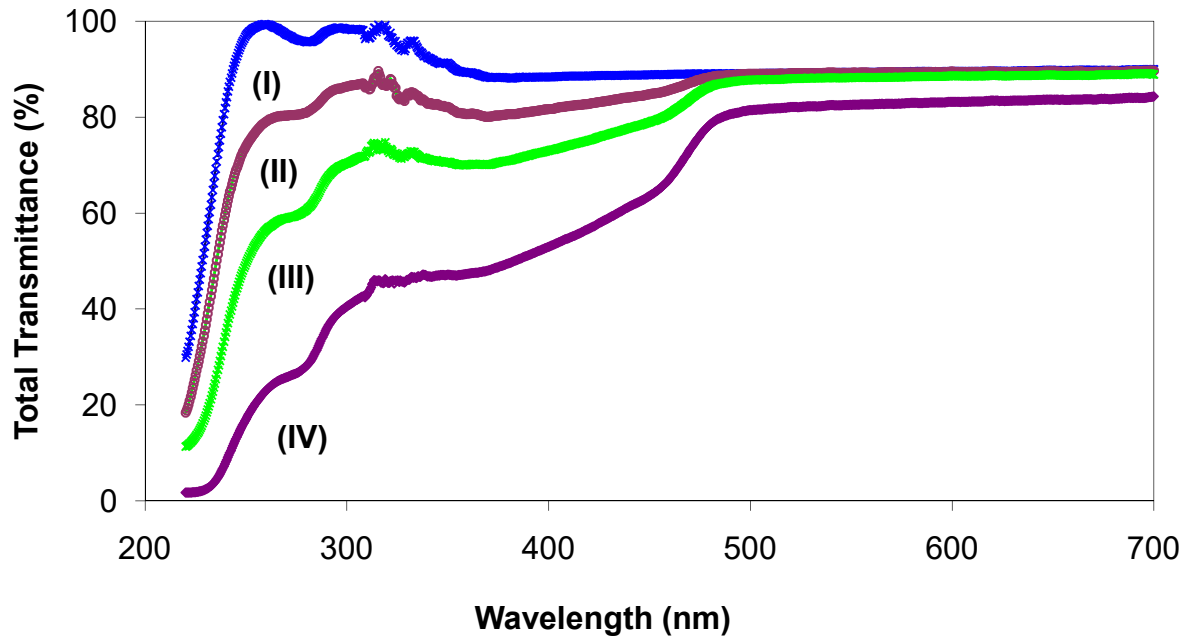
Figure 3.11. Total UV and visible light transmittance spectra of (I) neat EVA film of 100 μm thickness, and EVA films with mesoporous silica encapsulated CdS-ZnS QDs of different thickness (II) 100 μm, (III) 250 μm, and (IV) 500 μm (loading concentration: 0.5%).

The experimental films gave excellent visible light transmittance in comparison to the previously reported commercial greenhouse films [13] even at high loadings up to 1%. Since, the spectrophotometer scans the transmittance at the same wavelength as that of the incident light starting from higher wavelength towards lower wavelengths, there was no peak observed in the visible light range at wavelength higher than 470 nm. The UV transmittance in the case of neat EVA films is seen very high, almost 100%. In contrast, when loading QDs into the EVA films, a decreasing trend is observed starting from 470 nm which becomes more prominent in the UV region. This pattern is consistent with the absorption behaviour of the QDs as shown in Figure 3.4. For the same thickness, the visible transmittance of EVA films with and without QDs loading was found similar up to a loading concentration of 1.0 %.

The experimental light selective nanocomposite films containing only a small amount QDs@MSNs also showed high UV-shielding efficiency. When the QDs@MSNs concentration was increased from 0.1 to 1%, the UV-shielding performance of the EVA films increased significantly (Figure 3.12) and their transparency remained very high (more than 80% for 500 µm film and more than 85% for thickness less than 250 µm). These were almost the same as the plain EVA film. In the absence of QDs, MSNs (transparent under UV-visible light) incorporated EVA films showed almost similar UV transmission behaviour as neat EVA films (Figure 3.12, curve II). Compared to the bare CdS QDs, UV shielding is greater in the case of the core-shell CdS-ZnS QDs, as shown in Table 3.1. The UV absorption capacity of both of these experimental films was better than similar films with bare QDs or functionalized QDs even with higher loading concentrations [13, 47]. This is attributed to the mesoporous silica improving the photostability of QDs as shown in Figure 3.5 a. Mesoporous silica encapsulation also enhances the quantum yield of QDs (Figure 3.5 b), so a large fraction of this absorbed UV light is ultimately emitted as visible light which is more desirable. Therefore, by using these novel light selective films we are getting visible light not only by transmission, but also by emission. In this work, after incorporating mesoporous silica encapsulated both the CdS and CdS-ZnS QDs, the diffuse transmission (Haze) was also increased 20 to 50 %, without reducing the total visible light transmission through the

film (Table 3.1). Haze was increasing with increasing filler concentration from 0.1 % to 1.0 % , and film thickness from 100 µm to 500 µm (Table 3.1).

Table 3.1. Optical properties of neat EVA films, and silica encapsulated QDs incorporated EVA films at different loading concentrations and different thickness films.

Sample code	Loading (%)	Thickness of Films (µm)	% T (UV) (at 280 nm)	% T (visible) (at 550 nm)	% Haze (at 550 nm)
PEVA		100	96.2 ± 0.6	88.4 ± 0.1	17.5 ± 0.2
		250	95.6 ± 0.4	88.2 ± 0.1	17.8 ± 0.2
		500	78.4 ± 0.8	82.5 ± 0.2	21.8 ± 0.5
CdS@MSNs in PEVA	0.1	100	88.5 ± 0.8	87.4 ± 0.3	18.5 ± 0.2
		250	84.6 ± 0.6	86.8 ± 0.2	21.1 ± 0.2
		500	68.3 ± 1.2	81.4 ± 0.2	41.6 ± 0.4
	0.2	100	87.7 ± 0.4	87.5 ± 0.3	21.1 ± 0.3
		250	82.3 ± 0.6	86.8 ± 0.3	22.7 ± 0.2
		500	65.5 ± 0.8	80.5 ± 0.2	49.7 ± 0.8
	0.5	100	86.8 ± 0.3	87.6 ± 0.3	33.4 ± 0.4
		250	76.3 ± 0.4	86.5 ± 0.2	38.6 ± 0.4
		500	46.4 ± 0.6	80.1 ± 0.3	62.4 ± 0.5
	1.0	100	82.3 ± 0.3	87.0 ± 0.2	36.5 ± 0.2
		250	66.2 ± 0.4	85.6 ± 0.4	43.3 ± 0.5
		500	32.6 ± 0.3	79.7 ± 0.4	65.2 ± 0.4
CdS-ZnS@MSNs in PEVA	0.1	100	85.4 ± 0.3	88.2 ± 0.1	17.5 ± 0.3
		250	78.8 ± 0.2	88.0 ± 0.3	20.4 ± 0.2
		500	64.4 ± 0.5	82.5 ± 0.2	41.1 ± 0.3
	0.2	100	85.2 ± 0.3	88.2 ± 0.2	20.0 ± 0.1
		250	76.8 ± 0.5	87.8 ± 0.4	23.3 ± 0.3
		500	60.2 ± 0.7	82.5 ± 0.1	46.7 ± 0.5
	0.5	100	84.7 ± 0.2	88.0 ± 0.2	34.4 ± 0.3
		250	71.5 ± 0.4	87.6 ± 0.4	37.6 ± 0.6
		500	44.3 ± 0.3	82.4 ± 0.1	60.8 ± 0.4
	1.0	100	81.5 ± 0.3	87.5 ± 0.2	35.8 ± 0.4
		250	60.3 ± 0.6	86.8 ± 0.4	41.3 ± 0.4
		500	25.0 ± 0.4	82.2 ± 0.2	62.2 ± 0.6
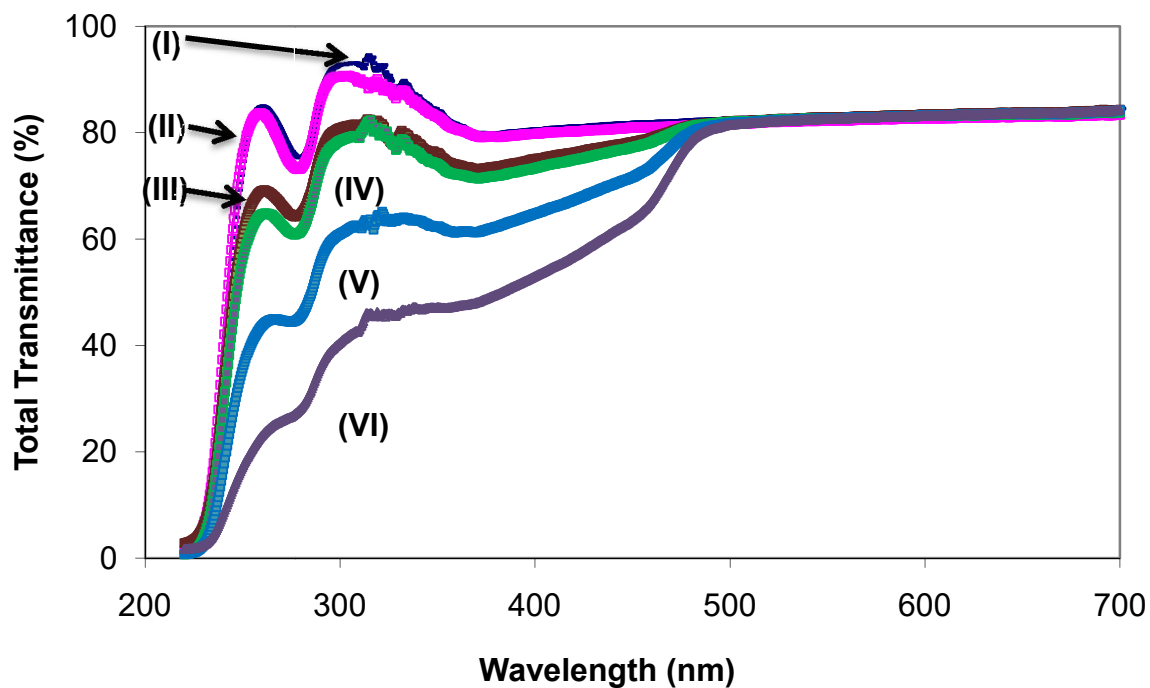
Figure 3.12. Total UV and visible light transmittance spectra: (I) neat EVA film, (II) Silica nanoparticles-EVA film (0.5%) and EVA films with mesoporous silica encapsulated CdS-ZnS QDs of different loading concentrations: (III) 0.1 %, (IV) 0.2 %, (V) 0.5 %, and (VI) 1 % (in all cases film thickness: 500 μm).

3.4. Conclusions

In summary, a facile and modified method for the synthesis of monodispersed and highly fluorescent bare CdS and core-shell CdS-ZnS QDs has been reported. Then both types of QDs were encapsulation in mesoporous silica through a simple microemulsion technique. The photo-bleaching properties of both the bare and core-shell QDs were prevented by the silica encapsulation layer under continuous exposure of UV light. In addition, the encapsulated QDs can still emit visible light under excitation with UV radiation, enhancing the photo-luminescence and quantum yield. The silica encapsulated QDs nanoparticles were easily incorporated into EVA co-polymer matrix by melt-mixing in a

twin-screw extruder. SIlica encapsulated QDs showed excellent compatibility with EVA by AFM analysis. The experimental films of different thickness were prepared for both types of QD samples at different loading concentrations. The light selective films with bare CdS QDs with encapsulation showed improved optical properties, showing a decrease of UV transmission and increase of diffuse transmission by retaining high visible light transmission. These optical properties were further enhanced in case of core-shell CdS-ZnS QDs, as the thin ZnS shell prevented the surface defect of core CdS. Therefore, these novel nanocomposite films with light selective properties would be an excellent candidate for greenhouse covering and PV encapsulants.

3.5. Acknowledgments

3.6. References

[1] Z. Xu, C.R. Hine, M.M. Maye, Q. Meng, M. Cotlet, Shell thickness dependent photoinduced hole transfer in hybrid conjugated polymer/quantum dot nanocomposites: from ensemble to single hybrid level, ACS Nano, 6 (2012) 4984-4992.

[2] J.H. Bang, P.V. Kamat, CdSe quantum dot–fullerene hybrid nanocomposite for solar energy conversion: electron transfer and photoelectrochemistry, ACS Nano, 5 (2011) 9421-9427.

[3] L. Wei, N. Hu, Y. Zhang, Synthesis of polymer—mesoporous silica nanocomposites, Materials, 3 (2010) 4066-4079.

[4] D. Sun, N. Miyatake, H.-J. Sue, Transparent PMMA/ZnO nanocomposite films based on colloidal ZnO quantum dots, Nanotechnology, 18 (2007) 215606-215611.

[5] D.T. Krizek, H.D. Clark, R.M. Mirecki, Spectral properties of selected UV-blocking and UV-transmitting covering materials with application for production of high-value crops in high tunnels, Photochemistry and Photobiology, 81 (2005) 1047-1051.

[6] M. Knausz, G. Oreski, G.C. Eder, Y. Voronko, B. Duscher, T. Koch, G. Pinter, K.A. Berger, Degradation of photovoltaic backsheets: comparison of the aging induced changes on module and component level, Journal of Applied Polymer Science, 132 (2015) 1047-1051.

[7] E. Schettini, L. Stefani, G. Vox, Interaction between agrochemical contaminants and UV stabilizers for greenhouse EVA plastic films, Applied Engineering in Agriculture, 30 (2014) 229-239.

[8] F. Liu, L. Jiang, S. Yang, Ultra-violet degradation behavior of polymeric backsheets for photovoltaic modules, Solar Energy, 108 (2014) 88-100.

[9] A.M. Abdel-Ghany, I.M. Al-Helal, S.M. Alzahrani, A.A. Alsadon, I.M. Ali, R.M. Elleithy, Covering materials incorporating radiation-preventing techniques to meet greenhouse cooling challenges in arid regions: a review, The Scientific World Journal, 2012 (2012) 1-11.

[10] L.H. Slooff, E.E. Bende, A.R. Burgers, T. Budel, M. Pravettoni, R.P. Kenny, E.D. Dunlop, A. Büchtemann, A luminescent solar concentrator with 7.1% power conversion efficiency, Rapid Research Letters, 2 (2008) 257-259.

[11] Y. Zhou, F.S. Riehle, Y. Yuan, H.-F. Schleiermacher, M. Niggemann, G.A. Urban, M. Krüger, Improved efficiency of hybrid solar cells based on non-ligand-exchanged CdSe quantum dots and poly (3-hexylthiophene), Applied Physics Letters, 96 (2010) 013304-013309.

[12] C.B. Murray, D.J. Norris, M.G. Bawendi, Synthesis and characterization of nearly monodisperse CdE (E= sulfur, selenium, tellurium) semiconductor nanocrystallites, Journal of the American Chemical Society, 115 (1993) 8706-8715.

[13] J.M. Allan, M.A. Mumin, W.Z. Xu, Q. Al Sharari, P.A. Charpentier, Surface functionalized bare and core–shell quantum dots in poly (ethylene-co-vinyl acetate) for light selective nanocomposite films, Solar Energy Materials and Solar Cells, 123 (2014) 30-40.

[14] W.Z. Xu, P.A. Charpentier, Light-selective nanofilms of quantum dot-poly (ethylene-co-vinyl acetate) synthesized with supercritical CO_2, The Journal of Physical Chemistry C, 113 (2009) 6859-6870.

[15] M. Darbandi, G. Urban, M. Krüger, A facile synthesis method to silica coated CdSe/ZnS nanocomposites with tuneable size and optical properties, Journal of Colloid and Interface Science, 351 (2010) 30-34.

[16] C.V. Durgadas, K. Sreenivasan, C.P. Sharma, Bright blue emitting CuSe/ZnS/silica core/shell/shell quantum dots and their biocompatibility, Biomaterials, 33 (2012) 6420-6429.

[17] N. Soltani, E. Saion, E. Erfani, M. Bahrami, M. Navaseri, K. Rezaee, M.Z. Hussein, Facile synthesis of ZnS/CdS and CdS/ZnS core-shell nanoparticles using microwave irradiation and their optical properties, Chalcogenide Letters, 9 (2012) 379-387.

[18] D. Gerion, F. Pinaud, S.C. Williams, W.J. Parak, D. Zanchet, S. Weiss, A.P. Alivisatos, Synthesis and properties of biocompatible water-soluble silica-coated CdSe/ZnS semiconductor quantum dots, The Journal of Physical Chemistry B, 105 (2001) 8861-8871.

[19] D. Bera, L. Qian, T.-K. Tseng, P.H. Holloway, Quantum dots and their multimodal applications: a review, Materials, 3 (2010) 2260-2345.

[20] Y. Yin, A.P. Alivisatos, Colloidal nanocrystal synthesis and the organic–inorganic interface, Nature, 437 (2005) 664-670.

[21] P. Thangadurai, S. Balaji, P. Manoharan, Surface modification of CdS quantum dots using thiols—structural and photophysical studies, Nanotechnology, 19 (2008) 435708-435715.

[22] A.P. Alivisatos, W. Gu, C. Larabell, Quantum dots as cellular probes, Annual Review of Biomedical Engineering, 7 (2005) 55-76.

[23] M. Bruchez, M. Moronne, P. Gin, S. Weiss, A.P. Alivisatos, Semiconductor nanocrystals as fluorescent biological labels, Science, 281 (1998) 2013-2016.

[24] M. Darbandi, R. Thomann, T. Nann, Single quantum dots in silica spheres by microemulsion synthesis, Chemistry of Materials, 17 (2005) 5720-5725.

[25] R. Koole, M.M. van Schooneveld, J. Hilhorst, C. de Mello Donegá, D.C.'. Hart, A. van Blaaderen, D. Vanmaekelbergh, A. Meijerink, On the incorporation mechanism of

hydrophobic quantum dots in silica spheres by a reverse microemulsion method, Chemistry of Materials, 20 (2008) 2503-2512.

[26] A.M. Mumin, J.W. Barrett, G.A. Dekaban, J. Zhang, Dendritic cell internalization of foam-structured fluorescent mesoporous silica nanoparticles, Journal of Colloid and Interface Science, 353 (2011) 156-162.

[27] B. Zhang, X. Gong, L. Hao, J. Cheng, Y. Han, J. Chang, A novel method to enhance quantum yield of silica-coated quantum dots for biodetection, Nanotechnology, 19 (2008) 465604-465612.

[28] Isanaeni, L.-H. Jin, Y.-H. Cho, Silica encapsulation of toluene soluble quantum dots with high photostability, Journal of Colloid and Interface Science, 395 (2013) 45-49.

[29] H. Han, G.D. Francesco, M.M. Maye, Size control and photophysical properties of quantum dots prepared via a novel tunable hydrothermal route, The Journal of Physical Chemistry C, 114 (2010) 19270-19277.

[30] K. Agroui, G. Collins, Characterisation of EVA encapsulant material by thermally stimulated current technique, Solar Energy Materials and Solar Cells, 80 (2003) 33-45.

[31] C. von Zabeltitz, Integrated Greenhouse Systems for Mild Climates, Springer Berlin Heidelberg2011, pp. 285-311.

[32] J. Jin, S. Chen, J. Zhang, UV aging behaviour of ethylene-vinyl acetate copolymers (EVA) with different vinyl acetate contents, Polymer Degradation and Stability, 95 (2010) 725-732.

[33] M. Faker, M.R. Aghjeh, M. Ghaffari, S. Seyyedi, Rheology, morphology and mechanical properties of polyethylene/ethylene vinyl acetate copolymer (PE/EVA) blends, European Polymer Journal, 44 (2008) 1834-1842.

[34] Y. Medina-Gonzalez, W.Z. Xu, B. Chen, N. Farhanghi, P.A. Charpentier, CdS and CdTeS quantum dot decorated TiO_2 nanowires. Synthesis and photoefficiency, Nanotechnology, 22 (2011) 065603-065610.

[35] N. Soltani, E. Gharibshahi, E. Saion, Band gap of cubic and hexagonal cds quantum dots-experimental and theoretical studies, Chalcogenide Letters, 9 (2012) 321-328.

[36] K. Park, H.J. Yu, W.K. Chung, B.-J. Kim, S.H. Kim, Effect of heat-treatment on CdS and CdS/ZnS nanoparticles, Journal of Materials Science, 44 (2009) 4315-4320.

[37] J. Liu, Z. Guo, W. Wang, Q. Huang, K. Zhu, X. Chen, Heterogeneous ZnS hollow urchin-like hierarchical nanostructures and their structure-enhanced photocatalytic properties, Nanoscale, 3 (2011) 1470-1473.

[38] B. Sahoo, K.S.P. Devi, S.K. Sahu, S. Nayak, T.K. Maiti, D. Dhara, P. Pramanik, Facile preparation of multifunctional hollow silica nanoparticles and their cancer specific targeting effect, Biomaterials Science, 1 (2013) 647-657.

[39] T. Jamieson, R. Bakhshi, D. Petrova, R. Pocock, M. Imani, A.M. Seifalian, Biological applications of quantum dots, Biomaterials, 28 (2007) 4717-4732.

[40] N. de la Rosa-Fox, M. Piñero, R. Litrán, L. Esquivias, Photoluminescence from CdS quantum dots in silica gel, Journal of Sol-gel Science and Technology, 26 (2003) 947-951.

[41] S.F. Wuister, A. Meijerink, Synthesis and luminescence of CdS quantum dots capped with a silica precursor, Journal of Luminescence, 105 (2003) 35-43.

[42] K. Pechstedt, T. Whittle, J. Baumberg, T. Melvin, Photoluminescence of colloidal CdSe/ZnS quantum dots: the critical effect of water molecules, The Journal of Physical Chemistry C, 114 (2010) 12069-12077.

[43] M.A. Hines, P. Guyot-Sionnest, Synthesis and characterization of strongly luminescing ZnS-capped CdSe nanocrystals, The Journal of Physical Chemistry, 100 (1996) 468-471.

[44] A. Pucci, M. Boccia, F. Galembeck, C.A. de Paula Leite, N. Tirelli, G. Ruggeri, Luminescent nanocomposites containing CdS nanoparticles dispersed into vinyl alcohol based polymers, Reactive and Functional Polymers, 68 (2008) 1144-1151.

[45] H.-M. Xiong, X. Zhao, J.-S. Chen, New polymer-inorganic nanocomposites: PEO-ZnO and PEO-ZnO-LiClO$_4$ films, The Journal of Physical Chemistry B, 105 (2001) 10169-10174.

[46] J.L. Koenig, Application of Fourier transform infrared spectroscopy to chemical systems, Applied Spectroscopy, 29 (1975) 293-308.

[47] X. Wang, S. Zhou, L. Wu, Facile encapsulation of SiO$_2$ on ZnO quantum dots and its application in waterborne UV-shielding polymer coatings, Journal of Materials Chemistry C, 1 (2013) 7547-7553.

Chapter 4

Multifunctional mesoporous silica nanoparticles in poly(ethylene-*co*-vinyl acetate) for transparent heat retention films

Abstract

Transparent inorganic-polymer nanocomposite films are of tremendous current interest in emerging solar coverings including photovoltaic encapsulants and commercial greenhouse plastics, but suffer from significant radiative heat loss. This work provides a new and simple approach for controlling this heat loss by using mesoporous silica/quantum dot nanoparticles in poly(ethylene-co-vinyl acetate) (EVA) films. Mesoporous silica shells were grown on CdS-ZnS quantum dot (QDs) cores using a reverse microemulsion technique, controlling the shell thickness. These mesoporous silica nanoparticles (MSNs) were then melt-mixed with EVA pellets using a mini twin-screw extruder and pressed into thin films of concentration variable controlled thickness. The results demonstrate that the experimental MSNs showed improved infrared and thermal wavebands retention in the EVA transparent films compared to commercial silica additives, even at lower concentrations. It was also found MSNs enhanced the quantum yield and photostability of the QDs, providing high visible light transmission and blocking of UV transmission of interest for next generation solar coatings.

4.1. Introduction

Over the last two decades, polymer nanocomposites have been the subject of intense scientific and technological efforts due to their unique physical and chemical properties [1-4]. The integration of inorganic nanoparticles into a polymer matrix allows combining and enhancing both properties, while advancing new functional materials [5, 6]. Recently, polymer nanocomposite films with light and heat selective properties for solar energy applications including photovoltaic (PV) encapsulants and commercial greenhouse coverings are becoming of increasing scientific interest [7-9]. Poly(ethylene-co-vinyl acetate) (EVA) films have been found as ideal encapsulants to surround PV cells, protecting the silicon wafers and module circuitry [10]. EVA plastic films are also widely used in commercial greenhouse coverings [11]. However, like most other thermoplastics, controlling the radiative heat loss is a current limitation of these films.

Controlling long-wave infrared and thermal radiation from inside a greenhouse or PV module to the outdoors can provide for longer material life-spans, while enhancing PV efficiencies by down-regulation, or increasing biomass production in greenhouses [12, 13].

In recent years, polymer-silica nanocomposites have attracted substantial research and technological interest, as silica based fillers exhibit remarkable improvements in the thermal properties over the native polymer [14]. Silica blocks infrared radiation and is bio-compatible, transparent, while its architecture can be tuned to be compatible with various polymer matrices [9, 15]. Thermic greenhouse plastic films that block infrared radiation are crucial for enhanced fruit and vegetable development and enhanced biomass production. These advanced plastics also minimize the risk of frost when the greenhouse is not heated and reduce the energy consumption when a heating system is used [16, 17]. Several commercial thermic EVA films use silica based additives such as mineral silica or layered silicates including talc, mica, kaolin or montmorillonite to reduce heat losses by radiation [16, 18]. Due to their large particle sizes, these thermic films suffer from a loss of transparency in the visible region of the solar spectrum which is important for the photosynthesis process [19, 20]. One possibility to overcome these drawbacks would be to use nanoparticles of silica well-dispersed in the polymer matrix.

Among the different types of silica additives, recently mesoporous silica nanoparticles (MSNs) have received much attention due to their nano-size, high surface-to-volume ratio, ordered structure and ease for surface and nanopore functionalization [21-23]. MSNs reinforced polymer composites are relatively new materials that have shown improved mechanical and thermal stabilities in polymers including polypropylene, polystyrene, polyimide, and PMMA [24-27]. No reports have examined MSNs-EVA nanocomposites, especially for applications in greenhouse coverings or PV encapsulants. Since EVA shows high compatibility with additives and fillers [28], we previously examined surface functionalized quantum dots (QDs) incorporated into an EVA matrix by melt-mixing [7]. The light selective films showed improved optical properties, showing a decrease of UV transmission and increase of diffuse transmission by retaining high visible light transmission. Separately, we also examined mesoporous silica

encapsulation of these QDs, where MSNs enhanced the quantum yield and photostability of QDs significantly [29].

In the present work, we examine thermal properties including thermicity and thermal conductivity of the nanocomposite films. We also prepare mesoporous silica encapsulated QDs with tunable silica thickness to evaluate the effect of thickness on these properties and compare to MSNs-EVA nanocomposites without the presence of QDs. The novel EVA nanocomposite films show the possibility of simultaneously enhancing both the light selective and heat retention properties by using a single nano-additive.

4.2. Experimental

4.2.1. Materials

Cyclohexane (99%), chloroform (99.8%), 1-hexanol (98%), tetraethyl orthosilicate (TEOS), ammonia solution (28%), were purchased from Sigma-Aldrich, Canada and were used as received. Ethylene vinyl acetate copolymer (Ateva®1075 with 9 wt% vinyl acetate content) was provided by AT Plastics, Canada. For CdS-ZnS quantum dots synthesis, cadmium chloride, sodium diethyldithiocarbamate trihydrate, zinc diethyldithiocarbamate (98%), trioctylamine (TOA) (98%,), trioctylphosphine (TOP) (97%), anhydrous ethanol (≥99.5%), methanol (≥99.9%), and toluene (≥99%) were also purchased from Sigma-Aldrich, Canada. Argon (ultra high purity, 99.9%, Praxair) was used without further purification.

4.2.2. Synthesis of CdS-ZnS QDs

The core-shell (CdS-ZnS) QDs were synthesized using a modified single-molecular precursor method, as previously reported [7].

4.2.3. Mesoporous silica nanoparticles and silica encapsulated QDs

Mesoporous silica nanoparticle formation and encapsulation of QDs was carried out by following a water-in-oil microemulsion method (also called reverse microemulsion) based on sol-gel chemistry by following a modification of the method reported previously [30, 31]. A homogeneous mixture of surfactant in oil phase was prepared by adding 2.6 mL of Triton X-100 (surfactant) and 2.5 mL of 1-hexanol (co-surfactant) in 20 mL of cyclohexane (oil). After 15 min, 1 mL of water was added under magnetic stirring at ambient temperature. For QD encapsulation, 800 µL of QDs solution (1 or 2 or 5 mg mL^{-1} in chloroform) was mixed into the emulsion. Then 160 µL of TEOS as the silica precursor was added to the microemulsion. After 1 hr, 300 µL of ammonia solution (28%) was added slowly as a catalyst of TEOS co-hydrolysis and silica polymerization. The reaction mixture was then stirred at the same temperature for 24 hrs. To separate and purify the desired nanoparticles, 30-50 mL of acetone was added to break the emulsion, followed by ultrasonication for 2 to 3 min and centrifugation at 6500 rpm for 10 min. Finally, the resultant NPs were washed at least 3 times with ethanol, acetone and water 1:1:1 and freeze dried for 2 to 3 hrs.

4.2.4. Silica encapsulated QDs-EVA nanocomposite films

Both the MSNs and encapsulated core-shell QDs were integrated into EVA resins through melt mixing. Five grams of EVA pellets were added to a Thermo Scientific HAAKE Mini-Lab II twin-screw micro-compounder at 130 $^{\circ}$C. The virgin PEVA was melted and cycled for 5 min at 50 rpm. Different loading concentrations (0.1%, 0.2%, 0.5%, and 1% by weight) of MSNs and MSNs encapsulated CdS-ZnS QDs were added to the molten PEVA and left to cycle for a further 15 min in the extruder. The resulting blend (0.03, 0.075, 0.15 g for 100, 250, and 500 µm films respectively) were pressed into thin films using a Spectra-Tech Universal Film Maker (UFM) kit and Carver hydraulic press. The platens of the UFM with samples in the desired thickness spacer were heated

to 120 $^{\circ}$C and placed under 2500 psi for 5 min. The films were left under pressure without heat for a further 10 min and then cooled for 5 min in a cooling chamber.

4.2.5. Material characterization

Transmission electron microscopy (TEM) images were recorded on a Philips CM10 transmission electron microscope to image the mesoporous silica encapsulated QDs to observe their size and shape at 80 kV. The TEM samples were prepared by drop casting ethanol dispersed samples on a copper grid covered with carbon film. The imaging of experimental films was carried out followed by thin slicing of the films with an ultramicrotome. For sample preparation, thin strips of the films were placed in an airtight gelatin capsule and filled with LR light, a polyhydroxy-aromatic acrylic embedded resin. The medium was placed in an oven to polymerize for 48 h at 60 $^{\circ}$C . This was used as a support for the films so they could be sectioned into thin slices using a Reichert Jung UltraCut Ultracrotome with a diamond knife, then placed onto copper grids. High-resolution transmission electron microscopy (HRTEM) images of both the bare and core-shell QDs were recorded with a JEOL 2010F FEG TEM/STEM at the Canadian Centre for Electronic Microscopy (McMaster University, Hamilton Ontario) operated at 200 kV. Scanning electron microscopy (SEM) was also utilized to study the morphology of silica nanoparticles by using a LEO (ZEISS) 1540XB FIB/SEM. Samples for SEM imaging were prepared by applying the nanopowder directly to aluminum stub on carbon adhesion tape. Elemental composition of QDs inside silica was confirmed and quantified using the energy dispersive X-ray detection (EDX) feature of the SEM.

The integrating sphere compartment of a Shimadzu UV-3600 UV-VIS-NIR spectrophotometer was used to measure the light transmittance and haze values of the experimental film samples. Infrared spectra were collected from 700 to 1400 cm^{-1} using a Nicolet 6700 FTIR spectrometer for the thermicity calculations explained previously [9]. A ZEISS LSM 5 Duo confocal microscope was used to take transmission and

fluorescence images of the experimental films (thickness 100 μm) using an argon laser at 488 nm. Small sections of surface film areas of approximately 500 μm were scanned using an objective of 20x magnification. A Veeco diMultiMode V atomic force microscope (AFM) was used to image the surface topography, roughness, and phase of the experimental films. The images were taken in tapping mode using an E scanner. Surface roughness and height values were calculated using Nanoscope V7.30 program software. Thermal conductivity of EVA,MSNs-EVA, and MSNs encapsulated QDs-EVA films were measured using a transient temperature system based on the experimental set-up and data analysis previously described by Lee [32].

4.3. Results and discussions

4.3.1. Morphology and distribution of silica encapsulated QDs in EVA nanocomposite films

The morphology of core-shell CdS-ZnS QDs was studied using TEM as shown in Figure 4.1a. Here the QD samples were present in a dispersed state, showing formation of individual nanoparticles. The thin ZnS shell helps to minimize any surface crystal defects and decrease the aggregation tendency of the bare CdS QDs [29]. The average particle size was estimated as 5 ± 0.5 nm, shown by the histogram data in Figure 4.1g. The formation of spherical silica nanoparticles and mesoporous silica encapsulation of the core-shell CdS-ZnS QDs with a narrow size distribution was directly visualized by TEM. The average particle size of the MSNs prepared using a reverse microemulsion method was estimated as 60 ± 5 nm, shown in Figure 4.1b.

MSNs were also prepared with different loading concentrations of QDs forming the core-shell nanostructure with tunable QD core size (Figure 4.1c to e). The silica surface after encapsulation remained smooth and uniform with a narrow size distribution, with no aggregation observed. The average particle size was 60 ± 5 nm with a tunable core size (mostly QD particles) from 5 to 40 nm. The incorporation of the hydrophobic QDs in the
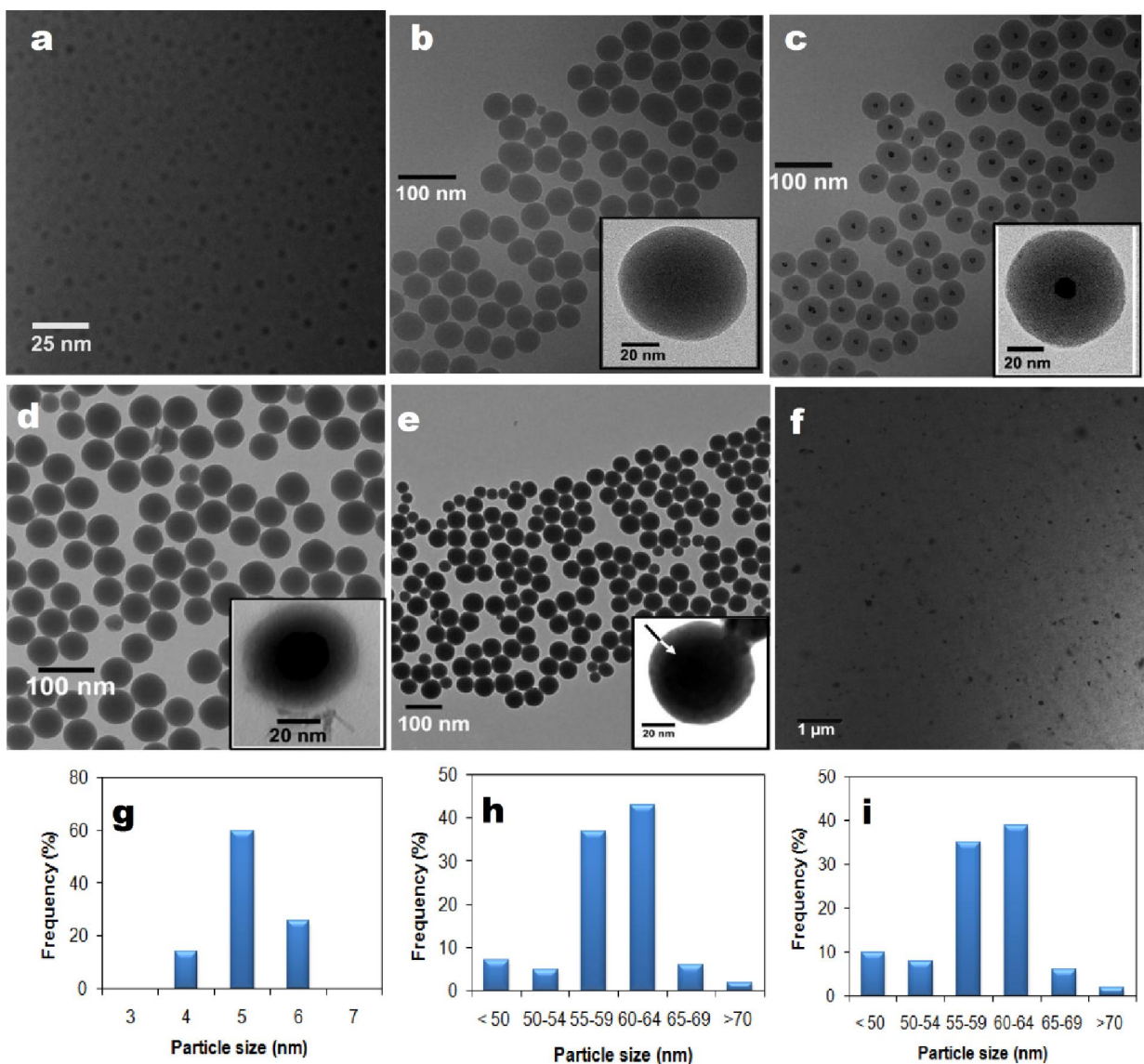
Figure 4.1. Transmission electron microscopy images of (a) CdS-ZnS QDs (b) Mesoporous silica nanoparticles (MSNs), (c-e) CdS-ZnS QDs encapsulation within mesoporous silica with different QDs loading concentrations in chloroform; (c) 1 mg mL^{-1}, (d) 2 mg mL^{-1}, and (e) 5 mg mL^{-1}, (f) MSNs encapsulated QDs loaded in EVA film; particle size distribution of (g) CdS-ZnS QDs [image a], (h) MSNs encapsulated QDs [image d], and (i) MSNs encapsulated QDs [image e] using ImageJ software considering at least 100 nanoparticles [all inset images represent single particle of corresponding types].

silica spheres is believed to follow the hydrophobic interaction mechanism, in which the long hydrocarbon chains of the non-ionic surfactant interacts with the hydrophobic QDs [33]. This makes the QD surface hydrophilic where the silica growth takes place at the micelle interior. The silica precursor (e.g., TEOS), and the amount of water and ammonia were maintained constant to control the MSN diameter. However the core size was tuned by changing the QD loading concentration. For the lowest concentration (1 mg mL^{-1} of chloroform) most silica spheres were found to contain a single QD (inset picture of Figure 4.1c). For the QD loading concentration 2 mg mL^{-1}, QDs containing core was increased to about 20 to 25 nm (Figure 4.1d). Upon further increasing the QD loading concentration (5 mg mL^{-1}), the cores became larger and denser with more QDs having an average 40 nm size (Figure 4.1e). Therefore, by using this loading dependent core size was tuned within the uniform sized silica spheres. This uniform size is important for further functionalization or processing of the silica nanoparticles. The uniform distribution of MSNs inside EVA films was observed as shown in the ultramicrotomed thin sections TEM image (Figure 4.1f).

The experimental films were also characterized using SEM and SEM-EDX elemental analysis. The particle size of MSNs found from SEM imaging was consistent as observed from TEM (Figure 4.2a). The surface texture of EVA films after MSN loading (Figure 4.2c) was different compared to plain EVA films (Figure 4.2b). The size of the particles present in the uneven surface features matches with the size of MSNs. Further analysis using EDX confirms that these particles were MSNs (Figure 4.2d). In the case of the experimental EVA films loaded with MSN encapsulated QDs, the semiconductor elements of the QDs were observed by EDX (Figure 4.2e). Therefore MSNs with or without QDs were successfully loaded into EVA films.
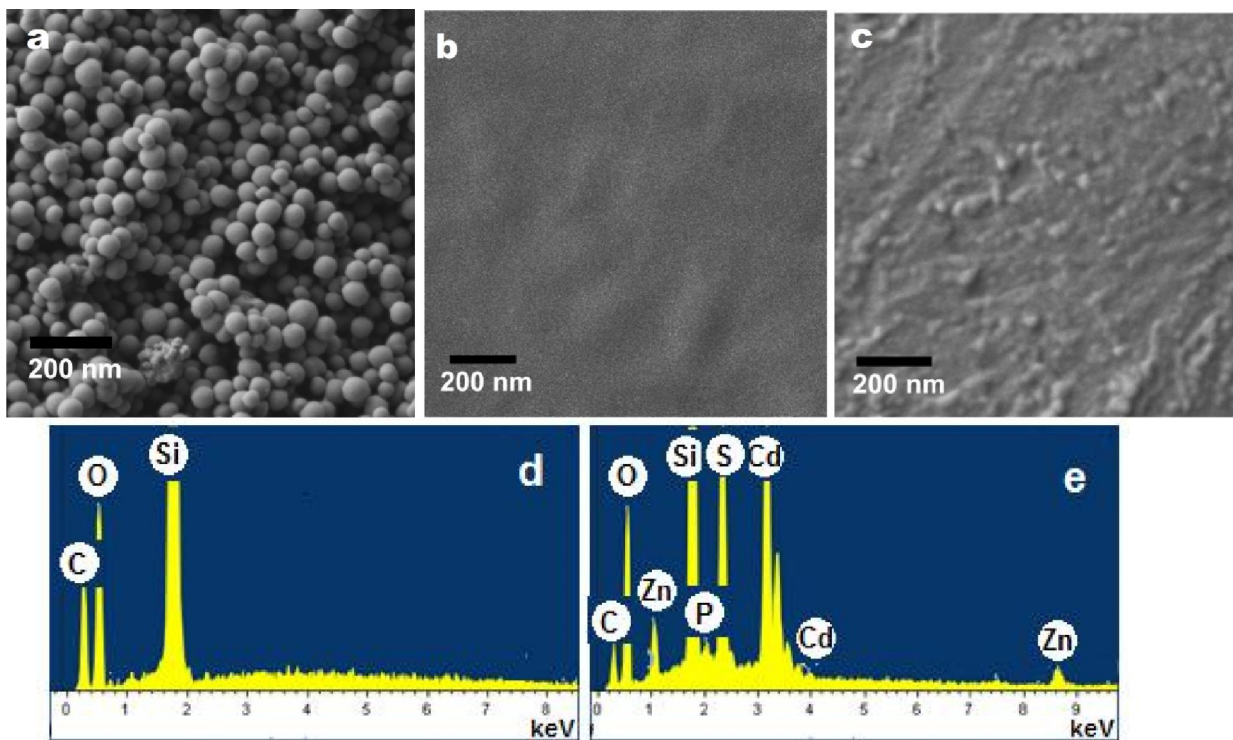
Figure 4.2. Scanning electron microscopy images of (a) Mesoporous silica nanoparticles (MSNs), (b) EVA film of 100μm thickness, (c) EVA film of 100μm thickness loaded with 1% MSNs, SEM-EDX elemental analysis of 100μm thick experimental EVA films loaded with 1% (d) MSNs, and (e) CdS-ZnS QDs encapsulation within MSNs.

The distribution of MSNs and surface properties (topography and phase) in the experimental EVA films was also examined using atomic force microscopy (AFM). The images were taken in tapping mode to avoid surface damage or deformation of the samples. Three dimensional topographical maps combining the height and phase data for neat EVA films and EVA films after MSNs loading can be seen in Figure 4.3 a to c. Circular topography features in Figure 4. 3 b and c represent the spherical MSNs which are dispersed throughout the polymer films without significant particle aggregation. After MSNs or MSNs encapsulated QDs loading this significant variation in the surface topography was visualized due to varying material density. Despite the variation of
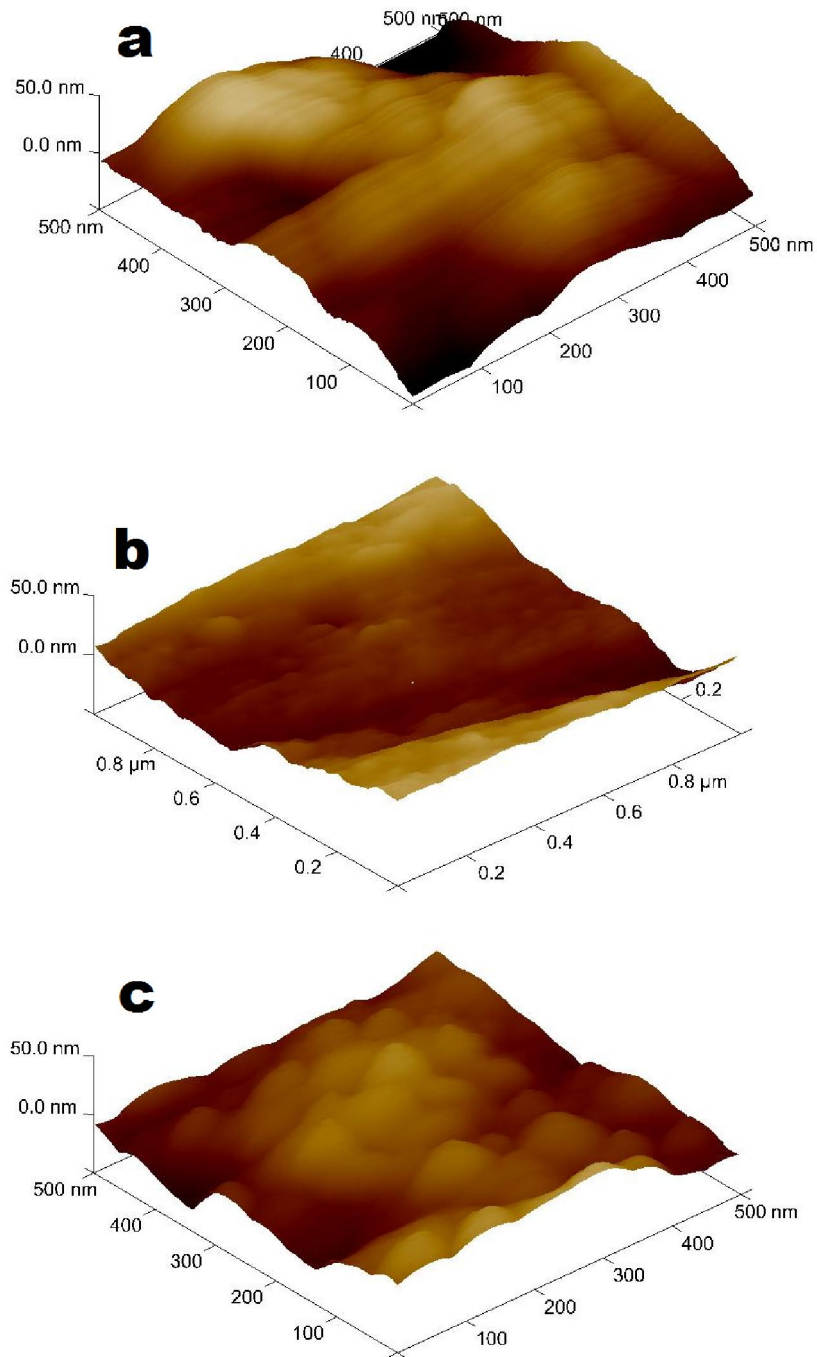
Figure 4.3. Atomic force microscopy 3D images of (a) EVA film; experimental EVA films loaded with 1% (b) MSNs, and (c) CdS-ZnS QDs encapsulation within MSNs (Film thickness: 250 μm).

surface features, it can be seen that continuous films without cracks were successfully formed for all types of MSNs used in this work.

The laser scanning confocal microscope (LSCM) was further used to examine the distribution of nanoparticles throughout the entire experimental films. Here, the focal planes were excited with an argon laser causing the QDs (inside the MSNs) dispersed in the polymer matrix to be identified as bright dots by their emission (Figure 4.4). During this analysis, the instrument divides the entire film thickness into sixty four planes with each focal plane imaged, then all planes stacked to get the final 3D image (Figure 4.4 d). For the QDs core size <10 nm, the bright spots were very tiny and less intense (Figure 4.4 a), whereas, with increasing QD core size, these bright spots become more prominent with enhanced fluorescence. From these images it can be seen that the QDs were well dispersed throughout the each plane and entire thickness of the film.
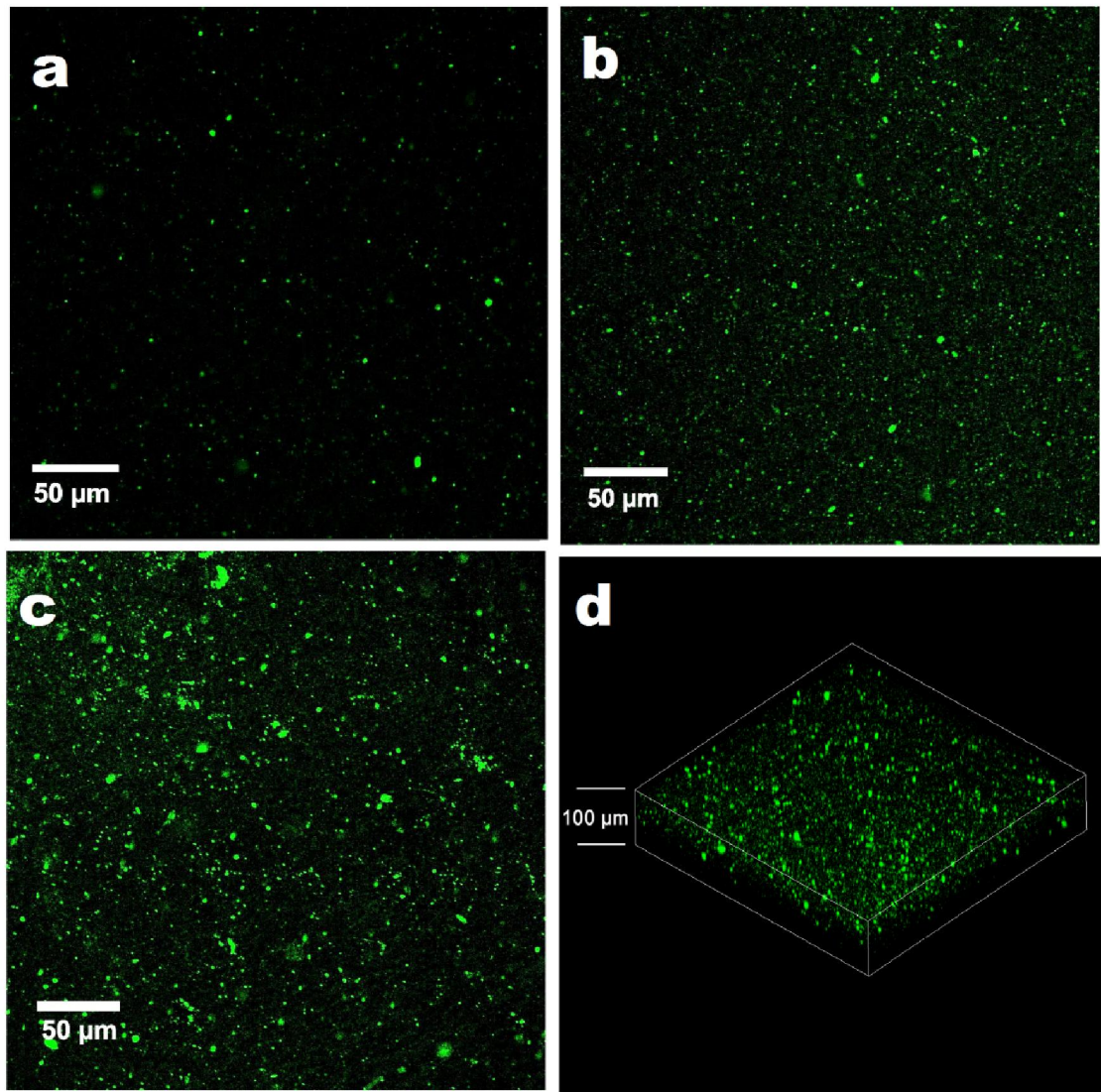
Figure 4.4. Laser scanning confocal microscopy images of experimental EVA films loaded with silica encapsulated CdS-ZnS QDs for different silica thickness with QDs core size (a) < 10 nm, (b) 20 nm, (c) 40 nm, and (d) 3D image of the experimental EVA films (Film thickness: 100 μm).

The MSNs with and without QDs, and after loading into EVA films were characterized by FTIR to identify the main functional groups, as seen in Figure 4.5. The spectra for MSNs before and after QDs encapsulation were found similar with a dominant peak at 1064 cm^{-1} and weaker peak at 804 cm^{-1} both due to Si—O—Si vibrations that are consistent with literature [34]. The intensity is much stronger than that for other silica based commercial fillers, e.g. silica areogel [9]. The small peak at 960 cm^{-1} (Si—OH) and broad peak at 3400 cm^{-1} (—OH) represent the presence of silanol structure at the silica surface. The major peaks for EVA were observed at 2750-3090 cm^{-1} and 1470 cm^{-1} (aliphatic C—H), 1745 cm^{-1} (C=O), 1247 and 1022 cm^{-1} (C—O—C stretch) that match with previous reports [9]. All these significant peaks were also seen after loading MSNs in EVA films, indicating successful integration. The appearance of a new broad band at 1070 cm^{-1} and small peak at 808 cm^{-1} confirmed the presence of silica in the experimental films.
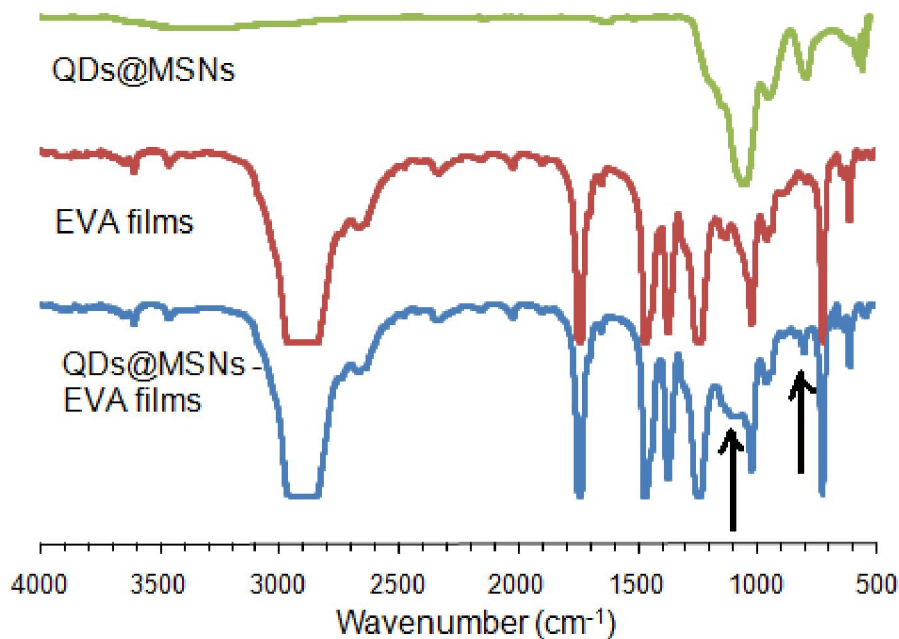
Figure 4.5. FTIR transmittance spectra of mesoporous silica encapsulated CdS-ZnS QDs, plain EVA, and mesoporous silica encapsulated CdS-ZnS QDs loaded EVA films (film thickness: 100 μm).

4.3.2 Thermal properties of the experimental EVA films

Primary radiative heat loss is an important physical property for the nanocomposite films, in which long-wave infrared and thermal radiation from inside the greenhouse (or PV module) radiates to the outdoor environment. The thermicity of the film plays a critical role to evaluate the heat loss. Higher thermicity values indicate higher transmissivity of infrared through the films, giving a greater rate of radiation heat loss.

Thermicity was calculated from the FTIR spectra as a ratio of the area under the transmittance curve from 700 to 1400 cm^{-1} to the area in the same region in the case of 100% transmittance [9]. As shown in Figure 4.6, the thermicity of the neat EVA film is very high, that can be seen to decrease with increasing film thickness. According to the Bouguer-Lambert-Beer law, the absorbance of a film is directly proportional to the film thickness [35], hence thicker films transmit less radiation.

Mesoporous silica was anticipated to block infrared transmission, therefore the MSN and MSN-QD samples were evaluated for thermicity. It was found that increased loading of MSNs gave decreased film thermicity, improving their efficiency at blocking infrared radiation to prevent heat loss. These thermicity values are better than commercial silica aerogels, even at five times higher loading in a similar polymer composite [9]. In the case of using mesoporous silica encapsulated QD nanoparticles having a QD core size less than 10 nm, the thermicity value was found almost the same shown by silica nanoparticles without QDs. However, for the same loading concentration, increasing QD concentration at the core gave slightly higher thermicity values. From this these small changes in thermicity, it is attributed that the core of the encapsulated MSNs is not purely QDs, rather QDs distribution within a mesoporous silica network. However, the outer shell of the encapsulated NPs is composed of silica as shown in TEM images (Figure 4.1). Therefore, mesoporous silica encapsulation not only improves the photo-physical properties of QDs [21] but also helps prevent heat loss from the films.
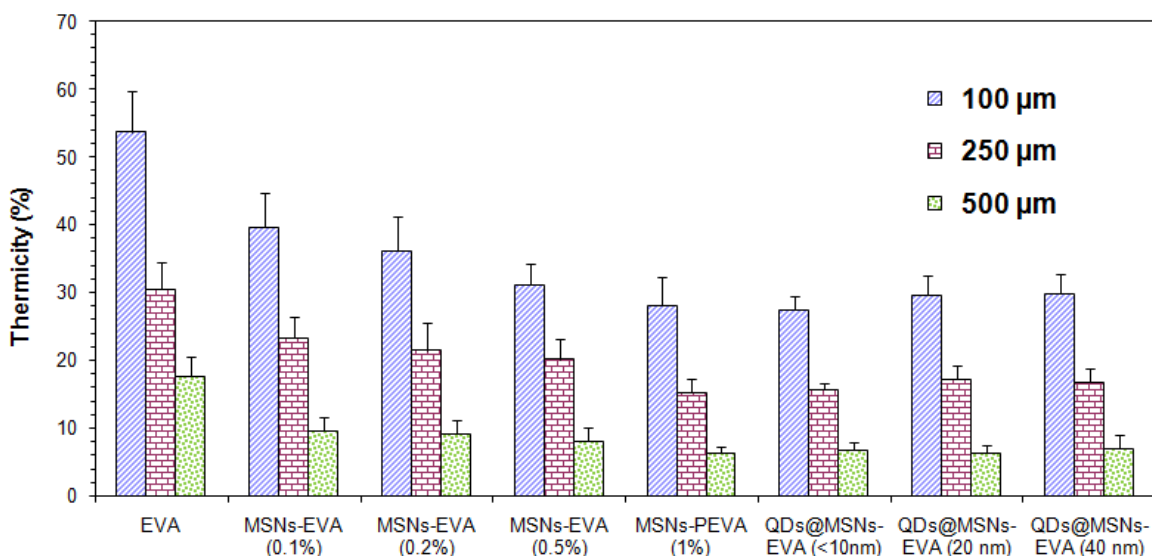
Figure 4.6. Thermicity of neat EVA films, mesoporous silica incorporated EVA films (at different loading concentrations) and mesoporous silica encapsulated QDs of different core (QDs) size loaded EVA (loading concentrations 1%). In all cases, analysis was carried out for film thickness 100, 250, and 500 μm.

Thermal conductivity is another important thermal property that is desired to be low for the thermic films. Thermal conductivity of EVA films and EVA films loaded with MSNs and QDs encapsulated in MSNs were measured experimentally to investigate the ability to prevent heat loss by conduction. The thermal conductivity of the EVA film was high and decreased with increasing weight fraction of nanoparticles loaded in EVA (Figure 4.7). For the lower fraction of MSNs (0.1%), the polymer was the dominant factor, and the thermal conductivity remained at a high value. However, upon further increasing the weight fraction of nanoparticles a decreasing trend was observed. From BET analysis it was observed that the MSNs possess high surface area (950 ± 50 m^2 g^{-1}) and mesoporous pores (3.8 ± 0.4 nm). Therefore, with increasing the weight fraction of MSNs the possibility of voids and porosity with the composites is increasing and results in a lowering of the thermal conductivity [36]. It was also previously reported that the thermal conductivity of polymer nanocomposites decreases with decreasing particle size at the same loading fraction of silica based additives [36].

103

Therefore, the nano sized mesoporous silica particles used here are more effective, even at a lower weight fraction than commercially available micro sized additives. In the case of lower concentration of QDs in the encapsulated MSNs, the thermal conductivity gave similar behaviour as thermicity. However, at the higher concentration of QDs, the thermal conductivity slightly increased, attributed to the semiconducting nature of the QD particles present within MSNs.
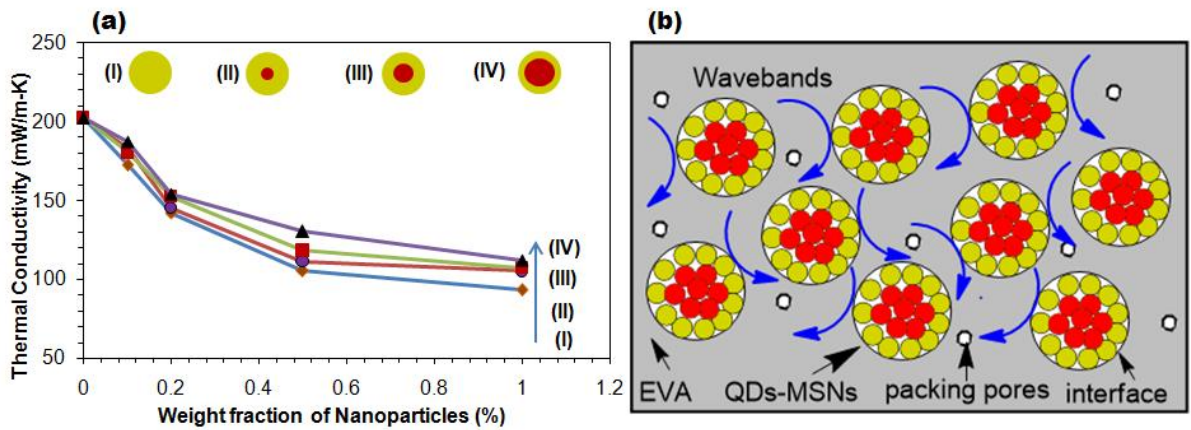
Figure 4.7. (a) Thermal conductivity of experimental EVA films loaded with different weight fractions of (I) MSNs, and MSNs encapsulated CdS-ZnS QDs of different silica thickness with QDs core size (II) < 10 nm, (III) 20 nm, (IV) 40 nm; (b) Schematics of the EVA films incorporated with MSNs encapsulated CdS-ZnS QDs after melt-mixing, and changed direction of heat transport path due to nano-porous structure of silica.

The thermal insulation and percololation threshold (here, heat transport path through the porous media) of MSNs-EVA nanocomposites depends on the inherent conductivity, concentration, size, shape, and orientation, extent of aggregation and dispersion of MSNs in EVA [37]. Silica has a low and stable thermal conductivity with changing the application temperature [38]. The thermal insulation performance of EVA composites is influenced by solid conduction, gas conduction, and radiative heat transfer. Gas conduction and radiative heat transfer can be decreased by nanopores of silica [38]. The porous network increases the heat transfer path by reflecting or scattering that improves

the thermal insulation. The three dimensional structure of silica nanoparticles that formed during sol-gel synthesis, also decreases the solid heat conduction [2]. The AFM and confocal images show isolated MSNs homogeneously dispersed throughout the EVA matrix, without remaining agglomerates.

4.3.3 Optical properties of the experimental EVA films

The optical properties including visible and UV light transmission of the experimental EVA films were investigated using UV-Vis Spectroscopy with an integrated sphere compartment. EVA films show high transparency of visible light (more than 80% for 500 μm film and more than 85% for thickness less than 250 μm). At the same time, the UV transmission is very high (> 90 %). Higher UV transmission is undesirable not only for stability of the films, also it retards photosynthesis and plant growth inside the greenhouses [7]. Although, MSNs improves heat retention and IR absorption properties of EVA films, it has no influence on UV-visible transmission of EVA films. This is because the MSNs are transparent in the UV and visible region [29]. However, mesoporous silica encapsulated CdS-ZnS QDs enhances the UV-shielding efficiency of EVA films even at low loading concentrations (less than 1%) as QDs can efficiently convert higher energy UV radiation into desirable lower energy visible wavelengths (Figure 4.8). The UV absorption capacity of these experimental films loaded with MSNs of tunable core-shell was found better than similar films with bare QDs or functionalized QDs even with higher loading concentrations [7, 39]. We have previously reported that mesoporous silica encapsulation enhances the photostability and the quantum yield of the QDs [29]. Due to high content of additives, commercially available thermic films are mostly less transparent with poor visible light transmission along with high UV transmission [7], but the experimental films show excellent potentiality to absorb undesired UV without compromising visible light transmission, while at the same time they provided improved heat retention properties.
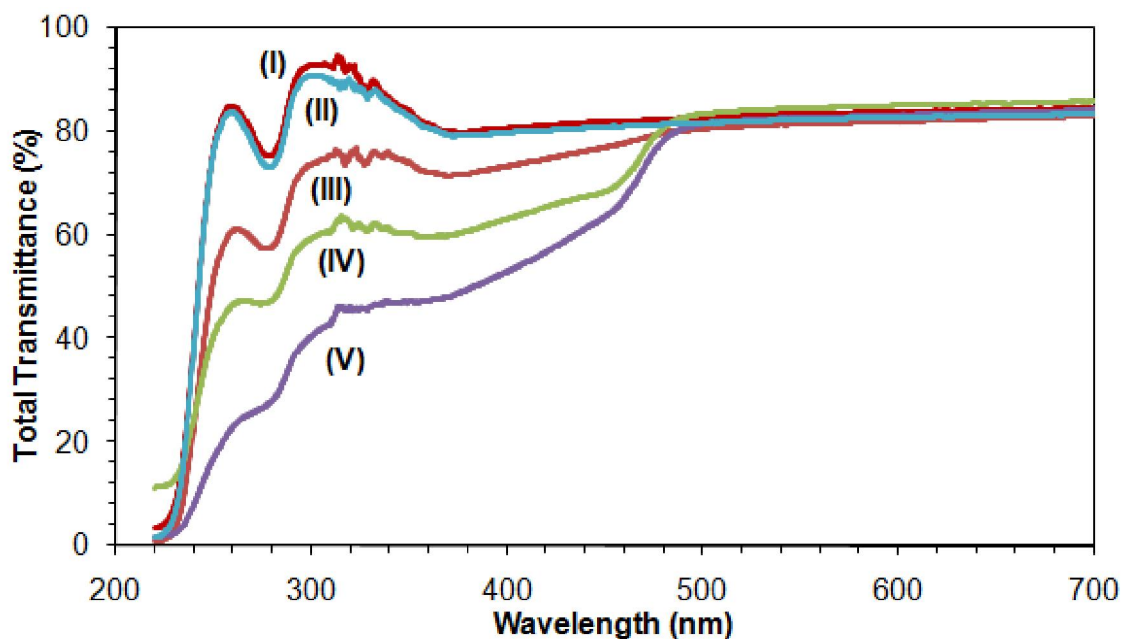
Figure 4.8. Total UV and visible light transmittance of (I) neat EVA film, (II) MSNs-EVA film, and MSNs encapsulated CdS-ZnS QDs-EVA films of variable silica thickness with QDs core size (III) < 10 nm, (IV) 20 nm, (V) 40 nm (loading content 1% and film thickness: 500 μm).

4.4. Conclusions

Core-shell CdS-ZnS QD semiconducting nanocrystals were successfully encapsulated in MSNs using a modified reverse microemulsion approach. The QD core and silica shell size was tuned in a controlled fashion by maintaining the overall particle size. Mesoporous silica enhanced both the quantum yield and photostability of the QDs. The MSNs showed excellent compatibility with EVA while MSNs with and without QDs nanoparticles were easily incorporated into EVA co-polymer matrix by melt-mixing in a

twin-screw extruder. Due to the excellent dispersion of MSNs, the experimental films showed both IR blocking efficiency and a significant reduction of thermal conductivity. When QDs were also integrated into the experimental films, improved optical properties were provided showing a significant decrease of UV transmission by retaining high visible light transmission. Both the thermal and optical properties could be tuned by controlling the thickness of the QD core and silica shell. Therefore, these novel nanocomposite films with both heat retention and light selective properties would be an excellent candidate for greenhouse covering and PV encapsulants.

4.5. Acknowledgements

4.6. References

[1] J. Jung, Y.J. Yoon, M. He, Z. Lin, Organic-inorganic nanocomposites composed of conjugated polymers and semiconductor nanocrystals for photovoltaics, Journal of Polymer Science Part B: Polymer Physics, 52 (2014) 1641-1660.

[2] M.E. Calvo, J.R. Castro Smirnov, H. Míguez, Novel approaches to flexible visible transparent hybrid films for ultraviolet protection, Journal of Polymer Science Part B: Polymer Physics, 50 (2012) 945-956.

[3] P. Rittigstein, R.D. Priestley, L.J. Broadbelt, J.M. Torkelson, Model polymer nanocomposites provide an understanding of confinement effects in real nanocomposites, Nature Materials, 6 (2007) 278-282.

[4] S. Kango, S. Kalia, A. Celli, J. Njuguna, Y. Habibi, R. Kumar, Surface modification of inorganic nanoparticles for development of organic–inorganic nanocomposites—A review, Progress in Polymer Science, 38 (2013) 1232-1261.

[5] S. Li, M.M. Lin, M.S. Toprak, D.K. Kim, M. Muhammed, Nanocomposites of polymer and inorganic nanoparticles for optical and magnetic applications, Nano Reviews, 1 (2010) 5214-5232.

[6] J.H. Bang, P.V. Kamat, CdSe quantum dot–fullerene hybrid nanocomposite for solar energy conversion: electron transfer and photoelectrochemistry, ACS Nano, 5 (2011) 9421-9427.

[7] J.M. Allan, M.A. Mumin, W.Z. Xu, Q. Al Sharari, P.A. Charpentier, Surface functionalized bare and core–shell quantum dots in poly (ethylene-co-vinyl acetate) for light selective nanocomposite films, Solar Energy Materials and Solar Cells, 123 (2014) 30-40.

[8] W.Z. Xu, P.A. Charpentier, Light-selective nanofilms of quantum dot-poly (ethylene-co-vinyl acetate) synthesized with supercritical CO_2, The Journal of Physical Chemistry C, 113 (2009) 6859-6870.

[9] J.M. Allan, M.A. Mumin, J.A. Wood, W.Z. Xu, W. Wu, P.A. Charpentier, Silica aerogel–poly (ethylene-co-vinyl acetate) composite for transparent heat retention films, Journal of Polymer Science Part B: Polymer Physics, 52 (2014) 927-935.

[10] K. Agroui, G. Collins, Characterisation of EVA encapsulant material by thermally stimulated current technique, Solar Energy Materials and Solar Cells, 80 (2003) 33-45.

[11] C. von Zabeltitz, Integrated Greenhouse Systems for Mild Climates, Springer Berlin Heidelberg2011, pp. 285-311.

[12] B. Richards, Enhancing the performance of silicon solar cells via the application of passive luminescence conversion layers, Solar Energy Materials and Solar Cells, 90 (2006) 2329-2337.

[13] G.A. Giacomelli, W.J. Roberts, Greenhouse covering systems, HortTechnology, 3 (1993) 50-58.

[14] H. Zou, S. Wu, J. Shen, Polymer/silica nanocomposites: preparation, characterization, properties, and applications, Chemical Reviews, 108 (2008) 3893-3957.

[15] A. Schmid, J. Tonnar, S.P. Armes, A New Highly Efficient Route to Polymer-Silica Colloidal Nanocomposite Particles, Advanced Materials, 20 (2008) 3331-3336.

[16] E. Espi, A. Salmeron, A. Fontecha, Y. García, A. Real, Plastic films for agricultural applications, Journal of Plastic Film and Sheeting, 22 (2006) 85-102.

[17] A. Shirazi, A.C. Cameron, Controlling relative humidity in modified atmosphere packages of tomato fruit, HortScience, 27 (1992) 336-339.

[18] A. Esfandiari, H. Nazokdast, A.-S. Rashidi, M.-E. Yazdanshenas, Review of polymer-organoclay nanocomposites, Journal of Applied Sciences, 8 (2008) 545-561.

[19] X. Hao, A.P. Papadopoulos, Effects of supplemental lighting and cover materials on growth, photosynthesis, biomass partitioning, early yield and quality of greenhouse cucumber, Scientia Horticulturae, 80 (1999) 1-18.

[20] C. von Zabeltitz, Integrated Greenhouse Systems for Mild Climates, Springer Berlin Heidelberg2011, pp. 145-167.

[21] L. Wei, N. Hu, Y. Zhang, Synthesis of polymer—mesoporous silica nanocomposites, Materials, 3 (2010) 4066-4079.

[22] V. Bounor-Legaré, P. Cassagnau, In situ synthesis of organic–inorganic hybrids or nanocomposites from sol–gel chemistry in molten polymers, Progress in Polymer Science, 39 (2014) 1473-1497.

[23] J. Yang, C.-R. Han, J.-F. Duan, F. Xu, R.-C. Sun, Interaction of silica nanoparticle/polymer nanocomposite cluster network structure: revisiting the reinforcement mechanism, The Journal of Physical Chemistry C, 117 (2013) 8223-8230.

[24] X. Ye, J. Wang, Y. Xu, L. Niu, Z. Fan, P. Gong, L. Ma, H. Wang, Z. Yang, S. Yang, Mechanical properties and thermostability of polyimide/mesoporous silica nanocomposite via effectively using the pores, Journal of Applied Polymer Science, 131 (2014) 41173 (41171-41178).

[25] C.J. Weng, K.Y. Huang, W.L. Chiu, J.M. Yeh, Y. Wei, S.P. Liu, S.S. Hwang, A comparative study of the preparation and physical properties of polystyrene–silica mesocomposite and nanocomposite materials, Polymer International, 60 (2011) 1129-1135.

[26] F.-A. Zhang, D.-K. Lee, T.J. Pinnavaia, PMMA/mesoporous silica nanocomposites: effect of framework structure and pore size on thermomechanical properties, Polymer Chemistry, 1 (2010) 107-113.

[27] Q. Dong, Y. Ding, B. Wen, F. Wang, H. Dong, S. Zhang, T. Wang, M. Yang, Improvement of thermal stability of polypropylene using DOPO-immobilized silica nanoparticles, Colloid and Polymer Science, 290 (2012) 1371-1380.

[28] M. Faker, M.R. Aghjeh, M. Ghaffari, S. Seyyedi, Rheology, morphology and mechanical properties of polyethylene/ethylene vinyl acetate copolymer (PE/EVA) blends, European Polymer Journal, 44 (2008) 1834-1842.

[29] M.A. Mumin, K.F. Akhter, P.A. Charpentier, Photo-physical properties enhancement of bare and core-shell quantum dots, AIP Conference Proceedings, 2014, pp. 259-265.

[30] S. Xu, S. Hartvickson, J.X. Zhao, Increasing surface area of silica nanoparticles with a rough surface, ACS Applied Materials & Interfaces, 3 (2011) 1865-1872.

[31] M. Darbandi, G. Urban, M. Krüger, A facile synthesis method to silica coated CdSe/ZnS nanocomposites with tuneable size and optical properties, Journal of Colloid and Interface Science, 351 (2010) 30-34.

[32] H. Lee, Rapid measurement of thermal conductivity of polymer films, Review of Scientific Instruments, 53 (1982) 884-887.

[33] R. Koole, M.M. van Schooneveld, J. Hilhorst, C. de Mello Donegá, D.C.'. Hart, A. van Blaaderen, D. Vanmaekelbergh, A. Meijerink, On the incorporation mechanism of hydrophobic quantum dots in silica spheres by a reverse microemulsion method, Chemistry of Materials, 20 (2008) 2503-2512.

[34] S.A. McCarthy, G.-L. Davies, Y.K. Gun'ko, Preparation of multifunctional nanoparticles and their assemblies, Nature Protocols, 7 (2012) 1677-1693.

[35] J.L. Koenig, Application of Fourier transform infrared spectroscopy to chemical systems, Applied Spectroscopy, 29 (1975) 293-308.

[36] A. Tessema, A. Kidane, Composite, hybrid, and multifunctional materials, Springer, New York, 2014 pp 151-156.

[37] M. Yoonessi, J.R. Gaier, Highly conductive multifunctional graphene polycarbonate nanocomposites, ACS Nano, 4 (2010) 7211-7220.

[38] D. Ge, L. Yang, Y. Li, J. Zhao, Hydrophobic and thermal insulation properties of silica aerogel/epoxy composite, Journal of Non-Crystalline Solids, 355 (2009) 2610-2615.

[39] X. Wang, S. Zhou, L. Wu, Facile encapsulation of SiO_2 on ZnO quantum dots and its application in waterborne UV-shielding polymer coatings, Journal of Materials Chemistry C, 1 (2013) 7547-7553.

Chapter 5

Supercritical CO_2 dispersion of quantum dots@silica nanoparticles in EVA nanocomposites and their optical properties

Abstract

Dispersed transparent polymer/inorganic nanocomposites are of great interest because they can significantly improve the properties of existing polymeric materials. However, achieving a high level of nanoparticle dispersion without compromising optical properties has been a key challenge in the production of such nanocomposites. In this paper, we explore a novel supercritical carbon dioxide ($scCO_2$) synthesis method that utilizes $scCO_2$ to enhance the dispersion of silica encapsulated core-shell quantum dots into poly(ethylene-co-vinyl acetate) (EVA).

The core-shell CdS-ZnS quantum dots (QDs) were first encapsulated with silica to improve their photoluminescence and stability. Vinyl groups were then introduced onto the surface of the silica encapsulated QDs by the addition of vinyltrimethoxy silane, (before or during polymerization). Dispersion of the nanoparticles in the EVA polymer matrix was characterized by SEM, TEM, and CLSM. The results demonstrated that $scCO_2$ improved dispersion of nanoparticles and uniform dispersion was observed for two-step process (functionalization before polymerization). FTIR confirmed the successful functionalization on silica surface. The vinyl acetate content of EVA copolymer and nanocomposite was 33.5% calculated using TGA weight loss data. The optical study shows that with a very low loading of nanoparticles (~1%), more than 50% UV transmission can be prevented while visible light transmission retained more than 95%.

5.1   Introduction

Polymer matrices reinforced with nanoscale inorganic materials have been studied extensively due to their unique physical and chemical properties, which combine the advantages of the inorganic nanoparticles and the organic polymers [1-3]. These hybrid materials provide high performance new functional materials that find applications in

many industrial fields [4, 5]. In general, there are two preparative methods (*in situ* and *ex situ*) reported for polymer-inorganic nanocomposites [6]. *In situ* synthesis provides a facile and one-step fabrication route where nanoparticles are nucleated from corresponding precursors and grown inside a polymer matrix [7]. The strong interaction between nanoparticles and polymer matrix is very important for successful synthesis of nanocomposites. However, controlled tailoring of the nanoparticles surface and coupling to the polymer matrix is difficult during *in situ* synthesis that leads to poor control of the monodispersity, crystallinity, and properties of the final products [8]. Moreover, the unreacted reactants and by-products can have adverse effects on the properties of the nanocomposites, which is another major drawback of this method [6].

Another important route is *ex situ* synthesis of polymer nanocomposites in which pre-made or functionalized inorganic nanoparticles are blended with polymers or in which polymerization occurs in the presence of these nanoparticles for direct coupling to the polymer matrix [6, 8]. Recently, we have reported polymer nanocomposite films with enhanced optical and thermal properties by using a reactive polymer processing approach, which is a simple and convenient way suitable for large scale industrial application [9-11]. However, due to the high surface energy of the nanoparticles and low compatibility with polymer, it becomes difficult to maintain good dispersibility of nanoparticles within the polymer matrix. This can lead to deterioration of the toughness and stability of the resulting composites for long span applications of nanocomposite films and coatings [6, 12]. The "*grafting-from*" technique, also called surface-initiated polymerization, has been shown as a very promising and versatile method [13]. Here, surface engineering minimizes the interfacial energy and increases the hydrophobicity, which with controlled polymerization on the modified nanoparticle surface enhances the chemical bonding, compatibility, and dispersibility of the nanoparticles within the polymer matrix [8, 12].

Recently, semiconductor nanocrystals, also known as quantum dots (QDs) incorporated in polymer composites have attained intense interest for potential applications in photovoltaic (PV) devices, PV encapsulants, greenhouse coverings, as well as biological tagging [9, 10, 14, 15]. The most intriguing feature about QDs is that their absorption,

emission, and band gaps can be tailored by changing the type, size, and shape of the QDs [16, 17]. Despite the potential advantageous optical properties of QDs, their reactivity, aggregation tendency, uncontrollable sizes, inconsistent emission, and photobleaching have hindered recent progress in polymer nanocomposites [9, 18]. We previously reported that surface functionalized bare and core-shell QDs could be incorporated into an ethylene-*co*-vinyl acetate (EVA) polymer matrix by melt-mixing [10]. However, long-term photostability of these functionalized QDs was limited, while coverage of the QD surface atoms by the organic ligands may cause steric hindrance during further processing [19, 20]. We have also examined another approach, mesoporous silica encapsulation of bare and core-shell QDs and loaded into EVA by melt-mixing [9]. A controlled thickness of the silica layer on the QDs showed enhancement of quantum efficiency and stability of the QDs. Also the optical properties of the nanocomposite films were improved significantly using this approach [9]. However, uniform distribution of silica nanoparticles into the polymer network and stability under prolonged photoexcitation without compromising their transparency and desired light transmittance are still major challenges. This led to our investigating a new approach to stabilize these nanoparticles into composites for long-term applications.

One of the key structural features of mesoporous silica is that the silica surface can be modified and conjugated with different functionalities for linking to polymeric species and biomolecules [21]. No reports have been published on mesoporous silica encapsulated QDs incorporated into EVA using graft polymerization, especially for applications in greenhouse coverings or PV encapsulants. Therefore, it is anticipated that by developing a novel facile approach to activate the surface of silica encapsulated QDs with a silane coupling agent followed by *grafting from* polymerization of ethylene and vinyl acetate monomers, both the distribution and stability of the nanoparticles as well as the optical properties of the nanocomposites can be improved.

As a viable "green" alternative to hazardous organic solvent, supercritical CO_2 ($scCO_2$) has emerged as a functional solvent which can facilitate both polymerization and material processing [22]. $ScCO_2$ has a reasonably accessible critical point ($T_c = 31.1$ $^{\circ}$C and $P_c = 7.4$ MPa) with other advantages, including, CO_2 is inexpensive, nonflammable, non-

toxic, and environmentally benign [23]. ScCO$_2$ enhances mass transfer and reaction kinetics, also allowing penetration of nanoparticles into pores of the polymer network [23]. Recently, QDs/polymer-based nanocomposites synthesis using scCO$_2$ has emerged and reported by different research groups [16, 24, 25], but the strong interactions, uniform distribution, and stability are still major challenges that play a key role for long term applications of these nanocomposites.

Herein, highly photoluminescent and monodispersed CdS-ZnS core-shell quantum dots were prepared by using a facile and modified colloidal synthesis approach. To make the QDs more resistant against photochemical reactions, a controlled mesoporous silica layer was grown on the QDs through a reverse microemulsion technique based on hydrophobic interactions. Then a *grafting from* polymerization of ethylene and vinyl acetate on the functionalized nanoparticles of silica encapsulated QDs were carried out under scCO$_2$. The functionalization and polymerization reactions were explored both by one-pot and two step techniques. The novel nanocomposites were then characterized in terms of their morphology, nanoparticles dispersion into the matrix, and optical properties.

5.2 Experimental

5.2.1 Materials

Instrumental grade CO$_2$ (99.99%, with dip-tube), ethylene (99.99%, polymer grade), and argon (ultra high purity, 99.9%) were purchased from Plaxair, Canada. Ethylene was further purified by passing through a column filled with 5 Å molecular sieves and 20% copper oxide/Al$_2$O$_3$ (Sigma-Aldrich, Canada) to remove the moisture and oxygen, respectively. Vinyl acetate (>99%, with 3-20 ppm hydroquinone as inhibitor) was purchased from Sigma-Aldrich, Canada. Before the polymerization reaction, hydroquinone was removed by passing the monomer through a disposable prepacked inhibitor remover column purchased from Sigma-Aldrich, Canada. Cadmium chloride, sodium diethyldithiocarbamate trihydrate, zinc diethyldithiocarbamate (98%), trioctylamine (TOA) (98%), triocylphosphine (TOP) (97%), cyclohexane (99%), chloroform (99.8%)m 1-hexanol (98%), tetraethyl orthosilicate (TEOS), ammonia

solution (28%), heptane (HPLC grade), 30% H_2O_2, ethyl choloroformate, glacial acetic acid, vinyl trimethoxysilane (VTMS) were also purchased from Sigma-Aldrich, Canada and used as received.

5.2.2 Synthesis of silica encapsulated CdS-ZnS QDs

The core-shell (CdS-ZnS) QDs were synthesized using a modified single-molecular precursor method, as previously reported [10]. The encapsulation reaction was carried out by following the water-in-oil microemulsion method based on sol-gel chemistry, as described earlier [9].

5.2.3. Preparation of DEPDC initiator

The initiator diethyl peroxydicarbonate (DEPDC) was synthesized as previously described [26]. The yield of DEPDC was measured using a standard iodimetric titration analysis and also verified by NMR analysis. To avoid highly reactive decomposition, concentrated DEPDC in heptane was stored at -20°C.

5.2.4. Functionalization of silica encapsulation of CdS-ZnS QDs

The vinyl functionalization of mesoporous silica encapsulated QDs was carried out based on modification of a previously reported method [27]. Typically, 50 mg of mesoporous silica encapsulated CdS-ZnS QDs was dispersed in 25 mL of toluene. 10-15 µL of miliQ deionized water was added and stirred vigorously for 1 hr to allow the water disperse through the mesoporous matrix and maximize hydroxylation of the silica surface [27]. Then, 0.77 mL of vinyl trimethoxysilane (VTMS) was added to the mixture and stirred for 12 hrs at room temperature. The product was collected by centrifugation, washed with excess of 2-propanol and dispersed in toluene (2 mL).

5.2.5. Synthesis of EVA nanocomposites of silica encapsulation of CdS-ZnS QDs

The synthesis of nanocomposites was carried out by using both a one-step and two-step process. In the one-step process, functionalization of nanoparticles was carried out during polymerization, while in the two-step process, pre-functionalized nanoparticles (as described in section 5.2.4) was added with monomer(s) before polymerization was initiated. The polymerization experiments were conducted in a 100 mL high-pressure stainless steel autoclave coupled with a digital pressure transducer and a temperature controller (Parr Instuments). The stirring speed was maintained at a constant speed of 300 rpm. In a typical one-step method, 9.22 mL of vinyl acetate (monomer), 0.9 mL of DEPDC (initiator), 50 mg of silica encapsulated CdS-ZnS QDs, 0.77 mL of VMTS (linker), and 1.14 mL of glacial acetic acid (as hydrolysis agent) were charged into the reactor, followed by purging with a flow of argon. Then the second monomer ethylene (1.07 mol) was pumped in using a syringe pump (Isco 100 DX) followed by pumping CO_2 (Isco 260D) into the reactor. The temperature of the reactor was then raised to let the reaction take place at 50 $^{\circ}$C under 27.5 MPa for 20 hours. After polymerization, CO_2 was carefully vented leaving the nanocomposite products in the reactor. The viscous product was collected from the reactor and subsequently dried under vacuum at 40 $^{\circ}$C overnight. Scheme 5.1 shows the functionalization and polymerization to prepare nanocomposites in $scCO_2$.

5.2.7 Material characterization

Mesoporous silica encapsulated QD nanoparticles and their dispersion in EVA composites were investigated using transmission electron microscopy (TEM). The micrographs were taken using a Phillips CM10 TEM with an accelerate voltage of 80 kV. TEM samples were prepared by drop-casting ethanol-dispersed nanoparticles and chloroform-dispersed nanocomposite samples on a copper grid covered with carbon film. Scanning electron microscopy (SEM) was also utilized to study the morphology of nanoparticles and nanocomposites by using a LEO (ZEISS) 1540XB FIB/SEM.

Elemental composition of QDs inside silica and EVA polymer composites was confirmed and quantified using the energy dispersive X-ray detection (EDX) feature of the SEM. A ZEISS LSM 5 Duo confocal microscope was used to take transmission and fluorescence images of the experimental films using an argon laser at 488 nm. A 250 μm film was prepared from 0.075 g for each nanocomposite products using a Spectra-Tech universal film maker (UFM) kit and Carver hydraulic press. A small section of the nanocomposite film areas of approximately 500 μm were scanned using an objective of 20X magnification. Infrared spectra were collected from 500 to 4000 cm^{-1} using a Nicolet 6700 FTIR spectrometer to examine functionalization of nanoparticles and also functionality presence in nanocomposites. Thermogravimetric analysis (TGA) was performed on a TA Instruments SDT Q600 with a temperature ramp from 30 to 700 ^{o}C at a heating rate of 10 deg/min under nitrogen atmosphere. Shimadzu UV-3600 UV-VIS-NIR spectrophotometer was used to measure the light transmittance of the film samples.
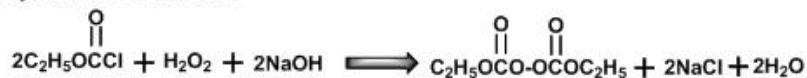
Scheme 5.1. Schematic illustration of (i) the overall reaction of synthesis of DEPDC (initiator), (ii) functionalization of silica encapsulated CdS-ZnS QDs using vinyl trimethoxisilane, (iii) *grafting from* polymerization of EVA in $scCO_2$.

5.3   Results and discussion

5.3.1 Structural characteristics

Silica encapsulated QDs before and after surface functionalization were characterized by FTIR. As shown in Figure 5.1a a strong peak at 1100 cm^{-1} and weaker peak at 790 cm^{-1} were observed for silica encapsulated QDs due to Si−O−Si vibrations, which is consistent with literature [28]. These significant peaks remained after vinyl functionalization. However, new peaks after functionalization at 2950 to 2860 cm^{-1} are assigned to the alkene C-H vibration and the aliphatic C-H vibrations respectively [27]. A small peak at 1604 cm^{-1} was also observed that represents C=C stretching vibration in the vinyl-functionalized samples. As seen in Figure 5.1b, the major peaks for EVA copolymer were observed at 2930, 2845, and 1470 cm^{-1} for aliphatic C-H vibrations, 1737 cm^{-1} for C=O stretching vibration, 1235 and 1022 cm^{-1} due to C−O−C stretching vibrations. These peaks match with previous report for EVA [11, 29]. All these significant peaks were also observed after nanocomposite formation, indicating successful integration of the nanoparticles into the EVA polymer matrix. The appearance of a new band at 1090 cm^{-1} and a small peak at 782 cm^{-1} (indicated with blue star in Figure 5.1b are because of Si−O−Si vibrations, confirming the presence of silica in the EVA nanocomposites. The lower intensity of these peaks are due to low loading concentration of nanoparticles during synthesis of the nanocomposites.
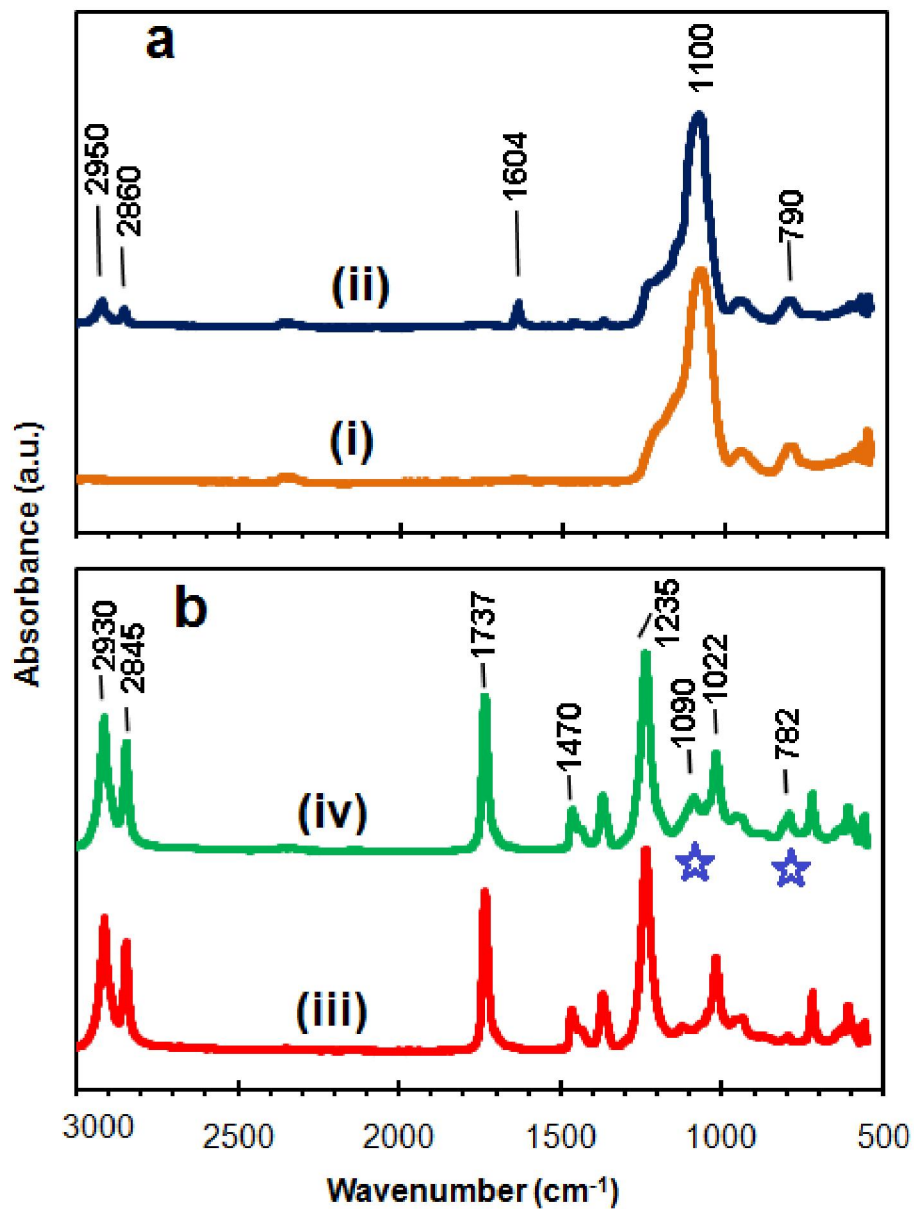
Figure 5.1. FTIR spectra of (a) silica encapsulated CdS-ZnS QDs (i) as synthesized, (ii) vinyl functionalized; (b) polymer nanocomposites synthesized under scCO$_2$ (iii) EVA copolymer, (iv) EVA nanocomposites incorporated with vinyl functionalized silica encapsulated CdS-ZnS QDs using two-step process.

TGA curves for QDs encapsulated MSNs before and after vinyl functionalization are shown in Figure 5.2. The weight loss of MSNs was about 17.8% for the whole temperature range, which is largely due to the removal of free water (adsorbed from atmosphere), the presence of any structural water and the dehydroxylation of silanol groups [30]. An additional 7.8% weight loss resulted from the attached organic units on the surface of the MSNs after functionalization. Similar weight loss has been reported for MSNs functionalization using other types of surface functionalization agents [8]. The thermograph of EVA co-polymer synthesized under $scCO_2$ is also shown in Figure 5.2. There were two stages of weight loss at approximately 360 and 475 ^{o}C. The first stage is attributed to the copolymer losing acetic acid and from this mass loss the wt% of VA (vinyl acetate) can be calculated [31]. The weight loss for the first stage was approximately 23.4 %. By multiplying this value by the ratio of the molecular weight of VA monomer to the molecular weight of acetic acid, the weight % of VA of the synthesized EVA copolymer was calculated as 33.5%. In the second stage temperature range 450 and 500 ^{o}C hydrocarbon chain decomposes to simple hydrocarbon ($CH_2=CH_2$, CH_4) and eventually to CO_2. Therefore, the weight was around zero. In the case of EVA nanocomposites with functionalized QDs encapsulated MSNs, there was no significant difference observed in the thermograph because of very low loading of NPs (~1%). After 500°C, the remained final weight around 1% is due to inorganic materials after complete decomposition of the polymer.
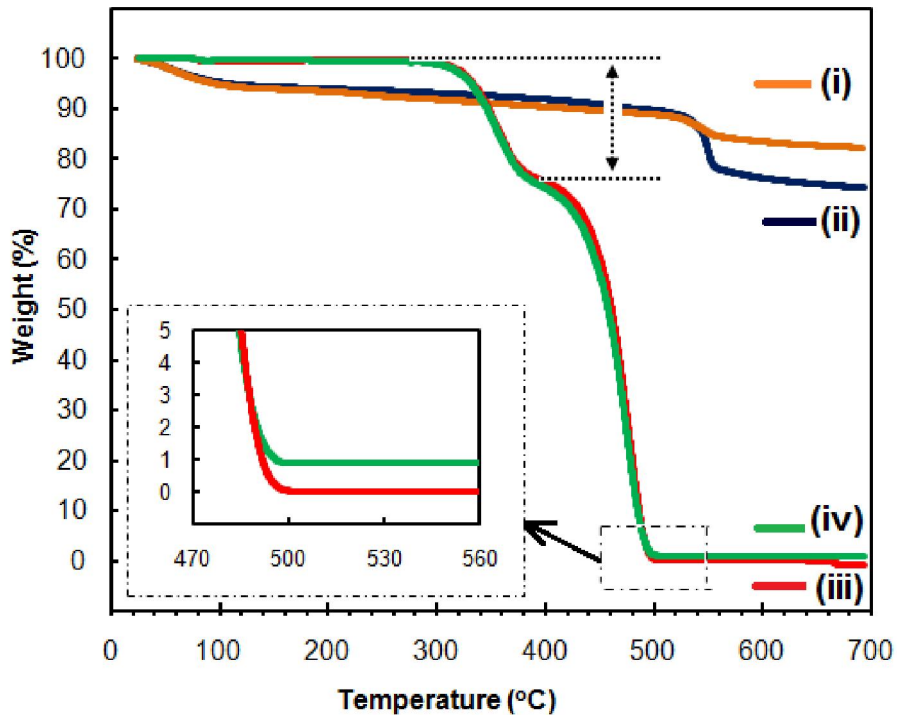
Figure 5.2. TGA plot of (i) silica encapsulated CdS-ZnS QDs (ii) silica encapsulated CdS-ZnS QDs after vinyl functionalization, (iii) poly(EVA), (iv) EVA nanocomposites grafted with silica encapsulated CdS-ZnS QDs using two-step polymerization process.

5.3.2 Morphology and distribution of nanoparticles in EVA

To improve compatibility and binding with the polymer, the synthesized silica encapsulated CdS–ZnS QDs were functionalized with vinyl trimethoxysilane (VTMS) as described by Scheme 5.1-step 2. The one-step process provides functionalization of silica encapsulated QDs and *grafting from* polymerization of EVA at the same time in the same reactor. The challenge of this process lies in the limited solubility of the nanoparticles in the vinyl acetate/initiator mixture. To minimize this, nanoparticle samples were dispersed

in glacial acetic acid that was used as a hydrolyzing agent during *grafting from* polymerization. However, in the two step process, the silica encapsulated QDs were dispersed separately in solvents, while vinyl functionalization was carried out before beginning the polymerization. Scanning electron microscopy (SEM) reveals the morphologies of the functionalized nanoparticles, EVA polymer, and EVA nanocomposites. Figure 5.3a presents the silica encapsulated QDs after vinyl functionalization. These modified QDs were formed as smooth nanospheres with less than 100 nm size. The surface features of EVA co-polymer (Figure 5.3b) and EVA nanocomposites incorporated with these functionalized silica encapsulated QDs using the two-step polymerization approach (Figure 5.2c) were the same. No significant nanoparticle agglomeration was observed on the polymer surface (Figure 5.1c) and also inside of the nanocomposites samples seen through cracks and edges. During SEM-EDX analysis, except carbon there were no significant peaks observed because of very low concentration (~1%) of nanoparticles and also no agglomeration of nanoparticles. The morphology in the case of EVA nanocomposites using the one-step process was also consistent with that for EVA polymers. However there were few bright spots observed on the polymer surface which were analyzed by EDX and found the presence of elements Si and O came from silica nanoparticles, and Zn, S, and Cd from the QDs. These elements content also varied from one region to the next because of the size and density of the agglomeration.

Transmission electron microscopy (TEM) was used to examine the size and size distribution of functionalized silica nanoparticles as well as to investigate the distribution of these nanoparticles throughout the EVA polymer matrix. Figure 5.4a shows a TEM image of the silica encapsulated CdS-ZnS QDs after vinyl functionalization, providing an average particle size 60±5 nm. This size range is consistent with the particle size of the silica encapsulated CdS-ZnS QDs reported previously [9]. The surface of the nano-spheres was rather smooth and uniform with narrow size distribution.
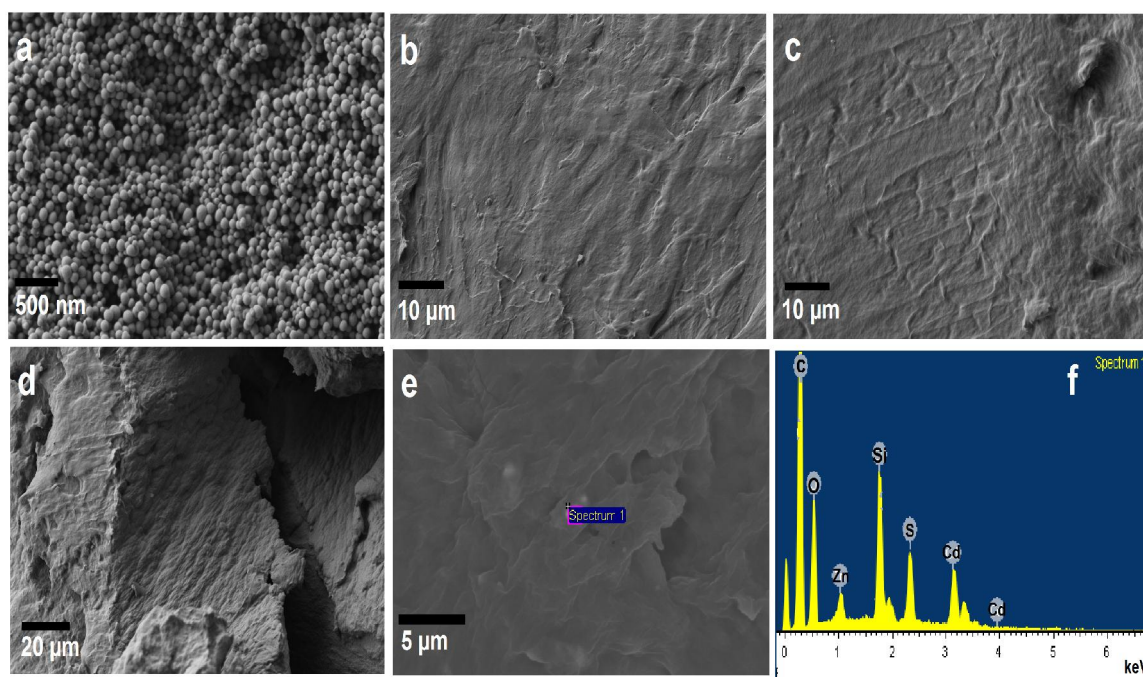
Figure 5.3. SEM images of (a) silica encapsulated CdS-ZnS QDs after vinyl functionalization, (b) poly(EVA), (c & d) EVA nanocomposites grafted with silica encapsulated CdS-ZnS QDs using two-step polymerization process, (e) EVA nanocomposites using one-step process, and (f) SEM-EDX of EVA nanocomposites using the one-step process.

Figure 5.4 b-d show the TEM images of neat EVA co-polymer and EVA nanocomposites with incorporation of functionalized silica encapsulated QD nanoparticles. It is clearly observed that the silica nanoparticles are rather well dispersed in the EVA matrix. However, in the case of nanocomposites prepared following the two step process a better homogeneous dispersion was observed without showing sign of any aggregation (Figure 5.4d). The two-step approach can efficiently utilize the surface functionalization ligand. In this case, functionalized nanoparticles were well dispersed in solvent before adding with monomer/initiator mixture, providing an enhanced compatibility and chemical linking between the polymer network and the nanoparticles. The nanoparticles distribution observed from the TEM analysis also corroborated the findings from SEM analysis.
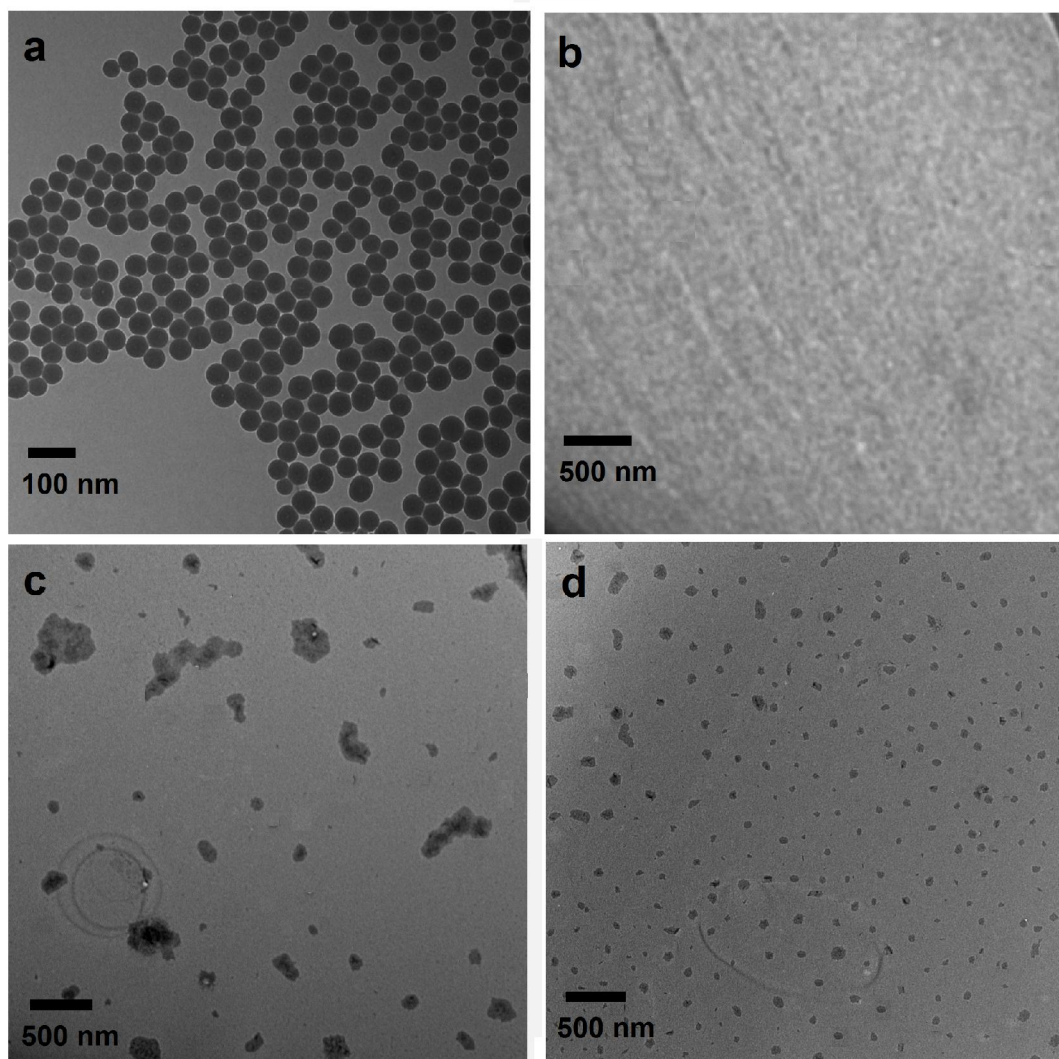
Figure 5.4. TEM images of (a) silica encapsulated CdS-ZnS QDs after vinyl functionalization, (b) poly(EVA), (c) EVA nanocomposites grafted with silica encapsulated CdS-ZnS QDs using one-step polymerization process, (d) EVA nanocomposites using the two-step process.

Beside electron microscopy imaging methods (SEM, TEM) which only provide an indication of nanoparticles distribution on a single plane of the surface, laser scanning confocal microscopy (LSCM) was used to examine the nanoparticle distribution throughout the EVA polymeric matrix. By preparing a 250 μm thickness film, the focal

planes of the EVA nanocomposite films were excited with an argon laser causing QDs emission showing as bright green dots. Figure 5.5 shows confocal images of a random plane approximately at the middle thickness of the nanocomposites films. From the bright green dots of these images, it can be seen that the silica encapsulated QDs were well dispersed throughout the EVA nanocomposites prepared both using the one-step and two-step approaches. However, consistent with the TEM results, the EVA nanocomposites prepared using two-step process showed uniform distribution of the nanoparticles throughout the polymer network. Polymer/inorganic nanocomposites synthesized using conventional solution mixing process suffers aggregation of filler particles because of slow solvent evaporation, as well as to get even a milligram of products can take more than a day [32, 33]. In the two-step approach, not only are toxic organic solvents avoided, in the presence of $scCO_2$, the filler nanoparticles were uniformly distributed throughout the polymer matrix. Also this process is more feasible and economic for large scale production.
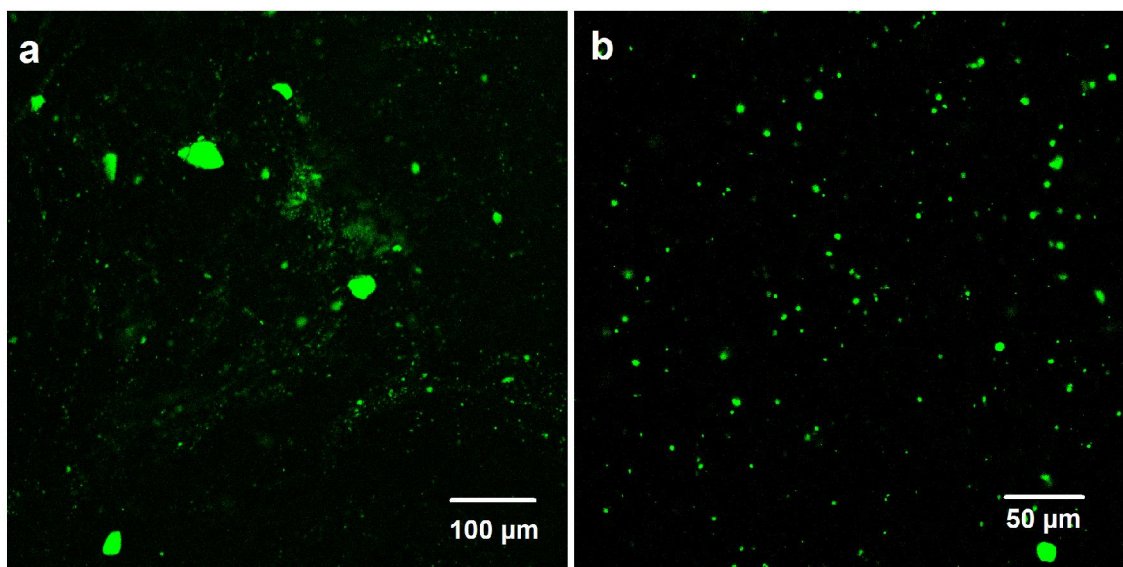
Figure 5.5. Laser scanning confocal microscopy images of EVA nanocomposites films loaded with vinyl functionalized silica encapsulated CdS-ZnS QDs prepared using (a) one-step polymerization process, (b) two-step polymerization process.

The synthesis technique of the polymer nanocomposite plays a critical role for uniform dispersion of NPs in the polymeric network. The blending method is the simplest and convenient approach for preparing nanocomposites. However, due to the high surface energy of the nanoparticles and low compatibility with polymer, it becomes difficult to maintain good dispersibility of nanoparticles within the polymer matrix [1, 6]. Surface functionalization or encapsulation of NPs or the uniform transparent dispersion of NPs in a solution of polymer or oligomers with reactive groups improves the compatibility of NPs with polymer [6, 9, 10]. *In situ* synthesis, the nanoparticles are nucleated and grown inside the polymer matrix, suppressing the undesirable irreversible particle aggregation caused by their isolation and handling process. The advantage of this route is the passivating or stabilizing effect of the polymer chain functional groups on the formed NPs, which can control particle size effectively, and thus prevent particle agglomeration whilst maintaining a good spatial distribution in polymer matrices [7, 8]. This is due to kinetic control because the polymers cannot provide a sufficiently fluid environment to allow individual particles to meet each other by diffusion. However, the drawback of this approach is that the unreacted reactants/precursors or byproducts might influence the properties of the nanocomposite products [6]. Compare to the above mentioned technique *in situ grafting* polymerization in presence of the NPs is a very promising and versatile method. A key challenge for this method is to be able to prepare NPs which possess good dispersibility in the polymer or its monomer, have long-term stability against aggregation, and do not negatively interfere with the *in situ* polymerization process in large enough amounts. In fact to solve this problem, the surface engineering of NPs is very important for minimizing the interface energies between nanoparticles and polymer matrix [8, 12]. As shown in Figure 5.4 and 5.5, the two step approach of *in situ grafting from* polymerization provides better surface engineering and dispersion of engineered NPs in the monomer/initiator mixtures. This approach results the most uniform distribution of silica encapsulated QDs in EVA network compared to the nanocomposite prepared using the one-step polymerization or melt- mixing method (chapter 3).

5.3.3 Optical properties

The optical properties of the EVA copolymer and EVA nanocomposites synthesized using both the one-step and two-step process were investigated using UV-vis spectroscopy. Figure 5.6 shows the total light transmittance in the UV and visible region. EVA shows high transparency of visible light as well as high UV transmission, approximately 98%. Higher UV transmission is undesirable not only for stability of the polymer, also limits short and long span practical applications [10]. The EVA nanocomposites incorporated with functionalized silica encapsulated CdS-ZnS QDs prepared using the one-step process under $scCO_2$ show a slight decrease in the visible light transmission (more than 92%) but a prominent decreasing trend was observed in the UV region. The lowering of this UV transmission is because of the absorption of higher energy UV radiation by CdS-ZnS QDs that can be efficiently converted into desirable lower energy visible light through emission and silica has no influence on UV-visible transmission of EVA nanocomposites [11]. The UV shielding performance of the EVA nanocomposites can be further increased (more than 50% at 260 nm) while their visible light transparency remained very high almost the same as plain EVA. It is attributed that uniform distribution of the QDs throughout the polymer network as shown in Figure 6.4 and 5.5 enhances UV blocking by absorption. The UV shielding performance can be further tuned by changing loading of the nanoparticles to EVA.
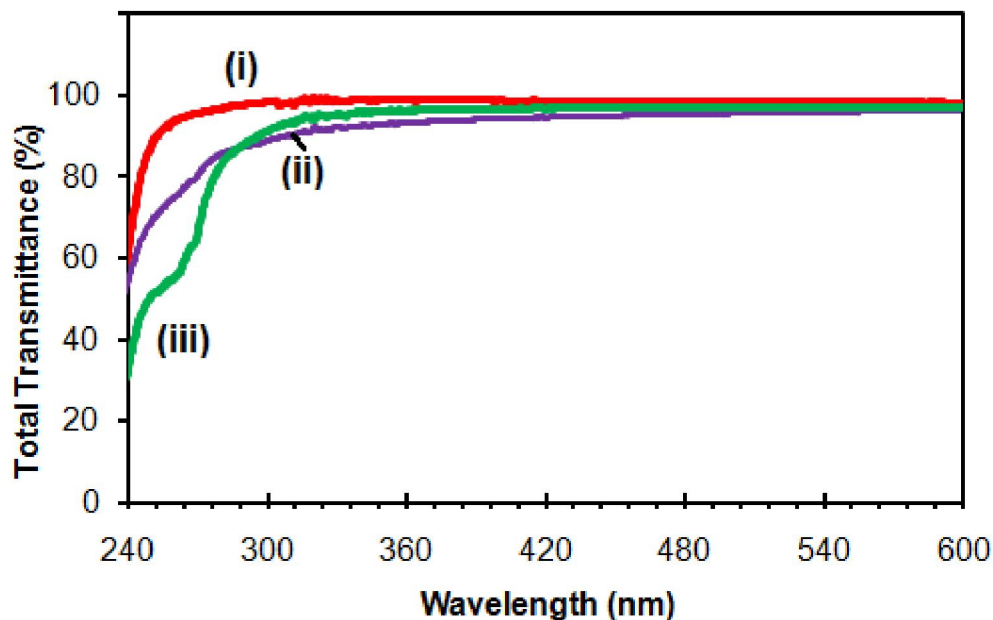
Figure 5.6. Total UV and visible light transmittance of (i) poly(EVA), and EVA nanocomposites grafted with silica encapsulated CdS-ZnS QDs using (ii) one-step, (iii) two-step polymerization process.

5.4   Conclusions

A *grafting from* polymerization of ethylene and vinyl acetate on the functionalized nanoparticles of silica encapsulated CdS-ZnS QDs in supercritical CO_2 was developed. Highly luminescent CdS-ZnS core-shell QDs with 5 nm size were synthesized using a modified approach based on pyrolysis of the single-molecule precursors and capping the CdS core with a thin layer of ZnS. The core-shell QDs were then encapsulated in mesoporous silica through a simple microemulsion method that enhanced both the photoluminescence and photostability of the QDs. Silica surface was functionalized to introduce vinyl groups by using vinyltrimethoxy silane. The functionalization and polymerization were explored both by the one-step (together) and two-step (separately) processes. The silica encapsulated QDs synthesized using by the two-step approach showed excellent compatibility and dispersion throughout the EVA network by TEM and

CLSM analysis. The novel light selective EVA nanocomposites also showed improved optical properties with high UV shielding and visible light transmission.

5.5 Acknowledgements

5.6 References

[1] S. Kango, S. Kalia, A. Celli, J. Njuguna, Y. Habibi, R. Kumar, Surface modification of inorganic nanoparticles for development of organic–inorganic nanocomposites—A review, Progress in Polymer Science, 38 (2013) 1232-1261.

[2] J. Hu, M. Chen, L. Wu, Organic-inorganic nanocomposites synthesized via miniemulsion polymerization, Polymer Chemistry, 2 (2011) 760-772.

[3] I.-Y. Jeon, J.-B. Baek, Nanocomposites derived from polymers and inorganic nanoparticles, Materials, 3 (2010) 3654-3674.

[4] S. Li, M.M. Lin, M.S. Toprak, D.K. Kim, M. Muhammed, Nanocomposites of polymer and inorganic nanoparticles for optical and magnetic applications, Nano Reviews, 1 (2010) 5241-5232.

[5] T. Hanemann, D.V. Szabó, Polymer-nanoparticle composites: from synthesis to modern applications, Materials, 3 (2010) 3468-3517.

[6] C. Lü, B. Yang, High refractive index organic–inorganic nanocomposites: design, synthesis and application, Journal of Materials Chemistry, 19 (2009) 2884-2901.

[7] S. Porel, S. Singh, S.S. Harsha, D.N. Rao, T. Radhakrishnan, Nanoparticle-embedded polymer: in situ synthesis, free-standing films with highly monodisperse silver nanoparticles and optical limiting, Chemistry of Materials, 17 (2005) 9-12.

[8] Y.-J. Kim, J.-H. Kim, S.-W. Ha, D. Kwon, J.-K. Lee, Polyimide nanocomposites with functionalized SiO_2 nanoparticles: enhanced processability, thermal and mechanical properties, RSC Advances, 4 (2014) 43371-43377.

[9] M.A. Mumin, W.Z. Xu, P.A. Charpentier, Quantum dots/silica/polymer nanocomposite films with high visible light transmission and UV shielding properties, Nanotechnology, 26 (2015) 315702-315715.

[10] J.M. Allan, M.A. Mumin, W.Z. Xu, Q. Al Sharari, P.A. Charpentier, Surface functionalized bare and core–shell quantum dots in poly (ethylene-co-vinyl acetate) for light selective nanocomposite films, Solar Energy Materials and Solar Cells, 123 (2014) 30-40.

[11] M.A. Mumin, K.F. Akhter, S. Dresser, S.T. van Dinther, W. Wu, P.A. Charpentier, Multifunctional mesoporous silica nanoparticles in poly (ethylene-co-vinyl acetate) for transparent heat retention films, Journal of Polymer Science Part B: Polymer Physics, 53 (2015) 851-859.

[12] X. Ji, J.E. Hampsey, Q. Hu, J. He, Z. Yang, Y. Lu, Mesoporous silica-reinforced polymer nanocomposites, Chemistry of Materials, 15 (2003) 3656-3662.

[13] L. Wei, N. Hu, Y. Zhang, Synthesis of polymer—mesoporous silica nanocomposites, Materials, 3 (2010) 4066-4079.

[14] E. Martínez-Ferrero, J. Albero, E. Palomares, Materials, nanomorphology, and interfacial charge transfer reactions in quantum dot/polymer solar cell devices, The Journal of Physical Chemistry Letters, 1 (2010) 3039-3045.

[15] A. Hezinger, J. Teßmar, A. Göpferich, Polymer coating of quantum dots–a powerful tool toward diagnostics and sensorics, European Journal of Pharmaceutics and Biopharmaceutics, 68 (2008) 138-152.

[16] W.Z. Xu, P.A. Charpentier, Light-selective nanofilms of quantum dot-poly (ethylene-co-vinyl acetate) synthesized with supercritical CO_2, The Journal of Physical Chemistry C, 113 (2009) 6859-6870.

[17] I. Coropceanu, M.G. Bawendi, Core/shell quantum dot based luminescent solar concentrators with reduced reabsorption and enhanced efficiency, Nano Letters, 14 (2014) 4097-4101.

[18] H. Han, G.D. Francesco, M.M. Maye, Size control and photophysical properties of quantum dots prepared via a novel tunable hydrothermal route, The Journal of Physical Chemistry C, 114 (2010) 19270-19277.

[19] A.P. Alivisatos, W. Gu, C. Larabell, Quantum dots as cellular probes, Annual Review of Biomedical Engineering, 7 (2005) 55-76.

[20] D. Bera, L. Qian, T.-K. Tseng, P.H. Holloway, Quantum dots and their multimodal applications: a review, Materials, 3 (2010) 2260-2345.

[21] A.M. Mumin, J.W. Barrett, G.A. Dekaban, J. Zhang, Dendritic cell internalization of foam-structured fluorescent mesoporous silica nanoparticles, Journal of Colloid and Interface Science, 353 (2011) 156-162.

[22] Q. Zhao, E.T. Samulski, In situ polymerization of poly (methyl methacrylate)/clay nanocomposites in supercritical carbon dioxide, Macromolecules, 38 (2005) 7967-7971.

[23] M.A. Mumin, G. Moula, P.A. Charpentier, Supercritical CO_2 synthesized TiO_2 nanowires covalently linked with core–shell CdS–ZnS quantum dots: enhanced photocatalysis and stability, RSC Advances, 5 (2015) 67767-67779.

[24] K. Matsuyama, Y.-k. Maeda, T. Matsuda, T. Okuyama, H. Muto, Formation of poly (methyl methacrylate)-ZnO nanoparticle quantum dot composites by dispersion polymerization in supercritical CO_2, The Journal of Supercritical Fluids, (2015).

[25] M.R. Mauricio, F.C. Manso, M.H. Kunita, D.S. Velasco, A.C. Bento, E.C. Muniz, G.M. de Carvalho, A.F. Rubira, Synthesis and characterization of ZnO/PET composite using supercritical carbon dioxide impregnation technology, Composites Part A: Applied Science and Manufacturing, 42 (2011) 757-761.

[26] W.Z. Xu, X. Li, P.A. Charpentier, In situ ATR-FT-IR study of the thermal decomposition of diethyl peroxydicarbonate in supercritical carbon dioxide, Polymer, 48 (2007) 1219-1228.

[27] L. Wei, Y. Zhang, Emulsion polymerization of ethylene from mesoporous silica nanoparticles with vinyl functionalized monolayers, Journal of Polymer Science Part A: Polymer Chemistry, 47 (2009) 1393-1402.

[28] S.A. McCarthy, G.-L. Davies, Y.K. Gun'ko, Preparation of multifunctional nanoparticles and their assemblies, Nature Protocols, 7 (2012) 1677-1693.

[29] W.Z. Xu, P.A. Charpentier, FTIR study measuring the monomer reactivity ratios for ethylene− vinyl acetate polymerization in supercritical CO_2, Industrial & Engineering Chemistry Research, 48 (2009) 1384-1390.

[30] Q. Zhang, Z. Ye, S.-T. Wang, J. Yin, Facile one-pot synthesis of PEGylated monodisperse mesoporous silica nanoparticles with controllable particle sizes, Chinese Chemical Letters, 25 (2014) 257-260.

[31] K.R. Williams, Analysis of ethylene-vinyl acetate copolymers: a combined TGA/FTIR experiment, Journal of Chemical Education, 71 (1994) A195.

[32] H.-M. Xiong, X. Zhao, J.-S. Chen, New polymer-inorganic nanocomposites: PEO-ZnO and PEO-ZnO-$LiClO_4$ films, The Journal of Physical Chemistry B, 105 (2001) 10169-10174.

[33] D. Sun, N. Miyatake, H.-J. Sue, Transparent PMMA/ZnO nanocomposite films based on colloidal ZnO quantum dots, Nanotechnology, 18 (2007) 215606-215611.

Chapter 6

Supercritical CO_2 synthesized TiO_2 nanowires covalently linked with core-shell CdS-ZnS quantum dots: enhanced photocatalysis and stability

Abstract

Semiconductor quantum dots (QDs) sensitized onto nano TiO_2 as heterogeneous photocatalysts have drawn considerable interest over the past few years. However, stability of the QDs attached to TiO_2 and consistent photocatalysis are still major challenges of this approach. We describe herein, a facile process to fabricate nanocomposites from porous TiO_2 nanowires and bare CdS and core-shell CdS-ZnS QDs, where the QD particles are linked covalently to the titania surface through a bifunctional organic linker, mercapto propionic acid (MPA). A thin layer of ZnS was grown on 6 nm CdS QDs to restrain the photocorrosion and passivate the trap states, enhancing the photoluminescence and quantum yield. The bifunctional linking molecule, MPA, was found to effectively disperse and stabilize the QD nanoparticles. The photocatalytic activities of the prepared catalysts were evaluated under ultraviolet and visible light solar irradiation for the photodegradation of methylene blue (MB), an organic dye. The decomposition rate of MB was enhanced as follows: CdSZnS-MPA-TiO_2 > CdS-MPA-TiO_2 > CdSZnS-TiO_2 > CdS-TiO_2 > TiO_2 > P25. A maximum photodegradation efficiency of MB dye (~88%) was obtained by core-shell CdS-ZnS QDs linked with nano TiO_2. After 3 cycling tests of degradation, the loss of photoactivity was significantly minimized (from 68% to 10%) by CdSZnS-MPA-TiO_2 compared to CdSZnS-TiO_2 (by direct deposition).

6.1. Introduction

Nanosized titanium dioxide (TiO_2), one of the most promising photocatalysts, has been extensively investigated for several decades in the area of solar cells and photocatalysis [1-3]. TiO_2 has several advantages owing to its low cost, abundance, nontoxicity, good stability, and unique optoelectronic properties [4]. However, due to its wide band gap (3.2 eV), TiO_2 can only be excited by a small UV fraction (less than 6 %) of solar light, making it impractical for use under natural sunlight [5]. The photogenerated

electrons/holes are easily consumed via recombination, resulting in a low quantum yield and poor efficiency in these applications [6].

To break the bottleneck, there have been various attempts to enhance and expand the optical absorption range of TiO_2 and improve the separation efficiency of photogenerated electron-hole pairs. Recently, semiconductor quantum dots (QDs) have been attracting extensive attention to sensitize TiO_2 due to their unique size dependent optoelectronic properties and the possibility of multiexciton generation. A lower band gap QD like CdSe, CdS with higher conduction band (CB) can enhance the electronic conversion efficiency of TiO_2 [7-9]. The photogenerated electrons from the CB of the light activated QD can be injected into the non-activated TiO_2, while the holes remain on the QD particles, leading to efficient and longer charge separation, increased UV absorption, as well as extending the absorption to the visible range [10, 11]. But, uniform deposition and stability of QD particles on TiO_2 is often a problem due to the lack of attachment approaches and poor surface interactions under typical experimental conditions [12]. A favourable link between QDs and TiO_2 nanoparticles can minimize these drawbacks, also enhancing the transfer of electron injection [7, 13].

Recently, intensive efforts have been undertaken to link bare QDs with nano TiO_2 for photocatalysis applications [14-16]. Mostly, long aging time (more than 24 hours) and high temperatures (200 - 400 ^{o}C) are required for improving the coupling of the two semiconductor materials and their crystallinity [17]. In previous works, most attention has been paid to the synthesis and optical properties rather than activity and stability during photodegradation. Possible interactions between porous 1D TiO_2 nanostructures and the effect of the bifunctional linking molecules to core-shell QDs needs to be investigated. Although, it has been reported by many researchers that compared to bare QDs, core-shell structured QDs with a thin shell of a higher band gap element are advantageous and have been shown to enhance photo-physical properties [18-20]. This is attributed to the surface defects in the core acting as temporary 'traps' for the electron, hole or excitons, quenching radiative recombination and reducing the quantum yield (QY) [21]. Notably, CdS is an important photosensitizer of TiO_2 and its size dependent optical properties have also been observed and reported by many researchers [6, 22].

Recently, we have shown that, by forming a thin shell of ZnS on CdS cores, the QY can be improved up to 50%, which is usually less than 20% for bare CdS QDs [23]. The thin shell also minimizes the surface crystal defects and aggregation tendency of CdS, resulting in better particle separation which is very important for the photosensitization of TiO_2 catalyst. Therefore, it is anticipated that by developing a novel facile coupling approach for more quantum efficient and stable core-shell QDs with $nanoTiO_2$ using mild conditions, the activity and stability of the TiO_2 photocatalyst can be improved.

Supercritical CO_2 ($ScCO_2$) has emerged as a viable "green" alternative to hazardous organic solvents, as CO_2 is cheap, non-toxic, non-flammable, and environmentally benign with low critical temperature and pressure (T_c = 31.1 ^{o}C, P_c = 7.38 MPa) [24]. The unique advantages of $scCO_2$ include: (i) a "zero" surface tension, allowing penetration into pores that is not possible with organic solvents, (ii) low gas-like viscosities that enhance mass transfer and reaction kinetics, (iii) a liquid-like density and a gas-like diffusivity, and the solubility of solute is tuneable with both temperature and pressure [25]. We recently reported that TiO_2 nanowires synthesized using a sol-gel method in supercritical carbon dioxide ($scCO_2$) are nano-structured with high specific surface area and porosity, and anatase in nature [25-28]. During sol-gel chemistry, $scCO_2$ has several roles, acting as a solvent, a modification agent, and a cleaning and a drying agent [29].

Structurally, TiO_2 exists in three polymorphs: anatase, rutile, and brookite. It is well accepted that anatase TiO_2 exhibits higher photocatalytic activities than rutile and brookite TiO_2 [30, 31]. The indirect band gap anatase shows a longer charge carrier lifetime to participate in surface reactions compared to direct band gap rutile and brookite TiO_2. Anatase TiO_2 also enhances faster migration of photogenerated electrons and holes from the interior to the surface, resulting in a lower recombination rate for charge carriers [30, 31]. However, the anatase phase is thermodynamically metastable, so synthesis of anatase TiO_2 with better quality including thermal stability is always an important parameter [13]. Compared to TiO_2 nanoparticles, TiO_2 nanowires or nanotubes have been shown to be more effective in solar harvesting applications as their orientation provides excellent percolation pathways for vectorial charge transfer [7]. Thakur et al. observed that the presence of CdS hinders the transformation of anatase to rutile even after

annealing at 600 ^{o}C, attributed to the surface defect sites of anatase particles being occupied by CdS [10]. However, they observed no specific morphology of both CdS and TiO$_2$ nanoparticles and irregular distribution. Therefore, besides the one-dimensional orientation and well crystallized anatase, the strong interactions and uniform distribution of quantum efficient QDs (e.g. core-shell QDs) with TiO$_2$ is still a major challenge that plays a key role to enhance both the activity and stability of the nanocomposite catalysts.

In the present work, highly photoluminescent and monodispersed CdS bare and CdS-ZnS core-shell quantum dots were prepared by using a facile and modified (changing reaction temperature and duration) colloidal synthesis approach. TiO$_2$ nanowires were synthesized in scCO$_2$ using sol-gel polycondensation of Ti-alkoxides and acetic acid. Then, by using a novel facile approach, calcined TiO$_2$ nanowires were functionalized by a commercially available bifunctional linker (mercapto-propionic acid) and covalently attached to bare or core-shell QDs. The photocatalyst samples were characterized in detail and the energy transfer mechanism investigated. Finally, the experimental catalysts were investigated for degradation of methylene blue, an organic dye under UV, visible, and also simulated solar lights and the results compared with bare TiO$_2$ and directly deposited QDs in TiO$_2$.

6.2. Experimental

6.2.1. Materials

All the reagents were used without further purification unless stated otherwise. Instrumental grade CO$_2$ (99.5% purity) was purchased from Praxair. Argon (ultra high purity, 99.9%, PRAXAIR). Titanium isopropoxide (TIP) (97%), glacial acetic acid (99.99%), Cadmium chloride, sodium diethyldithiocarbamate trihydrate, zinc diethyldithiocarbamate (98%), 3-mercaptopropionic acid (>99%), trioctylamine (TOA) (98%,), trioctylphosphine (TOP) (97%), methylene blue (0.05 weight % in water), anhydrous ethanol ($\geq$ 99.5%), methanol ($\geq$ 99.9%), and toluene ($\geq$ 99%) were purchased from Sigma-Aldrich, Canada.

6.2.2. Synthesis of TiO$_2$ nanowires

TiO$_2$ nanowires were synthesized in supercritical carbon dioxide (scCO$_2$) using a sol-gel technique we reported previously [27]. In a typical experiment, 3 mL of TIP and 9 mL of acetic acid were quickly placed in a 25 mL view cell. The cell was closed and CO$_2$ was pumped into the view cell using a syringe pump (Isco 260D). Final temperature and pressure were maintained at 60 $^{\circ}$C and 41.4 MPa respectively. Stirring was stopped after 24 h while allowed for five days of aging for complete reaction. After aging, the formed gel was washed using CO$_2$ at a rate at 0.2 mL min^{-1} for 24 h followed by controlled venting at 0.5 mL min^{-1} to prevent collapse of the solid network. The resulting powder was then calcined at 450 $^{\circ}$C in air (tubular furnace) using a heating rate of 10 $^{\circ}$C min^{-1} for 2 h.

6.2.3. Synthesis of CdS and CdS-ZnS QDs

Both bare (CdS) and core-shell (CdS-ZnS) QDs were prepared by following a single-molecular precursor method reported previously [32, 33]. To formulate the cadmium precursor, Cd[S$_2$CN$(C_2H_5)_2$]$_2$ for QD synthesis, equimolar (0.1 M) aqueous solutions of sodium diethyldithiocarbamate and cadmium chloride were mixed under vigorous stirring. The rapid reaction yielded a white precipitate that was collected using vacuum filtration. Further purification was achieved by washing with distilled water, and then dried in a vacuum oven overnight at 50 $^{\circ}$C. For QD synthesis, in a 250 mL three-necked flask under argon, when the temperature of 50 mL of trioctylamine (TOA) was stable at 235 $^{\circ}$C, a solution of 1 g of Cd[S$_2$CN$(C_2H_5)_2$]$_2$ in 18 mL of trioctylphophine (TOP) was rapidly injected into the flask and continued heating for 20 min. During cooling at approximately 75°C, a large excess of methanol was added followed by separation of the QDs through centrifugation. The nanoparticles were then dispersed into toluene and washed with methanol following by centrifugation for at least 3 times. In the case of

core-shell (CdS-ZnS) QDs, the temperature of TOA was maintained at 220 ^{o}C for 10 min after addition of the cadmium diethyldithiocarbamate solution, then a solution of 0.4 g of $Zn[S_2CN(C_2H_5)_2]_2$ in 6 mL of TOP was slowly added dropwise. After 20 min the reaction mixture was cooled and the product separated and washed by following the same method described for the CdS QDs.

6.2.4. Bifunctional linker coupling

The covalent attachment of CdS and CdS-ZnS QDs to the surface of the TiO_2 nanowires was achieved by using 3-mercaptopropionic acid (MPA), a bifunctional linker. In a 100 mL round bottom flask, 0.25 g of TiO_2 nanowires were introduced in 50 mL of ethanol. After adjusting the pH to 10 by using 0.2M NaOH, 200 µL of MPA was added to the solution and allowed to react for 4 h. The thiolated TiO_2 nanowires, in which strong Ti-O-C bonds are formed as a result of the reaction of the hydroxy groups of the titania surface with the carboxylic acid groups of MPA (Scheme 6.1), were collected as a precipitate. In a subsequent reaction, the functionalized TiO_2 nanowires were dispersed in 60 mL of THF. After adding QD nanoparticles (2, 5, 10, and 20 wt% with respect to TiO_2), the reaction was kept under argon atmosphere at 55°C for 4 h. The resulting composite particles were collected by washing with ethanol and dried in a vacuum oven overnight.

Direct deposition of QDs on TiO_2 was carried out following the previously reported method [7].

6.2.5. Material characterization

X-ray diffraction (XRD) with a Bruker D2 Phaser bench-top X-ray powder diffractometer using Cu Kα radiation (λ for Kα=1.54059 Å) at 30 kV and 10 mA was used to investigate the crystalline structure and chemical composition. Dry powder samples were used with patterns collected in step-scan mode with a small grazing angle of incident X-ray with a 2θ scan range of 10-80 and a step size of 0.25. Transmission electron microscopy (TEM) images were recorded on a Philips CM10 TEM to image the samples to observe their size and shape at 80 kV. The TEM samples were prepared by drop casting ethanol dispersed samples on a copper grid covered with carbon film. Scanning electron microscopy (SEM) was also done by using a LEO(ZEISS) 1540XB FIB/SEM. Samples for SEM imaging were prepared by applying the nanopowder directly to aluminium stubs on carbon adhesion tape. Elemental composition was confirmed and quantified using the energy dispersive X-ray detection (EDX) feature of the SEM. A Shimadzu UV-3600 UV-VIS-NIR spectrophotometer was used to measure the absorption spectrum of the photocatalyst samples and also methylene blue during photocatalytic activity studies. Infrared spectra were collected from 500 to 4000 cm^{-1} using a Nicolet 6700 FTIR spectrometer. The XPS analyses were carried out with a Kratos Axis Ultra spectrometer using a monocromatic Al Kα source (15mA, 14kV).
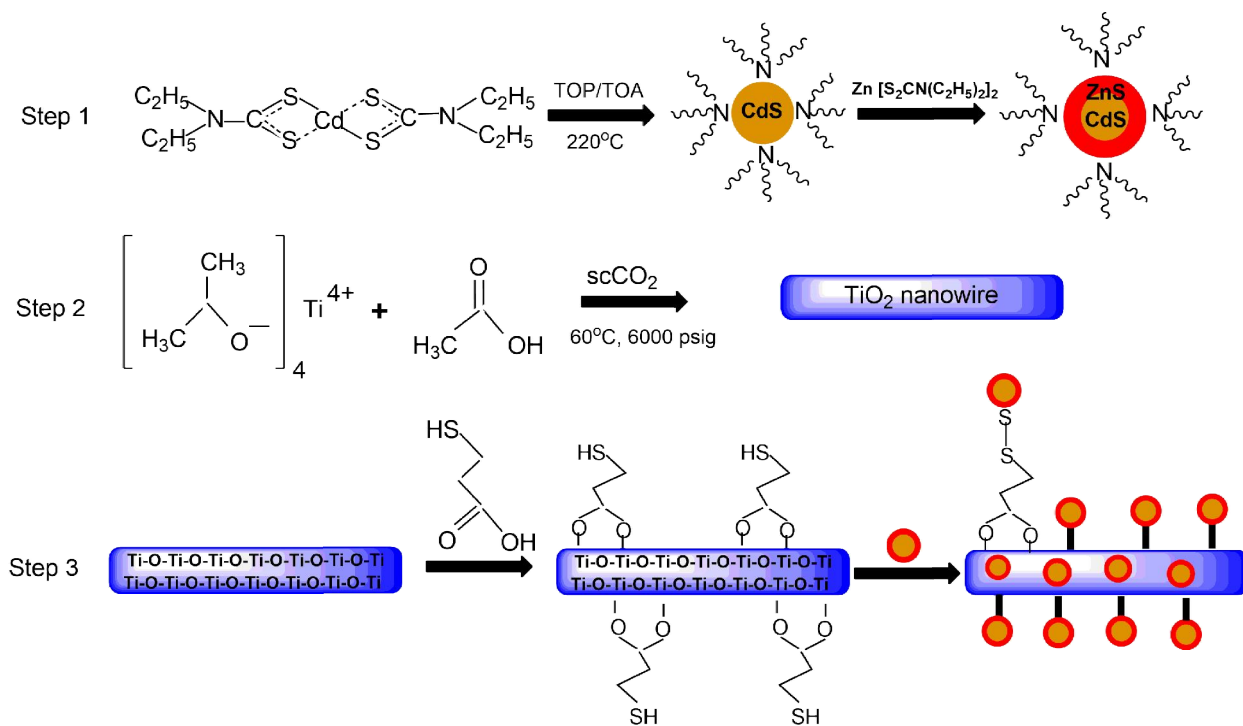
Scheme 6.1. Schematic illustration of (step 1) chemical reactions of bare CdS and core-shell CdS-ZnS QDs from single molecule precursors, (step 2) TiO$_2$ nanowires formation in scCO$_2$ using sol-gel method, and (step 3) functionalization of TiO$_2$ nanowires and covalent linking with QDs.

6.2.6. Photocatalytic activity measurements

Photodegradation of Methylene blue (MB), an organic dye was evaluated for both QDs-linker-TiO$_2$ and QDs-TiO$_2$ samples, under UV and solar irradiation. All experiments were conducted at room temperature in air. Typically, 0.08 g of as-synthesized catalyst was dispersed in 60 mL of MB solution (10 mgL^{-1} in water). For UV illumination, a 125 W high pressure mercury lamp (UVP-Blak-Ray, Model B 100AP) was used that emits UV light (365 and 313 nm). A solar simulator (Model: 69907 Newport) with a 100 W

xenon lamp equipped with an air mass filter and a UV cut-off filter (< 365 nm) provided the visible light source.

Prior to irradiation, the Pyrex beaker containing the dispersion was stored in the dark for 30 min to reach adsorption/desorption equilibrium. At a given time interval, 4 mL aliquots were sampled and centrifuged (6000 rpm, 10 min) to separate the particles. The MB concentration in the aliquots was measured by UV-visible spectrophotometer monitoring the absorption maximum at 664 nm. A calibration plot was established relating the absorbance to the concentrations of MB. In each case, blank experiments were also conducted with the catalysts in the absence of light and MB without the catalysts under light irradiation. Moreover, reference experiments were also performed under the same conditions with commercial TiO_2 (Degussa, P25) and synthesized TiO_2 nanowires.

The photodegradation of MB for CdSZnS-MPA-TiO_2 nanowires was also carried out under simulated sunlight (Model:LZCX1CH1, Luzchem, Canada, 300W Xenon Lamp) without using any UV cut off filter for two intensities, 14 and 28 mWcm^{-2} and variable catalyst loading concentrations. The UV intensity was measured by using a UV A/B meter (Model: ST513, Sper Scientific Ltd). To examine the production of hydroxyl radical (OH$^{\bullet}$) during photocatalytic reaction, a $3x10^{-4}$ M terephthalic acid solution in dilute NaOH solution ($2x10^{-3}$M) was mixed with the experimental photocatalysts under UV light illumination (intensity = 11.05 mWcm^{-2}) [34]. Then the photoluminescence (PL) emission at about 425 nm was observed at different intervals using the excitation wavelength of 315 nm [35].

6.3. Results and discussions

6.3.1. Morphology and structural characteristics

The crystallization or polymorphs of the TiO_2 framework is a key factor for any application that utilizes its semiconductor properties [14]. Crystalline structure and approximate particle size of both types of QDs were determined using XRD analysis. Figure 6.1 presents the XRD patterns of both the bare and core-shell QDs, TiO_2 nanowires, and TiO_2 nanocomposites covalently linked with both the bare and core-shell QDs. The bare CdS QDs show the most intense peaks at 2θ values of 24.2, 25.9, 27.8, 36.2, 43.5, 48, and 51.8, matched perfectly with the (100), (002), (101), (102), (110), (103), and (112) of wurtzite (hexagonal) phase of CdS (ICDD PDF 02-1310) [19].

Splitting to three peaks at angles (2θ degree) 24-30 region represents the formation of hexagonal crystallinity rather than a single broad peak representing the cubic CdS QDs [36]. In the case of CdS-ZnS core-shell QDs, the slight increase of the peaks at 28.2, 43.9, and 52.1 is due to the contribution of the planes (111), (220), and (311) of the zinc-blended ZnS nanocrystals (ICDD PDF 05-0566), which confirms the presence of ZnS with CdS [37]. After core-shell formation, no peak broadening or intensity lowering was observed, which is attributed to the high degree of crystallinity from the presence of the thin ZnS shell, that can preserve the quantum properties of the hexagonal CdS core [38]. Based on the Debye-Scherrer equation, the average particle size for CdS and CdS-ZnS QDs were calculated as 5.5 and 6.2 nm respectively. TiO_2 nanowires (Figure 6.1c) consists of the anatase phase with diffraction peaks at 25.2, 38, 48.2, 54.4, 63.1, 69.3, and 76.6 (JCPDC 21-1272) [14]. No peaks belonging to any other phase of TiO_2 were detected, indicating the high purity of the synthesized products. After low loading (< 5 weight%) of both types of QDs, the XRD patterns displayed rather weak QD peaks that were more prominent in the case of higher loading. Figure 6.1d and e shows bare CdS and core-shell CdS-ZnS QDs (10%) covalently linked with TiO_2 respectively. In both cases, there are additional peaks at 2θ of 28.2, 44, and 52.2, which are attributed to (101), (110), and (112) crystal planes of wurtzite CdS phase and (111), (220), and (311) of the zinc-blended ZnS. The other diffraction peaks of both CdS were not clearly resolved because they overlapped with that of anatase TiO_2. There was no significant change of the anatase TiO_2 peaks after QD loading, resulting from the high crystallinity of the nanocomposite products.
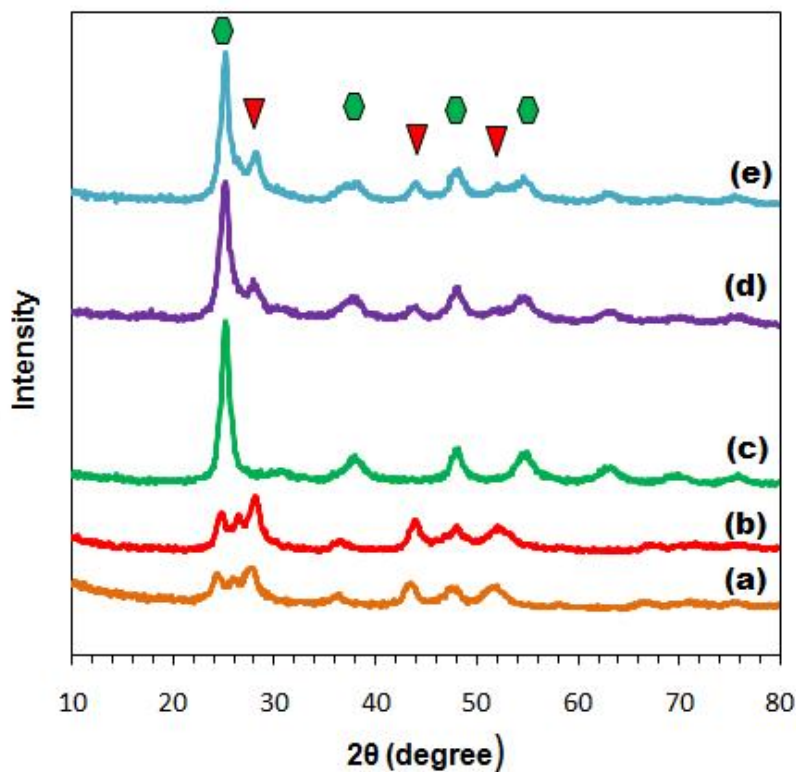
Figure 6.1. Powder X-ray diffraction pattern: (a) CdS QDs of hexagonal wurtzite, (b) CdS-ZnS core-shell QDs, (c) TiO_2 nanowires after calcination, (d) CdS linked with TiO_2 nanowires, and (e) CdS-ZnS linked with TiO_2 nanowires (green marker presents TiO_2 and red marker QDs).

The morphology of both types of QDs were studied using TEM as shown in Figures 6.2 a and b. Both samples were present in a dispersed state, showing formation of individual nanoparticles, although better particle separation was observed after core-shell formation. Here, the thin shell of ZnS minimizes the surface crystal defects and aggregation tendency of CdS. The average particle size was found as 6 ± 1 nm for both bare and core-shell QDs respectively.

As shown in Figure 6.2c, the TEM image reveals that TiO_2 formed nanowires had an average diameter of 50 nm with a smooth surface. Here, the formation of individual nanowires by inhibiting their agglomeration is due to controlled nanowire growth in the absence of surface tension under supercritical CO_2 [39]. In the case of direct deposition

by in situ CdS-ZnS QDs synthesis in the presence of TiO$_2$, QDs were observed agglomerated as seen in Figure 6.2d. There was also a decrease in nanowire length observed because of vigorous stirring under high temperature during pyrolysis of the QD precursor. Whereas when using MPA linker, the aggregation of nanowires was efficiently overcome and the dispersion of QDs on the TiO$_2$ surface was improved, which enhanced the interaction between QDs and TiO$_2$ (Figure 6.2 e and f). This close contact and porous nature of the nanowires is very useful for the electron transfer from QDs to TiO$_2$, which can potentially limit the recombination of photogeneration electrons and holes [40]. With a closer look at these nanowires (Figure 6.2 g and h), the dispersed dark and black spots confirms the QDs are bound to the nanowire surface of the TiO$_2$-QD assembly. The size of these dark spots matches with the size of the CdS and CdS-ZnS QDs. The chemical composition of these spots was further confirmed by SEM-EDX and XPS analysis (described below).
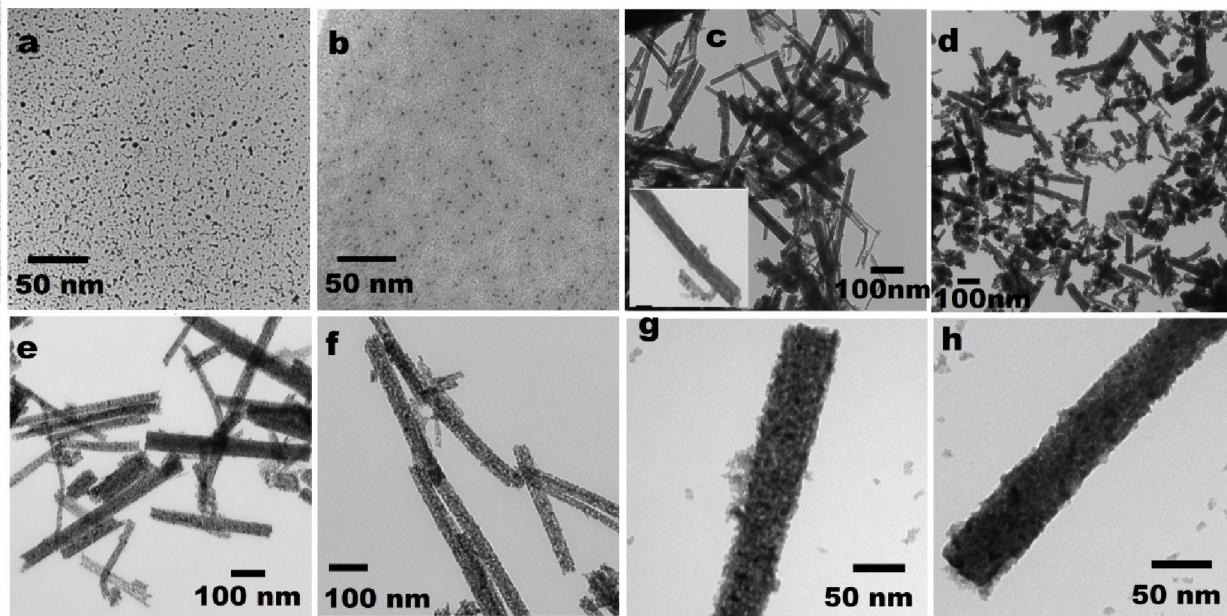
Figure 6.2. Transmission electron microscopy images of (a) CdS QDs, (b) CdS-ZnS QDs, (c) TiO$_2$ nanowires prepared under scCO$_2$, (d) CdS-ZnS direct deposited on TiO$_2$, (e) CdS linked with TiO$_2$, (f) CdS-ZnS linked with TiO$_2$, single TiO$_2$ nanowire after linking with (g) CdS, and (h) CdS-ZnS QDs.

The morphology of the pure TiO_2 and QDs/TiO_2 nanocomposites was also observed by SEM as shown in Figure 6.3. As is apparent from Figure 6.3a, the TiO_2 was formed as nanowires, which are 50 nm in diameter and 2-5 μm in length. The surface of the pure TiO_2 nanowires is relatively smooth. Similar to the TEM results, SEM analysis also shows agglomeration of QDs and TiO_2 in the case of direct deposition (Figure 6.3b). This agglomeration was effectively reduced after linking of both CdS and CdS-ZnS QDs with TiO_2 nanowires (Figure 6.3 c and d). In both cases, the surface became quite rough compared to pure TiO_2. The surfaces were analyzed by SEM-EDX, and the results reveal that all the heteroarchitectures are mainly composed of titanium (Ti), oxygen (O), cadmium (Cd), sulfur (S), and zinc (Zn), confirming that the CdS and CdS-ZnS QD particles were successfully loaded onto the TiO_2 nanowires.
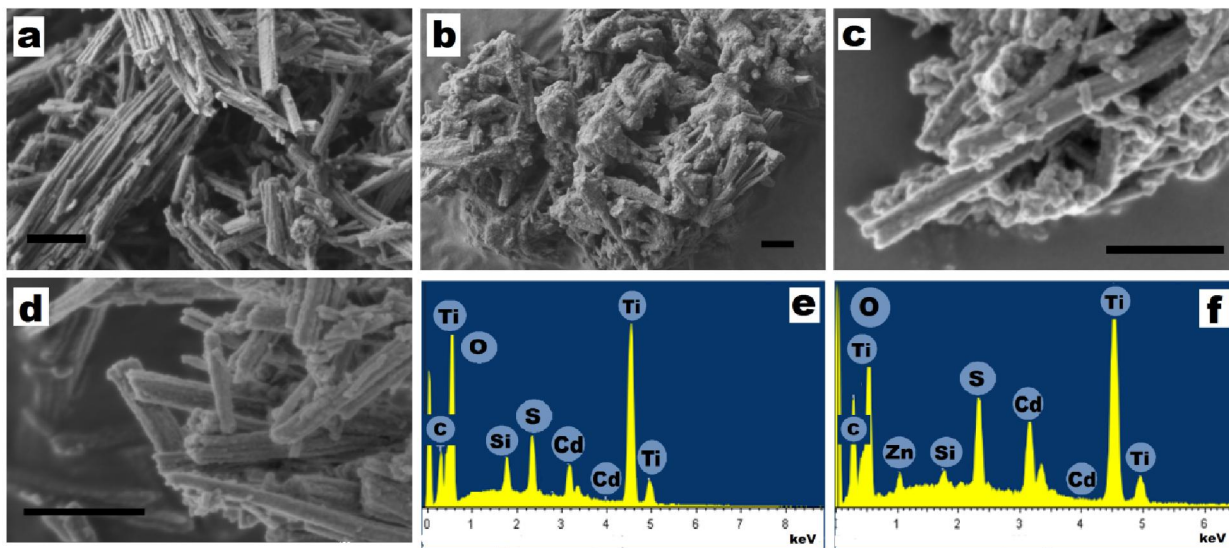
Figure 6.3. Scanning electron microscopy images of (a) TiO_2 nanowires prepared under $scCO_2$, (b) CdS-ZnS direct deposited on TiO_2, (c) CdS linked with TiO_2, (d) CdS-ZnS linked with TiO_2, SEM-EDX elemental analysis of (e) CdS linked with TiO_2, and (f) CdS-ZnS linked with TiO_2 [all scale bars indicate 200 nm]

During the synthesis of core-shell QDs, a TOA/TOP 2:1 ratio was used that was previously found best to form a thin layer on the QD surface, helping to minimize

agglomeration for enhancing optical properties [41]. TOA and TOP are organic and the resulting QDs hydrophobic in nature [42]. In the case of direct deposition, the QDs are less likely to adsorb to the hydrophilic surface of the TiO_2 nanowires. During the photocatalytic reactions and also washing in the case of cyclic operation, there is a possibility of desorption of these directly deposited QDs from the TiO_2 surface.

However, in the presence of mercaptopropionic acid (MPA), the mercapto end easily adsorbs onto the QD surfaces by replacing the initial surface passivation ligands (TOA/TOP). The carboxylic end of the linker binds with the hydrophilic surface of TiO_2 nanowires [42, 43]. Because of the excellent distribution of the QDs on TiO_2 and their better contact (as observed from TEM and SEM analysis), the covalently linked photocatalyst samples are anticipated to show enhanced photocatalytic efficiency than that obtained from direct deposition.

Figure 6.4 shows the FTIR transmission spectra of free MPA (bifunctional linker), calcined TiO_2 nanowires, and CdS-ZnS QDs linked with TiO_2 nanowires. FTIR was employed to examine whether the -COOH group of MPA was chemically linked to the TiO_2 nanowire surface and if the -SH group was chemically bonded to the QD surface. In the case of TiO_2, the band at about 1617 cm^{-1} corresponding to the bending vibration of H-O, and the broad band starting from 900 cm^{-1} is assigned to the stretching of Ti-O-Ti [10]. Free MPA provides strong bands at 1698 and 1424 cm^{-1}, are typical for the asymmetric C=O and symmetric C-O stretching peaks of carboxylate (Figure 6.4a). The 2500-2600 cm^{-1} band corresponds to the -SH group and a broad band in the range 2800-3200 cm^{-1} is attributed to the O-H band of MPA [14]. The FTIR spectra of bare TiO_2 was modified after linking CdS-ZnS QDs through the bifunctional linker MPA, as shown in Figure 6.4b. There are at least three significant changes between free MPA and QDs-MPA-TiO_2; (1) there is no C=O peak for QDs-MPA-TiO_2 at 1698 cm^{-1}, however, at the multiple carboxylate region (1510-1655 cm^{-1}), a well-resolved band at 1584 cm^{-1} is evolved; (2) the broad O-H band of carboxylate at 2800-3200 cm^{-1} is absent for QDs-MPA-TiO_2; (3) there is no -SH group peak at 2500-2600 cm^{-1}. The first two changes provide clear evidence for the attachment of the -COOH group of MPA to the TiO_2

surface, and the third change indicates the absence of the free mercapto groups and the formation of robust bonding between QD and MPA [14].
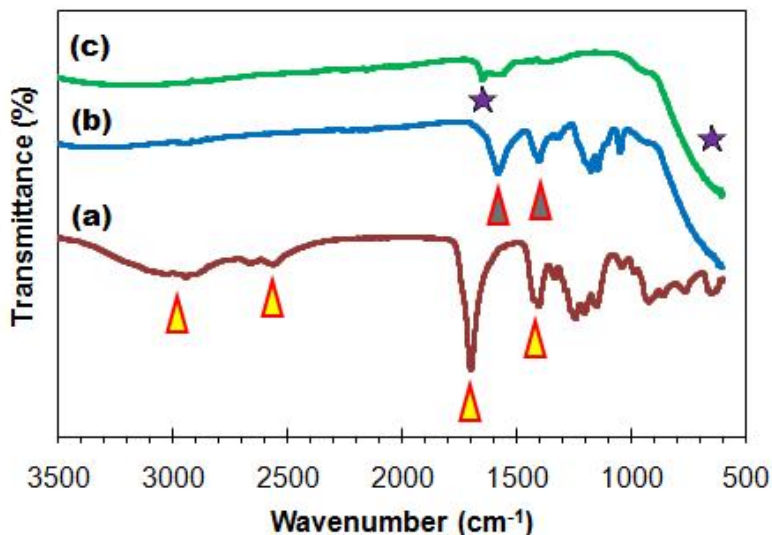
Figure 6.4. FTIR spectra of (a) 3-Mercaptopropionic acid (MPA), (b) CdS-ZnS QDs - MPA-TiO$_2$, and (c) TiO$_2$ nanowires prepared under supercritical CO$_2$ and calcined at 450°C.

XPS was carried out to further investigate QD nanoparticles linking to TiO$_2$, the chemical composition of the nanocomposites and the valence state of various species present therein. The full survey scan over a large energy range at low resolution indicates the presence of Ti, O, and C in TiO$_2$ (Figure 6.5a), and Ti, O, C, Cd, Zn, and S in CdS-ZnS QDs linked with TiO$_2$ (Figure 6.5b). In the high resolution XPS spectra it is clearly seen that, the spin-orbit components (2p$_{3/2}$ and 2p$_{1/2}$) of the Ti 2p peak were deconvoluted into two curves at 454.7 and 460.4 eV, corresponding to Ti^{4+} in a tetragonal structure. The measured separation between these two peaks was 5.7 eV, which is consistent with the binding energy separation observed for stoichiometric TiO$_2$ [6]. After both bare CdS and core-shell CdS-ZnS QDs linking with TiO$_2$, both these peaks exhibited a slight shift due to chemical attachment of QDs with TiO$_2$ through the linker and transferring the electrons from QDs into the TiO$_2$ lattice [29]. However, in both cases the separation of the peaks remained as 5.7 eV, confirming the high quality of TiO$_2$ after QD loading. The

C 1s spectrum exhibits two peaks located at 281.2 and 285.2 eV corresponding to C-H and C-O respectively. For bare TiO_2, hydrocarbon is related to the residual carbon coming from the decomposition of the titanium precursor and some surface contaminants during XPS analysis [44]. But the intensity of the same peak was increased after QD loading because of additional hydrocarbon from the linker molecule. The peak of C-O at 285.2 eV, and absence of any peak for C=O and O-C=O (at 288-290 eV) confirms the successful attachment of the linker with the TiO_2 surface. Similarly, the O 1s shows a major peak at 526.3 eV attributed to crystal lattice oxygen (O_{Ti-O}). There was no peak for surface hydroxyl group (O_{O-H}) at around 530 eV was observed. In the photoelectron spectrum of Cd 3d, the peaks at 401.5 and 408.2 eV are assigned for Cd $3d_{5/2}$ and $3d_{3/2}$ respectively. The spin-orbit separation of these peaks is 6.7 eV, which corresponds to the presence of the oxidation state +2 of Cd at the surface [6]. The S 2p core level spectrum indicates the significant peak at 159 eV corresponding to S^{-2} of QDs. The presence of other peaks at 165.2 eV is due to the formation of S-S bond between the linker and the QDs [37]. The Zn 2p core-level XPS spectrum of CdS-ZnS QDs before and after linked with TiO_2 showed the doublet spectral lines at 1018 eV (Zn $2p_{3/2}$) and 1041 eV (Zn $2p_{1/2}$) with a spin-orbit separation of 23 eV, which corresponds to the Zn^{2+} oxidation state and is in good agreement with the previously published value of ZnS [45]. The results of the XPS measurement, together with FTIR analysis and SEM-EDX measurement suggests that both QDs were successfully loaded and linked with TiO_2 nanowires.
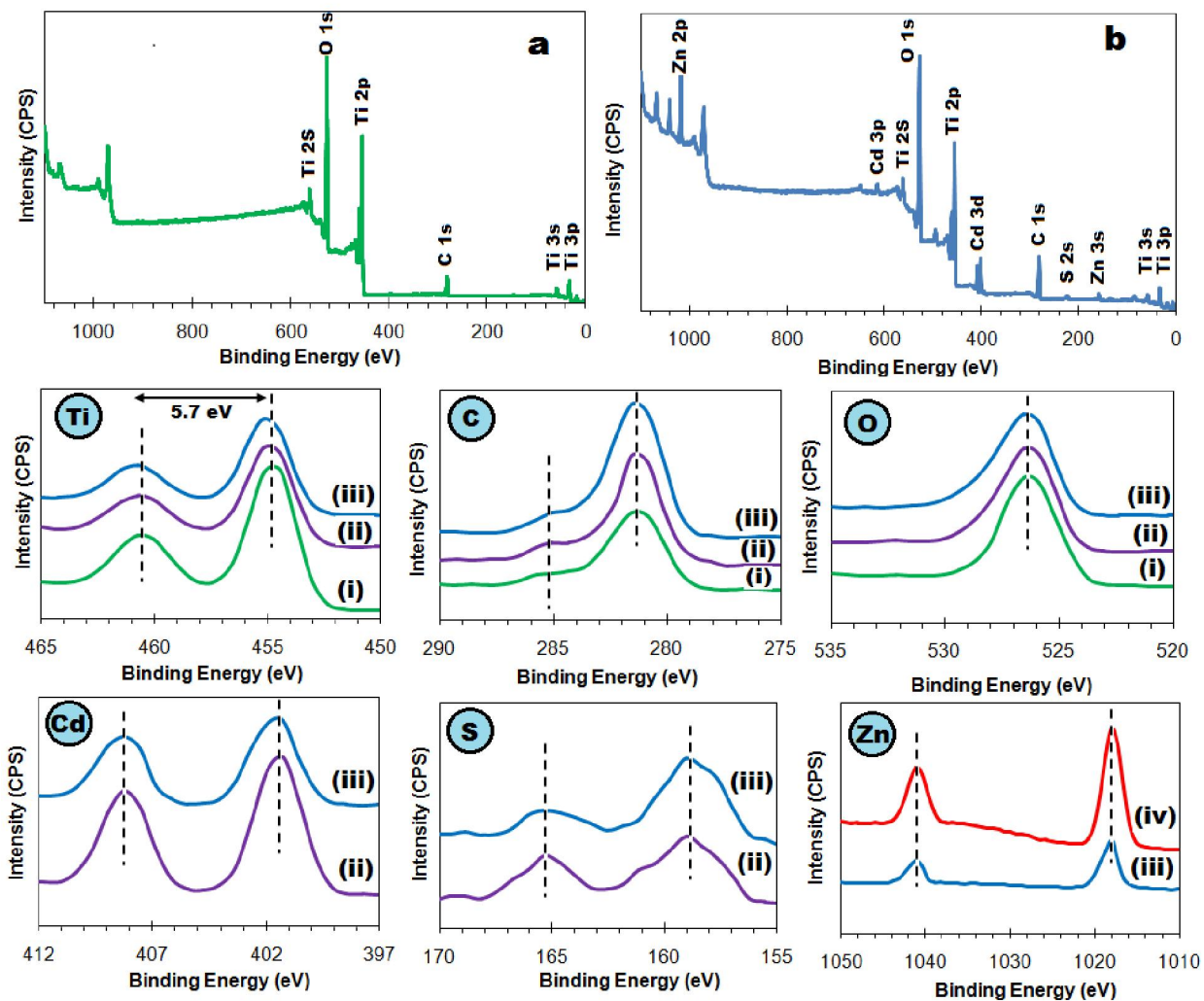
Figure 6.5. X-ray photoelectron spectroscopy (XPS) survey scan of (a) TiO_2 nanowires, (b) CdS-ZnS QDs linked with TiO_2 nanowires; high resolution XPS spectra of the principal elements Ti 2p, C 1s, O1s, Cd 3d, S 2p and Zn 2p for samples (i) TiO_2 nanowires, (ii) CdS QDs linked with TiO_2 nanowires, (iii) CdS-ZnS linked with TiO_2 nanowires, and (iv) CdS-ZnS QDs.

6.3.2 Optical properties

The UV-visible spectrum was examined to evaluate the optical response of TiO_2 nanowires after loading CdS-ZnS QDs, with and without linker, and also changing the concentration of QDs in TiO_2. It can be seen that the bare TiO_2 nanowires exhibit a fundamental sharp absorption edge at approximately 387 nm, with no significant absorption for visible light (Figure 6.6a). The band gap energy was measured by drawing a tangent line on the edge of the spectra to determine the cut off wavelength at y=0 [4]. The band gap energy for the bare TiO_2 was estimated as 3.2 eV, that matches with pure anatase TiO_2 [39]. CdS-ZnS QDs showed a broad and continuous excitation spectrum in the UV range and lower wavelength visible range with corresponding absorption edges at 510 nm and a band gap energy 2.5 eV, as shown in Figure 6.6a (line iv). TiO_2 nanowires loaded with CdS-ZnS QDs exhibit enhanced and broad absorption both in the UV and visible regions, indicating the effective combination of the absorption properties of TiO_2 and QDs in the UV region and QDs in the visible region. There was a blue shift of the absorption edge observed in the case of nanocomposites prepared using MPA linker compared to that for nanocomposites without linker (direct deposition). The reason behind this blue shift is the attachment of CdS-ZnS QDs onto the TiO_2 surface via the studied linker molecule [46]. A similar blue shift has also been observed for a similar linker for other types of QDs [14], Si-O-Cd covalent linkage in $CdS-SiO_2$ [47], and Ti-O-C bonding in TiO_2 with graphene [29]. The composites using a linker exhibited much stronger light absorbance in the visible range than those prepared by direct deposition. This higher absorption is attributed to both the excellent dispersion of CdS-ZnS QDs onto the TiO_2 surface and the strong covalent linkage between QDs and TiO_2 [39].

As shown in Figure 6.6b, the absorption intensity in the region 400-510 nm was increased with the increase of CdS-ZnS QDs linking to TiO_2. For the lower loading (< 5%), there was only a small change in the intensity, however in the case of 10% loading a stronger absorbance was observed in that region. With a further increase of QD loading, there was no significant change in the intensity, which can be attributed to the aggregation of QDs that causes non-radiative light emission, and also the crystal growth of QDs, leading to poor photo-sensitization [39]. It was also observed that with more than 10% loading,

TiO$_2$ loses its hydrophilicity nature, which will reduce the dispersion ability of those nanocatalysts in the aqueous solution of organic dye/pollutants during the photocatalytic activity study.

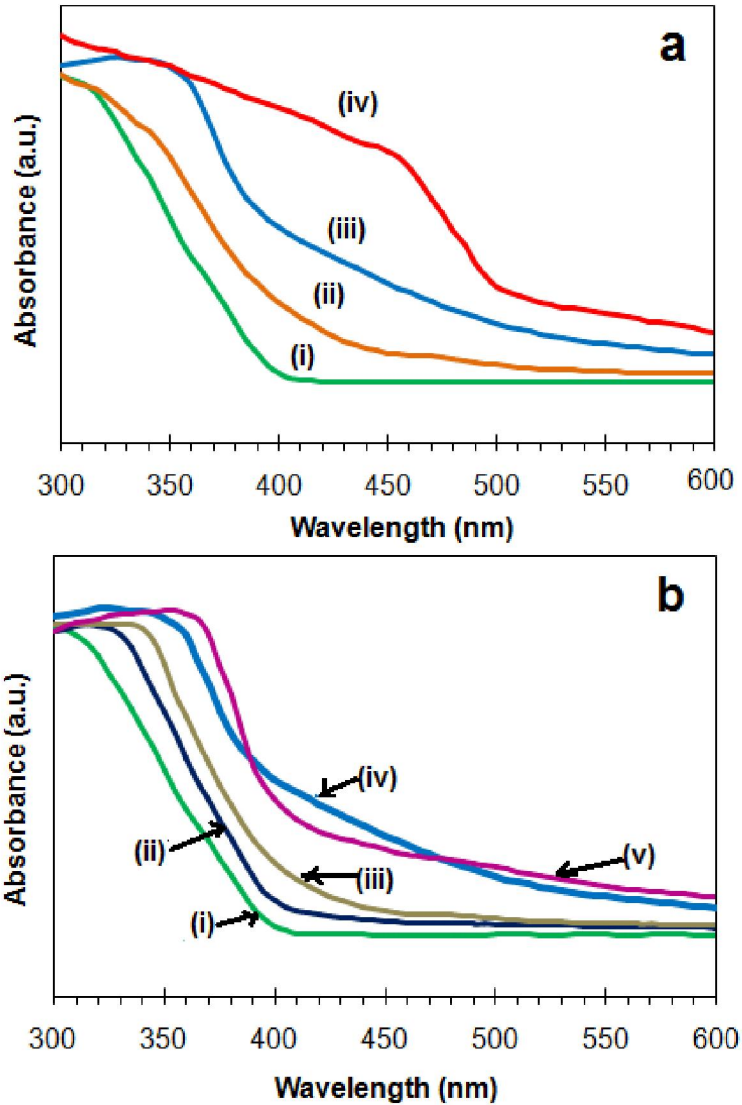Figure 6.6. UV-Vis absorption spectra of: (a) effect of linker: (i) TiO$_2$ nanowires synthesized under supercritical CO$_2$, (ii) CdS-ZnS QDs loaded TiO$_2$ via direct deposition, (iii) CdS-ZnS QDs loaded TiO$_2$ via linker, (iv) CdS-ZnS QDs; (b) effect of loading concentration: (i) TiO$_2$ nanowires, and CdS-ZnS QDs loaded TiO$_2$ via linker with QDs loading (weight %): (ii) 2%, (iii) 5%, (iv) 10%, and (v) 20%.

Although aqueous synthesis of QDs is convenient, the quality and stability of the QDs are better when synthesized in organic solution [42]. TOA/TOP capped QDs remain highly dispersible in organic solvents such as toluene and chloroform, and a stable photoluminescence was observed after two months for the samples kept under dark and at room temperature (data not shown). We have previously reported that, compared to a fluorescent dye, CdS QDs can minimizes photobleaching by 70% under continuous exposure of excited UV light [32]. In addition, a thin layer of ZnS on the CdS QDs further enhances the photostability, as the ZnS shell suppresses the photochemical degradation of CdS, protecting the exciton wavefunction from nonradiative recombination processes as surface traps [48]. When the QDs are attached with a linker or ligand, the optical properties and stability are often improved [33]. Therefore, it is anticipated that linking with MPA and loaded onto TiO_2 nanowires enhances the photostability of both the core CdS and core-shell CdS-ZnS QDs.

6.3.3 Photocatalytic performance

Photocatalytic activities of the CdS/TiO_2 and $CdS-ZnS/TiO_2$ heteroarchitectures with different amounts of QDs, with and without linker, and bare TiO_2 nanowires were verified through investigating the photo-degradation of methylene blue (MB) in aqueous solution under both UV and visible light irradiation. A decrease in sample absorbance at maximum wavelength for MB (664 nm) indicates degradation of MB. Both the blank experiments (i) with photocatalyst in the absence of irradiation and (ii) without photocatalyst in the presence of irradiation, were carried out to rationalize the photocatalytic activity of the synthesized photocatalysts. The degradation efficiency of the experimental photocatalysts was defined as *C/Co*, where *Co* is the initial concentration of MB after equilibrium adsorption, and *C* is the concentration at defined intervals during the experiment. Blank experimental results showed that MB could not be decomposed under dark even in the presence of the photocatalyst (Figure 6.7 b and c). The degradation of MB under light in the absence of photocatalysts is much slower, so that the impact of self-degradation could be ignored. Under UV irradiation as shown in

Figure 6.7b, the synthesized TiO$_2$ nanowires with and without loading of both CdS and CdS-ZnS QDs showed strong degradation efficiency. This is because both the TiO$_2$ and QDs exhibit very high absorption in the UV region as shown earlier (Figure 6.6). The degradation efficiency of the TiO$_2$ nanowires was more than 50% after the first 40 min, that was increased after QDs loading. The QD nanoparticles loaded on the TiO$_2$ nanowires act as the separation centres of electrons and holes, thereby improving the photocatalytic efficiency [6]. Compared to the direct deposition, covalent linking of QDs onto TiO$_2$ nanowires showed better efficiency because of excellent distribution of the QDs on TiO$_2$ and superior contact between them as observed from SEM and TEM analysis (Figure 6.2 and 6.3).

Between bare CdS and core-shell CdS-ZnS QDs, core-shell QDs linked on TiO$_2$ nanowires showed higher efficiency (88% compared to 64% in first 40 min). We previously reported that the thin ZnS shell helps to minimize any surface crystal defects and decrease the aggregation tendency of the bare CdS QDs, providing uniform dispersion and increasing the quantum yield from 25% to 48% [23]. In contrast, under artificial solar irradiation (> 365 nm), bare TiO$_2$ exhibited a very small activity up to 15% photo-degradation of MB (Figure 6.7b), mainly because of the absorption in the region 365-400nm. CdS-ZnS QDs-MPA-TiO$_2$ showed the highest MB decomposition under both visible and UV irradiation. After 180 min, 85% of MB was degraded with this photocatalyst, whereas 70 and 59% was decomposed by CdS-MPA-TiO$_2$ and CdSZnS-TiO$_2$ respectively. This result shows that both the UV and visible light induced catalytic efficiency of TiO$_2$ nanowires was significantly enhanced by QDs linking, especially core-shell QDs than bare QDs.
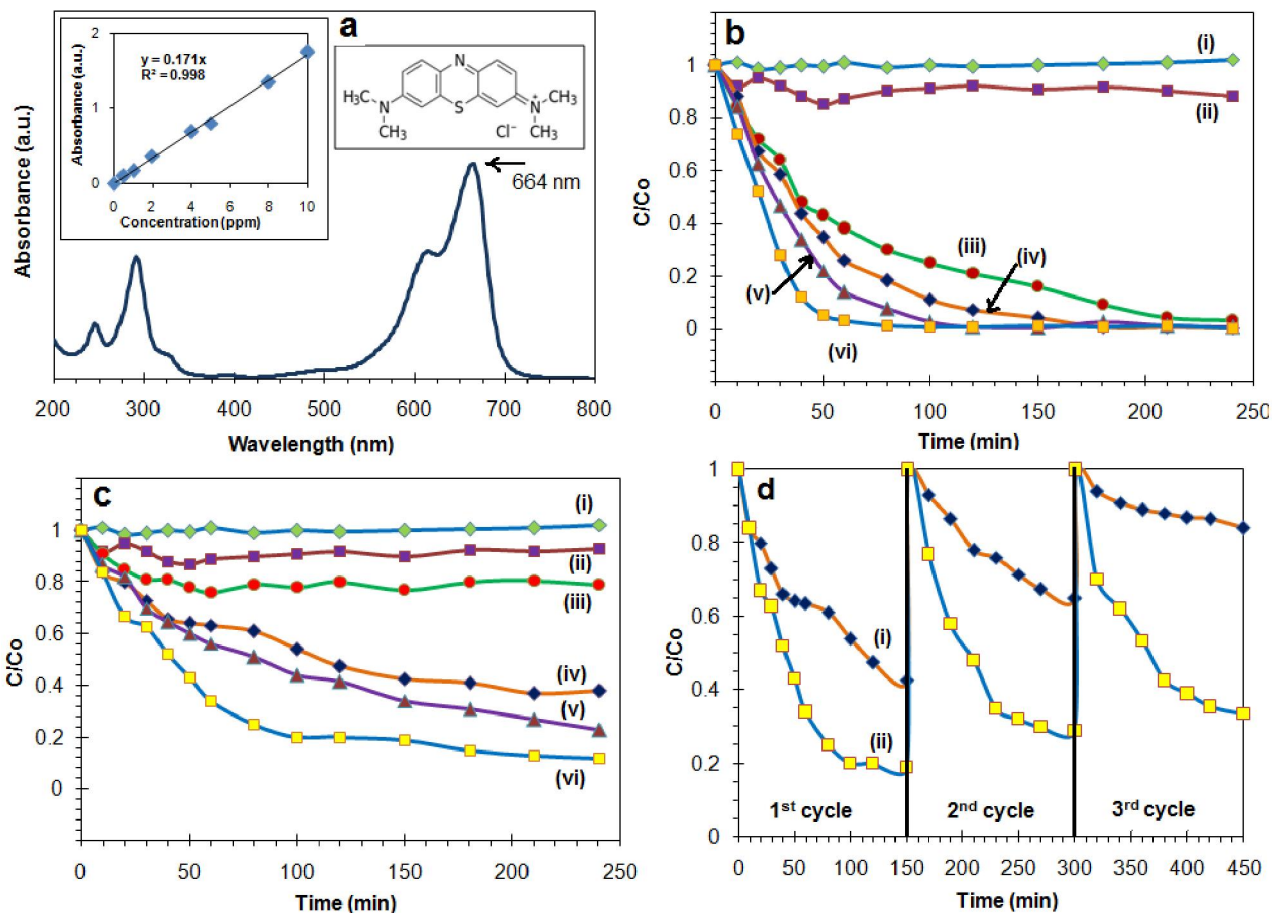
Figure 6.7. (a) UV-visible absorption spectrum, calibration curve, and molecular structure of methylene blue (MB) dye; photocatalytic degradation of MB under (b) UV only, (c) visible solar irradiation (>365 nm), in both cases (i) CdSZnS-MPA-TiO$_2$ + MB under dark, (ii) MB under irradiation, (iii) TiO$_2$ + MB, (iv) direct deposited CdSZnS-TiO$_2$ + MB, (v) CdS-MPA-TiO$_2$ + MB, (vi) CdSZnS-MPA-TiO$_2$ + MB; (d) cyclic runs in the photodegradation of MB using (i) direct deposited CdSZnS-TiO$_2$, (ii) CdSZnS-MPA-TiO$_2$ [QDs loading on TiO$_2$ =10%].

In addition, the synthesized nanocomposite catalysts can be recycled and reused several times without a significant loss of efficiency, which is a key requirement for large scale application [49]. In the case of direct deposited CdS-ZnS QDs onto TiO$_2$ nanowires, after the first cycle there was more than 50% decomposition of MB observed, whereas this

157

efficiency decreased significantly after the second and third cycles to 35 and 16 % respectively. This reduction of efficiency is attributed to detachment of QDs from TiO_2 surfaces during photocatalytic reaction and washing. In contrast, the covalently attached CdS-ZnS QDs on TiO_2 nanowires showed only 10% lowering of efficiency after the first cycle, and any further decrease is negligible after the second cycle. Therefore, the core-shell QDs linked with TiO_2 nanowires not only exhibits very good photocatalytic activity but also high stability. Similar observations have been reported earlier for CdS linked with TiO_2 nanofibers [14], CdS-graphene-TiO_2 nanotubes [50] and graphene modified nano-Ag_3PO_4 [51].

For a better comparison of the photocatalytic activities of the experimental samples with different loading concentration of both types of QDs, the reaction kinetics were calculated based on Langmuir-Hinshelwiid model, which can be expressed as [4];

$$-\frac{dC}{dt} = k_t \frac{K_a C}{1 + K_a C} \tag{6.1}$$

where ($-dC/dt$) is the degradation rate of MB, C is the concentration of MB in the solution at a reaction time of t, k_t is the reaction rate constant, and K_a is the adsorption coefficient of the reactant. $K_a C$ is negligible when the initial concentration of MB is very low. As a result equation (6.1) can be described as pseudo-first order kinetics. Setting equation (6.1) at the initial conditions, when $t=0$, $C=C_0$, it can described as;

$$ln\frac{C}{C_0} = -k_{app}t \tag{6.2}$$

where k_{app} is the apparent rate constant, that can be obtained from the plot of the experimental data.

Table 6.1. Apparent rate constants for the degradation of methylene blue (MB) with synthesized TiO_2 nanowires direct deposition and linking with different loading of bare and core-shell QDs.

Photocatalysts	k_{app} (min^{-1}) (UV)	k_{app} (min^{-1}) (visible)
TiO_2 nanowire	0.017	0.002
CdSZnS-MPA-TiO_2 2%	0.016	0.006
CdSZnS-MPA-TiO_2 5%	0.034	0.011
CdSZnS-MPA-TiO_2 10%	0.052	0.016
CdSZnS-MPA-TiO_2 20%	0.041	0.013
CdS-MPA-TiO_2 10%	0.027	0.009
CdSZnS-TiO_2 Direct deposition	0.020	0.007

Photocatalytic degradation of dyes generally follows pseudo-first order kinetics [52]. The apparent rate constant of different experimental photocatalysts for the fixed initial dye concentration and catalyst concentration are indicated in Table 6.1. For the bare TiO_2 nanowire, the value of k_{app} was minimum both under UV (0.017 min^{-1}) and visible (0.002 min^{-1}) lights. However, after QD loading, a significant enhancement of the k_{app} value was observed especially under visible solar irradiation. It was observed that the photocatalytic activity is governed by QD loading onto TiO_2 nanowires and also the mode of attachment between QDs and TiO_2. The results show that the rate of dye degradation increases with an increase of QD loading from 2 to 10%. In explanation, QDs produce more OH$^{\bullet}$ radicals, which are active oxidative species causing photodegradation of MB. At the same time, the QDs increase UV absorption, as well as extending the absorption to the visible range, while also helping to separate electrons and holes, thereby improving photodegradation of MB. Higher levels of loading favour the recombination of electrons and holes, leading to a lowering of photocatalytic efficiency [6]. According to the experimental kinetic data, 10% loading of CdS-ZnS QDs linked with TiO_2 nanowires exhibited the highest efficiency for MB degradation. Further increasing of QD loading causes aggregation of QDs as described earlier, leading to poor optical properties and photo-sensitization. The apparent kinetic rate constant was also increased in the case of QDs linked with TiO_2 compared to those prepared by direct deposition. The reason behind this, the linker molecule efficiently helps to overcome the aggregation of

nanowires, improving the dispersion of QDs on TiO_2, resulting in enhanced interaction between QDs and TiO_2 as shown earlier by SEM and TEM analysis.

Instead of using direct sunlight due to the large variation of UV levels [53], the photocatalytic degradation of dyes was investigated under simulated solar light (without using a UV cut off filter) for two intensities 14 and 28 mW cm^{-2} and variable catalyst loading concentrations. These results were then compared with the photocatalytic efficiencies observed under UV and visible light separately. Under both intensities, MB dyes did not show any degradation in the absence of the photocatalyst (Figure 6.8a). The results show that the UV intensity of solar light plays an important role in the degradation of MB. At 28 mW cm^{-2} for 1.2g L^{-1} catalyst loading, MB was decomposed completely within one hour. Increasing the UV intensity provides more energy to excite the electrons of TiO_2 and QDs, creating more electron-hole pairs and also producing more $OH^{\bullet}$ radicals, thus enhances the photocatalytic process [52]. The rate constant and half life at 14 mW cm^{-2} were calculated as 0.024 min^{-1} and 28.87 min respectively (Figure 6.8b). The half life under only UV and visible light were 13.3 and 43.3 min respectively. It is observed that compared to only visible light, the rate constant of the degradation reaction was relatively higher and the half life of the reaction was less under simulated sunlight, which leads to the faster degradation of MB under sunlight.

In the case of photodegradation of MB under UV and visible only light, a higher catalyst loading concentration (1.2 g L^{-1}) was used for faster photodegradation, as the increasing catalyst concentration will provide more active sites. For anatase TiO_2 catalyst, a critical catalyst loading of 2 g L^{-1} has been described [54]. At a concentration lower than this value, k_{app} increases with increasing catalyst concentration. Some research groups have reported catalyst loading concentrations of 1.2 g L^{-1} or higher for the decomposition of similar initial concentration of dyes [39, 51, 55]. In addition, the photocatalytic degradation of MB was also studied with changing catalyst (CdSZnS-MPA-TiO_2 nanowires) loading concentration under stimulated solar light as shown in Figure 6.8b. For the lowest concentration (0.3 g L^{-1}), the apparent rate concentration was 0.012 min^{-1}, and 70% of dye was decomposed in the first 2 hours. By further increasing the concentration to 0.6 g L^{-1}, 100% dye decomposition was observed in the first 2 hours

with a k_{app} 0.033 min^{-1}. For the highest dosage 1.2 g L^{-1}, the decomposition was very fast with a rate constant 0.047 min^{-1}. In considering the process economy, 0.6 g L^{-1} would be an optimum loading concentration as it shows a high photocatalytic degradation of MB dye in a reasonable time period.
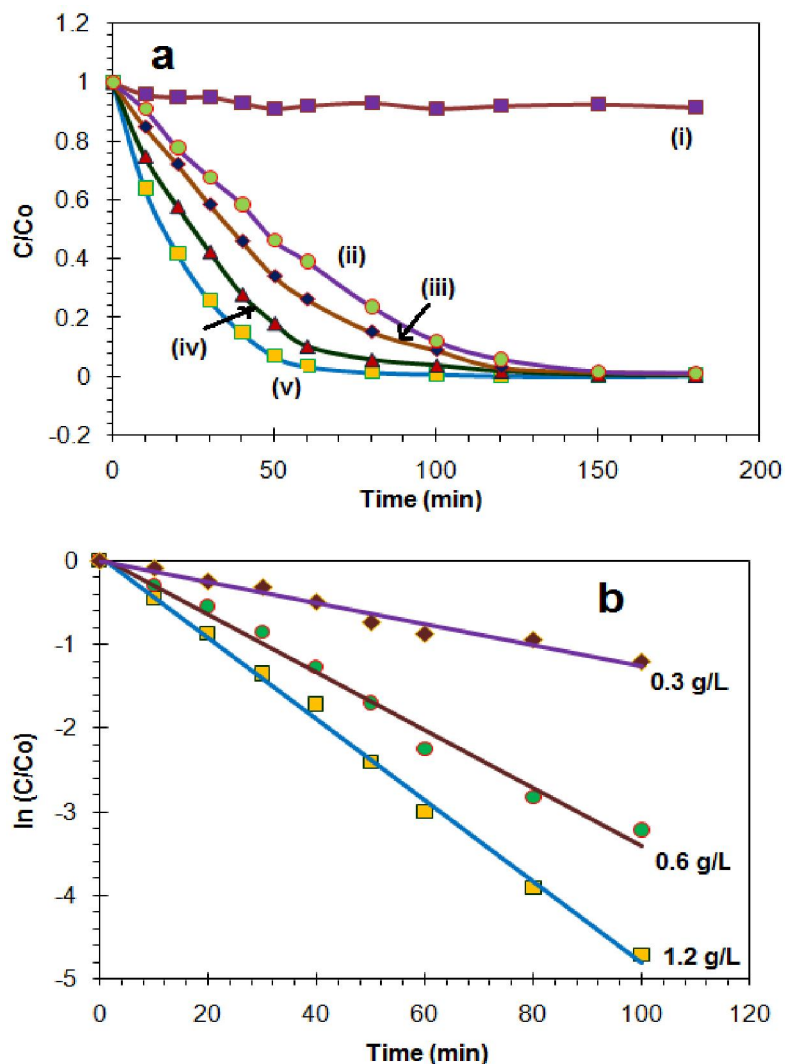
Figure 6.8. Photocatalytic degradation of methylene blue (MB) dye by CdSZnS-MPA-TiO$_2$ nanowires under simulated solar lights (without cut off filter) and the effect of UV intensity and catalyst dosage; (a) photocatalytic activity; (i) MB only at 28 mW cm^{-2}, (ii) 14 mW cm^{-2}, 0.6 g L^{-1}, (iii) 14 mW cm^{-2},1.2 g L^{-1}, (iv) 28 mW cm^{-2}, 0.6 g L^{-1}, (v) 28 mW cm^{-2}, 1.2 g L^{-1} ; (b) ln(C/Co) as a function of the irradiation time for changing catalyst loading concentration of CdSZnS-MPA-TiO$_2$ nanowires [initial MB concentration: 10 mg L^{-1}].

Figure 6.9 provides the OH$^{\bullet}$ production by the experimental photocatalyst (CdSZnS-MPA-TiO$_2$ nanowires) with terephthalic acid as a fluorescent probe. No peak was observed in the absence of light or photocatalyst samples. But in the presence of light, a gradual increase in PL intensity at about 425 nm was observed with increasing irradiation time (from 5 to 30 min). This has been shown to be from the formation of highly fluorescent product, 2-hydroxyterephthalic acid from the reaction of terephthalic acid and OH$^{\bullet}$ [51, 56]. Higher intensities indicate higher amounts of OH$^{\bullet}$ production, which is the major species responsible for the photocatalytic degradation of MB.
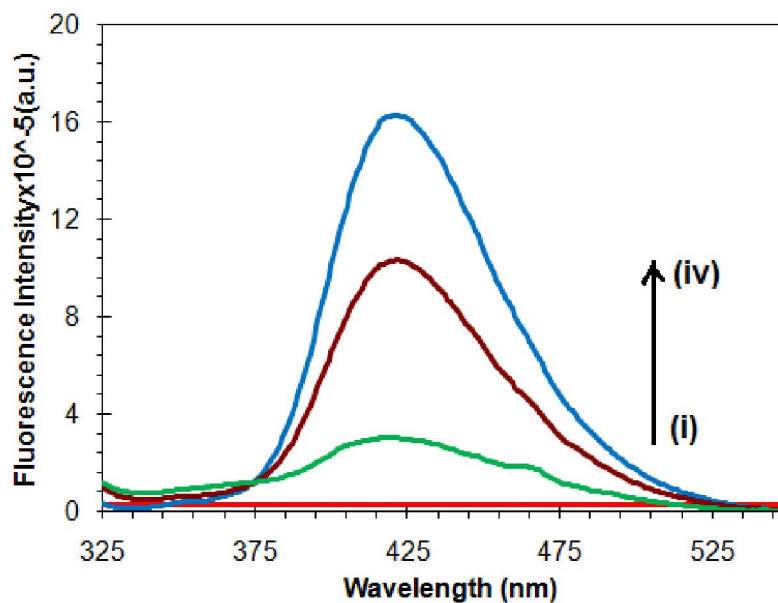
Figure 6.9. Photoluminescence spectral changes observed during UV irradiation of the CdSZnS-MPA-TiO$_2$ in a basic solution of terephthalic acid at (i) before irradiation, (ii) 5 min, (iii) 15 min, (iii) 30 min (excitation wavelength 315 nm).

A proposed mechanism of excitation and charge transfer process between the core-shell CdS-ZnS QDs and TiO$_2$ is shown in Figure 5.10. In this work, we fabricated CdS-ZnS QDs for broad absorption and efficient carrier extraction in TiO$_2$ assemblies. Due to the position of the conduction band (CB) and valence band (VB) of both QDs, the optimal

CB and VB edges are located in the core CdS QDs. The electron-hole recombination rate is much slower in the core-shell QDs than that of the core QDs because of instability of the core [57]. As the CB edge of TiO_2 is more positive than this optimal CB of the core-shell QDs, the photogenerated electrons are transferred to the CB of TiO_2, leading to a higher concentration of electrons. Meanwhile, the hole generated on the optimal VB of QDs remains instead of being transferred to the VB of TiO_2, as this optimal VB is more cathodic than that of TiO_2 [58].
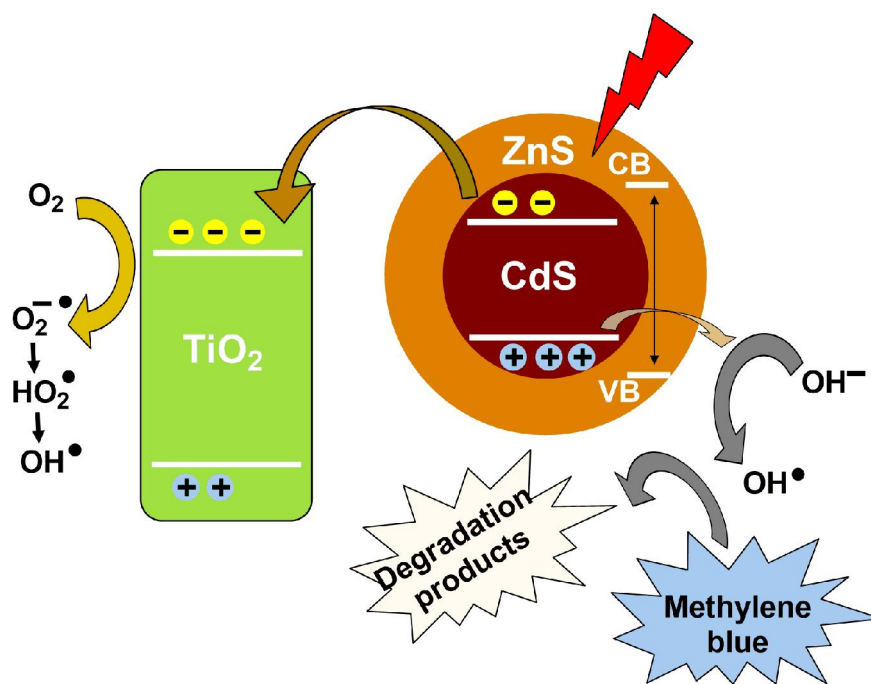
Figure 6.10. Schematic description of the charge transfer and separation between CdS-ZnS and TiO_2 in the CdS-ZnS QDs linked with TiO_2 nanowires under visible irradiation.

The electrons (e^-) accumulated at the CB of TiO_2 are scavenged by dissolved oxygen molecules in water to yield superoxide radial anions ($O_2^{-\bullet}$) (equation 6.4), yielding hydroperoxy radicals $HO_2^\bullet$ on protonation (equation 6.6), and finally hydroxyl radicals $OH^\bullet$ (equation 6.7). During this reaction, H_2O_2 is also formed which can be further reduced to $OH^\bullet$ (equation 6.8). Meanwhile, the holes on the optimal VB of the core-shell

QDs can potentially react with surface hydroxyl groups or physisorbed water molecules to form OH˙ radicals (equation 6.5). The highly reactive OH˙ radicals are strong oxidising agents which can decompose organic pollutants [46, 47]. The proposed mechanism illustrated in Figure 6.10 can be summarized as the following equations:

$$(CdSZnS - TiO_2) + h\vartheta \rightarrow TiO_2(e_{CB}^-) + CdSZnS(h_{VB}^+) \qquad (6.3)$$

$$TiO_2(e_{CB}^-) + O_2 \rightarrow TiO_2 + O_2^{-\blacksquare} \qquad (6.4)$$

$$CdSZnS(h_{VB}^+) + OH^- \rightarrow CdSZnS + OH^{\blacksquare} \qquad (6.5)$$

$$O_2^{-\blacksquare} + H_2O \rightarrow HO_2^{\blacksquare} + OH^- \qquad (6.6)$$

$$HO_2^{\blacksquare} + H_2O \rightarrow OH^{\blacksquare} + H_2O_2 \qquad (6.7)$$

$$H_2O_2 \rightarrow 2OH^{\blacksquare} \qquad (6.8)$$

$$Methylene\ blue + OH^{\blacksquare} \rightarrow Degradation\ products \qquad (6.9)$$
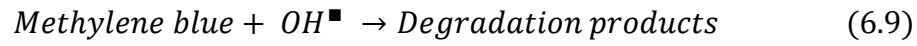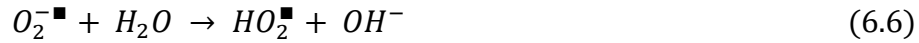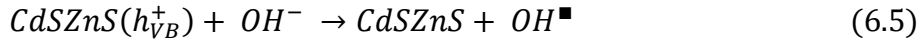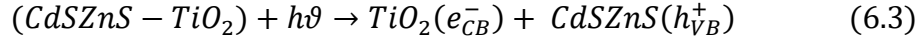
6.4. Conclusions

A new methodology was developed to efficiently link core-shell CdS-ZnS QDs to porous TiO_2 nanowires by using an abundant bifunctional linker, MPA. The core-shell QDs were synthesized based on pyrolysis of a single-molecule precursor method. The thin layer of ZnS grown on CdS core, inhibits the photocorrosion and passivates the trap states on CdS QDs, enhancing the photoluminescence and quantum yield. High quality anatase TiO_2 nanowires were prepared using a sol-gel technique in $scCO_2$. The morphology and distribution of QDs on the TiO_2 surface was confirmed by XRD, TEM, SEM, and XPS. The FTIR and XPS results also confirmed the successful linking between QDs and TiO_2. UV-visible absorption analysis showed that strong interactions using the linked QDs and loading concentration played a key role to enhance lower wavelength visible light absorption of TiO_2 nanowires. CdS-ZnS QDs linked with TiO_2 showed the highest

activity for photodecomposition of methylene blue with 10% QD loading. This study also showed that core-shell structure of QDs and covalent linking is important for both activity and stability of heterogeneous photocatalysts. This novel semiconducting heterojunction nanocatalyst with high photocatalytic activity and stability can be potentially applicable for removing undesirable organics from the environment.

6.5. Acknowledgements

6.6. References

[1] R. Daghrir, P. Drogui, D. Robert, Modified TiO_2 for environmental photocatalytic applications: a review, Industrial & Engineering Chemistry Research, 52 (2013) 3581-3599.

[2] S.G. Kumar, L.G. Devi, Review on modified TiO_2 photocatalysis under UV/visible light: selected results and related mechanisms on interfacial charge carrier transfer dynamics, The Journal of Physical Chemistry A, 115 (2011) 13211-13241.

[3] P. Roy, D. Kim, K. Lee, E. Spiecker, P. Schmuki, TiO_2 nanotubes and their application in dye-sensitized solar cells, Nanoscale, 2 (2010) 45-59.

[4] N. Farhangi, R.R. Chowdhury, Y. Medina-Gonzalez, M.B. Ray, P.A. Charpentier, Visible light active Fe doped TiO_2 nanowires grown on graphene using supercritical CO_2, Applied Catalysis B: Environmental, 110 (2011) 25-32.

[5] M.D. Hernández-Alonso, F. Fresno, S. Suárez, J.M. Coronado, Development of alternative photocatalysts to TiO_2: challenges and opportunities, Energy & Environmental

Science, 2 (2009) 1231-1257.

[6] C. Su, C. Shao, Y. Liu, Electrospun nanofibers of TiO_2/CdS heteroarchitectures with enhanced photocatalytic activity by visible light, Journal of Colloid and Interface Science, 359 (2011) 220-227.

[7] Y. Medina-Gonzalez, W.Z. Xu, B. Chen, N. Farhanghi, P.A. Charpentier, CdS and CdTeS quantum dot decorated TiO_2 nanowires: synthesis and photoefficiency, Nanotechnology, 22 (2011) 065603-065611.

[8] G.-S. Li, D.-Q. Zhang, J.C. Yu, A new visible-light photocatalyst: CdS quantum dots embedded mesoporous TiO_2, Environmental Science & Technology, 43 (2009) 7079-7085.

[9] L. Yang, S. Luo, R. Liu, Q. Cai, Y. Xiao, S. Liu, F. Su, L. Wen, Fabrication of CdSe nanoparticles sensitized long TiO_2 nanotube arrays for photocatalytic degradation of anthracene-9-carbonxylic acid under green monochromatic light, The Journal of Physical Chemistry C, 114 (2010) 4783-4789.

[10] P. Thakur, R. Chadha, N. Biswas, S.K. Sarkar, T. Mukherjee, S.S. Joshi, S. Kapoor, Synthesis and characterization of CdS doped TiO_2 nanocrystalline powder: A spectroscopic study, Materials Research Bulletin, 47 (2012) 1719-1724.

[11] M. Feng, H. Zhan, L. Miao, Facile assembly of cadmium sulfide quantum dots on titanate nanobelts for enhanced nonlinear optical properties, ACS Applied Materials & Interfaces, 2 (2010) 1129-1135.

[12] A. Pareek, R. Purbia, P. Paik, N.Y. Hebalkar, H.G. Kim, P.H. Borse, Stabilizing effect in nano-titania functionalized CdS photoanode for sustained hydrogen generation, International Journal of Hydrogen Energy, 39 (2014) 4170-4180.

[13] S. Arya, T. Vats, S.N. Sharma, K. Singh, A. Narula, Effect of mercaptopropionic acid as linker on structural, thermal, and optical properties of TiO_2–CdSe nanocomposites, Journal of Thermal Analysis and Calorimetry, 107 (2011) 555-560.

[14] S. Qian, C. Wang, W. Liu, Y. Zhu, W. Yao, X. Lu, An enhanced CdS/TiO_2 photocatalyst with high stability and activity: effect of mesoporous substrate and bifunctional linking molecule, Journal of Materials Chemistry, 21 (2011) 4945-4952.

[15] N. Guijarro, T. Lana-Villarreal, I. Mora-Seró, J. Bisquert, R. Gómez, CdSe quantum dot-sensitized TiO_2 electrodes: effect of quantum dot coverage and mode of attachment,

166

The Journal of Physical Chemistry C, 113 (2009) 4208-4214.

[16] D.R. Pernik, K. Tvrdy, J.G. Radich, P.V. Kamat, Tracking the adsorption and electron injection rates of CdSe quantum dots on TiO_2: linked versus direct attachment, The Journal of Physical Chemistry C, 115 (2011) 13511-13519.

[17] N. Ghows, M.H. Entezari, Sono-synthesis of core–shell nanocrystal (CdS/TiO_2) without surfactant, Ultrasonics Sonochemistry, 19 (2012) 1070-1078.

[18] M. Darbandi, G. Urban, M. Krüger, A facile synthesis method to silica coated CdSe/ZnS nanocomposites with tuneable size and optical properties, Journal of Colloid and Interface Science, 351 (2010) 30-34.

[19] M.N. Bahrami, K. Rezaee, M. Zobir, Facile synthesis of ZnS/CdS and CdS/ZnS core-shell nanoparticles using microwave irradiation and their optical properties, Chalcogenide Letters, 9 (2012) 379-387.

[20] C.V. Durgadas, K. Sreenivasan, C.P. Sharma, Bright blue emitting CuSe/ZnS/silica core/shell/shell quantum dots and their biocompatibility, Biomaterials, 33 (2012) 6420-6429.

[21] D. Bera, L. Qian, T.-K. Tseng, P.H. Holloway, Quantum dots and their multimodal applications: a review, Materials, 3 (2010) 2260-2345.

[22] H. Chen, W. Li, H. Liu, L. Zhu, Performance enhancement of CdS-sensitized TiO_2 mesoporous electrode with two different sizes of CdS nanoparticles, Microporous and Mesoporous Materials, 138 (2011) 235-238.

[23] M.A. Mumin, K.F. Akhter, P.A. Charpentier, Photo-physical properties enhancement of bare and core-shell quantum dots, AIP Conference Proceedings, 1590 (2014), pp. 259-265.

[24] P.A. Charpentier, W.Z. Xu, X. Li, A novel approach to the synthesis of SiO_2–PVAc nanocomposites using a one-pot synthesis in supercritical CO_2, Green Chemistry, 9 (2007) 768-776.

[25] R. Sui, P. Charpentier, Synthesis of metal oxide nanostructures by direct sol–gel chemistry in supercritical fluids, Chemical Reviews, 112 (2012) 3057-3082.

[26] N. Farhangi, S. Ayissi, P.A. Charpentier, Fe doped TiO_2–graphene nanostructures: synthesis, DFT modeling and photocatalysis, Nanotechnology, 25 (2014) 305601-305611.

[27] R. Sui, A.S. Rizkalla, P.A. Charpentier, FTIR study on the formation of TiO_2 nanostructures in supercritical CO_2, The Journal of Physical Chemistry B, 110 (2006) 16212-16218.

[28] R. Sui, A. Rizkalla, P.A. Charpentier, Experimental study on the morphology and porosity of TiO_2 aerogels synthesized in supercritical carbon dioxide, Microporous and Mesoporous Materials, 142 (2011) 688-695.

[29] A.I. Cooper, Porous materials and supercritical fluids, Advanced Materials, 15 (2003) 1049-1059.

[30] T. Luttrell, S. Halpegamage, J. Tao, A. Kramer, E. Sutter, M. Batzill, Why is anatase a better photocatalyst than rutile?-Model studies on epitaxial TiO_2 films, Scientific Reports, 4 (2014) 4043-4049.

[31] J. Zhang, P. Zhou, J. Liu, J. Yu, New understanding of the difference of photocatalytic activity among anatase, rutile and brookite TiO_2, Physical Chemistry Chemical Physics, 16 (2014) 20382-20386.

[32] M.A. Mumin, W.Z. Xu, P.A. Charpentier, Quantum dots/silica/polymer nanocomposite films with high visible light transmission and UV shielding properties, Nanotechnology, 26 (2015) 315702-315715.

[33] J.M. Allan, M.A. Mumin, W.Z. Xu, Q. Al Sharari, P.A. Charpentier, Surface functionalized bare and core–shell quantum dots in poly (ethylene-co-vinyl acetate) for light selective nanocomposite films, Solar Energy Materials and Solar Cells, 123 (2014) 30-40.

[34] K.-i. Ishibashi, A. Fujishima, T. Watanabe, K. Hashimoto, Quantum yields of active oxidative species formed on TiO_2 photocatalyst, Journal of Photochemistry and Photobiology A: Chemistry, 134 (2000) 139-142.

[35] K.-I. Ishibashi, A. Fujishima, T. Watanabe, K. Hashimoto, Detection of active oxidative species in TiO_2 photocatalysis using the fluorescence technique, Electrochemistry Communications, 2 (2000) 207-210.

[36] K. Park, H.J. Yu, W.K. Chung, B.-J. Kim, S.H. Kim, Effect of heat-treatment on CdS and CdS/ZnS nanoparticles, Journal of Materials Science, 44 (2009) 4315-4320.

[37] J. Liu, Z. Guo, W. Wang, Q. Huang, K. Zhu, X. Chen, Heterogeneous ZnS hollow urchin-like hierarchical nanostructures and their structure-enhanced photocatalytic

properties, Nanoscale, 3 (2011) 1470-1473.

[38] M. Bruchez, M. Moronne, P. Gin, S. Weiss, A.P. Alivisatos, Semiconductor nanocrystals as fluorescent biological labels, Science, 281 (1998) 2013-2016.

[39] Y. Huo, X. Yang, J. Zhu, H. Li, Highly active and stable CdS–TiO$_2$ visible photocatalyst prepared by in situ sulfurization under supercritical conditions, Applied Catalysis B: Environmental, 106 (2011) 69-75.

[40] D. He, M. Chen, F. Teng, G. Li, H. Shi, J. Wang, M. Xu, T. Lu, X. Ji, Y. Lv, Enhanced cyclability of CdS/TiO$_2$ photocatalyst by stable interface structure, Superlattices and Microstructures, 51 (2012) 799-808.

[41] W.Z. Xu, P.A. Charpentier, Light-selective nanofilms of quantum dot-poly (ethylene-co-vinyl acetate) synthesized with supercritical CO$_2$, The Journal of Physical Chemistry C, 113 (2009) 6859-6870.

[42] T.J. Macdonald, T. Nann, Quantum Dot Sensitized Photoelectrodes, Nanomaterials, 1 (2011) 79-88.

[43] H. Zhu, M.Z. Hu, L. Shao, K. Yu, R. Dabestani, M.B. Zaman, S. Liao, Synthesis and optical properties of thiol functionalized CdSe/ZnS (Core/Shell) quantum dots by ligand exchange, Journal of Nanomaterials, 2014 (2014) 1-14.

[44] M.N. Ghazzal, R. Wojcieszak, G. Raj, E.M. Gaigneaux, Study of mesoporous CdS-quantum-dot-sensitized TiO$_2$ films by using X-ray photoelectron spectroscopy and AFM, Beilstein Journal of Nanotechnology, 5 (2014) 68-76.

[45] Z.H. Ibupoto, K. Khun, X. Liu, M. Willander, Hydrothermal synthesis of nanoclusters of ZnS comprised on nanowires, Nanomaterials, 3 (2013) 564-571.

[46] J.C. Kim, J. Choi, Y.B. Lee, J.H. Hong, J.I. Lee, J.W. Yang, W.I. Lee, N.H. Hur, Enhanced photocatalytic activity in composites of TiO2 nanotubes and CdS nanoparticles, Chemical Communications, (2006) 5024-5026.

[47] H. Weib, A. Fernandez, H. Kisch, Electronic semiconductor–support interaction—A novel effect in semiconductor photocatalysis, Angewandte Chemie International Edition, 40 (2001) 3825-3827.

[48] T. Jamieson, R. Bakhshi, D. Petrova, R. Pocock, M. Imani, A.M. Seifalian, Biological applications of quantum dots, Biomaterials, 28 (2007) 4717-4732.

[49] M.T. Uddin, Y. Nicolas, C.l. Olivier, T. Toupance, L. Servant, M.M. Müller, H.-J.

Kleebe, J. Ziegler, W. Jaegermann, Nanostructured SnO2–ZnO heterojunction photocatalysts showing enhanced photocatalytic activity for the degradation of organic dyes, Inorganic Chemistry, 51 (2012) 7764-7773.

[50] J. Xian, D. Li, J. Chen, X. Li, M. He, Y. Shao, L. Yu, J. Fang, TiO_2 nanotube array-graphene-CdS quantum dots composite film in Z-Scheme with enhanced photoactivity and photostability, ACS Applied Materials & Interfaces, 6 (2014) 13157-13166.

[51] Q. Xiang, D. Lang, T. Shen, F. Liu, Graphene-modified nanosized Ag_3PO_4 photocatalysts for enhanced visible-light photocatalytic activity and stability, Applied Catalysis B: Environmental, 162 (2015) 196-203.

[52] M. Salehi, H. Hashemipour, M. Mirzaee, Experimental study of influencing factors and kinetics in catalytic removal of methylene blue with TiO_2 nanopowder, American Journal of Environmental Engineering, 2 (2012) 1-7.

[53] V.E. Fioletov, M.G. Kimlin, N. Krotkov, L. McArthur, J.B. Kerr, D.I. Wardle, J.R. Herman, R. Meltzer, T.W. Mathews, J. Kaurola, UV index climatology over the United States and Canada from ground-based and satellite estimates, Journal of Geophysical Research: Atmospheres 109 (2004) 1-13.

[54] E. Kapinus, T. Viktorova, Kinetics of the photocatalytic degradation of methylene blue on titanium dioxide, Theoretical and Experimental Chemistry, 46 (2010) 163-167.

[55] J. Pan, Y. Sheng, J. Zhang, J. Wei, P. Huang, X. Zhang, B. Feng, Preparation of carbon quantum dots/TiO_2 nanotubes composites and their visible light catalytic applications, Journal of Materials Chemistry A, 2 (2014) 18082-18086.

[56] J. Yu, W. Wang, B. Cheng, B.-L. Su, Enhancement of photocatalytic activity of mesporous TiO_2 powders by hydrothermal surface fluorination treatment, The Journal of Physical Chemistry C, 113 (2009) 6743-6750.

[57] W. Li, P. Sheng, H. Feng, X. Yin, X. Zhu, X. Yang, Q. Cai, Stable core/shell CdTe/Mn-CdS quantum dots sensitized three-dimensional, macroporous ZnO nanosheet photoelectrode and their photoelectrochemical properties, ACS Applied Materials & Interfaces, 6 (2014) 12353-12362.

[58] P. Chang, H. Cheng, W. Li, L. Zhuo, L. He, Y. Yu, F. Zhao, Photocatalytic reduction of o-chloronitrobenzene under visible light irradiation over CdS quantum dot sensitized TiO_2, Physical Chemistry Chemical Physics, 16 (2014) 16606-16614.

Chapter 7

Conclusions and Recommendations

7.1 Conclusions

Transparent polymer-inorganic nanocomposites films are of intense scientific and technological interest in recent years [1]. The integration of inorganic nanoparticles into a polymer matrix allows combining and improving both properties, while advancing new functional materials for multiple applications including photovoltaic (PV) encapsulants and commercial greenhouse coverings [2-4]. Poly(ethylene-*co*-vinyl acetate) (EVA) films have been found as ideal and widely used as PV encapsulants and commercial greenhouse coverings [5, 6]. Polymer films with luminescent nanomaterials offer a useful and promising approach to improve solar energy harvesting [7, 8]. Among different luminescent materials, semiconductor quantum dots (QDs) have the potential to abosorb broad range of UV light and selectively emit visible light, which can control plant growth in greenhouses or enhance PV panel efficiencies [2, 3, 9]. The principal objective of this work was to surface engineering of conventional cadmium based QDs to enhance both the photoluminescence and photostability, and incorporation within EVA films with improved dispersion and compatibility.

In the present work, highly photoluminescence and monodispersed CdS bare and CdS-ZnS core-shell quantum dots with 5 nm size were prepared by using a facile and modified (changed reaction temperature and duration) colloidal synthesis approach based on pyrolysis of the single molecule precursors and capping the CdS QDs with a thin layer of ZnS. To make both the bare and core-shell structure QDs more resistant against photochemical reactions, a mesoporous silica layer was grown on the QDs through a reverse microemulsion technique based on hydrophobic interactions. The QD core and silica shell size was tuned in a controlled fashion by maintaining the overall particle size around 60 nm. The photo-physical properties of encapsulated QDs were examined including morphology, absorption and emission, quantum yield, photostability etc. The photo-bleaching properties of both the bare and core-shell QDs were prevented by the silica encapsulation layer under continuous exposure of UV light. In addition, the encapsulated QDs can still emit visible light under excitation with UV radiation, enhancing the photo-luminescence and quantum yield.

The silica encapsulated QDs nanoparticles were easily incorporated into EVA co-polymer matrix by melt-mixing in a twin-screw extruder. SIlica encapsulated QDs showed excellent compatibility with EVA by AFM analysis. It was hypothesized that the polar siloxyl group of the silica nanoparticle surface would improve the dispersibility of the QDs in the EVA polymer network. The experimental films of different thickness were prepared for both types of QD samples at different loading concentrations. The light selective films with bare CdS QDs with encapsulation showed improved optical properties, showing a decrease of UV transmission and increase of diffuse transmission by retaining high visible light transmission. These optical properties were further enhanced in case of core-shell CdS-ZnS QDs, as the thin ZnS shell prevented the surface defect of core CdS.

Mesoporous silica nanoparticles (MSNs) layer not only improve the optical properties of QDs, it has potentiality to block long wave infrared light while transparent to UV and visible lights [10, 11]. This is one of the major limitations of commercial greenhouse films causing significant heat losses. Along with light selective properties, the thermal properties including thermicity and thermal conductivity of the experimental nanocomposite films were also examined. The effect of silica thickness on these thermal properties were also studied and compared with MSNs-EVA nanocomposites without the presence of QDs. The results demonstrate that the experimental MSNs showed improved infrared and thermal wavebands retention in the EVA transparent films compared to commercial silica additives, even at lower concentrations. Therefore, the novel EVA nanocomposite films show the possibility of simultaneously enhancing both the light selective and heat retention properties by using a single nano-additive.

Other than blending approach, EVA nanocomposites with silica encapsulated CdS-ZnS QDs were also synthesized by using a *grafting from* polymerization technique under supercritical CO_2. Silica encapsulated QDs were functionalized with a silane coupling agent followed by polymerization of ethylene and vinyl acetate monomers in presence of a synthesized initiator. The nanocomposite products showed enhanced distribution and stability of the nanoparticles as well as the optical properties.

The unique downshifting properties (converting UV to visible light) of QDs can also be used in photocatalysis applications by sensitizing TiO_2 with QDs as TiO_2, the mostly used photocatalyst can only be excited by a small UV fraction of solar light [12, 13]. In the present work, we have developed a facile process to fabricate nanocomposites from porous TiO_2 nanowires and bare CdS and core-shell CdS-ZnS QDs, where the QD particles are linked covalently to the titania surface through a bifunctional organic linker, mercapto propionic acid (MPA). High quality anatase TiO_2 nanowires were prepared using a sol-gel technique in $scCO_2$. The morphology and distribution of QDs on the TiO_2 surface was confirmed by XRD, TEM, SEM, and XPS. The bifunctional linking molecule, MPA, was found to effectively disperse and stabilize the QD nanoparticles. The FTIR and XPS results also confirmed the successful linking between QDs and TiO_2. UV-visible absorption analysis showed that strong interactions using the linked QDs and loading concentration played a key role to enhance lower wavelength visible light absorption of TiO_2 nanowires.

The photocatalytic activities of the prepared catalysts were evaluated under ultraviolet and visible light solar irradiation for the photodegradation of methylene blue (MB), an organic dye. The decomposition rate of MB was enhanced as follows: CdSZnS-MPA-TiO_2 > CdS-MPA-TiO_2 > CdSZnS-TiO_2 > CdS-TiO_2 > TiO_2 > P25. A maximum photodegradation efficiency of MB dye (~88%) was obtained by core-shell CdS-ZnS QDs linked with nano TiO_2 with 10% QD loading. After 3 cycling tests of degradation, the loss of photoactivity was significantly minimized (from 68% to 10%) by CdSZnS-MPA-TiO_2 compared to CdSZnS-TiO_2 (by direct deposition). This study also showed that core-shell structure of QDs and covalent linking is important for both activity and stability of heterogeneous photocatalysts.

7.2   Recommendations

The following recommendations will be useful in the future investigations of this study:

(a) It was observed that the ZnS thin shell significantly improves the fluorescence quantum yield and stability against photobleaching of core CdS QDs. Similar ZnS shells can also be examined for other non-cadmium based QDs, e.g. (Zn, Cu, In, Pb based).

(b) The successful encapsulation of both bare and core-shell QDs by mesoporous silica and the significant enhancement of both photoluminescence and photostability of QDs is encouraging to extend this method for encapsulating other QDs, especially non-cadmium based QDs.

(c) Both the encapsulated bare and core-shell QDs were integrated into EVA resins through melt-mixing by using a twin screw extruder for a fixed cycle time and rotation speed. These extrusion parameters can be varied to evaluate the effect on the optical properties of the films as well as the QDs distribution throughout the films.

(d) Silica encapsulation improved the photostability of both types of QDs, but photostability of these nanoparticles were not studied after incorporating within EVA matrix. The optical properties and stability of different types of experimental films can be investigated by keeping the film samples in a weathering chamber.

(e) In the case of *grafting from* polymerization under scCO$_2$, the vinyl acetate content of the nanocomposite was measured as around 33%, whereas the vinyl acetate content of EVA resin used during melt-mixing was around 10%. The amount of vinyl acetate monomer during polymerization can be optimized to change the final content to 10%. Then it is possible to compare the optical and thermal properties of the nanocomposites prepared by different approaches.

(f) Core-shell QDs covalently linked with TiO$_2$ nanowires showed the highest photocatalytic efficiency to degrade methylene blue, an organic dye. This can be done for

other pollutants of interest. The same nanocomposite materials can be used in photovoltaic cells and evaluate the photo-current efficiency.

(g) As silica encapsulated QDs showed better photostability, silica encapsulated QDs can be linked with TiO_2 nanowires and examine the photocatalytic efficiency. Proper selection or synthesis of the bi-functional linker is a critical part of the nanocatalysts fabrication.

7.3   References

[1] Z. Xu, C.R. Hine, M.M. Maye, Q. Meng, M. Cotlet, Shell thickness dependent photoinduced hole transfer in hybrid conjugated polymer/quantum dot nanocomposites: from ensemble to single hybrid level, ACS Nano, 6 (2012) 4984-4992.

[2] J.M. Allan, M.A. Mumin, W.Z. Xu, Q. Al Sharari, P.A. Charpentier, Surface functionalized bare and core–shell quantum dots in poly (ethylene-co-vinyl acetate) for light selective nanocomposite films, Solar Energy Materials and Solar Cells, 123 (2014) 30-40.

[3] W.Z. Xu, P.A. Charpentier, Light-selective nanofilms of quantum dot-poly (ethylene-co-vinyl acetate) synthesized with supercritical CO_2, The Journal of Physical Chemistry C, 113 (2009) 6859-6870.

[4] J.M. Allan, M.A. Mumin, J.A. Wood, W.Z. Xu, W. Wu, P.A. Charpentier, Silica aerogel–poly (ethylene-co-vinyl acetate) composite for transparent heat retention films, Journal of Polymer Science Part B: Polymer Physics, 52 (2014) 927-935.

[5] K. Agroui, G. Collins, Characterisation of EVA encapsulant material by thermally stimulated current technique, Solar Energy Materials and Solar Cells, 80 (2003) 33-45.

[6] C. von Zabeltitz, Integrated Greenhouse Systems for Mild Climates, Springer Berlin Heidelberg2011, pp. 285-311.

[7] L.H. Slooff, E.E. Bende, A.R. Burgers, T. Budel, M. Pravettoni, R.P. Kenny, E.D. Dunlop, A. Büchtemann, A luminescent solar concentrator with 7.1% power conversion efficiency, Rapid Research Letters, 2 (2008) 257-259.

[8] Y. Zhou, F.S. Riehle, Y. Yuan, H.-F. Schleiermacher, M. Niggemann, G.A. Urban, M. Krüger, Improved efficiency of hybrid solar cells based on non-ligand-exchanged CdSe quantum dots and poly (3-hexylthiophene), Applied Physics Letters, 96 (2010) 013304-013309.

[9] M.A. Mumin, W.Z. Xu, P.A. Charpentier, Quantum dots/silica/polymer nanocomposite films with high visible light transmission and UV shielding properties, Nanotechnology, 26 (2015) 315702-315715.

[10] M.A. Mumin, K.F. Akhter, S. Dresser, S.T. van Dinther, W. Wu, P.A. Charpentier, Multifunctional mesoporous silica nanoparticles in poly (ethylene-co-vinyl acetate) for transparent heat retention films, Journal of Polymer Science Part B: Polymer Physics, 53 (2015) 851-859.

[11] A. Schmid, J. Tonnar, S.P. Armes, A New Highly Efficient Route to Polymer-Silica Colloidal Nanocomposite Particles, Advanced Materials, 20 (2008) 3331-3336.

[12] G.-S. Li, D.-Q. Zhang, J.C. Yu, A new visible-light photocatalyst: CdS quantum dots embedded mesoporous TiO_2, Environmental Science & Technology, 43 (2009) 7079-7085.

[13] P. Thakur, R. Chadha, N. Biswas, S.K. Sarkar, T. Mukherjee, S.S. Joshi, S. Kapoor, Synthesis and characterization of CdS doped TiO_2 nanocrystalline powder: A spectroscopic study, Materials Research Bulletin, 47 (2012) 1719-1724.

Appendices

A-1 Biocompatibility of bare, core-shell, and silica encapsulated QDs

Semiconductor QDs are quickly becoming a critical diagnostic tool for discerning cellular function at the molecular level. They have tremendous potential as biological markers either *in vitro* or *in vivo*. This is due to their brightness, stability, and broad absorption and size-tunable controlled emission properties which sets them apart from conventional fluorescence dyes [1, 2]. However, toxicity and hydrophobicity of the as-prepared QDs limits their direct use in biological applications, requiring further processing or functionalization. Encapsulation of QDs by silica has been shown as an efficient approach providing long-term photostability and suitable photo-physical properties, while the silica surface can be modified or conjugated with various chemical functionalities for linking to biomolecules [3, 4].

Herein, human umbilical vein endothelial cell lines (HUVEC) were selected as an *in vitro* model to assess the vascular toxicity of both bare and core-shell QDs with and without silica encapsulation. HUVEC is the most commonly used cell type for *in vitro* study using cultured cell lines [5]. Endothelial cells synthesize and secrete various activators and inhibitors that influence the adhesion and aggregation of blood platelets. In addition, they also release mediators that control cell proliferation and modulate vessel wall tone [5]. HUVEC cell line have been used previously for cell uptake and biocompatibility study of various types of QDs [6-8] The internalization of the nanoparticles within the cell lines was visualized using Laser scanning confocal microscope (LSCM).

A-1.1 MTT Assay (biocompatibility study)

Human umbilical vein endothelial cell lines (HUVEC) EAhy926 (derived from the fusion of HUVEC with the A549 human lung epithelial carcinoma cell line) were cultured in a

medium (RPMI 1640 medium with glutamine and without sodium bicarbonate, purchased from Sigma-Aldrich, Canada) containing 10% fetal bovine serum and 1% penicillin/streptomycin amphotericin B antibiotic at 37°C under 5% CO_2 condition. Cells were seeded in 96 well plates at a density of $4x10^5$ cells/mL with different concentrations of QDs with and without encapsulation samples (0.5 – 500 µg/mL) and incubated for 24 hours. Cell viability was evaluated with the 3-(4,5-dimethylthiazol-2-yl)-2,5-diphenyltetrazolium bromide (MTT) assay.

After 24 hours, the culture medium was removed; 150µL MTT solution (0.5mg/mL) was added to each well and incubated for another 4 hours. Then, the medium was carefully removed from the plate, and DMSO was added to solubilize formazan produced from MTT by the viable cells. The amount of viable cells in each well was determined by the absorbance of solubilized formazan. Absorbance was measured at 540 nm using a microplate reader.

Biocompatibility is of prime importance for these nanomaterials using as cellular imaging probes and also to examine toxicological effect on human and animal health. Bare CdS QDs are reported to be toxic to cells, and their cytotoxicity becomes significant with increases in concentration of QDs (Figure A1-1). At a very low concentration (20 µg/mL) about 70% HUVEC cells were viable in presence of bare CdS QDs that was dropped down to less than 10% at a higher concentration of 1 mg/mL These observations are consistent with reported literature for similar type of QDs [7]. The higher level of cytotoxicity of bare QDs is due to the release of cadmium ions inside the living cells, leading to reactive oxygen species production and glutathione depletion [7]. A thin layer of nontoxic ZnS QDs on the CdS core can block the release of cadmium ions, hence increases the viability of the HUVEC cells. However, forming a perfect layer of ZnS on the CdS core is very difficult. Therefore, the silica layer is more effective to block the release of cadmium ions. As shown in Figure A1-1, the viability of the HUVEC cells was greatly enhanced in the case of silica encapsulated QDs. The cells viability was as high as more than 50% at the highest concentration of 1 mg/mL, highlighting the prominent biocompatibility achieved by the silica encapsulated QDs [7]. At a concentration of less than 20 µg/mL more than 90% HUVEC cells were viable.
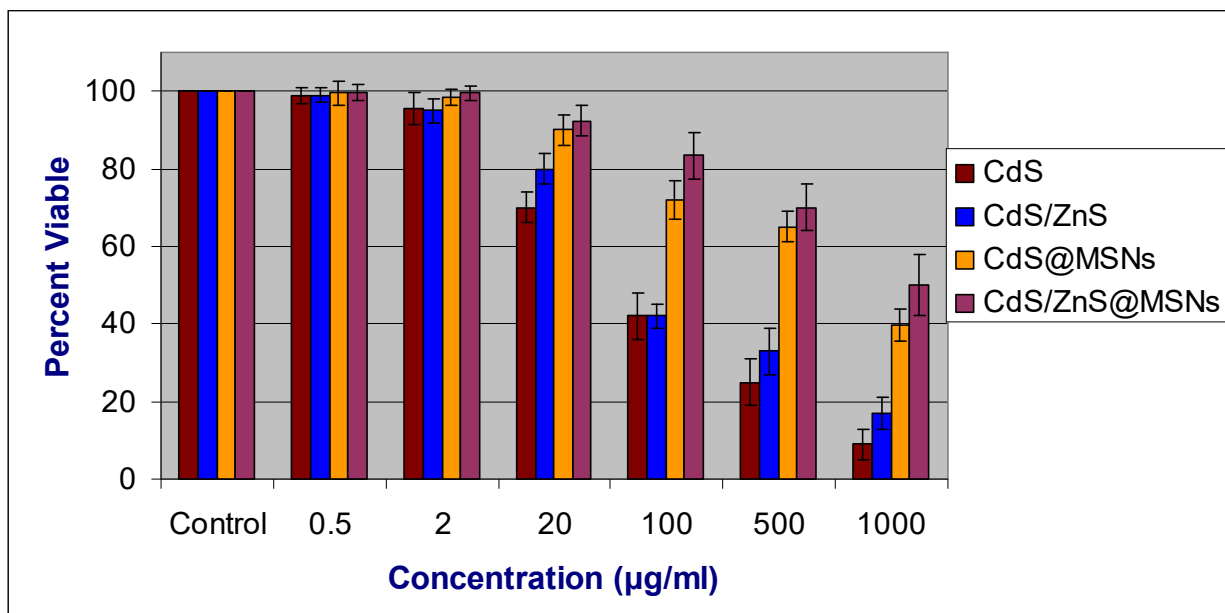
Figure A1-1. Cell viability of Human umbilical vein endothelial cell lines (HUVEC) labelled with different concentration of QDs with and without encapsulation for 24 h at 37°C as measured by MTT assay.

A-1.2 LSCM study (cell internalization)

The cellular uptake and endocytosis of the silica encapsulated CdS-ZnS QDs were studied by using a confocal microscope. The HUVEC cells were cultured with silica encapsulated QDs at a concentration of 50 µg/mL for 24 and 48 hrs at 37°C. After 24 and 48 h, the cells were separately washed 3X with PBS to remove extra nanoparticles that were not uptaken by the cells and imaged using laser scanning confocal microscopy. The images shown in Figure A1-2 give a bright green optical signal due to emission from the QDs in the cell interior. After 24 h most cells are uptaken by nanoparticles which is indicated by the green spots surrounding the nucleus. The intensity and saturation of green optical signal becomes even higher after 48 h clearly indicating the biocompatibility of the silica encapsulated QDs. There was no signs of morphological damage to the cells observed even after 48 h. Therefore, the observed results suggest that

silica encapsulated CdS-ZnS QDs are effective cell labels due to their enhanced photostability for extended period and their biocompatibility inside the cells.
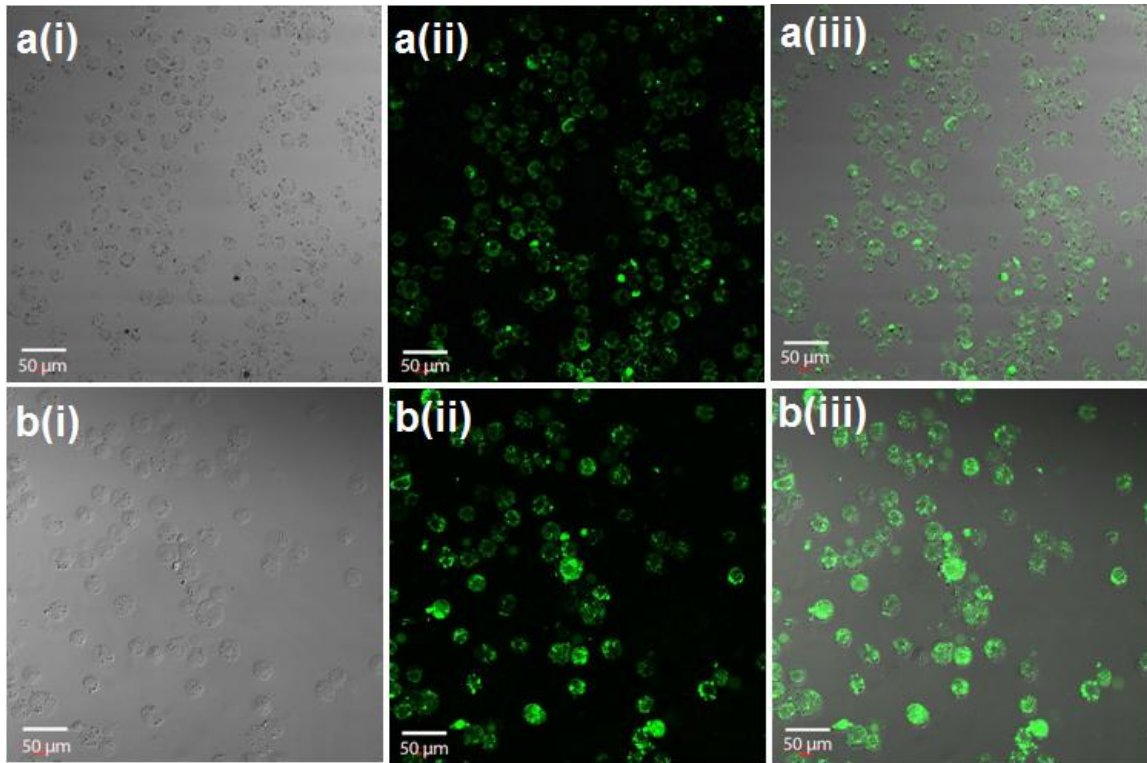

Figure A1-2. Laser scanning confocal microscopy images of Human umbilical vein endothelial cell lines (HUVEC) lebeled with different concentration of silica encapsulated CdS-ZnS QDs after (a) 24 h and (b) 48 h. [(i) bright field, (ii) fluorescence, and (iii) merged images].

A-1.3 References

[1] S.J. Rosenthal, J.C. Chang, O. Kovtun, J.R. McBride, I.D. Tomlinson, Biocompatible quantum dots for biological applications, Chemistry & Biology, 18 (2011) 10-24.

[2] C. Zhai, H. Zhang, N. Du, B. Chen, H. Huang, Y. Wu, D. Yang, One-pot synthesis of biocompatible CdSe/CdS quantum dots and their applications as fluorescent biological labels, Nanoscale Research Letters, 6 (2011) 31-35.

[3] M. Darbandi, G. Urban, M. Krüger, A facile synthesis method to silica coated CdSe/ZnS nanocomposites with tuneable size and optical properties, Journal of Colloid and Interface Science, 351 (2010) 30-34.

[4] M. Bruchez, M. Moronne, P. Gin, S. Weiss, A.P. Alivisatos, Semiconductor nanocrystals as fluorescent biological labels, Science, 281 (1998) 2013-2016.

[5] D.M. Morgan, Isolation and culture of human umbilical vein endothelial cells, Humana Press, New Jersey, (1996) pp101-109.

[6] I. Yildiz, B. McCaughan, S.F. Cruickshank, J.F. Callan, F.M. Raymo, Biocompatible CdSe− ZnS core− shell quantum dots coated with hydrophilic polythiols, Langmuir, 25 (2009) 7090-7096.

[7] S. Veeranarayanan, A.C. Poulose, M.S. Mohamed, Y. Nagaoka, S. Iwai, Y. Nakagame, S. Kashiwada, Y. Yoshida, T. Maekawa, D. Kumar, Synthesis and application of luminescent single CdS quantum dot encapsulated silica nanoparticles directed for precision optical bioimaging, International Journal of Nanomedicine, 7 (2012) 3769-3786.

[8] H. Li, M. Li, W.Y. Shih, P.I. Lelkes, W.-H. Shih, Cytotoxicity tests of water soluble ZnS and CdS quantum dots, Journal of Nanoscience and Nanotechnology, 11 (2011) 3543-3551.

Appendices A-2 (Copyright releases)

A-2.1

M. A. Mumin, W. Z. Xu, P. A. Charpentier, Quantum dots/silica/polymer nanocomposite films with high visible light transmission and UV shielding properties, *Nanotechnology* (2015) **26**, 3155702 (14pp)

Kathryn Shaw <Kathryn.Shaw@iop.org> on behalf of Permissions <permissions@iop.org>

Thu 2016-01-28 10:19 AM

To:Md Abdul Mumin <mmdabdul@uwo.ca>;

Dear M. Abdul Mumin,

Thank you for your email and for taking the time to seek this permission. I am sorry for any difficulty you have faced in finding the information which you seek. I hope that it has not caused too much inconvenience.

When you transferred the copyright in your article to IOP, we granted back to you certain rights, including the right to include the Accepted Manuscript of the article within any thesis or dissertation. Please note you may need to obtain separate permission for any third party content you included within your article.

Please include citation details and for online use, a link to the Version of Record.

The only restriction is that if, at a later date, your thesis were to be published commercially, further permission would be required.

Please let me know if you have any further questions.

In the meantime, I wish you the best of luck with the completion of your dissertation.

Kind regards,

Kathryn Shaw
Editorial Assistant
IOP Publishing

Please note: We do not usually provide signed permission forms as a separate attachment. Please print this email and provide it to your institution as proof of permission.

A-2.2

M. A. Mumin, K. F. Akhter, S. Dresser, S. T. vanDinther, W. Wu, P. A. Charpentier, Multifunctional mesoporous silica nanoparticles in poly(ethylene-co-vinyl acetate) for transparent heat retention films, *Journal of Polymer Science, Part B Polymer Physics*, (2015), **53**, 851-859

A-2.3

M. A. Mumin, G. Moula, P. A. Charpentier, Supercritical CO_2 synthesized TiO_2 nanowires covalently linked with core-shell CdS-ZnS quantum dots: enhanced photocatalysis and stability, *RSC Advances* (2015) **5**, 67767-67779.

Curriculum Vitae

Name:	Md Abdul Mumin

Post-secondary Education and Degrees:

The University of Western Ontario
London, Ontario, Canada
Sep. 2010- Apr. 2016 Ph.D.
Chemical and Biochemical Engineering

The University of Western Ontario
London, Ontario, Canada
Sep. 2008-Jul. 2010 M.E.Sc.
Chemical and Biochemical Engineering

Shahjalal University of Science and Technology
Sylhet, Bangladesh
B.Sc. Eng in Chemical Engineering and Polymer Science

Related Work Experience

Graduate Research Assistant
Laboratory of Alternative Solvents and Advanced Materials
The University of Western Ontario
Sep. 2010- present

Graduate Research Assistant
Multifunctional Nanocomposites Lab.
The University of Western Ontario
Sep. 2008- Aug. 2010

Teaching Assistant
The University of Western Ontario
Sep. 2008- Aug. 2014

Faculty
Chemical Engineering and Polymer Science
Shahjalal University of Science and Technology, Bangladesh
Feb. 2004 - Aug. 2008.

Publications:

- **M. A. Mumin**, W. Z. Xu, P. A. Charpentier, Quantum dots/silica/polymer nanocomposite films with high visible light transmission and UV shielding properties, *Nanotechnology* (2015) **26**, 3155702-315715.
- **M. A. Mumin**, G. Moula, P. A. Charpentier, Supercritical CO_2 synthesized TiO_2 nanowires covalently linked with core-shell CdS-ZnS quantum dots: enhanced photocatalysis and stability, *RSC Advances* (2015) **5**, 67767-67779.
- **M. A. Mumin**, K. F. Akhter, S. Dresser, S. T. vanDinther, W. Wu, P. A. Charpentier, Multifunctional mesoporous silica nanoparticles in poly(ethylene-co-vinyl acetate) for transparent heat retention films, *Journal of Polymer Science, Part B Polymer Physics*, (2015), **53**, 851-859.
- K. F. Akhter, **M. A. Mumin**, E. K. Lui, P. A. Charpentier, Microfluidic synthesis of ginseng polysaccharides nanoparticles for immunostimulating action on macrophage cell lines, *ACS Biomaterials Science and Engineering*, (2016) **2**, 96-103.
- J. M. Allan, **M. A. Mumin**, J. A. Wood, W. Z. Xu, Q. Sharari, P. A. Charpentier, Surface functionalized bare and core-shell quantum dots in poly(ethylene-co-vinyl acetate) for light selective nanocomposite films *Journal of Solar Energy Materials and Solar Cells*, (2014), **123**, 30-40.
- J. M. Allan, **M. A. Mumin**, W. Z. Xu, W. Wu, P. A. Charpentier, Silica aerogel-poly(ethylene-co-vinyl acetate) composite for transparent heat retention films *Journal of Polymer Science, Part B Polymer Physics*, (2014), **52**, 927-935.
- **M. A. Mumin**, K. F. Akhter, P. A. Charpentier, Photo-physical properties enhancement of bare and core-shell quantum dots, *American Institute of Physics Proceedings,*(2014) **1590**, 259-265.
- G. Moula, **M. A. Mumin,** Paul A. Charpentier, Enhancement of Photocurrent in dye-sensitized solar cells using Bismuth doped TiO_2-graphene as a hot carrier transport, *Journal of Nanomaterials and Molecular Nanotechnology*, (2013) (dx.doi.org/10.4172/2324-8777.S1-002).
- L. Chen, F. S. Razavi, **M. A. Mumin**, X. Guo, T-K. Sham, J. Zhang, Multifunctional nanoparticles for rapid bacterial capture, detection, and decontamination, *RSC Advances*, (2013), **3**, 2390-2397.
- **M. A. Mumin**, J. Barrett, G. Dekaban, J. Zhang, Dendritic cell internalization of foamed-structured fluorescent mesoporous silica nanoparticles, *Journal of Colloid and Interface Science,*(2011), **353**, 156-162.
- J. Li, J. Zhang, F. S. Razavi, **M. A. Mumin**, One-pot synthesis and characterization of rhodamine derivative-loaded magnetic core-shell nanoparticles, *Journal of Nanoparticle Research*, (2011), **13(5)**, 1909-1916.
- J. Zhang, L-M. Postovit, D. Wang, R. B. Gardiner, R. Harris, **M. A. Mumin**, A. A. Thomas, In situ loading of basic fibroblast growth factor (bFGF) within porous silica nanoparticles for a prolonged release, *Nanoscale Research Letter,* (2009), **4**, 1297-1302.
- J. Zhang, R. B. Gardiner, **M. A. Mumin**, R. Harris, Local release of basic fibroblast growth factor through silica nanoparticles laden biomimic matrix, *Mechanics of*

Biological and Biomedical Materials, MRS-Volume 1132E, Dec. (2008). 1132-Z09-07 (6 pages), Cambridge Journals Online.

- **M. A. Mumin**, M. M. R. Khan, K. F. Akhter, M. J. Uddin, Potentiality of open burnt clay as an adsorbent for the removal of Congo red from aqueous solution, *International Journal of Environmental Science and Technology*, (2007), **4(4),** 525-532.
- K. F. Akhter, **M. A. Mumin**, M. Z. Abedin, Determination and removal of Arsenic from water samples, *Sylhet International University Studies,* (2007), **1(2)**, 32-38.
- **M. A. Mumin**, K. F. Akhter, M. Z. Abedin, M. Z. Hossain, Determination and characterization of Caffeine in Tea, Coffee and Soft drinks by Solid phase extraction and High performance liquid chromatography (SPE-HPLC), *Malaysian Journal of Chemistry*, (2006), **8(1),** 45-51.
- K. F. Akhter, **M. A. Mumin**, M. Z. Abedin, M. N. Siddiquee, Determination of total vitamin C in various fruits and vegetables by SPE and Spectrophotometric method, *Oriental Journal of Chemistry*, (2005), **21(3),** 401-410.

Conferences Presentation:

- **M. A. Mumin**, P. A. Charpentier, Light selective nanocomposite films of poly(ethylene-co-vinyl acetate) incorporated with silica encapsulated quantum dots synthesized with supercritical CO_2 (oral presentation), 98th CSC conference and exhibition, Ottawa, ON, Canada (Jun. 2015).
- **M. A. Mumin**, P. A. Charpentier, Surface engineered quantum dots in poly(ethylene-co-vinyl acetate) for light selective nanocomposite films (oral presentation), 97th CSC conference and exhibition, Vancouver, BC, Canada (Jun. 2014).
- **M. A. Mumin**, P. A. Charpentier, Photovoltaic encapsulants with enhanced solar energy manipulation potentiality (poster presentation), Distinguished Lecture and Research Day, Centre for Advanced Materials and Biomaterials Research (CAMBR), the University of Western Ontario, London, ON, Canada (Nov. 2013).
- **M. A. Mumin**, J. Allan, P. A. Charpentier, Surface engineered quantum dots for light selective polymer films (oral presentation), American Institute of Chemical Engineering (AIChE) annual meeting, San Francisco, USA (Nov. 2013).
- **M. A. Mumin**, P. A. Charpentier, Photo-physical properties enhancement of bare and core-shell quantum dots, (Oral presentation) International Conference on Nanomaterials, the University of Western Ontario, London, ON, Canada (Aug. 2013)
- **M. A. Mumin**, P. A. Charpentier, Surface functionalized nanocrystals for solar-polymer films and photovoltaics, (poster presentation), Distinguished Lecture and Research Day, Centre for Advanced Materials and Biomaterials Research (CAMBR), the University of Western Ontario, London, ON, Canada (Nov. 2012).
- **M. A. Mumin**, G. Moula, J. Allan, P. A. Charpentier, Engineered quantum dots for light selective films with high photoluminescence and photostability, (oral presentation), American Institute of Chemical Engineering (AIChE) annual meeting, Pittsburgh, PA, USA (Nov. 2012).

- **M. A. Mumin**, P. A. Charpentier, Silica encapsulated quantum dots for light selective films with high photoluminescence and photostability, (poster presentation), 62nd Canadian Society of Chemical Engineering (CSChE) conference, Vancouver, BC, Canada (Oct. 2012).
- **M. A. Mumin**, P. A. Charpentier, Engineered quantum dots with high photoluminescence, photostability and biocompatibility, (oral presentation), 24th Canadian Material Science conference, UWO, London, ON, Canada (Jun. 2012)
- J. Allan, **M. A. Mumin**, and P. A. Charpentier, Light and heat selective polymer nanocomposites films for greenhouses (oral presentation), 61st Canadian Society of Chemical Engineering (CSChE) conference, London, ON, Canada (Oct. 2011)
- **M. A. Mumin**, J. Li, L. Chen, A. K. Ray and J. Zhang, Rapid pathogen capture by using "smart" nanoprobes (poster presentation), World discoveries research showcase, London, ON, Canada (Jan. 2010).
- **J. Zhang**, L. Postovit, M. A. Mumin, and A. A. Thomas, Prolonged delivery of basic fibroblast growth factor (bFGF) through silica nanoparticles-laden biomimic matrix (poster presentation), 8th world congress of chemical engineering, Montreal, QB, Canada (Aug. 2009).
- **M. A. Mumin**, R. B. Gardiner, L. Postovit, D. Wang, and J. Zhang, Photostable fluorescent loaded silica nanoparticles for biomedical applications (poster presentation), 2nd annual particle technology research centre conference, the University of Western Ontario, London, ON, Canada (Jul. 2009).
- **M. A. Mumin**, R. B. Gardiner, L. Postovit, D. Wang, and J. Zhang, Synthesis and characterization of fluorescent nanoparticles for bio-imaging (poster presentation), 92nd CSC conference and exhibition, Hamilton, ON, Canada (May 2009).
- **M. A. Mumin**, K. F. Akhter, M. Z. Abedin, and M. N. Siddiquee, Determination of Ascorbic acid and Dehydroascorbic acid in various fruits and vegetables of greater Sylhet area by HPLC (oral presentation). 15th Bangladesh Chemical Society Conference, Chittagong, Bangladesh (Mar. 2008).
- **G. M. Khan**, M. A. Mumin, and A. Yousuf, Removal of Arsenic from contaminated drinking water with locally available natural adsorbents; A low cost and sustainable arsenic mitigation approach for the poor village folks of Bangladesh (oral presentation). 9th ICOBTE, Beijing, China (Jul. 2007).

Honors & Awards:

- Awarded **MITACS** with industrial partner **S2E Technologies Inc.** for Sep.- Dec. 2013.
- Awarded **Ontario Graduate Scholarship (OGS) with Distinction** for 2013-2014.
- Awarded **Ontario Graduate Scholarship (OGS)** for year 2012-2013.
- Offered **Queen Elizabeth II Scholarship of Science and Technology** for 2012-2013.
- **Ivan Malek scholarship** (2011), awarded to a graduate student every year by the department of Chemical and Biochemical Eng, UWO, engaged in research in Biochemical Engineering.
- Awarded best session-oral presentation

(Title: Engineered quantum dots for light selective films with high photoluminescence and photostability)**;** Session-Functionalized materials and thin coating**,** American Institute of Chemical Engineering (AIChE) annual meeting/conference, Pittsburgh, PA, USA (Oct-Nov 2012)

- Awarded best oral presenter (second prize), Annual "Research Bridges" symposium for grad students of Chemical and Biochemical Eng, UWO, Sarnia, ON (May 2010)
- Vice Chancellor award: for outstanding result (First class first in the undergraduate level), SUST, Bangladesh.

Other Activities:

- Councilor of Society of graduate students (SOGS), University of Western Ontario, 2010-2013 (elected by Western Engineering students).
- Councilor of Western Engineering Society (WES), University of Western Ontario, 2010-2012 (elected by Western Engineering students).
- Steward, Graduate Teaching Assistants (GTA) union, University of Western Ontario, 2011-2012.
- Member of Chemical Engineering Grad Society (CGS), University of Western Ontario, 2010-2012 (Newsletter and social activities).
- Member of TA needs and bursaries (TANB) evaluation committee 2011-2012 (University of Western Ontario).
- Hosted a national conference as co-chair of graduate student committee, 61st Canadian Society of Chemical Engineering (CSChE) conference, London ON, Canada (Oct. 2011).
- Hosted a workshop on Nanobiotechnology for annual Canadian medical hall of fame/TD discovery day, the University of Western Ontario, London, ON, Canada (May 2009).